Nonlinear optoacoustics method for crack detection and characterization

Sylvain Mezil

▶ To cite this version:

Sylvain Mezil. Nonlinear optoacoustics method for crack detection and characterization. Other [cond-mat.other]. Université du Maine, 2012. English. NNT : 2012LEMA1029 . tel-01037936

HAL Id: tel-01037936
https://theses.hal.science/tel-01037936

Submitted on 23 Jul 2014

HAL is a multi-disciplinary open access archive for the deposit and dissemination of scientific research documents, whether they are published or not. The documents may come from teaching and research institutions in France or abroad, or from public or private research centers.

L'archive ouverte pluridisciplinaire **HAL**, est destinée au dépôt et à la diffusion de documents scientifiques de niveau recherche, publiés ou non, émanant des établissements d'enseignement et de recherche français ou étrangers, des laboratoires publics ou privés.

NONLINEAR OPTOACOUSTICS METHOD FOR CRACK DETECTION & CHARACTERIZATION

Sylvain Mezil

Doctoral thesis in Acoustics

Laboratoire d'Acoustique de l'Université du Maine UMR-CNRS 6613
LUNAM Université, Université du Maine, Le Mans, France, 2012

V. Tournat	CNRS Researcher, LAUM (Le Mans)	Supervisor
N. Chigarev	Engineer, LAUM (Le Mans)	Co-supervisor
V. Gusev	Professor, IMMM (Le Mans)	Co-supervisor
C. Prada	CNRS Research Director, ESPCI (Paris)	Reviewer
O. Bou Matar	Professor, IEMN (Lille)	Reviewer
D. Fournier	Emeritus Professor, INSP (Paris)	Chairman
T. Dehoux	CNRS Researcher, I2M (Talence)	Examiner
L. Ganjehi	Research Engineer, CEA (Saclay)	Examiner

LUNAM, Université du Maine, Académie de Nantes
Doctoral School of Science Engineering, Geoscience and Architecture

Doctoral Thesis in Acoustics

NONLINEAR OPTOACOUSTICS METHOD FOR CRACK DETECTION & CHARACTERIZATION

Sylvain Mezil

Defended on the 6th November 2012 in front of the examining committee:

Vincent Tournat	CNRS Researcher, LAUM (Le Mans)	Supervisor
Nikolay Chigarev	Engineer, LAUM (Le Mans)	Co-supervisor
Vitalyi Gusev	Professor, IMMM (Le Mans)	Co-supervisor
Claire Prada	CNRS Research Director, ESPCI (Paris)	Reviewer
Olivier Bou Matar	Professor, IEMN (Lille)	Reviewer
Danièle Fournier	Emeritus Professor, INSP (Paris)	Chairman
Lili Ganjehi	Research Engineer, CEA (Saclay)	Examiner
Thomas Dehoux	CNRS Researcher, I2M (Talence)	Examiner

LUNAM, Université du Maine, Académie de Nantes
École Doctorale: Sciences Pour l'Ingénieur, Géosciences, Architecture

Thèse de doctorat
Spécialité : Acoustique

MÉTHODE OPTOACOUSTIQUE NON LINÉAIRE POUR LA DÉTECTION ET LA CARACTÉRISATION DE FISSURES

Sylvain Mezil

Soutenue le 6 novembre 2012 devant le jury composé de :

Vincent Tournat	Chargé de Recherches CNRS, LAUM (Le Mans)	Directeur de thèse
Nikolay Chigarev	Ingénieur, LAUM (Le Mans)	Co-encadrant de thèse
Vitalyi Gusev	Professeur, IMMM (Le Mans)	Co-directeur de thèse
Claire Prada	Directrice de Recherches CNRS, ESPCI (Paris)	Rapporteure
Olivier Bou Matar	Professeur, IEMN (Lille)	Rapporteur
Danièle Fournier	Professeure Émerite, INSP (Paris)	Présidente du jury
Lili Ganjehi	Ingénieure-Chercheure, CEA (Saclay)	Examinatrice
Thomas Dehoux	Chargé de Recherches CNRS, I2M (Talence)	Examinateur

GENERAL INTRODUCTION

Ultrasounds are commonly used in nondestructive testing techniques. The use of ultrasounds allows to reach high frequencies, with short wavelengths, which is a usual condition required to detect small defects. The generation and detection of ultrasounds by lasers is at the basis of the laser ultrasonic techniques, or opto-acoustic techniques, which present the advantage, among others, of allowing contactless studies of a sample. Such absence of contacts makes the laser ultrasonic techniques suitable for any pressure and temperature conditions and suitable for nondestructive testing from a distance. It avoids the use of contact transducers which are sources of nonlinearities. The optoacoustic technique also provides a high spatial resolution because of the possibility to focus the beam down to micrometers. However, optoacoustic methods generally share the limitation to be weakly sensitive due to the poor optoacoustic conversion efficiency. On the other hand, nonlinear acoustic methods have been shown to be much more sensitive than linear ones.

Nonlinear optoacoustic techniques for nondestructive testing combine the contactless aspect of optoacoustics with the high sensitivity of nonlinear methods. Such a technique should improve the contrast of defect detection, important for many industrial applications. The present work explores a method for crack detection using a nonlinear optoacoustic method. The samples selected for the study are glass plates containing a crack -centimeter length and micrometer thick- prepared by thermal loading.

The developed method is based on the absorption of two light beams, independently modulated, and focused at the same location on the sample. This causes the generation of two waves, by thermal expansion.

The first one is a thermo-elastic wave at low frequency f_L ($\sim$ Hz), and the second is an acoustical one at high frequency f_H (tens of kHz). The thermoelastic wave can generate a crack breathing when a crack is present in the heated zone. The crack is expected to close when the intensity of the heating laser modulated at f_L is important and to open back when the intensity diminishes. This breathing influences the acoustic wave generated in the vicinity of the crack at f_H. As a result, there is a nonlinear frequency-mixing process, leading to the generation of new frequencies in the system, $f_H \pm nf_L$ ($n = 1, 2, \ldots$). The detection of these mixed-frequencies indicates the presence of a crack.

In a first part, one-dimensional and two-dimensional scans are achieved and demonstrate a clear crack detection and localization capability of the method. The influence of the pump frequency f_L, and of the beams focusing on the nonlinear sidelobe amplitudes (or mixed-frequency amplitudes) are theoretically and experimentally analyzed. The

spatial resolution, which depends on the method parameters and the crack properties, is also studied. It is demonstrated that, due to heat diffusion, the crack breathing can be achieved with a pump beam focused outside of the crack. Acoustic waves generated far from the crack can also propagate and interact with the breathing crack and in turn lead to the generation of nonlinear mixed-frequencies.
Two all-optical set-ups are proposed. Detection of the nonlinear mixed-frequencies can be achieved with vibrometry or deflectometry techniques. Detection by means of a lock-in amplifier is also realized and allows the use of the phase informations to detect cracks.

In a second part, the influence of the pump power on the nonlinear sidelobe amplitudes is studied. Nonmonotonous behaviors of the nonlinear sidelobe evolutions as a function of the pump power are detected and compared with theoretical predictions. The matching between theoretical and experimental evolutions leads to the evaluation of several crack parameters. In particular, the crack rigidity and the distance between the crack faces are estimated. The values of the forces and the temperature rises required to close and open the crack are also determined.
The evolution of the phase of the nonlinear sidelobes as a function of the pump power demonstrates the same minima, and also provide the possibility to observe the onset of the clapping, i.e., when the crack starts to breathe.

In a third part, a theoretical model is developed to consider the situation when the laser beams are focused at some distance from the crack. The model demonstrates that two processes can be responsible for the nonlinear frequency-mixing generation: the modulation of the crack rigidity or the modulation of the crack thermal resistance. The latter does not play a role for a symmetrical heating. Both phenomena generate the same nonlinear sidelobe amplitude evolutions as a function of the pump power. However, the process of thermal resistance modulation becomes dominant as the asymmetry increases. It is also observed that no acoustic wave can be doubly modulated by the crack rigidity and the crack thermal resistance modulations.

ACKNOWLEDGEMENTS

This thesis was done in the Laboratoire d'Acoustique de l'Université du Maine (LAUM) in Le Mans, France, and is the result of the work realized over three years: from October 2009 to October 2012. I would like to thank the people who contributed to this present work, either by direct contribution of the work or by making this PhD experience enjoyable.

My first thought goes to my supervisors Dr. Vincent Tournat, Dr. Nikolay Chigarev and Pr. Vitalyi Gusev. I am extremely grateful to them for their confidence in me, their numerous advises and their encouragements during this whole period. I especially appreciated the dynamism, pedagogy and constant enthusiasm they shared with me all along my PhD. Thanks to them I have been able to get involved in several aspects of research which was very formative. I know I would not have achieved that work without their help and I consider myself very lucky to have had Vincent, Nikolay and Vitalyi as supervisors. I also hope we will have other opportunities, in the future, to work together on other subjects.

I am very grateful to Dr. Claire Prada and Pr. Olivier Bou Matar for having reviewed this *'dense'* thesis, and to Pr. Danièle Fournier, Dr. Lili Ganjehi and Dr. Thomas Dehoux for their participation in the examination. Their interest in the methods developed here were particularly appreciated. Their comments and corrections helped me in having a more mature overview of my work and new perspectives for the future.
I am also thankful to Pr. Olivier Bou Matar and Pr. Pascal Ruello, in the frame of the thesis following committee, for their interest in my work and the precious advices they gave me all along my PhD.

I do not forget to thank James Blondeau for the technical help on the experiments, and the informatics softwares to control the equipments. He made several experiments possible and I want to thank him for his help.
Many thanks to Chenyin Ni with whom I shared the experimental room and some experimental tips.

The scientific context of this work also played an important role. I want to thank the director and co-director of LAUM, Yves Aurégan and Rachid El Guerjouma, respectively, and Joël Gilbert and Laurent Simon who succeeded their position. I want to thank them for their enthusiastic reception in the laboratory and their contribution to the life of

Université du Maine.

My financial support was provided by the Ministère de l'Éducation Nationale et de la Recherche Scientifique, and financial support for materials was provided by the French region Pays de la Loire. Thanks to those two organisations for supporting research.

I also want to thank particularly Jacques Cuenca and Frédéric Ablitzer for the constant help to my numerous questions, with a special gratitude to Jacques who read my PhD to correct the English.
I am also indebted to Bertrand Dubus for his several advices and suggestions, combined with support, all along this work.

I do not forget to thank the colleagues with whom I worked in the preparation of teaching laboratory sessions and tutorials: Jean-Michel Génevaux, Olivier Dazel, Charles Pézerat, Jean-Pierre Dalmont, Guillaume Pénelet, Philippe Béquin, André Almeida, Frédéric Ablitzer, Aurélien Merkel, Matthieu Guedra, Baptiste Bergeot, and Navid Nemati.

I am also grateful to my office colleagues for the good but nevertheless working ambient: Jacques Cuenca, Adrien Pelat, Jean-Michel Génevaux, Navid Nemati, Yousra Baccouche, and Antonin Tribaleau.

More generally, I would like to thank the PhD and post-doctorate students as well as all the staff of LAUM with whom I shared these three years and had numerous coffees and other drinks -including non non-alcoholic ones-, soccer games and several caustic moments. I think especially, in nonlinear order, to Jacques Cuenca, Frédéric Ablitzer, Georgios Theocharis, Tony Valier-Brasier, Jean-Philippe Groby, Vincent Tournat, Christophe Ayrault, Christoph Klieber, Matthieu Guédra, Thomas Pézeril, Vitalyi Gusev, Bruno Brouard, Gaël Favraud, Marcos Pinho, Ygaäl Renou, Simon Félix, Nikolay Chigarev, Clément Lagarrigue, Benoît Mérit, Bertrand Lihoreau, Aurélien Merkel, Jérémy Cabaret, Antonin Novák, Hélène Pichard, Gwenaëlle Vaudel, Vivien Denis, Miguel Moleron, and lots of others I probably forgot to quote. Thanks to all of them without whom this experiment would not have been that pleasant.

Finally, I also want to thank my friends and my family for their constant support and encouragements throughout the ups and downs, as well as for the different good times we shared together during all this time.

CONTENTS

List of symbols

The following list summarizes the main mathematical symbols used throughout this document, with their respective unit and a short description. Where no unit is given, the symbol is unitless.

General symbols

$\mathbb{R}$	Set of real numbers.
$\mathbb{N}$	Set of natural numbers.
$\mathbb{Z}$	Set of integers numbers.
m, n	Elements of $\mathbb{N}$.
$\Re e(z)$	Real part of z.
$\Im m(z)$	Imaginary part of z.

Time, frequency, space and wavenumber variables

t	s	Time.
f	s^{-1}	Frequency.
ω	$rad \cdot s^{-1}$	Circular frequency.
r, ϕ	m	Spatial coordinates in cylindrical coordinates system.
x, y	m	Spatial coordinates in the cartesian coordinates system.
i, j, k	m	Global coordinates system.
z	m	Space variable normal to the sample surface.

General physical parameters

T	K	Temperature.
σ	Pa	Stress.
u	m	Mechanical displacement.
U		Acoustic strain.
φ	rad	Phase shift.
c	$m \cdot s^{-1}$	Velocity of longitudinal waves.
F	$N.m^{-2}$	Force acting on a unit surface.
Λ	m	Acoustic wave wavelength.

Physical parameters of the sample and of the crack

ρ	kg·m^{-3}	Density.
K	Pa	Bulk modulus.
β	K^{-1}	Bulk thermal expansion coefficient.
μ	Pa	Shear modulus.
χ	m^2·s^{-1}	Thermal diffusivity.
c_p	J·kg^{-1}·K^{-1}	Specific heat.
κ	W·m^{-1}·K^{-1}	Thermal conductivity.
α	K^{-1}	Linear thermal expansion coefficient.
τ_T	s	Characteristic thermal relaxation time.
ω_T	Hz	Thermal relaxation frequency ($\tau_T = 1/\omega_T$).
η	N.m^{-3}	Rigidity of the crack per unit surface.
ν		Poisson's ratio.
R	K·m^2·W^{-1}	Thermal boundary resistance.
Q	W· m^{-2}	Heat flow.
d	m	Depth of the crack.

Physical parameters of the laser light

I_0	W·m^{-2}	Laser light intensity.
I	W·m^{-2}	Absorbed part of laser light intensity.
P	W	Power.
λ	m	Laser light wavelength.
a	m	Beam radius.
ш		Modulation depth of the laser beam ($0 \leqslant ш \leqslant 1$).
ℓ	m	Penetration length of light into the sample.
r		Reflection coefficient of light on the sample.
$f(t)$		Modulation of laser intensity in time.
$\Psi(x)$		Laser distribution in space on the sample surface.

Operators and miscellaneous symbols

$\jmath$		Imaginary number, $\jmath^2 = -1$.
∇	m^{-1}	Del vector differential operator.
Δ	m^{-2}	Laplacian operator.
$\widetilde{g}$		Fourier transform of g, defined as $\widetilde{g}(\omega) = \int_{-\infty}^{+\infty} g(t)e^{\jmath\omega t}dt$. Inverse Fourier transform is $g(t) = (2\pi)^{-1}\int_{-\infty}^{+\infty} \widetilde{g}(t)e^{-\jmath\omega t}d\omega$.
$\widehat{g}$		Laplace transform of g, defined as $\widehat{g}(p) = \int_0^{+\infty} g(t)e^{-px}dx$. Inverse Laplace transform is $g(x) = (2\pi\jmath)^{-1}\int_{-\jmath\infty}^{\jmath\infty} \widehat{g}(p)e^{px}dp$.
ε		Error estimation.
Erf		Error function, defined as $\mathrm{Erf}(x) = \frac{2}{\sqrt{\pi}}\int_0^x e^{-t^2}dt$.
Erfc		Complementary error function, defined as $\mathrm{Erfc}(x) = 1 - \mathrm{Erf}(x)$.
Erfi		Imaginary error function, defined as $\mathrm{Erfi}(x) = -\jmath \cdot \mathrm{Erf}(\jmath x)$.

Ei	Exponential integral, defined as $\mathrm{Ei}(x) = \int_{-\infty}^{x} \frac{e^t}{t} dt$.
δ	Kronecker symbol $\delta_{ij} = \begin{cases} 1 & \text{if } i = j; \\ 0 & \text{if } i \neq j. \end{cases}$
$\mathcal{I}_n$	Modified Bessel function of first kind of order n, defined by the contour integral: $\mathcal{I}_n(z) = \frac{1}{2\pi \jmath} \oint e^{(z/2)(t+1/t)}/t^{(n+1)} dt$.
sgn	Sign function $\mathrm{sgn}(x) = \begin{cases} 1 & \text{if } x > 0; \\ 0 & \text{if } x = 0; \\ -1 & \text{if } x < 0. \end{cases}$

Chapter 1

Introduction

Abstract

This study deals with the non destructive testing (NDT) with the goal of crack detection by a nonlinear optoacoustic technique. Before introducing the method itself, a summary of the generation of an acoustic wave by a laser beam in a solid is done. Then, an overview of the most common acoustic NDT methods in relation with the developed method is proposed. Finally the experimental set-up, together with a summary of the associated theoretical model are presented.

1.1 Generation of an acoustic wave by a laser

Optoacoustics and acoustooptics refer to the interactions between optical waves (i.e., electromagnetic waves), and acoustical waves. The difference between optoacoustics and acoustooptics is based on is based on the type of such interaction. An optoacoustic phenomenon or technique involves the influence of an electromagnetic wave on an acoustic wave such as the generation of acoustic waves by a light source. Conversely, acoustooptics denotes the effects of the propagation of an acoustic wave on an optical wave.

The interaction between these two different type of waves has first been observed by Bell in 1880 [6]. In his experiment, a closed gas volume is excited by a modulated light beam and an acoustic wave can be, as a result, heard. This discovery has shortly been confirmed by Tyndall [57] and Röntgen [49]. Then, a few other studies related to this observation have been realized but remained limited because of the difficulties to use a good light source. The apparition of maser in the late 50's and then of laser, providing a very good spatially localized amplified light source, opened new possibilities and led to lots of work on optoacoustics. Among them, the works of Askar'yan and Prokhorov in the USSR or White [59, 60] in the USA have been pioneer in the theoretical and experimental studies of optoacoustics.

The generation of an acoustic wave in a solid or a liquid can be achieved with a laser excitation. The excitation can be realized with a continuous laser modulated in intensity or a pulsed laser, such as picosecond or femtosecond lasers. Several physical mechanisms can lead to the generation of acoustic waves with a laser excitation. These mechanisms can either excite an acoustic wave at the same frequency as the electromagnetic wave or at the intensity modulation frequency, which is at much lower frequency. Piezoelectric and piezomagnetic mechanisms refer to the first case, whereas electrostriction, magnetostriction or thermal expansion, for example, to the second case. This work is focused only on the generation of an acoustic wave in a solid, supposed isotropic, by the thermal effect of a continuous wave laser (cw laser) modulated in intensity.

1.1.1 Optical excitation of sound in an isotropic solid

The generation of an acoustic wave by a cw intensity modulated laser can be the consequence of the thermoelastic effect. In the following description, the solid is supposed to be opaque at the wavelength of the laser: the solid absorbs at least part of the energy of the electromagnetic wave. This absorbed electromagnetic energy is converted into a thermal energy, provoking a local rise of the temperature. Consequently, a strain is created. Due to thermal diffusion, and in order to go back to its equilibrium state, the heat is transported into the sample. If the intensity of the electromagnetic wave is modulated at frequency f, the local temperature rise, and consequently the strain, is also modulated at frequency f. This modulation induces the generation of an acoustic wave at frequency f in the sample.
Analytically, this can be expressed writing firstly the equation of motion of an elastic medium:

$$\rho \frac{\partial^2 u_i}{\partial t^2} = \frac{\partial \sigma_{ik}}{\partial x_k}, \tag{1.1}$$

where the Einstein notation (summation over repeated indexes) is adopted, here and in the following. The stress is expressed as

$$\sigma_{ik} = -K\beta T \delta_{ik} + K u_{ll} \delta_{ik} + 2\mu \left(u_{ik} - \frac{\delta_{ik} u_{ll}}{3} \right), \tag{1.2}$$

with

$$u_{ik} = \left(\frac{\partial u_i}{\partial x_k} + \frac{\partial u_k}{\partial x_i} \right) \Big/ 2, \tag{1.3}$$

[27], leading to:

$$\rho \partial_{tt}^2 \vec{u} = -K\beta \nabla T + \left(K + \frac{1}{3}\mu \right) \nabla \left(\nabla \cdot \vec{u} \right) + \mu \Delta \vec{u}. \tag{1.4}$$

The other main equation of the optoacoustic problem is the heat conduction equation. The heat source is the laser, irradiating the surface sample (x, y). In its three dimensional form, for cartesian coordinates, and assuming the laser electromagnetic waves propagate in z direction, normal to the sample surface, the heat equation can be expressed as:

$$\frac{\partial T}{\partial t} = \chi \Delta T + \frac{I}{\ell \rho c_p} f(t) \Psi(x, y) e^{-z/\ell}. \tag{1.5}$$

The definition of the laser intensity distribution $\Psi(x, y)$ on the surface and its intensity modulation in time $f(t)$, combined with the sample parameters and the boundary conditions on temperature, allow to solve Eq. (1.5). The solution of Eq. (1.5) can be inserted in Eq. (1.4). With this solution, and the boundary conditions on strain it is possible to solve Eq. (1.4).

1.2 An overview of several relevant nonlinear NDT methods

Non-destructive testing deals with the detection of defects through the evaluation of some properties of the tested sample, and without damaging it. Numerous methods, involving various fields such as electromagnetism, optics, thermodynamics or mechanics have been developed to control and/or evaluate the sample under interest. Depending on the sample properties and on those of the defects that could be present in it, one or another technique can be more appropriate. However, they all share the ultimate goal to be sensitive and to have a high spatial resolution, relatively to the size of the defects. The need of an early detection of a defect generation necessitates a sensitive detection with a precise localization.

Nonlinear acoustic techniques are known to be very sensitive in the detection of defects such as cracks, delaminations, flaws, etc., [10, 34, 36, 55]. Numerous different physical nonlinear phenomena can be used such as self-action [41], acoustic harmonic generation [10, 37, 43, 55], acoustic subharmonic generation [53, 55], rectification [35], modulation transfer [67, 68], ... Techniques involving nonlinear acoustic approaches already provided the opportunity to realize two dimensional scans of a surface area and to detect and localize a defect [16, 34, 36, 48, 55, 70]. A short description of some of these methods are herein presented.

1.2.1 Nonlinear modulation of high-frequency bursts by a low frequency wave

The method developed by Kazakov *et al.* [34] consists in emitting with piezo-transducers two acoustic waves at very different frequencies. The sinusoidal low frequency wave ($\sim$ Hz) is combined with a group of high frequency tone bursts (of $\sim$ MHz central frequency). Phase and amplitude of each reflected tone burst are recorded. If the reflection comes from a linear scatterer, e.g., a hole or a material boundary, the tone bursts amplitude and phase remain constant. At the opposite, if they are reflected from a nonlinear scatterer, they are modulated by the low frequency wave.
The major drawback of this technique is the use of in-contact transducers for the excitation and the detection, which induces spatial resolution limitations. Firstly, it limits the size for defect detection: the high frequency wavelength must be similar to or smaller relative to the defect size to interact efficiently with it. MHz frequency range leads to a millimetric scale limitation. Secondly, spatial resolution is also limited by the estimation of the propagation time. In [34], for example, the time is recorded and digitized at rate 0.6 µs. For metals, with a sound velocity around 5000 m.s^{-1}, it gives an uncertainty of the defect position in the order of some millimeters. Finally, the transducer aperture

also limits the spatial resolution. In [34], authors indicate a 19 mm beam width, 100 mm away from the transducer.

1.2.2 Acoustic wave interaction with a defect

Thermographic methods use the local variation of the elastic and thermal properties [16, 48]. Elastic properties variations modify the stress field which, in turn, influences the conversion of acoustic energy into heat. As a consequence it results in a local temperature elevation, around the defect. Moreover, thermal properties variations influence the thermal waves transport. These two effects induce transient thermal anomalies around the defect which can be detected via an infrared camera, insuring the crack detection. This technique allows multiple types of defects detection such as cracks, delaminations, holes, scratches, ...

Spatial resolution is firstly limited by the IR camera resolution. In [16], the IR camera contains a 256×256 InSb focal plane array. Spatial resolution then inversely depends of the size of the analyzed image. For an image of about 12×12 mm^2, it goes down to about 47 microns by 47 microns per pixel [29]. Unfortunately, the local temperature elevation depends on the movement of the opposing surfaces of the defect. The distance and the rigidity between these opposing surfaces evolve along the defect and thus, the temperature elevation is not initiated at the same moment for the whole crack. Due to thermal diffusion, this elevation does not stay localized but is transported in the sample, which directly reduces the spatial resolution. Indeed, the defect presence is revealed by the mark corresponding to the thermal conversion (Fig. 1.1(a)), broadening in time as the heat is transported by diffusion process (Fig. 1.1(b) exhibits the same crack as in Fig. 1.1(a) taken 50 ms after). As a consequence, the spatial resolution of the images is limited by the detected thermal phenomenon itself. In Fig. 1.1(a), the spatial resolution can be estimated to ∼400 µm. Its ultimate resolution, assuming all the thermal heat is generated at the same time, is proportional to the square root of the thermal diffusivity of the sample and the time spent between two successive images from the IR camera. In [16], the delay between two images is of 1 ms and the sample is Al alloy. Thermal diffusivity of Al alloy is between 0.6 to 1 $\text{cm}^2.\text{s}^{-1}$. This leads to an ultimate resolution of $2 \cdot \sqrt{\chi \Delta t / \pi}$ between 280 and 360 µm, where the factor two describes the energy transport in the two opposite directions along the surface. Smaller defects would appear, if detected, with these dimensions. This technique allows more a detection than a localization. Besides, although millimetric length defects are detected, there are no publications, to our knowledge, demonstrating the feasibility of the technique for micrometric defects.

1.2.3 Nonlinear acoustic harmonics generation

The method proposed by Krohn *et al.* [36] and Solodov *et al.* [55] is an excitation of an acoustic wave, at frequency f, by transducers in contact with the sample. The detection of this frequency and the sub-, ultrasub- and/or super-harmonics is then realized by a laser vibrometer. A process, which is understood only qualitatively, makes some of the sub- and super-harmonics stay localized nearby the defects, where they have been generated. The decay of the acoustic wave amplitudes with distance influences this localization but the localization of these sub- and super-harmonics can be much better than the acoustical

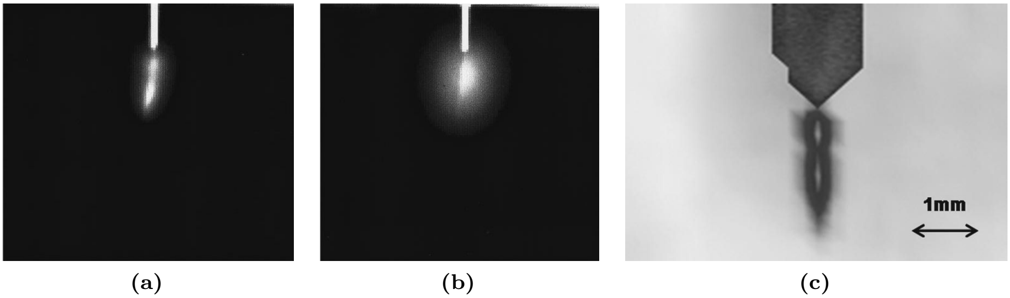

(a) (b) (c)

Figure 1.1: (a-b): Selection of two frames from [16] of sonic IR images of the crack taken immediately following the emission of the acoustical pulse (a) and after the 50 ms sonic excitation (b). (c): Image from [55] of a fatigue crack recorded by the ultrasubharmonic at 70 kHz and driven by 20 kHz input.

wavelength of the detected harmonic. In [55] for example, a 2,5 mm long, 5 µm thick crack in Ni-base superalloys is clearly detected with an apparent spatial resolution of hundreds of micrometers whereas the acoustic wavelength of the ultrasubharmonic at 70 kHz can be estimated at several centimeters (Fig. 1.1(c)). As long as the sub-, super- and suprasubharmonic localization process remains badly understood, one cannot say if a better spatial resolution is possible. The detection, realized with a laser vibrometer, can also play a role. In [55], there is no indication of the beam radius of the vibrometer. It is possible to focus the beam radius down to ∼10 µm, but it is not clear if the spatial resolution would be improved by this focusing or if the spatial resolution is limited by the harmonic localization.

The main drawback of the method is the contact between the emitter and the sample. This leads to the generation of spurious harmonics, which then mix with those due to the defect. These harmonics can also be generated during the wave propagation in the sample if the acoustic level and the propagation distance are important enough. As a consequence, there is a non negligible false alarm risk. In [36], on a healthy location, second and third harmonics are 10 dB over the noise while on a cracked location these harmonics are 40 dB over the noise. Thus, one cannot say if there is or not a crack with the result on the healthy location only. Another possible limitation is its spatial resolution.

1.2.4 Nonlinear interaction of an acoustic wave with a crack modulated by a heat flux

Zakrzewski *et al.* [70] suggest an excitation at two different frequencies f_L and f_H, both in a range of several tens of kHz. The first one, the pump wave, is launched by a piezoelectric transducer, in contact with the sample, whereas the second one, at f_H, the probe wave, is photoacoustically emitted through heating of the sample surface by an intensity-modulated laser beam. The amplitude of the pump wave is thus several orders of magnitude higher than the amplitude of the probe wave because of the low optoacoustic conversion efficiency. The resulting wave amplitudes at frequencies f_H, f_L,

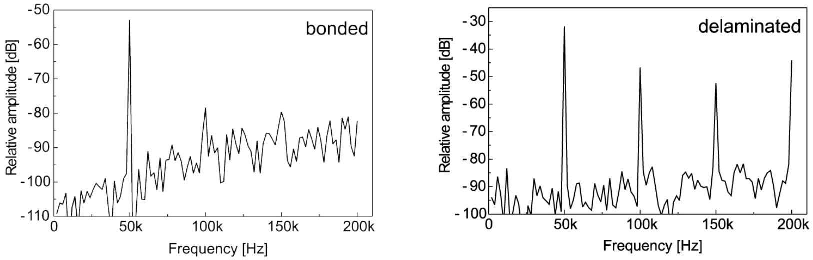

(a) **(b)**

Figure 1.2: (a-b): Spectra from [36] obtained for a delaminated Glass Fiber Reinforced Polymer (GFRP) sample when the vibrometer is focused off (a) and on the defect (b).

their harmonics, $2f_L$, $3f_L$, $2f_H$, . . . and also frequency-mixing at $f_H \pm f_L$ are detected by means of an accelerometer or a piezoelectric transducer, glued on the surface.
Several hypotheses have been proposed to explain this parametric modulation of a weak amplitude wave by a strong amplitude one in the vicinity of the crack. Firstly, the strain due to the pump wave modulates the crack width at frequency f_L. The mechanical strain of the acoustic wave excited by the piezoelectic transducer has been estimated as 10^{-6}, sufficient to influence the crack width. The one from the modulated laser, estimated as 3×10^{-11}, does not change the crack properties. This low strain is mainly due to the aluminium properties, in particular high reflectivity, and thermal diffusion. The reflection/transmission of acoustic waves incident on the crack is modulated at f_L by the pump wave. The thermal resistance of the crack is also modulated. Because a part of the laser field penetrates inside the crack, then the optical absorption in the vicinity of the crack could be also modulated by the pump wave. The combination of these three phenomena induces a modulation at frequency f_L of the acoustic waves of frequency f_H. This method offers a high spatial resolution as it is limited by the dimensions of the probe laser spot (∼200 µm in diameter in [70]) and not the acoustical wavelength (∼0.5 m in [70]). Moreover, the frequency-mixing process avoids problems of harmonic generation due to contacts between transducers and the sample. The main disadvantage of this method is the poor contrast obtained between the mixed frequency images and the linear images. Both linear and nonlinear frequencies have an amplitude contrast around 10 dB. This indicates that the excited nonlinearities are not much higher than those of the intact material. This is due to an insufficient modulation of the crack by the pump acoustic field emitted by the piezoelectric transducer. The mechanical strain is not important enough to induce at least partial crack closing.

1.3 Principle of the present method

1.3.1 Experimental set-up

The present method was first proposed by Chigarev *et al.* [14] and is based on the one proposed by Zakrzewski *et al.* (Sec. 1.2.4). The set-up has been improved in order to

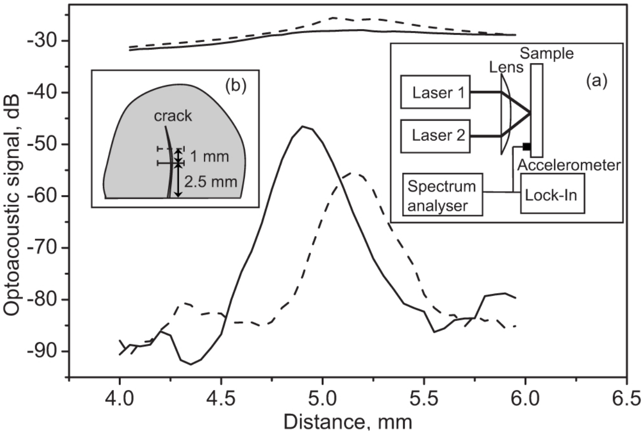

Figure 1.3: 1D scans from [14] of the photoacoustic signal at f_H (upper curves) and $f_H + f_L$ (lower curves) along the trajectories crossing the crack. The dashed and solid curves correspond to two trajectories marked in inset (b) respectively. Inset (a): the experimental set-up.

enhance the acoustical wave amplitudes inducing the nonlinear processes, and thus, the sensitivity of the method.
In order to avoid the nonlinearities due to contacts between transducers and samples, optical excitation is chosen in this work. The excitation is all-optical: both frequencies are photoacoustically generated, with two independent intensity-modulated laser beams at frequency f_L and f_H and focused on the same spot. The photo-generated thermoelastic wave, at frequency f_L, and the acoustic wave at f_H generated by the second intensity-modulated laser beam, are referred as the pump and the probe beams, respectively, in the following.
This technique has important differences with the earlier described (Sec. 1.2.4): the pump wave is generated with a laser at a lower frequency and the sample is changed for a glass plate instead of an aluminium plate.
A direct consequence of focusing the excitation is that the thermoelastic strain due to the pump can be locally much higher. The glass also favours higher strains for a laser excitation because of its low reflectivity ($\mathsf{r} \leqslant 10\%$ with a 800 nm laser wavelength as in [14]) and low thermal diffusion ($\chi = 5.0 \cdot 10^{-7}$ m^2·s^{-1}) compared to aluminium ($\mathsf{r} \simeq 0.9$, $\chi = 8.42 \cdot 10^{-5}$ m^2·s^{-1}). The strain in the center of the beam is estimated as 10^{-3}, several orders of magnitude higher than in [70]. The crack can be closed with such a strain. The radial displacement of the particles in the heated region is estimated up to 100 nm. It has already been demonstrated that surface crack closing is achievable with thermoelastic stresses [14, 18, 62, 63].
The frequency f_L is chosen several orders of magnitude lower than previously, down to $\sim$ Hz. With a low frequency intensity-modulated laser irradiation it is possible to ensure successively crack closing and opening. This corresponds to crack breathing [14].

An opened crack can be modeled by to parallel faces separated by a gap. Then, an acoustic wave with a frequency f_H, propagating toward the crack is totally reflected

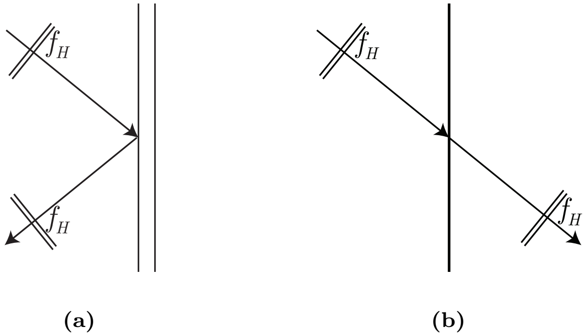

Figure 1.4: (a): Schematic representation of an acoustic wave reflected by an opened crack. (b): Schematic representation of an acoustic wave transmitted by a closed crack.

by the crack. The reflected wave propagates from the crack with the same f_H frequency (Fig. 1.4(a)).
A completely closed crack can be modeled as if there is no crack. The transmission of the acoustic wave by the crack is total and does not modify the frequency of the acoustic wave either (Fig. 1.4(b)). Both opened and closed crack interactions with an acoustic wave are linear processes.
If the width of the crack is modulated, at frequency f_L, from an opened crack to a closed crack by an external loading, it produces a nonlinear process. The acoustic wave is partly reflected and partly transmitted. The amplitudes of the reflected and transmitted waves are modulated low frequency f_L. It is common to say that the wave interacting with the crack is parametrically modulated, i.e., is modulated by the variation of the crack parameters. The modulation of the monochromatic wave amplitude in the time domain is equivalent to frequencies mixing in the spectral domain. The frequency of each of the waves (both of the reflected and of the transmitted), is influenced by its interaction with the crack, breathing at frequency f_L. It results in the nonlinear generation of the mixed-frequencies $f_H \pm f_L$ both in reflection and in transmission. The generation of nonlinear frequency-mixing by the interaction of an acoustic wave with a breathing crack has been already demonstrated experimentally [10, 41, 52, 70] and theoretically [19, 21, 22, 23, 24, 26].
The method is based on the presence of a pump beam, intensity modulated at f_L, coincident with a probe beam, intensity modulated at f_H (Fig. 1.5). The pump beam modulates the crack width in order to provide the crack breathing. The probe beam generates an acoustic wave which interaction with the breathing crack induces the generation of the nonlinear mixed-frequencies.

A complete breathing ensures much higher acoustical nonlinearities compared to only crack width variations [70]. Among the different phenomena evoked in Sec. 1.2.4, acoustic reflectivity between the crack faces, in particular, varies up to 100% between an opened crack and a completely closed one. It is theoretically demonstrated that the changes of the state of the crack, opened or closed, influence the efficiency of the

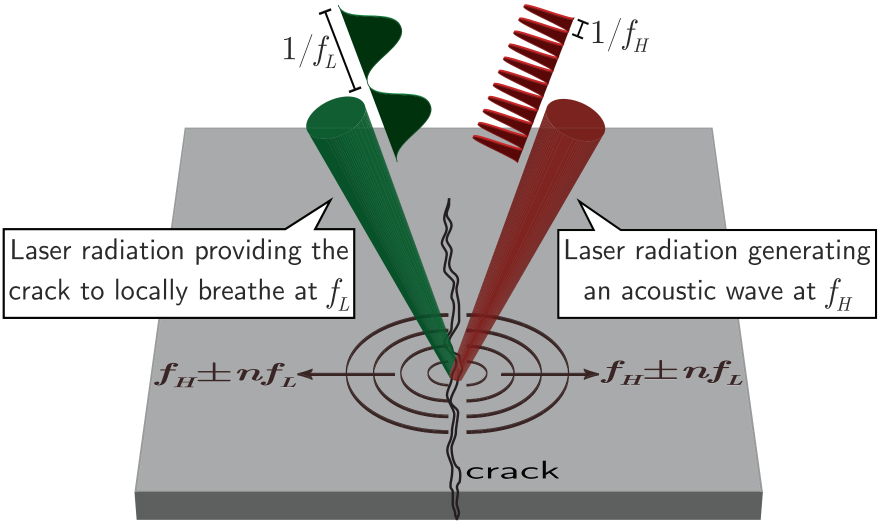

Figure 1.5: Schematic representation of the principle of the method.

thermoacoustic conversion, resulting in the frequency-mixing [20]. Consequently, the contrast of frequency-mixing components compared to linear components is drastically larger in this technique (Fig. 1.3). The elasticity of the crack and the distance between its faces are the two parameters influencing the breathing, so the method. Other parameters which do not influence the crack motion, such as the crack orientation, are irrelevant.
The mixed acoustic frequencies $f_{m\pm n} = mf_H \pm nf_L$ are necessarily generated by nonlinear processes and not by a cross-talk between the independent excitation lasers. This is an advantage in comparison to methods relying on sub- and superharmonic excitation [36, 53, 55]. Moreover, nonlinearities due to the clapping of a crack are several orders of magnitude higher than those possible due to the intrinsic sample properties [14].
Another benefit of laser excitation is its spatial resolution. The method is based on the presence of crack breathing in the acoustic wave generation spot. Consequently, the two beams must be superposed and can be focused down to diameter of about a hundred micrometers.
The signal detection is achieved with an accelerometer, placed far enough from the excitation to receive a small signal amplitude, especially from the thermoelastic wave, in order to avoid additional nonlinearities.
The method relies on the breathing dependance, ∼100 nm thick cracks or locally thin slots, for example, can be detected but not bigger defects or defects such as scratches where no breathing can occur.

1.3.2 Theoretical model

An analytical model has been developed in order to explain the apparition of the mixed acoustic frequencies [20]. This section is a brief summary of the main steps to solve this theoretical problem.
The resolution of the problem is done for a 1D geometry. The sample is assumed infinite

to ensure no reflected wave by the boundaries for simplicity. The origin of x-axis is defined as the center of the crack (Fig. 1.6(b)). The sample is separated into two half-infinite domains, one for x positive and one for x negative. The probe and the pump beams are supposed to heat the crack symmetrically from each face. Then, it is possible to study only one of the half-infinite domain. The one for positive x is chosen.
As the sample is supposed infinite, thermal expansion is unrestricted. Then, as the crack has a certain rigidity, thermal expansion induced by a constant heating is transported to infinity where the motion is assumed unconstrained. Consequently, the crack width cannot be influenced by a constant heating. Constant heating due to the laser beams, especially to the probe beam, can be neglected in this idealized theory.

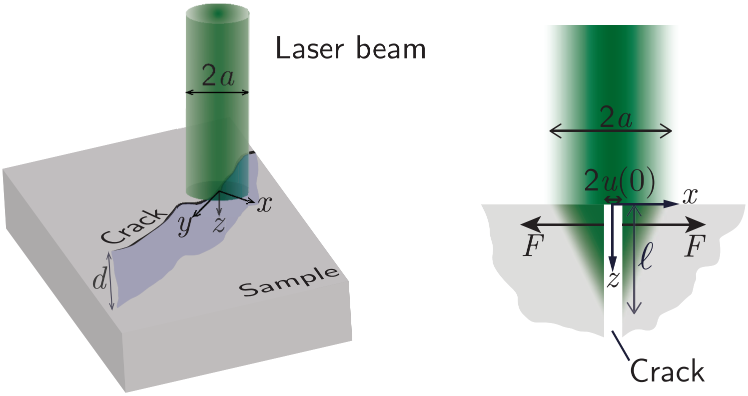

(a) **(b)**

Figure 1.6: (a): Schematic presentation of the relative positions of the laser beam of radius a, and the crack of the characteristic depth d. (b): Section view presenting the penetration length ℓ, the force F and the displacement $u(0)$.

The crack is idealized by two parallel faces and, due to the 1D assumptions, infinite in depth. Figure 1.6(a) and 1.6(b) are schematic representations of the problem. The penetration length of the light is assumed infinite in the z axis. On the surface, the optical absorption of the laser beam is localized at a distance of one beam radius for each half-infinite domain. The boundary conditions at the crack faces, at $x = 0$, are specific to this problem. The crack can be seen as two surfaces in $x = 0^-$ and $x = 0^+$ interacting through the surface force $F[u(x = 0^+) - u(x = 0^-)]$ depending on the relative displacement of the faces. The boundary conditions for the total stress can then be written: $\sigma(x = 0^+) = -F[u(x = 0^+) - u(x = 0^-)] = \sigma(x = 0^-)$. Due to the assumption of a symmetrical loading, it follows that $u(x = 0^-) = -u(x = 0^+)$ and thus $\sigma(x = 0) = -F[2u(x = 0)]$. Finally, it appears that $2u(0)$ represents the initial crack width, where the notation $u(0)$ refers to $u(x = 0)$ [2, 3, 7, 26, 30, 38, 41, 44].

Now that the boundary conditions are established, the problem can be solved using Eq. (1.1) and Eq. (1.2) reduced for a one dimensional isotropic solid, so there is only one index left. The equations of motion and the boundary condition can then be presented:

$$\frac{\partial^2 u}{\partial x^2} - \frac{1}{c^2}\frac{\partial^2 u}{\partial t^2} = \frac{K\beta}{\rho c^2}\frac{\partial T}{\partial x}, \tag{1.6}$$

$$\frac{\partial u}{\partial x}(0) - \frac{K\beta}{\rho c^2}T(0) = -\frac{F[2u(0)]}{\rho c^2}. \tag{1.7}$$

The problem is then solved applying a Fourier transform over time and a Laplace transform over space. The condition of radiation takes the form:

$$\left(-\jmath\frac{\omega}{c}\right)\widetilde{u}(\omega,0) - \frac{\widetilde{F}[2u(0)]}{\rho c^2} = -\frac{K\beta}{\rho c^2}\left(-\jmath\frac{\omega}{c}\right)\widehat{T}\left(\omega,-\jmath\frac{\omega}{c}\right), \tag{1.8}$$

where $\widehat{T}(\omega,p)$ corresponds to the temperature in the Fourier-Laplace domain. The acoustic strain can also be calculated. It is defined as the derivative of the acoustical displacement over x: $U = \partial u/\partial x$. The strain spectrum is equal to:

$$\widetilde{U}(\omega) = \frac{K\beta}{2\rho c^3}(\jmath\omega)\left[\widehat{T}\left(\omega,\jmath\frac{\omega}{c}\right) - \widehat{T}\left(\omega,-\jmath\frac{\omega}{c}\right)\right] - \frac{\widetilde{F}[2u(0)]}{\rho c^2}, \tag{1.9}$$

where the first terms, containing $\widehat{T}$, represent the acoustic strain generated near a mechanically free surface and the last term, containing $\widetilde{F}$, the variation in time of the effective interaction force F between the crack faces.

The determination of both the crack motion from Eq. (1.7) and the acoustic spectrum Eq. (1.9) necessitates the evaluation of the laser-induced temperature variations $\widehat{T}(\omega,p)$ in the Fourier-Laplace domain. Eq. (1.5) should then be solved for the 1D model. However, the temperature growth induced by cw laser heating is saturated due to the 3D character of the heat conduction process. In the 1D approximation, thermal diffusion does not compensate the temperature rise. Consequently, the solution of Eq. (1.5) diverges up to infinity. In order to avoid this issue and take into account the physical saturation, a characteristic thermal relaxation term is added into the 1D heat equation. This relaxation time has a sense of cooling time of the laser heated region in the 3D geometry due to the heat transport in the two additional directions y and z. An estimation of this time, as a function of the parameters of the heated sample and of the exciting laser, is proposed in Sec. 5.2.2. Meanwhile, the 3D equation (Eq. (1.5)) modified into a 1D form with the introduced thermal relaxation time τ_T becomes:

$$\frac{\partial T}{\partial t} + \frac{T}{\tau_T} = \chi\frac{\partial^2 T}{\partial x^2} + \frac{I}{\ell\rho c_p}f(t)\Psi(x). \tag{1.10}$$

The solution in Fourier-Laplace domain of Eq. (1.10), using the condition of radiation for thermal waves [31] and the boundary condition $\partial T/\partial x = 0$ at $x = 0$ (due to the symmetrical heating) is:

$$\widehat{T}(\omega,p) = \frac{I}{\ell\kappa}\cdot\frac{1}{p^2 - {p_T}^2}\left[\frac{p}{p_T}\widehat{\psi}(p_T) - \widehat{\Psi}(p)\right]\widetilde{f}(\omega), \tag{1.11}$$

with $p_T = \sqrt{(\omega_T - \jmath\omega)/\chi}$ ($\Re e(p_T) \geqslant 0$) the thermal wave number and $\omega_T = 1/\tau_T$.

For a monochromatic modulation of laser radiation $f(t) = [1 + \text{ш}\cos(\omega t)]$. Eqs. (1.8), (1.9), and (1.11) lead to the description of the harmonic generation [19, 26, 41]. Eq. (1.8) can be reduced using (1.11). In the time domain, it has the following form:

$$\frac{\partial u(0)}{\partial t} - \frac{1}{\rho c} F[2u(0)] = -|A(\omega)| I \text{ш} \cos[\omega t - \varphi(\omega)], \tag{1.12}$$

with

$$A(\omega) = |A(\omega)| e^{\jmath\varphi(\omega)} = -\frac{K\beta}{\ell\kappa\rho c^2} \cdot \frac{\jmath\omega}{\left(\frac{\omega}{c}\right)^2 + {p_T}^2} \left[\frac{\jmath\omega/c}{p_T}\widehat{\psi}(p_T) + \widehat{\Psi}(-\jmath\frac{\omega}{c})\right]. \tag{1.13}$$

Eq. (1.12) takes the form of the equation of a nonlinear relaxator driven by a monochromatic excitation [26]. In this analysis, this equation is generic for the description of the interaction of the acoustic wave generated in the vicinity of the crack with the crack itself.
In the case of an excitation by two lasers intensity modulated at two different cyclic frequencies ω_L and ω_H, it follows that $If(t) = I_L[1 + \text{ш}_L \cos(\omega_L t)] + I_H[1 + \text{ш}_H \cos(\omega_H t) - \varphi_{HL}]$ where φ_{HL} is the phase shift. Assuming that, as $\omega_L \ll \omega_H$, the presence of additional high-frequency excitation on the crack motion is negligible compared to the low-frequency excitation. Mathematically, it can be expressed $|A(\omega_H)| I_H \text{ш}_H \ll |A(\omega_L)| I_L \text{ш}_L$. We retrieve Eq. (1.12) written for the low-frequency excitation wave:

$$\frac{\partial u_L(0)}{\partial t} - \frac{1}{\rho c} F[2u_L(0)] = -|A(\omega_L)| I_L \text{ш}_L \cos[\omega_L t - \varphi(\omega_L)]. \tag{1.14}$$

The mechanical relaxation frequency of the crack ω_R, proportional to the crack rigidity, is introduced. At instant t, $\omega_R = 2\eta/(\rho c)$, where $\eta = \eta(t)$ can be modified by laser heating. For a linear interaction between the faces of the crack, $F[2u(0)] = -\eta u(0)$. The acoustic strain can be rewritten as:

$$\widetilde{U}(\omega) = \frac{K\beta}{2\rho c^3}(\jmath\omega)\left[\widehat{T}\left(\omega, \jmath\frac{\omega}{c}\right) - \widehat{T}\left(\omega, -\jmath\frac{\omega}{c}\right) + \frac{2\omega_R}{\omega_R - \jmath\omega}\widehat{T}\left(\omega, -\jmath\frac{\omega}{c}\right)\right], \tag{1.15}$$

where only the third term depends on the rigidity of the crack whereas the first two describe the sound generation near a mechanically free surface [4]. Consequently, this third term is the one responsible for the parametric frequency-mixing process and is the only one studied, denoted with a subscript η. The first two terms are omitted. The solution for the acoustic strain wave in the time domain -with $\tau = t - x/c$ the retarded time frame- and for a monochromatic laser intensity modulation at ω_H described as previously, can be obtained by inverse Fourier transform of Eq. (1.15). It reads:

$$U_\eta(\tau) = -\frac{1}{c}\left|A(\omega_H)\right| I_H \text{ш}_H \frac{\omega_R}{\sqrt{{\omega_R}^2 + {\omega_H}^2}} \cos\left[\omega_H \tau - \varphi(\omega_H) - \operatorname{atan}(\omega_H/\omega_R) - \varphi_{HL}\right]. \tag{1.16}$$

From Eq. (1.16) it follows that both the amplitude and the phase of high-frequency wave emitted at ω_H are affected by the evolution of the mechanical relaxation frequency of the crack as it depends on $\eta = \eta(t)$. So, Eq. (1.16) demonstrates that by changing $\eta(t)$, it is possible to modulate the harmonic signal amplitudes. It is now required to evaluate the variation of the crack width from Eq. (1.14), and to evaluate the evolution of ω_R in time.

An approximation of the force F between the crack faces as a function of the width $2u(0)$ of the crack is proposed [11, 12, 19, 26, 30, 32, 33, 41, 52]. This model (Fig. 1.7(b)) is a piece-wise linear approximation of a real dependence (Fig. 1.7(a)). The crack is assumed to be able to be in two different states with different crack widths: opened or closed. To each state corresponds a different rigidity, η_o (η_c) when the crack is opened (closed). The transition between the states occurs when the distance between the faces is h_i. Above and below this transition, the crack is considered opened and closed, respectively. Fig. 1.7(b) is a schematic representation of the evolution of the force F between the crack faces as a function of the width $2u(0)$ of the crack, where F_c (F_o) is the force required to close (open) the crack. A pattern of the evolution of $F[2u(0)]$ is presented in Fig. 1.7(c), assuming that the loading force reaches a force F higher than F_c, required to make the crack breath. Without any external force, the crack is at its stable position h_o, denoted by A in Fig. 1.7(c). Then, when a force is applied, the crack width diminishes until reaching point 'B'. If the force still increases, the crack suddenly closes and 'jumps' to position 'C'. Afterwards, it goes up to position 'D' which corresponds to the maximum thermal stress of the excitation. The intensity then goes down and the crack opens back. It opens back beyond position 'C': the crack width $2u(0)$ increases, but the crack remains in closed state, until position 'E'. Then, it suddenly goes back to position 'F' and continuous to decrease to position 'A', its initial position. The path, 'F'→'A' however, assumes that the excitation frequency is small enough for the crack to restore its initial position: the movement is quasistatic. For non-quasistatic cases, the crack does not retrieve completely its initial width when the excitation process is on, but goes back to an intermediate position, between 'F' and 'A'.

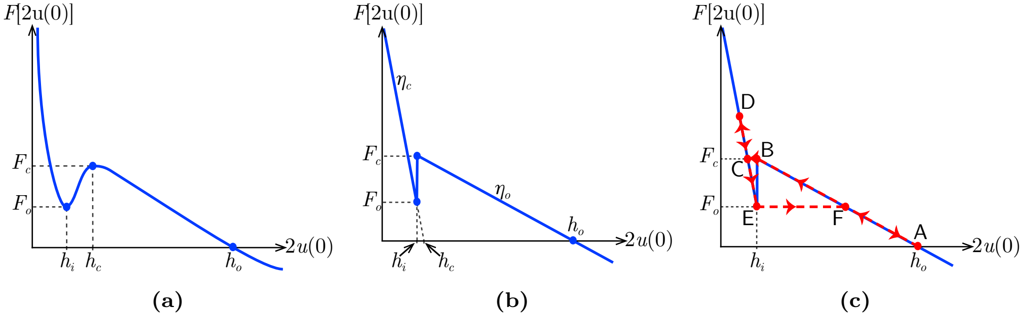

(a) (b) (c)

Figure 1.7: Interaction force F between the crack faces as a function of the width $2u(0)$ of the crack. (a): Qualitative realistic representation, (b): the accepted piece-wise linear approximation, and (c): illustration of the crack width variation under quasistatic loading assuming the loading force exceeds the force F_c required to close the crack; otherwise, the rigidity of the crack does not change in time.

For $F_o \leqslant F[2u(0)] \leqslant F_c$ three different crack widths are possible in Fig. 1.7(b). However, as the crack 'jumps' from one state to the other (from 'B' to 'C' or 'E' to 'F'), only two are stable and the section 'B' to 'E' is not relevant. Mathematically, this behavior can be described as:

$$F[2u(0)] = \begin{cases} -\eta_o[2u(0) - h_o] & \text{if } h_i \leqslant 2u(0) \leqslant \infty, \\ -\eta_c[2u(0) - h_c] & \text{if } 0 \leqslant 2u(0) \leqslant h_i. \end{cases} \tag{1.17}$$

Eq. (1.17), leads to $F_{c,o} = \eta_{o,c}(h_{o,c} - h_i)$. It is physically meaningful that the crack is more rigid in the closed state than in the opened state, which corresponds mathematically to the condition $\eta_o \ll \eta_c$. Mechanical relaxation frequencies of the crack can also be introduced. They characterize the crack motion in the state, either opened or closed, of the crack and are defined as: $\omega_{o,c} = 2\eta_{o,c}/(\rho c)$.
The forces, defined in the problem, correspond to the forces acting on the unit surface. So the forces are in $\mathrm{N.m}^{-2}$ and the rigidity are in $\mathrm{N.m}^{-3}$.

Assuming that the crack mechanical relaxation frequencies are much higher than the cyclic frequency ω_L at which the probe beam is intensity modulated, $\omega_L \ll \omega_{o,c}$, the problem is quasistatic. Then, the first term of Eq. (1.14) is omitted, and this equation becomes:

$$F[2u_L(0)] = \rho c|A(\omega_L)|I_L \text{Ш}_L \cos[\omega_L t - \varphi(\omega_L)]. \tag{1.18}$$

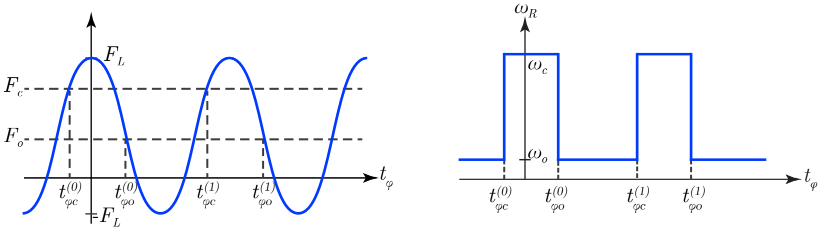

(a) **(b)**

Figure 1.8: (a): Graphical evolution of the force under sinusoidal thermoelastic loading of the crack as a function of the time. The times $t_{\varphi o}^{(r)}$ and $t_{\varphi c}^{(r)}$ correspond to crack opening and closing, respectively, and include the phase delay. (b): Variation in the crack mechanical frequency ω_R between its value in opened state ω_o and in closed state ω_c in response to sinusoidal loading presented in (a).

From Fig. 1.8 and Eq. (1.18), the crack is closed during the time $T_c = [\arccos(F_o/F_L) + \arccos(F_c/F_L)]/\omega_L$ and is opened during the time $T_o = 2\pi/\omega_L - T_c$. This model is used to describe the periodic variation in the mechanical relaxation frequency ω_R in time. It is finally possible to rewrite Eq. (1.16):

$$\begin{aligned} U_\eta(\tau) = & \frac{1}{c}|A(\omega_H)|I_H \text{Ш}_H \frac{\omega_H(\omega_c - \omega_o)}{\sqrt{{\omega_c}^2 + {\omega_H}^2}\sqrt{{\omega_o}^2 + {\omega_H}^2}} \frac{1}{\pi} \sum_{n=-\infty}^{+\infty} |A_n| \times \cos[(\omega_H + n\omega_L)\tau + \\ & - \varphi_n - \varphi(\omega_H) - n\varphi(\omega_L) - \operatorname{atan}(\omega_H/\omega_c) - \operatorname{atan}(\omega_H/\omega_o) - \varphi_{HL} - \pi/2], \end{aligned} \tag{1.19}$$

with

$$|A_n| = \left|\frac{1}{n}\sin\left[n\frac{1}{2}\omega_L T_c\right]\right| \tag{1.20a}$$

$$= \left|\frac{1}{n}\sin\left[n\frac{1}{2}\left(\text{acos}\left[\frac{F_c}{F_L}\right] + \text{acos}\left[\frac{F_o}{F_L}\right]\right)\right]\right| \tag{1.20b}$$

and

$$\varphi_n = -n\frac{1}{2}\left[\text{acos}\left(\frac{F_c}{F_L}\right) - \text{acos}\left(\frac{F_o}{F_L}\right)\right] - \text{acos}\left(\frac{A_n}{|A_n|}\right). \tag{1.21}$$

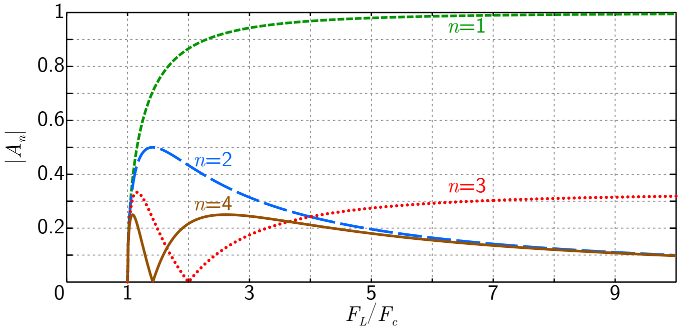

Figure 1.9: Dependence of the amplitude $|A_n|$ of the first four sidelobes as a function of the continuously varying amplitude of the normalized force F_L/F_c loading the crack at frequency f_L in the absence of hysteresis between F_c and F_o.

The functions $|A_n|$ and φ_n describe the dependence of the amplitude and phase, respectively, of the n^{th} sidelobe as a function of the loading amplitude F_L, where the n^{th} sidelobe corresponds to the sidelobe at frequency $\omega_H \pm n\omega_L$. Both the amplitude and the phase of a sidelobe are symmetrical between the sidelobes $+n$ and $-n$.

The crack width is influenced by the modulated part of the loading pump. The evolution of the crack rigidity as a function of the loading is defined in Eq. (1.17), and results in a non-sinusoidal crack breathing (Fig. 1.8(b)). The spectrum of the signal depends on the parameters of this breathing (Eq. (1.19)). In particular, the nonlinear sidelobes amplitude depends on the function $\sin(n\omega_L T_c/2)$ where n is the rank of the considered harmonic, and T_c the time spent by the crack in the closed state (Eq. (1.20a)). For a given sidelobe, and for a fixed frequency of the pump beam, T_c is the only parameter which can evolve.

From Fig. 1.7, and the definition of T_c ($T_c = [\text{acos}(F_o/F_L) + \text{acos}(F_c/F_L)]/\omega_L$), it appears that if the loading increases, T_c increases. This demonstrates that it is possible to influence the time spent in the closed region by varying the pump loading and that such variations influence the amplitude of the sidelobes (Eq. (1.20a)).

For an infinite loading with a 100% modulation, the crack spends half time of the pump period in the closed state and the other half in the opened state ($T_c = T_o = \pi/\omega_L$). Then, by increasing the pump loading, T_c can vary from 0 to $T_L/2$, where T_L is the pump period.

This sinus dependence implies that the evolution of the sidelobes as a function of the pump loading is non monotonous. Besides, for particular values of T_c, the sidelobe amplitude can be null. From Eq. (1.20a), this condition is fulfilled if $n\omega_L T_c/2 = k\pi$ ($k \in \mathbb{R}$), equivalent to $T_c = k/(n-k) \cdot T_o$. This indicates that for a specific time spent in the closed state, a sidelobe amplitude can be null.
A first observation is that if $T_c = 0$ or $T_c = 2\pi/\omega_L$, corresponding to the cases of an opened and a closed crack, respectively, the amplitude of all sidelobes is null. This correlates with the previous discussion on these linear cases and the necessity of the crack breathing. In the following, T_c is assumed to be larger than 0.
For $n = 1$, the amplitude is null if the crack spends the whole period in the closed state which is impossible (as $0 \leqslant T_c \leqslant T_L/2$). The first sidelobe can never have a zero amplitude.
The second sidelobe can have a zero amplitude if $T_c = T_o$, corresponding to the case where the crack spends half time of the pump period in both state. Mathematically, this is possible for an infinite loading. It can be easily demonstrated that the zero amplitude for an infinite loading is observed for all even nonlinear sidelobes.
For higher sidelobes, the time spent in the closed state by the crack required to obtain a zero amplitude decreases. Then, it is possible, by modifying the pump loading, to observe a zero amplitude, on one sidelobe, at a specific loading. For example, it can be demonstrated that the amplitude of the third sidelobe is null if the crack spends one third of the pump period in closed state. Assuming no hysteresis ($F_o = F_c$), Eq. (1.20b) indicates that this condition is fulfilled for $F_L/F_c = 2$. Consequently, for the particular case where the maximum of the pump loading equals twice the force F_c required to close the crack, the amplitude of the third sidelobe is null. The sixth sidelobe amplitude, and all $(3n)^{\text{th}}$ sidelobe amplitudes, are also null for this particular loading.
The same logic is valid for higher sidelobes. As n increases, more minima are observed on the sidelobes.

An evolution of the sidelobes up to $n = 4$, assuming a case without hysteresis, $F_c = F_o$, is presented in Fig. 1.9. The horizontal axis is the ratio F_L/F_c, starting when the crack begins to breathe, for $F_L = F_c$.
The amplitude minima on the third and fourth sidelobes for $F_L/F_c = 2$ and 1.41, respectively, is clear. The vanishing of the even sidelobes also appears.
The first nonlinear sidelobes ($n = \pm 1$) are, as predicted, the only monotonous sidelobes. Their amplitudes increase as the loading force increases. However, the growth rate reduces as the loading force increases. Almost 90% of the amplitude maximum is reached for $F_L/F_c = 2$. At the opposite, evolutions of higher sidelobes ($|n| > 1$) are clearly non monotonous. The second sidelobes quickly increase until $F_L/F_c \simeq 1.4$ and then slowly decrease. Consequently, for $F_L/F_c > 1.4$, an increase of the pump power leads to a decrease of the second sidelobe amplitudes. For higher sidelobes the behavior becomes more complicated due to the appearance of the amplitude minima.

This overview of the theoretical model is focused on the parts that are used in the following and is a summary of [20]. The influence of other parameters, and much deeper descriptions are proposed in [20].

Structure of the document

Part I deals with the experimental set-up in order to better understand the influence of each parameters, the limitation of the technique, and to improve the set-up. In chapter 1, the experimental set-ups and parameters are described and one-dimensional (1D) and two-dimensional (2D) scans are achieved. Chapter 2 demonstrates the importance of the crack breathing and the spatial resolution of the method is evaluated as a function of the different parameters involved. Finally, thanks to the better understanding of the method, improvements of the set-up are realized.

Part II discusses the role of the pump power on the evolution of the nonlinear sidelobes. The theoretical model is improved and compared with experimental results. From this comparison, the evaluation of crack parameters is achieved. A second chapter studies the other phenomena related to the pump power. Among them, an important part is dedicated to experiments with unexpected observations.

Part III consists in the development of the theoretical model. The introduction of asymmetrical heating, in relation to the crack, into the generation of the frequency-mixing components is proposed.

Part I

Characterization of the set-up and propositions for improvements

CHAPTER 2

PRESENTATION OF THE GENERAL SET-UP

Abstract

The goal of this chapter is to present the experiment in detail, to test it and to experimentally demonstrate the necessity of both beams. In a first part the two different set-ups used during the experiments are presented. The experimental parameters are then described. The validation of the method with a 1D scan is proposed and the importance of both beams is studied. Two-dimensional scans of a crack are also achieved.

2.1 Optical Excitation

One of the main differences in the excitation of the set-up from [14] is the use of a 532 nm, 2 W cw laser (Coherent Inc., Verdi) for the laser pump. Modulation of pump beam intensity is realized by an acousto-optic modulator (AA Opto-Electronics Inc., Model MQ180) controlled by a generator (Agilent 33120A). The 100% modulation is possible taking advantage of the first order diffracted beam after the AOM. This allows a more efficient crack breathing as the latter depends on the temperature difference of the heated point, defined by the difference between the maximum and the minimum temperature rise in time (see Chap. 3). The use of the first order diffracted beam by the AOM drastically reduces the power of the pump beam. However, the 2 W possibility of the cw laser,

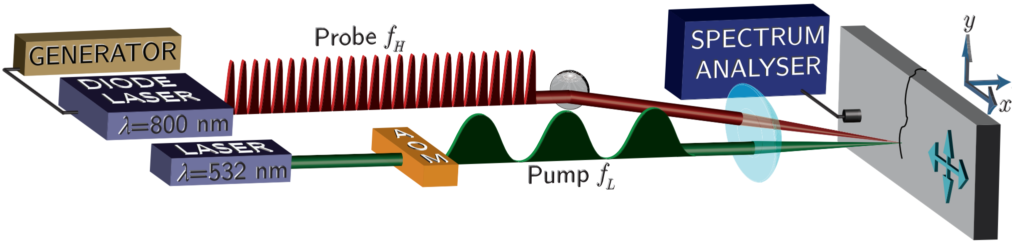

Figure 2.1: Schematic representation of the set-up denoted as Υ_2 and corresponding to the case where the excitation of the pump and probe beams are achieved by two different lasers.

compared to the power needed to provide crack breathing (from tens to a few hundreds of milliwatts in the experiments) is found to be sufficient.

The probe beam is generated by two means, depending on the situation: either as in [14] with a diode laser (Thorlabs LDC 220) (Fig. 2.1), modulated at high frequency ($\sim$ tens of kHz) by modulation of the current from its power supply with a generator (Agilent 33120A), either by the Verdi laser (Fig. 2.2) by the use of a second acousto-optic modulator. In both cases, the probe beam intensity is 100% modulated. As a consequence, in all the experiments, all the beams are 100% intensity modulated, leading to the fact that the modulation coefficient $\mathbb{m}$ is systematically equal to 1. When both beams are emitted by the Verdi laser, the initial beam is polarized elliptically with a half-wave plate. Then the beam is split into two beams by means of a polarizing beamsplitter cube. This allows to modulate independently both the probe and the pump beam to avoid the generation of nonlinear frequency-mixing in the excitation device itself. Then, both beams are merged with the use of a second polarizing beamsplitter cube.

In both cases, the two beams are focused on a single spot on the sample with different radii for the pump and the probe beams, varying from a few tens micrometers up to about a hundred micrometers.

In the following, the set-up where the excitation process is realized only with the Verdi laser, corresponding to Fig. 2.2, is referred as Υ_1, whereas the second set-up with the use of the Verdi and the diode laser, Fig. 2.1, is referred as Υ_2. Note that the subscript corresponds to the number of lasers involved in the experiment.

These two different set-ups, Υ_1 and Υ_2 have their own advantages and drawbacks. The bad beam quality of the diode laser provides a lower quality focusing than the one of the Verdi laser. Consequently, Υ_1 offers a set-up where both beams have a high quality and high focusing. On the other hand, because of the use of a single laser, the power of the probe and pump beams cannot be controlled independently. This necessitates another step in the experimental process to optimize the power ratio on each beam (See Sec. 2.4), and thus Υ_2 can be considered more practical for a faster crack detection. The change of the wavelength, between 800 and 532 nm, does not affect a lot the properties involved in the experiments -penetration length of light into the sample and reflection coefficient of light by the sample- (see Sec. 2.2).

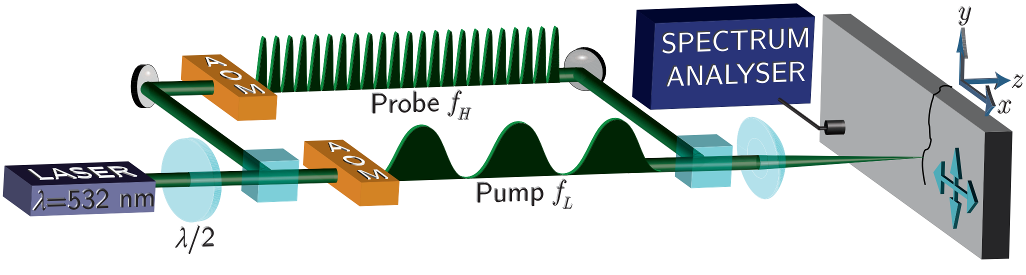

Figure 2.2: Schematic representation of the set-up denoted as Υ_1 and corresponding to the case where the excitation of both pump and probe beams are done by the same verdi laser. The $\lambda/2$ plate polarizes the beam, influencing the intensity of one and the other beam.

The modulation frequency f_H is chosen to maximize the amplitude of the detected signal. The frequencies used in the experiments are estimated to correspond to one of the standing wave resonances of the asymmetric Lamb modes propagating parallel to the long side of the plate. The acoustic resonances due to the symmetric Lamb modes are expected at frequencies exceeding tens of kHz. The dominant component of the plate surface motion, induced by the flexural waves, is the out-of-plane surface displacement which favours its detection by laser.

The choice of frequency f_L strongly influences the breathing efficiency. Indeed, the temperature rise and thermal relaxation are processes with characteristic times of the order of some seconds. Heating a sample with a continuous beam would provoke a temperature rise tending toward to its maximum value after some seconds. At the opposite when the heating stops, some seconds are required to distribute the heat in all the sample and to cool down the sample to the room temperature by heat conduction processes into air and into the supports of the sample. Consequently, for a modulated beam, the frequency f_L influences the reached maximum and minimum temperatures because of the characteristic times involved. Unfortunately, acquisition time increases when diminishing the pump frequency. As the thermal phenomenon has characteristic times of the order of some seconds, a frequency of hundreds of mHz induces a temperature difference close to the maximum. In our experiments, f_L is in general of 1 or 2 Hz, which is a good compromise between the breathing efficiency in relation to acquisition time. A detailed analysis of the pump frequency influence, theoretical and experimental, is proposed in Sec. 3.3.

The nonlinear acoustic process of the interaction of the acoustic waves of frequency f_H with the thermoelastic motion of the crack at frequency f_L results in the excitation of new spectral components $f_{m\pm n} = mf_H \pm nf_L$ [20]. In our experiments the signals with the highest amplitudes lie at those frequencies $f_{\pm n} = f_H \pm nf_L$, which are inside the width of the plate resonance, associated to $m = 1$ and $n \leqslant 10$.
In the following, except if the text specifies it, the detection is realized by an accelerometer of ~100 kHz bandwidth glued to the sample. The signal is examined with a spectrum analyzer (Agilent 89410A). The frequency window considered is $f_H \pm 10f_L$.

The sample is a plate of colored glass. Its surface is of some square centimeters and is 3 mm thick. The crack is artificially created by thermal shock. It crosses completely the sample thickness and has a length of several centimeters. The sample is fixed on a two-dimensional motorized translation stage by the mean of a soft adhesive with a thickness of a few millimeters, in order to isolate the sample from external vibrations. The motorized translation stage offers the possibility to map the surface. The basis (x, y, z) is defined relatively to the sample. Axis x and y delimit the plane of the sample surface where y corresponds to the main direction of the crack and x is orthogonal to y. Axis z is orientated into the sample depth. Consequently, a 1D scan corresponds to a displacement along x, and a 2D scan along x and y.

A lot of samples with various configurations have been tested during this work. Thus, many cracks have been tested in different configurations.

2.2 Experimental parameters

In the experiments, the same common glass is used for the sample. The exact composition of this glass is unknown and physical parameters of glass fluctuate a lot, as a function of its composition. A few experiments have been realized to extract some information on this glass in order to know which glass it is. Velocity of acoustical longitudinal waves and linear thermal expansion coefficient have been measured as a function of the temperature. For the measurement of the velocity of acoustical longitudinal waves, acoustic pulses are generated in the sample by a sub-nanosecond laser and propagate in the sample. Detected with a delay at some distances, the velocity of these waves is established. The experiment is repeated at different temperatures to evaluate the acoustical longitudinal wave velocity evolution.
In order to measure the linear thermal expansion coefficient α, a micrometer gauge is fixed on one edge of the sample and detects the linear thermal expansion under thermal loading. As the sample is assumed isotropic and the considered expansions are small, $\beta = 3\alpha$, where β is the bulk thermal expansion coefficient.
The sample is heated by a hair-drier and controlled by a thermometer. Both velocity of acoustical longitudinal waves and linear thermal expansion coefficient are observed to decrease as the temperature increases. These observations make soda lime silica glass a good candidate as it is one of the only glasses to have such behavior. This is consistent with the fact it is one of the most widely used glasses.
Then, parameters involved in the calculations, κ, c_p, K, and ν, not experimentally estimated, come from literature on soda lime silica glass [15, 28, 58].

The sample parameters experimentally estimated are the density and the thermal linear expansion coefficient.

On the optical part, the power of the beams are measured with a power meter.
The reflection coefficient of light by the sample is quantified comparing the reflection on a silver mirror, assumed ideal ($\mathsf{r} = 1$), to the reflection by the glass sample.
Measuring the intensity with and without the material, of thickness h, (I_{sample} and I_{empty}, respectively) allows an estimation of the light absorption length ℓ into the sample using the Beer-Lambert-Bouguer law: $I_{\text{sample}} = (1 - \mathsf{r}) \cdot I_{\text{empty}} \cdot e^{-h/\ell}$.

On the acoustical part, only the velocity of acoustical longitudinal waves are measured.

Tab. 2.1 lists the constant experimental values. All the parameters related to the sample properties evolve as a function of the temperature. This effect is not taken into account in order to simplify the calculations. The values are given at room temperature ($T \simeq 293$ K). The beam radii, the light intensity modulation frequencies and the beam powers, controlled by the experiment, are not referenced. However, an order of magnitude can be proposed. The beam powers are between some tens of up to two hundreds milliwatts. The light intensity modulation frequency is about 1 Hertz for the pump probe and several tens of kHz for the probe beam. The beam radii are between few tens and a hundred micrometers. If the experiment is realized with the set-up Υ_1 both beam radii are similar. On the contrary, when the acoustic wave is generated by the diode laser

Parameter	Value
ℓ_{532}	0.31 mm
ℓ_{800}	0.22 mm
r_{532}	0.11
r_{800}	0.14
κ	1.03 W.m^{-1}.K^{-1}
ρ	2616 kg.m^{-3}
c_p	720 J.kg^{-1}.K^{-1}
c	5750 m.s^{-1}
α	5.5×10^{-6} K^{-1}
K	38.9 Gpa
ν	0.22

Table 2.1: Values of sample parameters used in the following, where the subscript 532 (800) indicates the value corresponding to the laser which wavelength is at 532 nm (800 nm).

(set-up Υ_2), the probe beam can be up to ~5 times larger than the pump beam due to the bad quality of the diode laser beam in comparison to the one of the cw laser.

2.2.1 Evaluation of the beam radii

The beam radii are measured with the knife-edge technique. This technique involves the measurement of the laser intensity with a power meter. A blade is fixed on one edge of the sample, in the (x, y) plan, on the way of the laser beam to the power meter. It first stops the beam (Fig. 2.3(a)). Then, the blade is moved step by step along the x-axis (Fig. 2.3(b)) until the complete beam irradiates the power meter (Fig. 2.3(c)). The power evolution is recorded. The power corresponds to the integral of beam intensity multiplied by a coefficient б. The intensity follows a Gaussian evolution. Then, the optical power can be written as a function of (x, y):

$$\begin{aligned}
P(x,y) &= \int_{-\infty}^{\infty}\int_{-\infty}^{X} \text{б} \cdot e^{-\frac{x^2+y^2}{a^2}}\,dx\,dy \\
&= \text{б}\int_{-\infty}^{\infty} e^{-\frac{y^2}{a^2}}\,dy \left[\int_{-\infty}^{0} e^{-\frac{X^2}{a^2}}\,dx + \int_{0}^{x} e^{-\frac{x^2}{a^2}}\,dx\right] \\
&= \text{б}a\sqrt{\pi}\left[\frac{a\sqrt{\pi}}{2} + \frac{a\sqrt{\pi}}{2}\mathrm{Erf}\left(\frac{X}{a}\right)\right] \\
&= \text{б}\frac{a^2\sqrt{\pi}}{2}\left[1 + \mathrm{Erf}\left(\frac{X}{a}\right)\right], \qquad (2.1)
\end{aligned}$$

where X corresponds to the blade position relatively to the center of the beam. It is possible to fit the experimental curve with the theoretical one using the beam radius a and the amplitude coefficient б for parameters. An example of such result is illustrated in Fig. 2.3(d). This experiment, for example, gives the values of б = 112.1 and $a = 161$ µm.

Only the value of the beam radius presents an interest and is presented in the following. The vertical axis in Fig. 2.3(d) is in Volt because the power meter is connected to a voltmeter in order to automatize the set-up. This only affects the value of б.

The beams are focused on the sample by the mean of a lens with a focal length of several centimeters (generally 5 or 10 cm). For a focal length of f=5 cm and the Verdi laser ($\lambda = 532$ nm), it leads to a beam radius on the sample of $a = \lambda f/(\pi a_0) \simeq 17$ µm, with a_0 the beam radius before the lens ($a_0 \simeq 500$ µm). The Rayleigh length is equal to $\pi a^2/\lambda \simeq 1.7$ mm. The blade, used to measure the beam radius is about 100 µm thick. Then, the blade thickness is negligible in comparison to the Rayleigh length of the beam. The beam radius, measured on the blade, can thus be considered equal to the one on the sample surface.

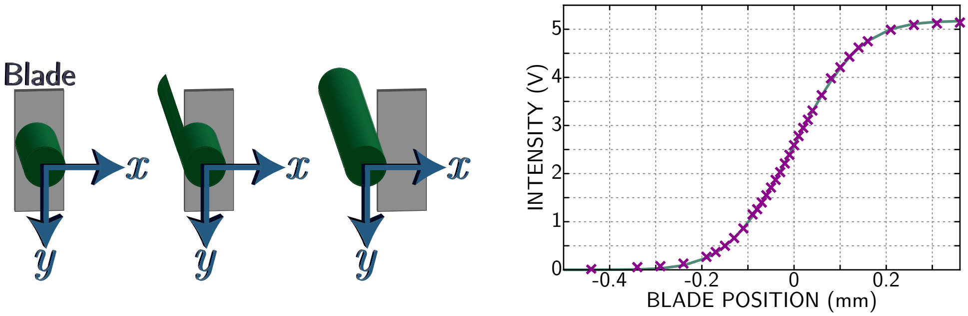

(a) (b) (c) (d)

Figure 2.3: Schematics of the method to measure beam radius. (a-c): Schematic representation of three successive positions of the blade relative to the laser beam, when the blade stops the beam (a), stops only part of the beam (b), and does not stop the beam anymore (c). (d): Experimental (×) and corresponding fit (—) evolution of the intensity as a function of the relative position of the blade edge and the beam axis.

This method gives the $1/e$ radius as the intensity is decreased by the factor $1/e$ one radius far from the beam center.

2.2.2 Spatial resolution of the method

In order to discuss the spatial resolution of the method, the spatial resolution first needs to be defined. The resolving power of the method is the minimum distance between distinguishable cracks. However, none of the samples presents two cracks at a known fixed distance.

The spatial resolution is then defined by the characteristic dimension of the minimum surface area where the presence of the crack can be guaranteed by our measurements. The beam radii are estimated by a $1/e$ decrease of the intensity (Sec. 2.2.1). To a decrease of $1/e$ of the nonlinear signal intensity produced by the crack corresponds an amplitude decrease of $1/\sqrt{e}$. The spatial resolution is defined by $1/\sqrt{e}$ fall of the amplitude of the signal (~ 4.3 dB). The $1/\sqrt{e}$ fall, instead of the $1/e$ fall, is also motivated by the possibility to define the spatial resolution in more cases and for more nonlinear sidelobes. Due to the finite number of experimental points, the experimental results are fitted by a polynomial function in order to smooth the curve and to have a precise result on the 4.3 dB variation. The distance for the $1/\sqrt{e}$ amplitude decrease is measured from this fitted curve and not from the experimental results.

The amplitude of the acoustic strain is proportional to the probe power (Eq. (1.19)) and is influenced by the loading force (Eqs. (1.19) and (1.20b)) which is proportional by the pump power (Eq. (1.18)). Then, it firstly appears that both pump and probe amplitudes influence the amplitude of the nonlinear sidelobes.
The theoretical model in [20] assumes the coincident presence of the pump and the probe beam. Then, the spatial resolution is potentially defined by the overlapping of both beams (Fig 2.4). In the experiments, both beams are adjusted to be coincident. The overlap corresponds to the smallest of the beam radii.
The penetration of light into the sample could also play some role by increasing heated surface area beyond the dimensions of the pump beam radius, when the penetration depth is larger than the pump beam radius. In general, this condition, $a < \ell$, is fulfilled.
The proposed definition of potential ultimate resolution also neglects the interaction of acoustic waves propagating toward the breathing crack and interacting with it (in the case of a probe beam non-overlapping with the crack) or the possibility to provide a crack breathing outside the pump diameter by heat diffusion (in the case of a pump beam non-overlapping with the crack).
However, the overlap of both beams appears to be a good opportunity to estimate the spatial resolution in a first approximation. The influence of each beam radius and power are discussed in more details in Chap 3.

2.3 Realization of a one-dimensional scan

At first, a 1D scan is performed to validate the set-up. As previously explained, the beams are focused on a single point. The sample is progressively moved step by step in a direction perpendicular to the crack faces, (in the x-axis). The step, corresponding to the distance between the consecutive image points, coincides, in general, to about a diameter of the smallest radius in order to scan the complete line. At each step, the signal is acquired by an accelerometer and analyzed by a spectrum analyzer. Fig. 2.5(a) is a schematic representation of the realization of a 1D scan. For this experiment, the set-up Υ_1 is used in order to demonstrate that the 532 nm laser wavelength provides the possibility to detect the crack as the possibility with diode lasers has already been demonstrated [14].

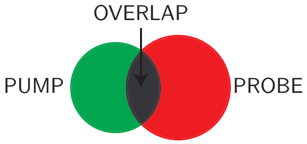

Figure 2.4: Schematic representation of the overlap region of the pump and probe beams.

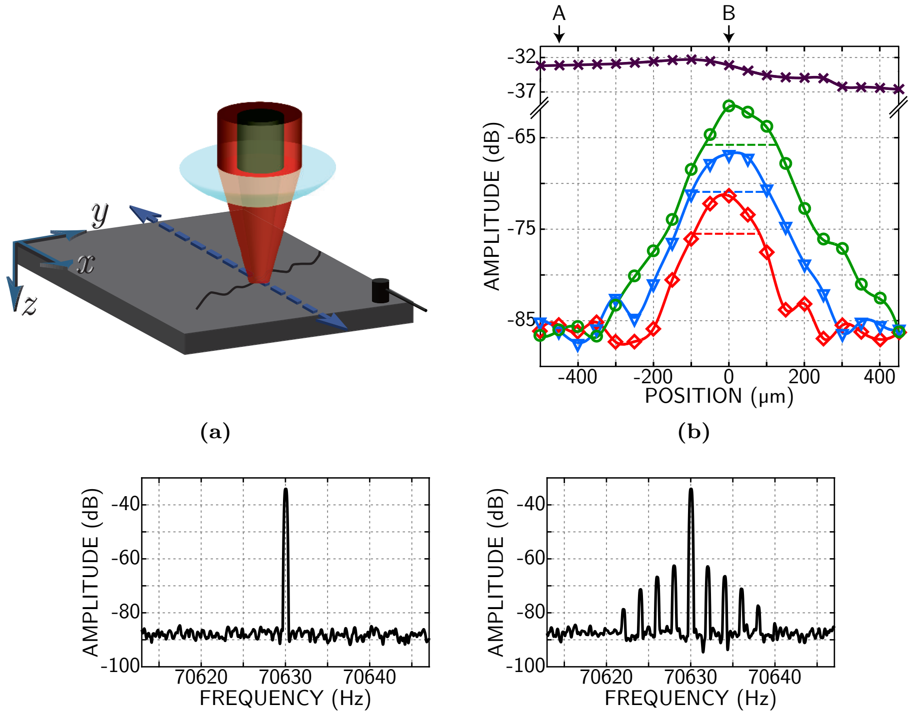

(a) (b)

(c) (d)

Figure 2.5: (a): Schematic representation of a 1D scan set-up. (b): Evolution of the main peak at f_H (×) and of the first three nonlinear left sidelobes $f_H - f_L$ (○), $f_H - 2f_L$ (▽) and $f_H - 3f_L$ (◇) amplitudes as a function of the spot beams relatively to the crack position. Filled lines: Interpolation of the experimental results. Dashed horizontal lines: -4.3 dB limit from the maximum of the sidelobe evolution. (c-d): Spectra recorded outside the crack, at $x = -0.45$ mm (c) and on the crack, at $x = 0$ mm (d), related to points A and B, respectively, in Fig. 2.5(b).

In this experiment, the pump beam has a radius of 95 μm, a power of 90 mW and frequency f_L is chosen at 2 Hz. The probe beam has a radius of 106 μm, a power of 120 mW and a frequency f_H of 70.6 kHz, respectively. The step is of 50 μm, which corresponds to about half of each beam radius.

The evolutions of the main peak and of the nonlinear sidelobes amplitudes as a function of the distance are analyzed from the corresponding spectrums. The evolution of the amplitudes of the main peak at f_H and of the first three left nonlinear mixed-frequencies $f_H - f_L$, $f_H - 2f_L$ and $f_H - 3f_L$ are presented in Fig. 2.5(b). The evolution of the main peak amplitude does not contain useful information, but the one of the nonlinear sidelobes clearly demonstrates the presence of the crack and can be used to localize it. The spatial resolution, for a $1/\sqrt{e}$ decrease, is of 191, 203 and 175 μm for the first, second and third left sidelobe respectively. Results on the right sidelobes are similar on the behavior and the spatial resolution (193, 189 and 190 μm). These results on the spatial resolution fits well the diameter of the beams: 212 (190) μm for the probe (pump) beam.

Figs. 2.5(c), 2.5(d) present two spectra illustrating the generation of the nonlinear sidelobes on the crack. In the latter spectra, the first four sidelobes are generated.
In other experiments, the generation up to the tenth sidelobe can be observed. The difference between the main peak amplitude and the nonlinear sidelobes amplitude can also be much more reduced.

In the following, several experiments are carried out on the evolution of the main peak and the nonlinear sidelobes amplitudes as a function of one particular parameter. For such experiments, a 1D scan of the crack is firstly realized and then the sample is moved in the x direction, in order to make the excitation coincide with the location of the crack, where the nonlinear sidelobes have their larger amplitude. After that, the study of the frequency-mixing amplitude as a function of the studied parameter is performed.

2.4 Influence of probe and pump beams powers

A first experiment taking advantage of the presence of the half-wave plate and the polarizing beamsplitter cube in the set-up Υ_2 (Fig. 2.2) is realized. A change of polarization of the beam influences the power of one beam, relatively to the other. Evolution of the main peak and of the nonlinear sidelobe amplitudes as a function of the pump and probe powers is recorded.

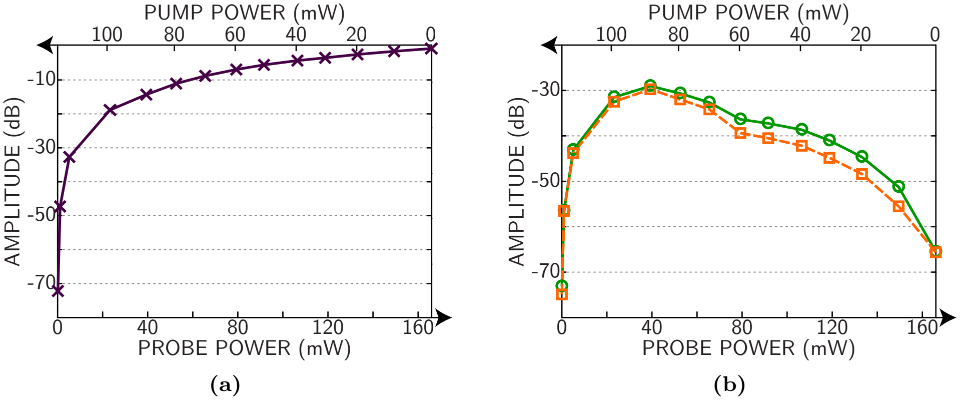

Figure 2.6: Evolution of the main peak amplitude at f_H (a) and the left and right nonlinear sidelobes (b) at $f_H - f_L$ (○) and $f_H + f_L$ (□), respectively, as a function of the pump and probe beam powers. The beam powers evolve by the change of the beam polarization before the polarized beamsplitter cube.

In this experiment (Fig. 2.6), only the main peak and the first nonlinear sidelobes amplitude are presented, corresponding to $n = 0$ and $n = \pm 1$, respectively. The probe (pump) beam is focused down to 19.4 µm (20.7 µm) and is intensity modulated at frequency 90.4 kHz (1 Hz). The difference between the probe and the pump maximum power, 165 and 110 mW, respectively, is only due to a better focusing of the probe beam on the Bragg cell of the AOM.

The amplitude of the main peak increases monotonously as a function of the probe power (Fig. 2.6(a)), which is an expected result. The evolution of the nonlinear sidelobe amplitudes (Fig. 2.6(b)), on the contrary, is non monotonous. If all the power is on the pump, the crack easily breathes but, as there is no acoustic wave generation due to the absence of probe beam, no frequency-mixing can be generated. If all the power is on the probe, the crack does not breathe, which also prevents the generation of frequency-mixing. Thus, this confirms that the nonlinear mixed frequencies are generated due to the combination of both crack breathing and acoustic wave generation, by probe laser beam.

The optimum of the relative powers between both beams, however, cannot be easily predicted. The crack breathing requires a certain amount of energy, depending on the crack parameters, in particular the distance between its faces and its rigidity. Once the probe power is high enough, a first approach would be to let the amount of left energy on the pump to insure the best breathing possible. The optimum in Fig. 2.6(b) of ∼90 mW on the pump and ∼40 mW on the probe is associated to this particular position on the crack. However, as long as both beam have a sufficient power ($P_{H,L} \geqslant 20$ mW in Fig. 2.6(b)), the crack remains detectable.

In Fig. 2.6(a) the amplitude of the main peak is highly influenced by the pump beam for very low probe powers. When the probe power evolves from 0 to 1 mW, the amplitude of the signal at the probe frequency increases by 25 dB. Without the pump beam, the amplitude increase at f_H if only of 2 dB.

This effect is attributed to the crack closing induced by the pump beam, and is discussed in Sec. 3.1. The experiment is repeated for a pump beam modulated at much higher frequency ($f_L = 1$ kHz). The same 25 dB amplitude increases is observed. It is demonstrated in Chap. 3 that such frequency can provide a closing of the crack but not a crack breathing. This indicates that this is the crack closing that is responsible for the magnification of the amplitude.

2.5 Realization of a two-dimensional scan

The detection of a crack in a 1D scan is demonstrated (Sec. 2.3 and [14]) and thus, there is no additional difficulty to perform 2D scans. It is an important step to evaluate if the crack can be detected on a whole surface. As the micro-contacts between the crack faces evolve on a 2D scan, this influences the crack rigidity and the distance between the crack faces. Evolution of the nonlinear frequency-mixing amplitude should provide qualitative information on the changes of these parameters along the crack.

An optical image of the scanned surface area, of 1.8×8.6 mm^2, is presented in Fig. 2.7(a). It is obtained through the registration of light transmission by a microscope. The crack has been initiated next to the position $x = 1$, $y = 0$ mm. In the region denoted as region ‘A’ in the following (see Fig. 2.7(a)), the crack appears wider, this is due to its oblique in-depth orientation. In this region, the crack is buried and not present on the surface where the laser irradiation takes place. The possibility of the crack detection in this region is discussed.

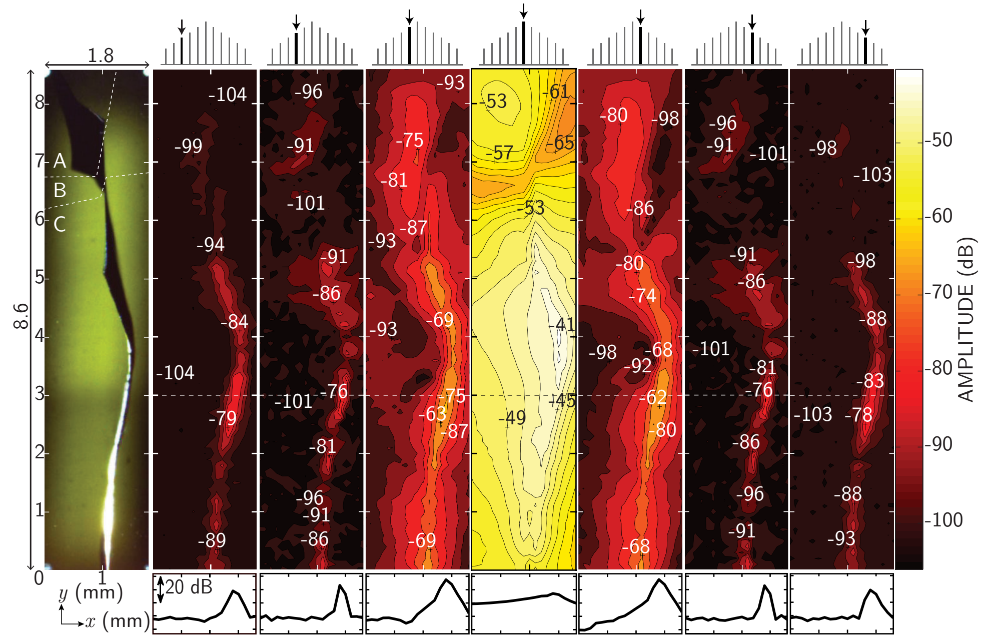

(a) **(b)** **(c)** **(d)** **(e)** **(f)** **(g)** **(h)**

Figure 2.7: (a): Photograph of the scanned area with the crack. Areas 'A', 'B' and 'C' are depicted. (b-h): **Top**: Schematic representation of the analyzed spectrum component. **Middle**: Two dimensional scans of the crack achieved by detection of different sidelobes at $f_H \pm nf_L$. From left to right the first three nonlinear left sidelobes: $n = -3$ (b), $n = -2$ (c), $n = -1$ (*d*), the main peak, at f_H (e), and the first three nonlinear right sidelobes for $n = 1, 2, 3$ (f,g,h). All scans are represented with the same amplitude scale. Amplitude difference between two isolines is of 2 dB for $n = 0$, 6 dB for $n = \pm 1$, and 5 dB for $n = \pm 2, \pm 3$. **Bottom**: Scan section along x for $y = 3$ mm (dotted line in middle figures). All scans are represented with the same amplitude scale.

The results of the crack imaging are presented in Fig. 2.7((b)-(h)). The first three left and right sidelobes ($f_H \pm nf_L$, $n = 1..3$) and the main peak (f_H) scans are demonstrated. In this experiment, the Υ_2 set-up is used. The pump beam has a radius of 54 µm, a power of 76.3 mW and is intensity modulated at 1 Hz. The probe beam parameters are $a_H = 164$ µm, $P_H = 46.5$ mW, and $f_H = 25$ kHz. The step in both x and y direction is 100 µm, comparable with the pump beam diameter (108 µm).

The two-dimensional scans are presented with isolines. The same colorbar is proposed for all the scans to exhibit the amplitude differences between the main peak and the nonlinear sidelobes and to emphasize the amplitude dynamic of each frequency amplitude. The amplitude between two isolines is 2, 6, 5 and 5 dB for the scans at the main peak ($n = 0$) and sidelobes ($n = \pm 1$, $n = \pm 2$ and $n = \pm 3$), respectively. Thus, Fig. 2.7, combined with the amplitude difference between two isolines, indicates that the main peak amplitude variations are much smaller than those of any of the sidelobes. One dimensional scans along x, for $y = 3$ mm, are also presented in Fig. 2.7 (bottom).

Firstly, the scan images at nonlinear mixed-frequencies exhibit a high sensitivity to the crack. Similarity of the nonlinear optoacoustic images to the optical one (Fig. 2.7(a)) clearly demonstrates the accuracy of the method. It also appears that the image at the probe frequency (f_H) signal is much less sensitive and precise, and has a rather different shape than the image of nonlinear sidelobes. The amplitude of the nonlinear sidelobes tends to decrease as n increases, but, the sidelobes up to $n = 5$ clearly detect the crack.

The scan at the main peak frequency f_H, has an amplitude contrast of almost 30 dB (Fig. 2.7(e)). Two distinct phenomena occur. One in the area B and the other in the areas A and C (see Fig. 2.7(a)).

In areas A and C, the amplitude contrast at f_H follows the crack geometry. However, the amplitude variations are much smaller and take place on much larger distances in comparison to nonlinear frequency-mixing (Fig. 2.7, bottom). So crack detection is uncertain with the information at this only frequency. The phenomenon leading to the amplitude rise, on the crack, at f_H, remains badly understood for the moment. Nevertheless, several hypothesis can be made. Cascade frequency-mixing process is one of them. For example, the mixing of frequencies $f_H \pm nf_L$ and nf_L can generate $f_H \pm 2nf_L$ but also f_H. So the amplitude at f_H is influenced by cascade nonlinear processes. It could be also influenced by higher-order nonlinear processes [56].

Besides, interaction between two waves having different frequencies and amplitudes in a hysteretic nonlinear medium can lead to non-simplex regimes [25, 65]. The presence of a crack, which is hysteretic and nonlinear, combined with the important difference of the pump and probe frequencies, can be responsible for such non-simplex regimes. Increase or decrease of the absorption of one or the other acoustic wave may occur in this case [25, 65]. This can influence the amplitude of the acoustic wave at f_H and/or of the nonlinear sidelobes. However, the quantification of this phenomenon has not been realized. In the following, a simplex regime is assumed.

Finally, multiple reflections due to the crack geometry lead to partial capture of laser irradiation inside the crack. The energy is then more efficiently absorbed than for a simple reflection on an intact surface.

The other part of the amplitude contrast is the consequence of a fall of 15 dB in area B. It is directly linked to the choice of f_H. The probe frequency is chosen coincident with a resonance frequency of the sample to maximize the signal-to-noise ratio of the detected signal.

It is well known that at a resonant frequency, the normal displacement of the solid depends on the spatial location. Associated with each resonant frequency is a distinct modal shape (or spatial pattern) that develops in the plate as it vibrates. The modal shape of displacement is composed of nodes and antinodes where the normal displacement is null and maximum, respectively, and with smooth variations in-between.

For a forced excitation, induced by a point-source of displacement, the amplitude of the mechanical wave is proportional to the normal displacement at this location. Excitation on an antinode maximizes the amplitude of the acoustic wave. At the opposite, it is impossible to excite the solid at one of its resonant frequencies by exciting it on a node of displacement as the displacement is null. It is possible to map a surface with a point-source in order to reconstruct the modal shape.

The same logic is valid with a local source of deformation and the modal shape of deformation, associated to the resonant frequency. The resonant frequencies of the solid are identical but the modal shape varies as the deformation corresponds to the derivative of the displacement. The reasoning is also similar for the detection: it is maximized on an antinode.

In the present experiment, the resonant frequency is chosen to maximize the amplitude of the probe wave. The thermoelastic generation corresponds to a thermal stress. This stress induces a dilatation, resulting in a deformation. In other words, the optoacoustics process depends on the deformation in the spot zone. If the excitation is on an antinode of deformation, the amplitude of the acoustic wave at f_H is amplified. This is the reason to choose a probe frequency at a resonant frequency of the sample.

For the detection, the accelerometer is sensitive to the acceleration, and thus, to the displacement. It appears that the ideal resonance frequency f_H corresponds to a maximum of deformation at the excitation point and a maximum of displacement at the detection point.

On large scanned areas, the deformation pattern evolves. This evolution provokes variations in the generation efficiency of the high-frequency acoustic wave by the probe beam. It results changes in the amplitude of the main peak at f_H, as observed in the experiments.

In the particular case where a deformation node is present in the excitation zone, no acoustic wave is generated. In this case, it would be necessary to realize another scan at another resonance frequency (with another modal shape) to provide the missing information. As nonlinear mixed-frequencies are detectable in area B, the second scan is unnecessary in this experiment.

Numerical estimations demonstrate that for a probe frequency in the tens of kHz range, and with similar dimensions of the sample, the modes correspond to one of the first mechanical resonances of the plate. Therefore, the number of nodes and antinodes are small and they are distant in a centimeter scale. It is not possible to alternate deformation node and antinode in very small distances.

Finally, these main peak amplitude variations on the scan are not problematic because they are not used to detect the crack. These variations influence the nonlinear frequency-mixed amplitudes, which is why the excitation on antinodes of displacement is the ideal case, but not their generation, which is the indicator of the presence of a crack. Taking advantage of the modal shape also offers the possibility to reduce the irradiated energy of the probe beam. A too large irradiated energy could close the crack (Chap. 3) or damage the sample. Thus, the probe energy must be as low as possible, as long as the signal-to-noise ratio is good enough.

The first nonlinear sidelobes, at $f_H \pm f_L$ (Figs. 2.7(d), 2.7(f)), have a 40 dB contrast and very precise spatial localization, even if their amplitudes are $\sim$20 dB lower than the one of the main peak. The spatial resolution evolves along the crack. For $y \leqslant 5$ mm, the mean value is 190 µm, in-between the pump and probe diameter, with a standard deviation of 40 µm. The extrema, in the same region are 120 and 340 µm. The maximum then corresponds to the probe diameter.

The first nonlinear sidelobe amplitudes are supposed to increase monotonously as a function of ratio of the loading force on the forces F_c and F_o required to close and open the crack, respectively (Sec. 1.3.2). These forces are proportional to the crack rigidity and the distance between the crack faces. As the loading is constant during the experiment, the amplitude of the first nonlinear sidelobe on the crack increases if the forces $F_{c,o}$ decrease. It appears from Figs. 2.7(d) and 2.7(f) that the maximum of the first nonlinear sidelobe amplitudes is in the region $y \in [2; 5]$ mm. This can be attributed to lower forces F_c and F_o in this region.

The amplitude of the nonlinear sidelobes falls down in the area A. As explained previously, the crack is buried in this area. Nevertheless, the detection is still possible in the present case, but the crack localization is less accurate. The mean spatial resolution in this region is around 450 µm, larger than the beam diameters, and much larger than the spatial resolution in area A.

It can be observed that even far from the crack, the first nonlinear sidelobes are generated. This phenomenon is discussed in the next chapter (Sec. 3.5).

The other sidelobes (Figs. 2.7(b), 2.7(c), 2.7(g), 2.7(h)) also reveal the crack presence, with a precise localization and with a reduced, but nevertheless high, amplitude contrast: ~30 dB for the second, ~25 dB for the third and the fourth sidelobes over the whole scan. In some areas, even if the signal amplitude is lower than for the first nonlinear sidelobes, the spatial localization can be better because the amplitude evolution is more sharpened. In Fig. 2.7 bottom, the spatial resolutions are of 190, 100 and 175 µm for the first, second and third left sidelobes, respectively. The spatial resolution for $n = 2$ is twice better than for $n = 1$. The lowest spatial resolutions along the whole crack are of 75 and 95 µm for the second and third left sidelobes, respectively, in comparison to 120 µm for the first one. These values are smaller than both beam diameters. In general, the higher sidelobes are more spatially localized than the first one. However, because of the lower amplitudes involved, some scans, even if the crack is detected, do not have a 4.3 dB dynamic, and thus, no spatial resolution can be determined.

For example, one can see that the detection in the previously discussed area C is almost not possible for these higher harmonics.

The evolution of the nonlinear-frequency sidelobes for $n > 1$ present non-monotonous behavior as a function of the ration F_L/F_c (Sec. 1.3.2). Consequently, the previous observations on the crack parameters as a function of the amplitude of $f_H \pm f_L$ is not possible anymore this way. Evolution of these higher sidelobes as a function of the loading force, in order to extract crack parameters, is presented in Part II.

The symmetry of the sidelobes, at $f_H + nf_L$ and $f_H - nf_L$ ($\forall$ n), is clearly noticeable on the scans (Fig. 2.7), as theoretically predicted [20] and is also observed in the spatial resolution values.

Conclusion

The experimental set-up, consisting in two laser beams, independently intensity-modulated at f_L and f_H, and focused on a single spot is described. Both laser wavelengths, 532 and 800 nm, demonstrate the possibility to provide the crack breathing and to generate an acoustic wave. This leads to the generation of the mixed-frequencies. The experimental set-up is validated on one and two-dimension scans.

The glass parameters used in the experiments are reported for further estimations.

The importance of the two beams, in the nonlinear frequency-mixing process, is demonstrated. Both crack breathing and acoustic wave generation are required to generate the nonlinear sidelobes.

The spatial resolution is defined as the minimum distance required to observe an amplitude decrease of 4.3 dB from the maximum. Its evolution is studied as a function of the sidelobe and of the crack parameters evolution. Higher sidelobes appear to have a better spatial resolution than the first nonlinear sidelobes.

The first nonlinear sidelobe, associated to $f_H \pm f_L$ is monotonously increasing with the ratio of the pump loading over the force required to close the crack. Its evolution along the crack, for a two-dimensional scan, qualitatively informs on the evolution of the forces F_c and F_o, required to close and open the crack, respectively.

Chapter 3

Importance and optimization of the breathing

Abstract

In this chapter, the importance of the crack breathing is studied. In a first part, an all-optical set-up demonstrates this breathing and its importance on the nonlinear frequency-mixing.
In order to evaluate the influence of the pump frequency or the pump power, the 3D heat equation is solved. It allows estimation of the temperature rise for any parameter dependence and at any location and time in the sample. Theoretical estimations on the influence of the pump frequency and the beam focusing is performed and compared to experimental results. Finally, the influence of the powers and the positions of the beam on the nonlinear frequency-mixing process and the spatial resolution is discussed.

3.1 Evidence of the crack breathing[1]

A first step to better understand the phenomenon is to clearly demonstrate that the crack is breathing and that this breathing, combined with the acoustic wave generation, is responsible for the frequency-mixing process. With this purpose, two experiments are realized. For both of them, the set-up is very similar. The excitation is realized with set-up Υ_2. The pump radius is estimated of 100 µm. The probe beam is modulated at 16 kHz. The detection however is changed for a commercial vibrometer (Polytec, Inc., Model OFV302). This vibrometer utilizes an integrated Mach-Zehnder heterodyne interferometer. The beam is split by a beamsplitter into a reference beam and the measurement one. The latter passes through a Bragg cell and a second beamsplitter and is then focused onto the considered object which reflects it. This reflected beam is deflected by the previous beamsplitter and is merged with the reference beam thanks to a third beam splitter. Both beams are finally focused onto a detector. A Doppler frequency shift, measured at a one wavelength thanks to the Bragg cell, leads to the determination of the velocity. The interference between the reference and the measurement beams

---

[1] This section 3.1 is part of an article published during the thesis [39].

modulates the total intensity on the photodetector and is function of the path length between both beams and then to the wavelength propagating on the surface.
The challenge is then double: firstly, to demonstrate the predominant role of the crack breathing on the studied nonlinear process. Secondly, to demonstrate that the amplitudes of the out-of-plane displacements of the plate surface, that are generated by the acoustic nonlinearities of the crack are sufficiently high to be detected by a commercial vibrometer. The use of a vibrometer for the detection is particularly interesting in this set-up in order to propose an all-optical set-up for crack detection.
The relative variation of the power, linked to the interferometric sensitivity, with a Mach-Zehnder interferometer, is given by [40, 47]:

$$\frac{\Delta P}{P} = \frac{4}{\pi} \cdot \frac{\pi^2}{\lambda} \cdot u. \tag{3.1}$$

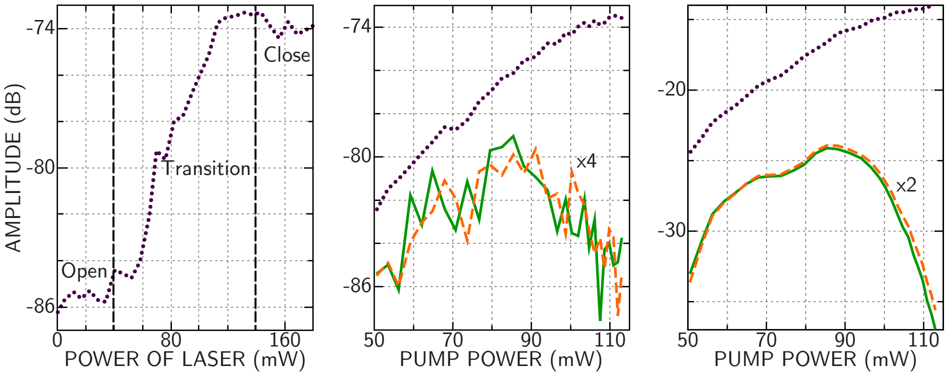

(a) (b) (c)

Figure 3.1: The dependence of the photoacoustic signal amplitude on the power of the heating laser at frequencies f_H (•••), $f_H + f_L$ (- -), $f_H - f_L$ (—). (a): nonmodulated laser heating, detection by laser vibrometer; (b): modulated laser heating, detection by laser vibrometer; (c): modulated laser heating, detection by in-contact accelerometer. The amplitudes of the mixed frequencies in (b) and (c) are multiplied by 4 and by 2, respectively.

The results of the first experiment, which could be called static, are presented in Fig. 3.1(a). In this experiment the heating of the crack is generated by a nonmodulated green laser, $f_L = 0$ Hz, so that there are no frequency-mixing processes. The dependence of the acoustic signal on the power of the heating laser at the fundamental frequency $f_H = 16$ kHz, which is detected by the vibrometer, is determined. The experimental data in Fig. 3.1(a) indicate a transition from low to high efficiency of the optoacoustic conversion at the frequency f_H, when the power of the cw heating laser increases from 40 mW to 120 mW. The strongest dependence of the optoacoustic conversion efficiency on the power of the heating laser is found at approximately 80 mW. This 'maximization' phenomenon was documented earlier [14] in the experiments, where the acoustic waves were detected by a sensitive, in-contact accelerometer. Theory [20] attributes these observations to heating-induced transition of the crack from an open to a closed state.

From a physics point of view, thermoelastic generation of sound near the faces of an open crack is similar to the one near a mechanically free surface and can be very inefficient [27]. Thermoelastic expansion of the locally heated region could first lead to creation of a small number of contacts between the crack faces and then to complete local closing of the gap between them. This process is accompanied by an increasing mechanical loading of one face of the crack by another, which can be viewed as a process of increasing the crack rigidity [20], with a consequent increase in the optoacoustic conversion efficiency.

The results presented in Fig. 3.1(a) indicate that the rigidity of the crack is the most sensitive to external action (the crack is the most nonlinear acoustically) when the power of the heating laser is about 80 mW. This expectation is confirmed by the results of the frequency-mixing experiments, presented in Figs. 3.1(b), 3.1(c). In these experiments the heating green laser is intensity modulated at $f_L = 1$ Hz and the acoustic signals at frequencies f_H and $f_H \pm f_L$ are detected by a laser vibrometer (Fig. 3.1(b)) and by an in-contact accelerometer for comparison (Fig. 3.1(c)). In Figs. 3.1(b) and 3.1(c) the amplitudes of the mixed frequencies in (b) and in (c) are multiplied by 4 and by 2, respectively, for better visibility simultaneously with the fundamental frequency. The maximum signals at mixed frequencies are detected at approximately 80 mW average power of the heating laser, where the nonlinear behavior of the crack is the highest. The results in Fig. 3.1 demonstrate that the crack local nonlinearity, both in the open and closed states, corresponding to heating powers lower than 40 mW and higher than 120 mW, respectively, is weak in comparison with the nonlinearity of the crack in the state that is transitional from the open to the closed one. This transitional state is characterized by the incomplete local contact between the crack faces. Both, in the open state, where there are no contacts between the asperities located at opposite faces of the crack, and in the closed state, where the contact between the crack faces is nearly perfect, crack rigidity weakly depends on elastic loading. Weak nonlinearity of the open state is due to the absence of the highly nonlinear weakly loaded contacts between the asperities located at opposite faces of the crack. In the closed state the contacts between the asperities are strongly loaded, weakly nonlinear, and the material behaves as nearly intact.

One can see that if the results demonstrate the feasibility of the detection of the vibrometer, the efficiency of this detection is much lower than with an accelerometer. In 3.1(b) and 3.1(c), the loss is of about 50 dB. This explain why the nonlinear signal is much more noisy than the linear one. Another consequence is that the higher sidelobes ($n = \pm 2, \pm 3, \dots$) are lost in the noise and cannot be detected without improvement in the signal-to-noise ratio. In order to allow the detection of numerous sidelobes, and drastically improve the signal-to-noise ratio without increasing too much the acquisition time, the following experiments make use of an accelerometer for detection, but one should emphasize, however, that the crack detection is possible with a commercial vibrometer, providing a first possibility of an all-optical set-up.

3.2 Resolution of the 3D heat equation

In order to determine the temperature field induced by the lasers in the set-up, the heat diffusion equation, with an intensity-modulated laser for the heat source, needs to be solved (Eq. (3.14) in [27]). Let us rewrite Eq. (1.5) in cylindrical coordinates, more suitable for a gaussian beam profile:

$$\frac{\partial T}{\partial t} = \chi \Delta T + \frac{I}{\ell \rho c_p} f(t) \Psi(r,\phi) e^{-z/\ell}. \tag{3.2}$$

The laser excitation beams, assumed gaussian, (Figs. 1.6(a) and 1.6(b)) can be described by:

$$\Psi(r,\phi) = e^{-(r/a)^2}. \tag{3.3}$$

The product of the intensity by the spatial distribution needs to be normalized in order to respect the conservation energy law:

$$I \cdot \Psi(r,\phi) = \frac{(1-\mathsf{r}) \cdot P \cdot \Psi(r,\phi)}{\int_0^\infty \int_0^{2\pi} r \, \Psi(r,\phi) dr d\phi} \tag{3.4a}$$

$$= (1-\mathsf{r}) \cdot \frac{P}{\pi a^2} \cdot \Psi(r,\phi) \tag{3.4b}$$

In the following, the intensity is defined by $I = (1-\mathsf{r}) \cdot P/(\pi a^2)$. Light intensity modulation is defined:

$$f(t) = \frac{1}{2}[1 + \text{ш} \cos(\omega t)]. \tag{3.5}$$

In our experiments ш is always equal to 1, but the calculation is made for the general case.

The crack is assumed to be at $\phi = 0$ $[\pi]$ and the heating, induced by the laser, to be symmetrical to the axis. The domain can be split into two subdomains : $0 \leqslant \phi \leqslant \pi$ and $\pi \leqslant \phi \leqslant 2\pi$. Because of the symmetry, results for both half subdomains are equal. Moreover, the temperature rise is considered to be initially zero and heat flux from the sample to the air is neglected. Mathematically, it leads to the equations:

$$T(t=0) = 0, \tag{3.6a}$$

$$\partial_z T\big|_{z=0} = 0, \tag{3.6b}$$

$$\partial_\phi T\big|_{\phi=0\ [\pi]} = 0. \tag{3.6c}$$

With these initial and boundary conditions (Eqs. (3.6)), the Green function of Eq. (3.2) for $0 \leqslant r < \infty$, $0 \leqslant \phi \leqslant \phi_0$, and $0 \leqslant z < \infty$ is [45]:

$$G(r,\phi,z,r_1,\phi_1,z_1,t) = \frac{1}{2\sqrt{\chi \pi t}} \left(e^{-\frac{(z-z_1)^2}{4\chi t}} + e^{-\frac{(z+z_1)^2}{4\chi t}} \right) \frac{1}{\chi \phi_0 t} e^{-\frac{r^2+r_1^2}{4\chi t}} \left[\frac{1}{2} \mathcal{I}_0 \left(\frac{r r_1}{2\chi t} \right) + \right.$$

$$\left. + \sum_{n=1}^{\infty} \mathcal{I}_{\frac{n\pi}{\phi_0}} \left(\frac{r r_1}{2\chi t} \right) \cos\left(\frac{n\pi\phi}{\phi_0} \right) \cos\left(\frac{n\pi\phi_1}{\phi_0} \right) \right]. \tag{3.7}$$

Solving the problem requires the evaluation of the following integral:

$$T(r,\phi,z,t)=\int_0^t\int_0^\infty\int_0^{\phi_0}\int_0^\infty \frac{I[1+\text{ш}\cos(\omega t_1)]}{2\ell\rho c_p}\cdot e^{-\left(\frac{r_1}{a}\right)^2}\cdot e^{-\frac{z_1}{\ell}}\cdot G(r,\phi,z,r_1,\phi_1,z_1,t-\tau)\cdot r_1 \, dr_1 dz_1 d\phi_1 dt_1. \tag{3.8}$$

In the present case, $\phi_0=\pi$. This simplifies the term depending on ϕ_0 in the infinite sum. Besides, the laser pulse is ϕ-independent. Thus, the integral over ϕ_1 in the infinite sum is reduced to integration of $\cos(n\phi)$ between 0 and π leading to only null terms. After the integral over ϕ_1, the only term remaining is the one containing $\mathcal{I}_0$ with a factor π.

Introducing $\tau=t-t_1$ and isolating the different integrals, it follows:

$$T(r,z,t)=\frac{I}{8\ell\rho c_p\sqrt{\pi}\chi^{3/2}}\int_0^t \frac{1+\text{ш}\cos[\omega(t-\tau)]}{\tau^{3/2}}\cdot \overbrace{\left[\int_0^\infty e^{-\frac{z_1}{\ell}}\cdot\left(e^{-\frac{(z-z_1)^2}{4\chi\tau}}+e^{-\frac{(z+z_1)^2}{4\chi\tau}}\right)dz_1\right]}^{A}\times$$
$$\times\underbrace{\left[\int_0^\infty e^{-\left(\frac{r_1}{a}\right)^2-\frac{r^2+{r_1}^2}{4\chi\tau}}\mathcal{I}_0\left(\frac{rr_1}{2\chi\tau}\right)r_1dr_1\right]}_{B}d\tau. \tag{3.9}$$

The integral over z_1 gives (Sec. A.1)

$$A=\sqrt{\pi\chi\tau}\cdot e^{\frac{\chi\tau}{\ell^2}}\cdot\left[e^{-\frac{z}{\ell}}\operatorname{Erfc}\left(\frac{\sqrt{\chi\tau}}{\ell}-\frac{z}{2\sqrt{\chi\tau}}\right)+e^{\frac{z}{\ell}}\operatorname{Erfc}\left(\frac{\sqrt{\chi\tau}}{\ell}+\frac{z}{2\sqrt{\chi\tau}}\right)\right], \tag{3.10}$$

and the one over r_1 (Sec. A.2),

$$B=\frac{2\chi a^2\tau}{a^2+4\chi\tau}\cdot e^{-\frac{r^2}{a^2+4\chi\tau}}. \tag{3.11}$$

Once all the spatial integrals are solved, the following form is obtained:

$$T(r,z,t)=\frac{a^2I}{4\ell\rho c_p}\int_0^t\frac{1+\text{ш}\cos[\omega(t-\tau)]}{a^2+4\chi\tau}\cdot e^{\frac{\chi\tau}{\ell^2}}\cdot e^{-\frac{r^2}{a^2+4\chi\tau}}\times$$
$$\times\left[e^{-\frac{z}{\ell}}\cdot\operatorname{Erfc}\left(\frac{\sqrt{\chi\tau}}{\ell}-\frac{z}{2\sqrt{\chi\tau}}\right)+e^{\frac{z}{\ell}}\cdot\operatorname{Erfc}\left(\frac{\sqrt{\chi\tau}}{\ell}+\frac{z}{2\sqrt{\chi\tau}}\right)\right]d\tau \tag{3.12}$$

This last integral, over time, cannot be done analytically. It is possible to estimate Eq. (3.12) with a numerical approach. Unfortunately, under this form, numerical estimations do not converge well because of the exponential function. It is analytically stabilized with the error function, and Eq. (3.12) needs to be rewritten. An interesting manner is to develop the complementary error function into limited series. From [1], and for $y \in \mathbb{R}_+$, it follows:

$$\operatorname{Erfc}(y) = e^{-y^2}\left[\frac{\text{ч}_1}{1+py} + \frac{\text{ч}_2}{(1+py)^2} + \frac{\text{ч}_3}{(1+py)^3}\right] + \varepsilon(y), \tag{3.13}$$

where $|\varepsilon(y)| \leqslant 2.5\cdot 10^{-5}$, $p = 0.47047$, $\text{ч}_1 = 0.3480242$, $\text{ч}_2 = -0.0958798$, $\text{ч}_3 = 0.7478556$.

In (3.12) the argument of the first error function is negative for $\tau \leqslant z\ell/(2\chi)$. Thus, the limited development of Erfc for a negative argument is required. Using $\operatorname{Erf}(-y) = -\operatorname{Erf}(y)$, it can be demonstrated that for $y \in \mathbb{R}_-$, the limited development of the error function is:

$$\operatorname{Erfc}(y) \simeq 2 - e^{-y^2}\left[\frac{\text{ч}_1}{1-py} + \frac{\text{ч}_2}{(1-py)^2} + \frac{\text{ч}_3}{(1-py)^3}\right]. \tag{3.14}$$

Finally, the integral of Eq. (3.12) is split into two: one for $\tau \in [0\ ;\ z\ell/(2\chi)]$, where the development of Erfc functions is done with Eq. (3.14) and Eq. (3.13) and one for $\tau \in [z\ell/(2\chi)\ ;\ t]$ using Eq. (3.13) for each development. If $t \leqslant z\ell/(2\chi)$ the second integral is evidently null. It results:

$$\begin{aligned} T(r,z,t) \simeq \frac{Ia^2}{4\ell\rho c_p}\Bigg(&\int_0^{\frac{z\ell}{2\chi}} \frac{1+\text{ш}\cos[\omega(t-\tau)]}{a^2+4\chi\tau}\cdot e^{-\frac{r^2}{a^2+4\chi\tau}}\cdot\Bigg[2e^{\frac{\chi\tau}{\ell^2}-\frac{z}{\ell}}+ \\ &+e^{-\frac{z^2}{4\chi\tau}}\cdot\sum_{i=1}^{3}\frac{\text{ч}_i}{\left(1+p\left[\frac{\sqrt{\chi\tau}}{\ell}+\frac{z}{2\sqrt{\chi\tau}}\right]\right)^i}-\frac{\text{ч}_i}{\left(1-p\left[\frac{\sqrt{\chi\tau}}{\ell}-\frac{z}{2\sqrt{\chi\tau}}\right]\right)^i}\Bigg]d\tau+ \\ +\int_{\frac{z\ell}{2\chi}}^{t}\frac{1+\text{ш}\cos[\omega(t-\tau)]}{a^2+4\chi\tau}\cdot&\left[\sum_{i=1}^{3}\frac{\text{ч}_i\cdot e^{-\left(\frac{r^2}{a^2+4\chi\tau}+\frac{z^2}{4\chi\tau}\right)}}{\left(1+p\left[\frac{\sqrt{\chi\tau}}{\ell}+\frac{z}{2\sqrt{\chi\tau}}\right]\right)^i}+\frac{\text{ч}_i\cdot e^{-\left(\frac{r^2}{a^2+4\chi\tau}+\frac{z^2}{4\chi\tau}\right)}}{\left(1+p\left[\frac{\sqrt{\chi\tau}}{\ell}-\frac{z}{2\sqrt{\chi\tau}}\right]\right)^i}\right]d\tau\Bigg). \end{aligned} \tag{3.15}$$

Eq. (3.15) allows to estimate the temperature variations at any point (r,z) in the sample volume and for any time.

Evaluation of the maximum temperature rise

The temperature can be estimated at any point and for any moment with Eq. (3.15). However, it has the drawback to require numerical integration. If only the maximum temperature increase is wanted, e.g., to control that the sample will not burn, it requires to do this numerical estimation for a time long enough. The numerical calculation can last several minutes.

The maximum temperature rise is necessary in the center of the spot beam, for $r = 0$ and $z = 0$. In order to simplify even more the calculation, it is realized for a nonmodulated laser: $f = 0$ Hz, or $f(t) = 1$. For a modulated laser, the temperature rise is lower than this upper limit.

With these new conditions, Eq. (3.12) becomes:

$$T(r=0,z=0,t)=\frac{a^2 I}{\ell\rho c_p}\int_0^t \frac{e^{\frac{\chi\tau}{\ell^2}}}{a^2+4\chi\tau}\cdot \mathrm{Erfc}\left(\frac{\sqrt{\chi\tau}}{\ell}\right)d\tau. \tag{3.16}$$

Even for this simplified case, analytical solution of the maximum temperature as a function of the time does not appear easy to determine. However, the maximum value, reached for an infinite time, is easier. It is possible to demonstrate the following limit:

$$\int_0^\infty \frac{e^y}{x+y}\cdot \mathrm{Erfc}(\sqrt{y})dy = e^{-x}\cdot\left[\pi \mathrm{Erfi}(\sqrt{x})-\mathrm{Ei}(x)\right]. \tag{3.17}$$

Thus, Eq. (3.16) can be rewritten under this form:

$$\lim_{t\to\infty} T(0,0,t)=\frac{a^2 I}{4\ell\kappa}\cdot e^{-\left(\frac{a}{2\ell}\right)^2}\cdot\left[\pi \mathrm{Erfi}\left[\frac{a}{2\ell}\right]-\mathrm{Ei}\left[\left(\frac{a}{2\ell}\right)^2\right]\right], \tag{3.18}$$

with $x=[a/(2\ell)]^2$, and $y=\chi\tau/\ell^2$.

Eq. (3.18) leads to an estimation of the maximum temperature rise, corresponding to the upper limit reached. This simple evaluation can be used for estimating the temperature rise and checking that the sample will not be affected by such heating.
If the modulation frequency is high enough, such as for the probe beam, the variations of temperature can be neglected and the cosinus term in the function $f(t)$ is omitted. Thus, $f(t)$ is reduced to 1/2, which corresponds to half of a nonmodulated beam. The maximum heating for such beam can then be evaluated as half of the temperature rise estimated by Eq. (3.18):

$$\lim_{t\to\infty} T(0,0,t)=\frac{a^2 I}{8\ell\kappa}e^{-[a/(2\ell)]^2}\left[\pi \mathrm{Erfi}\left[\frac{a}{2\ell}\right]-\mathrm{Ei}\left[\left(\frac{a}{2\ell}\right)^2\right]\right]. \tag{3.19}$$

As a summary, the 3D heat equation is solved. Temperature can be estimated for any moment and at any place of the sample for a modulated beam heating the sample with a simple numerical integration.
The maximum temperature rise of a nonmodulated beam and a high frequency modulated beam is obtained analytically. In particular, the probe beam heating can be estimated by Eq. (3.19). However, in the theoretical model [20], the constant heating is neglected because of the assumptions on the infinite dimensions of the sample and the non-null rigidity of the crack (Sec. 1.3.2).
It is now possible with the theoretical predictions of the temperature field to study the influence of the parameters on the experiment and to compare theoretical predictions and experimental results.

3.3 Influence of the pump frequency

As previously evoked (Sec. 2.1), the choice of the pump frequency influences the breathing efficiency. In a first approach, the best frequency has been estimated at a few hundreds of millihertz due to the characteristic times of the temperature rise and thermal relaxation ($\propto$ s). With Eq. (3.15), it is now possible to make numerical simulations of the temperature evolution at any point of the sample and for any frequency and to compare them with experimental results.

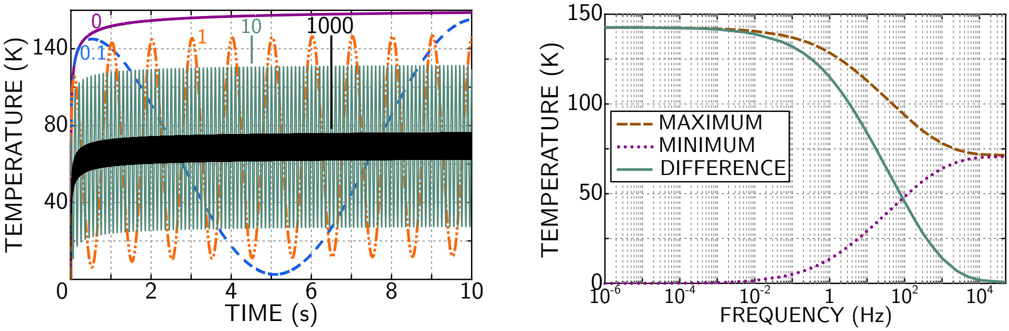

(a) (b)

Figure 3.2: (a): Temperature evolution as a function of time in the center of the beam for the frequencies f_L = 0, 0.1, 1, 10 and 1000 Hz. (b): Evolution of the temperature extrema (maximum T_M, minimum T_m and difference $T_M - T_m$) in the center of the beam as a function of the modulation frequency. (a-b): Parameters: $a = 20$ µm, $P = 100$ mW, $r = 0$, $z = 0$.

The evolution of the temperature rise as a function of time, at the hottest point, corresponding to the center of the beam, is studied for various frequencies. For a continuous beam, equivalent to $f_L = 0$ Hz, the temperature rise is monotonously increasing up to the asymptotic value T_{M0} determined by Eq. (3.18) (Fig. 3.2(a)). The breathing amplitude is influenced by the crack face displacements which are themselves influenced by the temperature difference $\Delta T = T_M - Tm$, where T_M (T_m) is the maximum (minimum) temperature rise induced by the heating modulation. The ideal is a frequency for which $T_M \to T_{M0}$ and $T_m \to 0$.

For $f_L \to \infty$, the variations of the beam intensity are too fast to make temperature variations: $\Delta T \to 0$. However, a constant heating is present. The temperature evolution as a function of time is similar to the temperature evolution of a continuous beam, divided by two in intensity due to the modulation (Sec. 3.2). It also corresponds to the average heat of a heating intensity modulated at any frequency: $(T_M + T_m)/2$.

For $0 < f_L < \infty$, the temperature difference ΔT diminishes as the frequency f_L increases, because of the characteristic times involved in heating and cooling the sample. Fig. 3.2(a) demonstrates that for a constant heating, the temperature rise lasts several seconds before it can be considered almost constant. For an infinite time, Eq. (3.18) predicts a maximum temperature rise T_{M0} of 141.9 K. Simulations show that it takes ~35 seconds to reach 99% of T_{M0} (T = 140.5 K), which is considered to be close enough to the asymptotic value. It leads to an ideal frequency close to $f_L = 14$ mHz. However, this estimation is valid for a laser intensity modulated in a square waveform. For a sinusoidal waveform, simulations indicate that the frequency is about 3.5 mHz. Simulations are realized for the parameters of the experiment described below: $a = 20$ µm and $P = 100$ mW (Fig. 3.2(a)). The evolution of heating for $f_L = 0$, 0.1, 1, 10 and 10^3 Hz are presented. The shift of the maximum and the minimum temperature rise when the frequency increases clearly appears. As predicted, $f_L = 100$ mHz is close to provide $T_M \simeq T_{M0}$ and $T_m \simeq 0$. The melting point of glass is much higher than the ones reached: for a 140 K increase, the glass is then at $293 + 140 \simeq 433 \ll 1090$ K, where 1090 K is the temperature of fusion of a borosilicate glass containing 80% of silica.

In Fig. 3.2(b) the temperature maximum T_M, minimum T_m and difference, ΔT, is plotted for frequencies $f_L \in [10^{-6}; 10^4]$ Hz. The temperature variations are estimated at the center of the beam for the same radius and power: $a = 20$ µm and $P = 100$ mW.
For $f_L \leqslant 1$ mHz, the temperature difference is practically stable because the frequency is low enough to closely reach the ideal case.
For $f_L \geqslant 10$ mHz, ΔT diminishes as f_L increases. For $f_L \in [1; 100]$ Hz, the decrease of ΔT can be considered linear on the logarithmic scale: consequently, it follows an exponential decay.
Beyond $f_L \geqslant 1$ kHz, the temperature oscillations are almost negligible. The temperatures T_M and T_m can be considered equal: $T_M \simeq T_m$. The temperature rise in such case can be evaluated with Eq. (3.19).
It can be observed that the maximum T_M and the minimum T_m, which are functions of the frequency f_L, evolve symmetrically from the maximum temperature rise reached for an infinitely high-frequency modulated beam. Mathematically, it corresponds to $T_{M0} - T_M = T_m - 0$. It implies that the average heating corresponds to the case $f_L \rightarrow \infty$, analytically determined by Eq. (3.19).

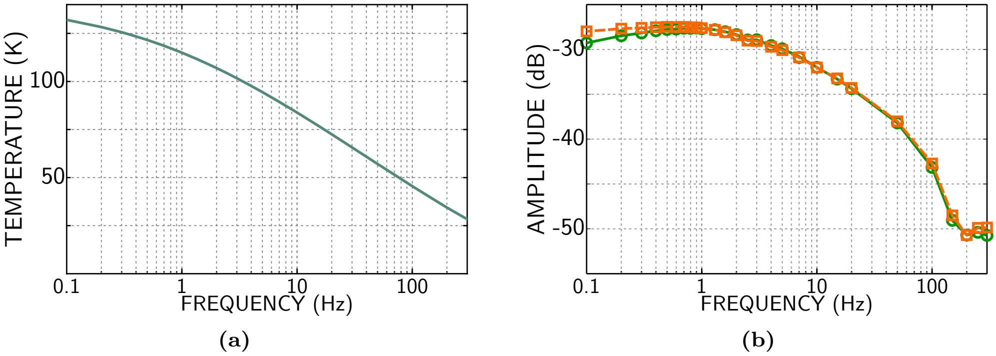

(a) **(b)**

Figure 3.3: (a): Evolution of the temperature difference $T_M - T_m$ in the center of the beam as a function of the modulation frequency. (b): Evolution of the amplitude on the left and right sidelobes at $f_H - f_L$ (○) and $f_H + f_L$ (□) as a function of the modulation frequency. (a-b): Parameters: a=20 µm, $P = 100$ mW, $f_L \in [0.1; 300]$ Hz.

An experiment is realized on a crack at different frequencies between $f = 100$ mHz up to 300 Hz with the Υ_1 set-up. The beam diameter and power are of $a = 20$ µm and $P = 100$ mW for the pump and of $a = 19.2$ µm, $P = 35$ mW for the probe beams. The probe beam intensity modulation frequency is $f_H = 90.4$ kHz. As previously said, the simulations of 3.2(b) are performed with these parameters for the pump beam.
In Fig. 3.3(b) the amplitudes of the main peak and of the first nonlinear sidelobes are plotted as a function of the pump frequency. Fig. 3.3(a) is a zoom of the theoretical temperature difference for the same range of frequencies.
The main peak remains constant for all the frequencies which is logical as the only changed parameter is the pump frequency. The amplitudes of first nonlinear sidelobe amplitudes, can be considered constant for $f_L \leqslant 1$ Hz. The temperature differences are estimated of 132 and 115 K for $f_L = 0.1$ and 1 Hz, respectively. The breathing is influenced by the temperature difference, the distance between the crack faces and the crack rigidity (Sec. 1.3.2). The crack closing can never be perfect due to the imperfect crack faces and the numerous micro-contacts. However, as the distance between the crack faces diminishes, i.e., as the crack closing improves, the rigidity increases, and then the forces required to improve the closing also increases. For tiny displacements near a perfect closing, the changes in the loading force can be huge (Fig. 1.7(a)). The constant amplitude for $f_L \in [0.1; 1]$ Hz is attributed to this phenomenon. The changes in the temperature difference as the frequency evolves are not important enough to induce significative change in the crack closing and thus, in the nonlinear sidelobe amplitudes. For $f_L \in [1; 100]$ Hz, the nonlinear sidelobes amplitudes decrease because the breathing quality is affected by the diminution of the temperature difference. Finally, for $f_L > 100$ Hz, the nonlinear sidelobe amplitudes are lost in the noise because the temperature rise ($T_M < 94$ K) is not sufficient to close the crack.

As a conclusion, it is demonstrated that the amplitude of the nonlinear mixed-frequencies decreases as the frequency f_L increases. Unfortunately, the acquisition time increases as the pump frequency decreases because the considered frequency window, $f_H \pm f_L$ diminishes. As an example, for ten averages of the signal, it takes about half an hour for $f = 100$ mHz, whereas it takes a little more than 3 minutes for $f = 1$ Hz and about 20 seconds for $f = 10$ Hz. A compromise between the time spent for the experiment and the efficiency of the temperature difference of the heating is required.
The importance of the temperature difference, for a given frequency, is influenced by the beam power, the beam focusing and the sample thermal characteristics. The experimental parameters a and P influence T_M and T_m and thus the time needed to reach them. The thermal glass parameters influence the required time to heat up to T_M and to cool down to T_m. Simulations and experimental results confirm that $f_L \sim 1$ Hz is suitable for our experiments.

3.4 Influence of focusing on the nonlinear frequency-mixing amplitude

The focusing affects the spatial resolution of the method and the amplitude of the nonlinear frequency-mixing. The latter influence is discussed herein whereas the former is discussed in the next section (Sec. 3.5).

The intensity is defined as $I = P/(\pi a^2)$, so it is inversely proportional to the square of the beam radius. For a constant power, as the focusing increases, the intensity increases too. Numerical estimations demonstrate that in the near field of the source, the temperature rise is influenced by the focusing. Indeed, in the spot beam area, the temperature rise is increased (Fig.3.4(b)). Far from the spot area, the thermal field is very similar for different focusings because the power is constant. However, it can be noted that the less focused source induces a temperature rise slightly larger than the more focused one in the far field (Fig. 3.4(b), Inset). This is the consequence of the energy conservation.

Considering a quasistatic motion of the crack ($\omega_L \ll \omega_{o,c}$), the crack motion can be estimated with the evaluation of the sample dilatation. The dilatation corresponds to the integral of the temperature field multiplied by the thermal expansion coefficient. In one dimension, it reads:

$$\Delta L = \alpha \int_0^\infty T(r)dr. \tag{3.20}$$

The total displacement induced by the heating is twice the result of the integral as each crack faces dilates under the thermal loading.

The integral of the temperature over the complete volume is independent of the focusing because of the energy conservation law. Fig. 3.4(a) demonstrates the temperature rise decreasing as a function of the distance for $a_L = 20$ µm, $P_L = 100$ mW and $f_L = 1$ Hz. In the 1D approach, the temperature rise is larger in the near field but lower in the far field (Fig. 3.4(b)). The numerical estimation of the dilatation resulting from Eq. (3.20) for different focusings demonstrate very similar results: $\Delta L \simeq 469$ and 459 nm for $a_L = 20$ and 50 µm, respectively.

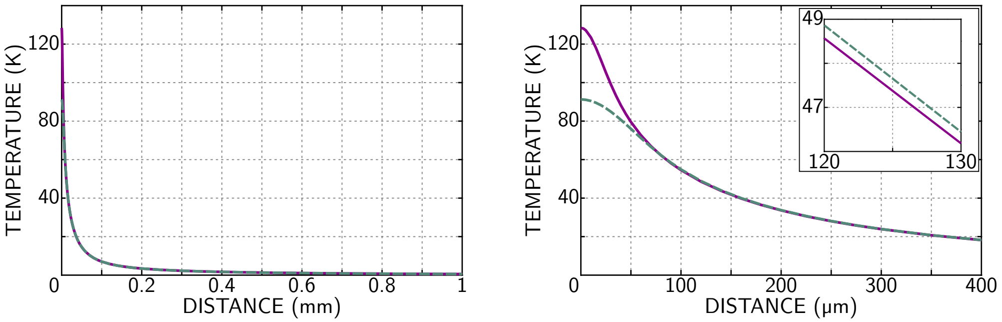

(a) **(b)**

Figure 3.4: (a-b-Inset): Theoretical evolution of the maximum temperature rise, T_M, as a function of the distance from the center of the beam for $P_L = 100$ mW, $f_L = 1$ Hz and $a_L = 20$ µm (—), $a_L = 50$ µm (- -).

The amplitude of the acoustic wave, generated at f_H, depends on the magnitude of the temperature rise of the surface. Neglecting the attenuation, the acoustic wave amplitude is expected to be enhanced with the focusing as the maximum temperature rise is increased in the center of the beam.
The acoustic strain is proportional to the probe wave amplitude (Eq. (1.19)) and thus, the nonlinear sidelobe amplitudes are expected to increase as well.

Then, the nonlinear sidelobes should not be influenced by the focusing of the pump as the related dilatation is equal, but only by the focusing of the probe which increases the acoustic wave amplitude.

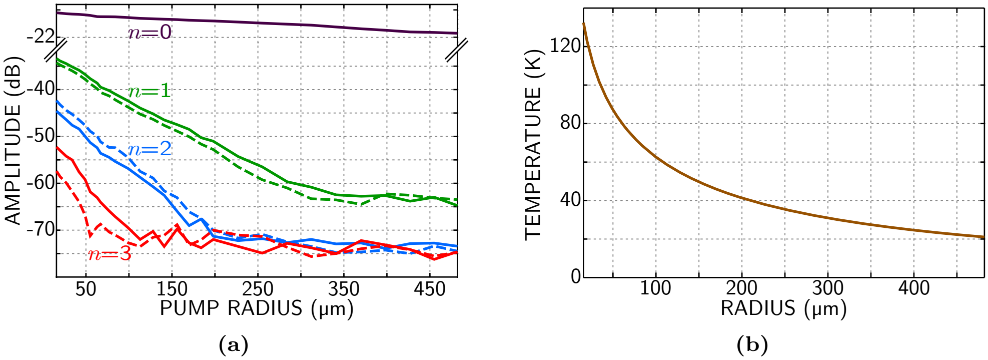

Figure 3.5: (a): Experimental dependence of the amplitude of the main peak and of the first three left (—) and right (- -) sidelobes on the focusing of the beams on the sample. (b): Theoretical evolution of the maximum temperature rise T_M in the center of the beam as a function of the beam radius.

An experiment is realized and presented in Fig. 3.5(a). The sample is moved in the z-axis to control the focusing of both beams on the crack. The radii vary for both beams between 16 μm and 457 and 482 μm for the probe and the pump beam, respectively. Both beams are adjusted to be very close, but the difference between the two radii increases as the radii increase. The pump beam has the following characteristics: P_L = 100 mW and f_L = 1 Hz, and the probe beam: P_H = 20 mW and f_H = 91.4 kHz.
The pump power is chosen five times larger than the probe one to enhance the possibility to evaluate if the crack breathing is affected by the pump focusing.
A 1D scan is realized firstly with the best focusing ($a_H = a_L$ = 16 μm). This insures the beams to remain focused on the crack as the focusing evolves.
The decrease of the first three sidelobes is similar. The amplitude, in decibels, varies linearly as a function of the focusing until 300, 200 and 100 μm for the sidelobes associated to n = 1, 2 and 3, respectively. Consequently, it demonstrates an exponential decay of the amplitude of the nonlinear sidelobes as a function of the focusing. Due to their non-monotonous behavior revealed earlier (Sec1.3.2), the sidelobes for $n > 1$ do not necessarily evolve monotonously as a function of the focusing. For large radii ($a_L \geqslant$ 300 μm), the first nonlinear sidelobe is not lost in the noise and its amplitude is constant.

The main peak also decreases as the focusing decreases. However, the amplitude variation is much smaller: ∼4 dB for the main peak in comparison to ∼32 dB for the first left nonlinear sidelobe. It corresponds to an influence of the focusing more than 600 times larger on the nonlinear sidelobes than on the main peak.
The previous discussion on the influence of the pump and the probe focusings is then not valid. This observation shows that the quasistatic assumption is not valid experimentally. In Chap. 5, a model without this assumption is developed.
However, it is important to also consider the fact that the above discussion concerns an idealized crack and a 1D geometry. Because of the micro-contacts and the rugosity of the real crack in the 3D geometry, the theoretical analysis is much more complex. In particular, the focusing influences the intensity of the laser field penetrating inside the crack. This should increase the thermoelastic wave amplitude.

In Fig. 3.5(b) the estimated evolution of the maximum temperature rise, at the center of the beam, for the frequencies involved in the experiment, is presented. One can see the exponential decay of the temperature as a function of the defocusing, as for the amplitudes of the main peak and the nonlinear sidelobes. A change of the focusing appears to induce an important change in the mixed-frequencies generation. It indicates that it influences importantly the crack breathing quality.

3.5 Spatial resolution determination

The generation of the mixed-frequencies corresponds to the location where the generated acoustic wave is coincident with the breathing crack. In the scans (Secs. 2.3 and 2.5) the crack is localized by the maximum of the nonlinear frequency-mixing amplitudes.
The spatial resolution is determined by the $1/\sqrt{e}$ decrease of the photoacoustic signal (or -4.3 dB from the maximum) because these nonlinear mixed-frequencies are also generated when the beams are focused nearby the crack and not precisely on it. Fig. 2.7 clearly demonstrates the generation of the first nonlinear sidelobes when both beams are far from the crack. Fig. 3.6(a) is an example of a spectra where the beams are focused 800 µm far from the crack. The distance is ∼2.5 and ∼8 times larger than the probe and pump diameter, respectively. It corresponds to the spectra from Fig. 2.7, for $y = 1$ and $x = 0.3$ mm. The first nonlinear sidelobe is generated with an amplitude of 10 dB over the noise (Fig. 3.6(a)).
Moreover, for several 1D sections, the first nonlinear sidelobe evolutions demonstrate not one but two successive locations with the amplitude maxima (Fig. 3.6(b)). Due to the factor 3 between the pump and probe beam radii, it corresponds to cases where the probe beam remains on the crack but not the pump beam.
These effects show the possibility to generate the mixed-frequency components without the condition of both beams focused on the crack. In order to explain the phenomena involved, a slightly different set-up, based on Υ_1, is developed in order to be able to move one of the beams only (Fig. 3.6(c)).
The fixed beam is focused on the sample in a radius of 19 µm. The second beam is moved, as for a 1D scan, along the x-axis. The shift is achieved taking advantage of the imperfections of the lens, by shifting the beam from its center. This technique has the drawback that the beam radius is modified by this shift. In order to neglect the influence

of the radius changes on the experiment, the number of steps is limited. It follows that the radius of the shifted beam is of 20 ± 2 µm. Then a 1D scan can be achieved shifting only one beam. The same 1D scan can be achieved for several powers of each beam, independently controlled, in order to observe the influence of the pump and the probe localization and power. The pump beam is intensity-modulated at $f_L = 1$ Hz and the probe beam at 91.4 kHz.

First, the influence of the power and the location of the pump beam are analyzed by shifting and amplifying the latter (Sec. 3.5.1). Second, the same analysis is done inverting the beams, so that the probe beam is shifted and amplified (Sec. 3.5.2). Third, the influence of the breathing -controlled by the pump power- and the probe beam location is studied by shifting the probe beam and increasing the pump beam power (Sec. 3.5.3). Finally, the conclusions are compared with the influence of the focusing on the spatial resolution (Sec. 3.5.4).

As the first nonlinear sidelobes are the only one which amplitudes monotonously increase as a function of the pump loading (Sec. 1.3.2, Fig. 1.9), the interpretations of their evolutions are easier. The evolution of these sidelobes only is discussed in this section.

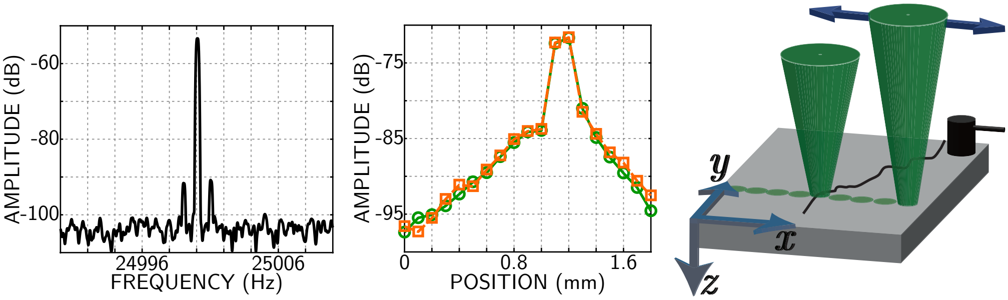

(a) (b) (c)

Figure 3.6: (a): Spectrum extracted from Fig. 2.7 for $y = 1$ mm, 800 µm far from the crack. (b): Scan section from Fig. 2.7 along x for $y = 1.6$ mm for the first nonlinear left (○) and right (□) sidelobes. (c): Schematic representation of the new set-up.

3.5.1 Influence of the pump far from the crack

It is firstly necessary to remind that the nonlinear frequency-mixing process is associated to the modulation of an acoustic wave on a breathing crack. The breathing crack, provoked by the pump loading, is responsible for this nonlinear phenomenon and not directly the pump beam.

The thermal diffusivity is at the origin of the heat transport in all the sample. In order to make the crack breath it needs to be periodically heated; a constant heat can just close it permanently (Sec. 3.1). The modulation of the heat, as the pump beam is intensity modulated, is propagated for about one thermal wavelength. Beyond, the sample is constantly heated. The thermal wavelength is defined by $\lambda_{th} = 2\sqrt{\pi\chi/f}$. This leads to $\lambda_{th} \simeq 2.6$ mm for a frequency of 1 Hz, larger than the penetration length of light into the sample ($\lambda_{th} > 8\ell$) and the beam radius ($\lambda_{th} \simeq 50a$ for a radius of 50 µm). The theory then predicts there are temperature oscillations at $f_L = 1$ Hz far from the irradiated area.

Numerical simulations confirm that at distances larger than the thermal wavelength, there is almost no more modulation. The thermal wave will additionally decay proportionally to $1/r$ (with r the distance from the source). This effect is not taken into account in the latter formula, so the real value is smaller than 2.6 mm.
Consequently, it should be possible to make the crack breath up to a few hundreds of micrometers far from the crack, assuming the power is sufficient. With the powers involved, the temperature rise decreases ∼100 times over a millimeter distance (Fig. 3.4(a)).

For the probe beam, due to the high frequency f_H, the thermal wavelength is much reduced: $\lambda_{th} \simeq 26$ µm for $f_H = 10$ kHz. Thus, the temperature oscillations at f_H are only in the region of the direct heating by laser radiation. Besides, these oscillations are also much reduced in amplitude. Fig. 3.2(b) demonstrates that for f_H the temperature difference is negligible in comparison to the temperature difference induced by the pump beam, even in the center of the beam. Thus, the probe beam role is to generate the propagating acoustic waves and not to drive the crack breathing.

To demonstrate that it is possible to make the crack breathe with a pump radius focused outside of the crack, a first experiment is done. The probe beam is focused on the crack with a power of 35 mW. The pump beam is moved by a 1D scan shifting. The same 1D scan is accomplished for several pump powers in order to observe its influence.

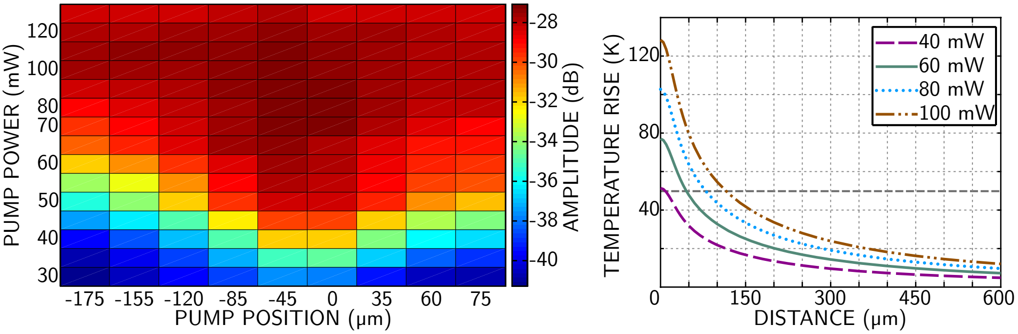

(a) (b)

Figure 3.7: (a): Evolution of the first right sidelobe at $f_H + f_L$ as a function of the pump position relatively to the crack position (horizontal direction) and for different pump powers (vertical direction). The probe beam is focused on the crack at 0 with a power of 35 mW. (b): Evolution of the maximum temperature rise at the center of the beam as a function of the distance for $P = 40$, 60, 80 and 100 mW. The 50 K temperature rise limit is marked by a dashed line.

In Fig. 3.7(a) the experiment scans for the powers contained between 10 and 130 mW with power steps of 5 or 10 mW are presented. They show the evolution of the first nonlinear right sidelobe amplitude. For low powers ($P < 40$ mW), the crack is hardly detectable because the pump is insufficient to make the crack breathing correctly. However, a slight increase in the nonlinear sidelobe amplitude is noticed. It can be attributed to partial contacts, i.e., to the creation of few micro-contacts between the crack faces. The crack starts to be detected for $P \simeq 40$ mW. It means that the required temperature to close the crack is about 50 K which corresponds to the temperature rise for $P = 40$ mW. The consideration of the maximum temperature rise is a very simplified approach. A better approach for the quasistatic problem would be to estimate the dilatation induced at this temperature with Eq. (3.20). However, this would not take into account the location of the pump in comparison to the location of the crack. Besides, the influence of focusing (Sec. 3.4) indicated that the quasistatic assumption may be not fulfilled experimentally. Thus, let us, in a first approach, consider that the crack breathing is related to the temperature rise on the crack. With this information, it is possible to predict theoretically the distance from the pump beam where this temperature is reached. In Fig. 3.7(b) the theoretical evolutions of temperature as a function of the distance are presented for the different powers $P = 40$, 60, 80 and 100 mW . These predictions demonstrate the crack could breathe by a pump beam located rather far from the crack. This is confirmed by the experimental results, demonstrating a clear decrease of the spatial resolution with power increase.

For the most important powers, $P \geqslant 100$ mW, the crack is not detectable anymore in the experimental results, even when the pump beam is focused 175 µm far from the crack -corresponding to $\sim 8a_L$. Nonlinear mixed-frequencies are generated all over the scan with almost the same efficiency, as if the crack breathing is optimum. Fig. 3.7(b) demonstrates that it is possible to reach the 50 K temperature rise up to ~115 µm far from the center of the beam for $P = 100$ mW. This estimation is a bit lower than the results on the experiment as nonlinearities are clearly detected up to a distance of 175 µm between the pump beam and the position of the crack for $P = 100$ mW. However, the phenomenon is clearly identified.

For $50 < P < 60$ mW, the first nonlinear sidelobe starts being generated for a pump focused outside the crack but the crack remains a little detectable as the amplitude of the nonlinear sidelobe is larger on the crack. This can be attributed to a better breathing when the pump is focused on the crack.

If the temperature rise is sufficient to close the crack far from the irradiated region, the temperature difference decreases with the distance and increases with the power. For example at $P = 50$ mW, the temperature difference at the center of the beam is of 57 K, whereas for $P = 100$ mW and 175 µm far from the center of the beam it is of 25 K. However, this difference is not visible on the amplitude of the nonlinear sidelobe. It demonstrates that the amplitude is mainly controlled by the change between the opened and closed state, and the quality of each state more than the temperature difference.

The spatial resolution can then clearly be affected by the pump power. In this case, the spatial resolution can be defined only for $P = 35$ to 45 mW. It varies between 157 and 201 µm. Below 35 mW, the nonlinear frequency-mixing amplitude is not important enough to detect a 4.3 dB decrease whereas when the power is larger than 45 mW, the distance covered by the pump beam is not important enough to make the nonlinear frequency-mixing amplitude decrease by 4.3 dB. The spatial resolution varies importantly as a function of the pump power. For example, for a power step of 5 mW (from $P = 35$ to 40 mW) the spatial resolution is more than 40 µm better in the latter case. At the opposite, it increases of ~20 µm for another 5 mW increase on the pump power. Thus, the evolution of the spatial resolution, as a function of the pump power, is not monotonous (Fig. 3.12(a)).

This result explains why in the previously described 2D scans, some scans have two maxima in a row as the probe beam radius is 3 times exceeding the one of the pump and the step is chosen coincident with the pump diameter (Fig. 3.6(b)).
The main peak amplitude increases monotonously as a function of the pump power (up to 7 dB for the whole experiments) with a slight maximum of a few dB on the crack, as predicted and generally observed.

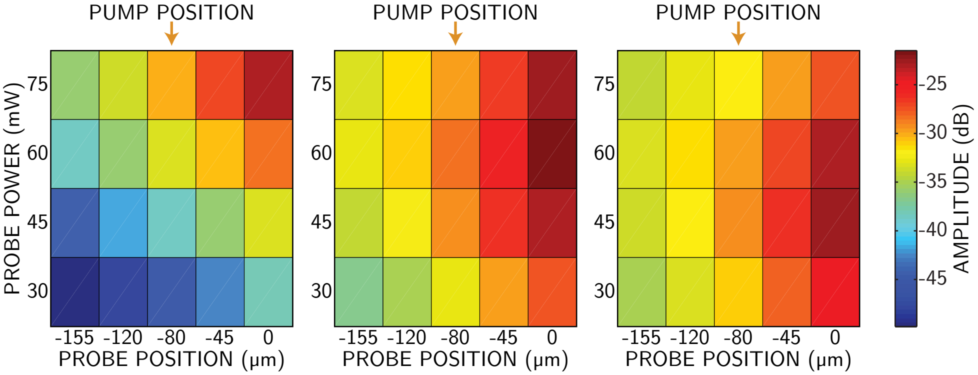

(a) (b) (c)

Figure 3.8: Evolution of the first right sidelobe at $f_H + f_L$ as a function of the probe position relatively to the crack position (horizontal direction) and for different probe powers (vertical direction). The pump beam is focused at -80 µm from the crack. The pump power is $P_L = 30$ mW (a), $P_L = 60$ mW (b), and $P_L = 100$ mW (c). All scans are represented with the same amplitude scale.

Another experiment is realized. The pump beam is fixed 80 µm outside the crack ($\sim 4a_L$) and the probe is shifted as for a 1D scan (Fig. 3.8). The power of each beam is independently modified. In Fig. 3.8 the position of the pump beam is indicated: $x = -80$ mm, the crack is at $x = 0$ mm. The same 1D scan for different probe powers (vertical direction) and pump powers (horizontal direction between the Figs) are presented.
As predicted, for a low pump and probe power ($P_L = 30$ mW, $P_H = 30$ mW), the crack does not breathe and is not detected. When the pump increases the detection of the crack is achieved ($P_L = 100$ mW, $P_H = 30$ mW). This demonstrates again the possibility to achieve the crack breath with a pump beam focused outside of the crack. It also demonstrates that the probe beam is a limiting factor in the spatial resolution as the crack is detected only when the probe is focused on it. The nonlinear mixed-frequencies generation increases on and outside the crack when the pump power increases and/or when the probe power increases. In both case, this effect is attributed to the improvement of the crack breathing.
It can also be observed that if the pump power is low ($P_L = 30$ mW, Fig. 3.8(a)), the crack is detected only for a high probe power. For a more important probe power ($P_H = 75$ mW), the crack is detected in each scan. The nonlinear mixed-frequency amplitude maximum increases as the probe power increases in the former case (Fig. 3.8(a)). The nonlinear sidelobe amplitude maximum is obtained for $P_H = 75$ mW. At the contrary,

in the latter case (Fig. 3.8(c)), this maximum is for $P_H = 60$ mW, and the amplitude of the nonlinear sidelobes diminishes for $P = 75$ mW. Fig. 3.8(b) looks closely similar to Fig. 3.8(c) shifted for higher probe powers and with a more important change between $P_H = 30$ and 45 mW than between $P_H = 60$ and 75 mW.
Theoretically, the nonlinear sidelobe amplitude is supposed to be proportional to the probe power (Eq. (1.19)). However, Fig. 3.8 demonstrates that this increase is not independent of the pump power: the amplitude rise between $P_H = 30$ and 75 mW is of ~15 dB for $P_L = 30$ mW (Fig. 3.8a) and of ~6 dB for $P_L = 60$ mW (Fig. 3.8b).

These experiments also demonstrate the possibility to realize 1D scans for a pump beam spot situated next to the crack. This result confirms the capacity of the thermoelastic wave, generated by the pump beam, to make the crack breath. It also demonstrates that the probe beam is a limiting factor as the scan accurately localize the crack depending on the only probe position.
The reduced number of experimental points does not allow the possibility to estimate the spatial resolution for this experiment.

3.5.2 Influence of the probe power

It has been just demonstrated in the last experiments that the nonlinear sidelobe amplitude is not always proportional to the probe power (Fig. 3.8c), and that the amplitude variations due to probe power changes depend on the pump power too (Figs. 3.8a and 3.8b). Both results are different from the theoretical predictions (Eq. (1.19)).
For a monochromatic modulation of the laser intensity in time, $If(t) = I[1 + \text{ш}\cos(\omega t)]/2$. The spectrum envelope, in the Fourier domain, can be written $\widetilde{f}(\omega) = \pi\left(\delta(0) + \text{ш}/2 \cdot [\delta(\omega - \omega_0) + \delta(\omega + \omega_0)]\right)$. Consequently, the effect of an intensity modulated beam heating on a sample can be separated into two parts: a constant part ($\propto \delta(0)$) and a modulated one ($\propto \delta(\omega \pm \omega_0)$). In [20] the constant part is neglected because the sample is supposed infinite (Sec. 1.3.2).

It has been demonstrated that the heating of a beam, intensity modulated at a frequency of tens of kHz (as for the probe beam), is similar to a heating of a nonmodulated beam with half of the intensity (Secs. 3.2 and 3.3). A constant beam heating a crack can close it (Sec. 3.1). Then, a probe beam is also expected to be able to close the crack.

An experiment similar to the previous one (Sec. 3.5.1) is achieved. This time, the pump beam is fixed and focused on the crack and the probe beam is shifted in order to realize a 1D scan (Fig. 3.9). The scan is repeated at different probe beam powers. The beams are inverted in comparison to the previous experiment, then the radii are inverted too: the pump radius is of 19 µm, the probe beam radius of 20 ± 2 µm.

Fig. 3.9 exhibits the evolution of the first nonlinear right sidelobe as a function of the position of the probe and as a function of the probe power. One can see that even for very low probe power, the crack is detected. This demonstrates the important efficiency of the nonlinear frequency-mixing generation when the crack breathes.

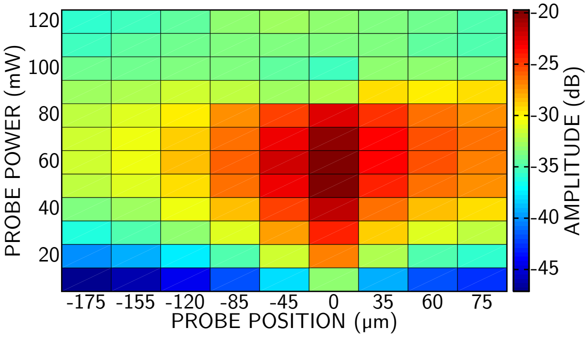

Figure 3.9: Evolution of the first right sidelobe at $f_H + f_L$ as a function of the probe position relatively to the crack position (horizontal direction) and for different probe powers (vertical direction). The pump beam is focused on the crack at 0 with a power of 50 mW.

Then, as the probe power increases (for $P_H \leqslant 80$ mW), the crack remains clearly detected and the amplitude of $f_H + f_L$ logically increases as predicted by the theory (Eq. (1.19)). For $P_H \in [10; 50]$ mW, the increase of the first nonlinear sidelobe amplitude is of $\sim$13 dB. The nonlinear mixing-frequency generation for a probe next to the crack is also observed. The pump is focused on the crack to provide the breathing. The acoustic wave, generated far from the crack, propagates in all the directions. The part of the acoustic wave propagating toward the part of the crack which is locally breathing then interacts with it to generate the nonlinear sidelobes. The interaction of the acoustic wave with a crack when the probe beam is focused far from the crack is discussed in Sec. 3.5.3.
For a probe power of $P_H = 80$ mW, in the crack area, the nonlinear sidelobe amplitude decreases in comparison to $P_H = 70$ mW. The difference is of 2 dB on the crack and is also observed next to the crack in the same order of difference.
For $P_H > 80$ mW, the nonlinear sidelobe amplitude suddenly importantly falls down and the crack is not detected anymore. For probe powers of 70 and 90 mW and a 22 µm radius spot, the temperature rise, in the center of the beam, is estimated at $\sim$48 and $\sim$62 K, respectively. The crack is expected to close around 50 K -although this estimation did not take into account the temperature rise from the probe beam. The crack is closed by the probe and cannot breathe. The mixed-frequencies can no longer be generated. This is consistent with the explanations above: the distance between the crack faces can be influenced by constant heating provided by the probe beam.

Consequently, if the pump beam power is not important enough to make the crack breath efficiently, an important probe power can reduce the distance between the crack faces and improve the breathing efficiency.
In the previous section, in Fig. 3.8(a), the pump power ($P_L = 30$ mW) is not focused on the crack and is weak to influence strongly the distance between the crack faces and the crack rigidity. Then, for a weak probe power the crack is almost not detected. The maximum of the nonlinear sidelobe is observed for the maximum probe power as it reduces the distance between the crack faces and favors the crack breathing induced by the pump beam.

If the pump power is already large enough, a diminution of the distance between the crack faces by an important probe power reduces the crack breathing amplitude and thus the nonlinear frequency-mixing process. In Fig. 3.8(c), with $P_L = 100$ mW, the maximum of $f_H + f_L$ amplitude is for $P_H = 60$ mW and not 75 mW as previously. This is also confirmed by the diminution of the nonlinear frequency-mixing amplitude when the probe power changes from $P = 70$ mW to 80 mW in Fig. 3.9.

The spatial resolution is not much affected by the increase of the pump power for $P \in [0.7;\ 80]$ mW. Even for $P_H = 0.7$ mW, the crack is detectable and the dynamic offers the possibility to define a spatial resolution: 83 µm for the first right nonlinear sidelobe. It is not as good as the following ones, e.g., 66 µm for the same sidelobe for $P_H = 10$ mW. However, it demonstrates the important effect of the breathing on the acoustic wave modulation efficiency.

As the probe power increases, for $P_H \in [10;\ 70]$ mW, the spatial resolution slowly diminishes, from 69 µm to 116 µm by steps of ~10 µm as the probe power increases by 10 mW. For $P_H = 80$ mW, just before the closing, it suddenly falls to 147 µm. Then, as the crack is closed, no spatial resolution can be determined anymore (Fig. 3.12(a)). The decrease of the amplitude of the nonlinear sidelobes as the probe power increases from $P_H = 70$ to 80 mW can be attributed to the distance decrease between the crack faces. The decrease of the spatial resolution, for $P_H \in [10;\ 70]$ mW, is discussed in the next section (Sec. 3.5.3).

3.5.3 Influence of the acoustic wave generated far from a breathing crack

It is clear from the different experiments that the nonlinear sidelobes can be generated when the probe beam is focused far from the crack (Figs. 2.7 and 3.9). Similarly as when the acoustic wave is generated on the crack, the involved phenomenon is the interaction of the acoustic wave with a breathing crack. The amplitude of the acoustic wave decreases with the distance (in $1/r$ for a spherical wave). Then, the part of the acoustic wave interacting with the breathing crack reduces as the distance between the crack and the spot where the probe beam is focused increases. Consequently, the nonlinear sidelobe amplitudes decrease.

It has been demonstrated that on a crack, and for probe power close to zero, the acoustic wave amplitude at f_H is importantly influenced, depending on either the crack is breathing or no. The generation of frequency-mixing component appears possible even for very low probe powers. In Sec. 2.4, with a probe power of only 1 mW, the amplitude of the acoustic wave at f_H is 25 dB over the noise, providing a ~18 dB amplitude for the first nonlinear sidelobe. Similarly, in the previous section (Sec. 3.5.2), the crack is localized with a probe power of 0.7 mW. The amplitude of the nonlinear sidelobes is a function of the probe power (Sec. 3.5.2) but their generation remains possible for very low probe powers.

On the contrary, in order to efficiently generate the $f_H \pm nf_L$ components when the probe beam is focused outside from the crack, the acoustic wave amplitude must be large enough. As the distance increases, the nonlinear process requires more probe power to be efficient. This is experimentally shown in Fig. 3.9 with the triangle shape of the highest amplitudes of the first right nonlinear sidelobe: as the probe power increases, the efficiency of this interaction increases, and the distance where the generation of nonlinear frequency components is possible also increases. This explains the decrease of the spatial resolution as a function of the probe power. Except for when the probe power is sufficient to close the crack ($P_H \geqslant 90$ mW in Fig. 3.9), the maximum of the nonlinear sidelobe remains on the crack because the acoustic wave amplitude is necessarily higher when generated on the crack. Then, the crack is always detected by a maximum.

The spatial resolution is affected by the probe power in Fig. 3.9 because the amplitude of the acoustic waves generated next to the crack increases with the probe power. At the opposite, the spatial resolution is not expected to be affected by the quality of the breathing for a 1D scan with the probe beam. Another experiment is realized in that sense. Similarly as the previous one (Sec. 3.5.2), the probe beam is shifted with a pump constantly focused on the crack. Instead of changing the probe power for each 1D scan, the pump power, so the breathing efficiency, is modified. The probe power is fixed at $P_H = 35$ mW in order to reduce the influence of the probe beam on the distance between the crack faces when the probe is focused on them. Results are presented in Fig. 3.10.

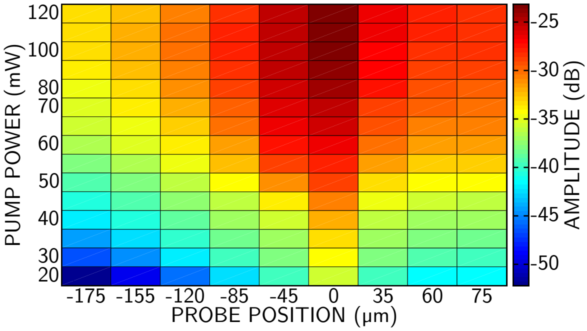

Figure 3.10: Evolution of the first right sidelobe at $f_H + f_L$ as a function of the probe position relatively to the crack position (horizontal direction) and for different pump powers (vertical direction). The pump beam is focused on the crack at 0 and the probe beam is of 35 mW.

Again, a triangle shape is observed: for low pump power the breathing is not efficient enough to generate nonlinear sidelobes efficiently. Only the case when the probe beam is focused on the crack generate detectable nonlinear sidelobes. As the pump increases, the breathing quality increases. This increases the amplitude of the nonlinear frequency-mixing sidelobes. It also increases the distance from the crack for which the interaction of the acoustic wave at f_H with the breathing crack in the nonlinear process is efficient. As predicted the amplitude of the nonlinear sidelobes increases monotonously as the pump power increases. The spatial resolution can be defined for all scans, even for a pump power of 120 mW. It decreases as a function of the pump power, which is not expected, but remains contained between ~75 and ~126 µm. However, the decrease of the spatial resolution by a factor 1.7 needs to be compared to the increase of the pump power by

a factor 10. This is the only case (compared to Secs. 3.5.1 and 3.5.2) where the spatial resolution can be defined for each experimental power.
For $P_L \leqslant 70$ mW, the spatial resolutions of this experiment (Fig. 3.10) and the previous one (Fig. 3.9) are close (Fig. 3.12(a)). For important pump powers ($P_L \geqslant 100$ mW), the spatial resolution is improving as the pump increases, which is yet unexplained.

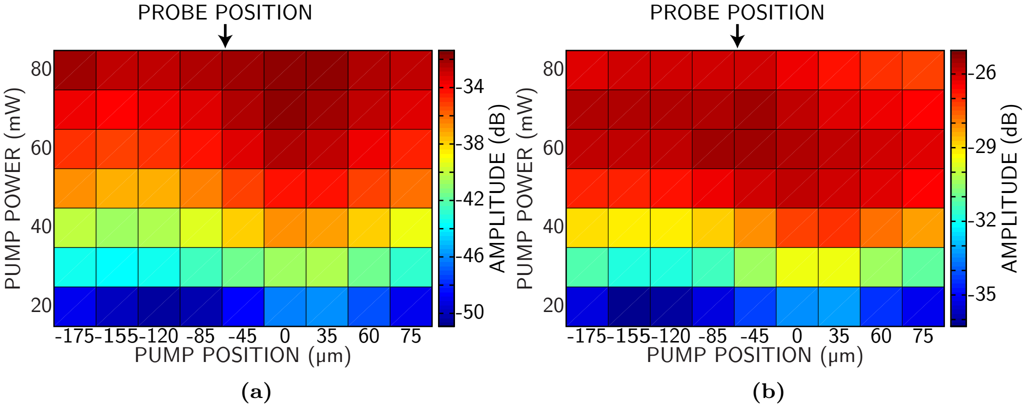

(a) (b)

Figure 3.11: Evolution of the first right sidelobe at $f_H + f_L$ as a function of the pump position relatively to the crack position (horizontal direction) and for different pump powers (vertical direction). The probe beam is focused at -60 µm from the crack. The probe power varies from $P_H = 20$ mW (a), to $P_H = 60$ mW (b).

Finally, another experiment is realized, similarly to the second one proposed in Sec. 3.5.1. In this case, the beams are inverted: the probe beam is focused 60 µm away from the crack ($\sim 3a$) and the pump beam is shifted along the x-axis. Different pump and probe powers are tested. Results are presented in Fig. 3.11.
For low pump powers the crack can be detected. This is due to the quality of the crack breathing: if the power is small, the breathing is more efficient on the crack and the interaction with the acoustic wave is more efficient, offering the possibility to detect the crack. The amplitudes of the nonlinear sidelobes are reduced compared to the configuration where the probe is focused on the crack.
As the pump power increases, the distance from which the crack starts breathing increases (Sec. 3.5.1). Thus for important pump power the crack is no more detected because the probe beam is focused outside the crack and the pump beam provides the crack breath far from the crack.
As previously, due to the reduced number of points, the spatial resolution determination is not possible for this experiment.

Higher Sidelobes

These sections only dealt with the first nonlinear sidelobe evolutions. This choice was made because of the monotonous evolution of the sidelobe amplitude as a function of the pump loading. Fig. 3.12(a) presents the different results on the spatial resolution of the previous experiments. The higher sidelobes, associated to $n = 2, 3, \ldots$ can also be considered.

For very low powers (around $P \leqslant 20$ mW), the higher order nonlinear sidelobes amplitude dynamics are usually too low to localize the crack with a $1/\sqrt{e}$ decrease. However, for larger powers, their spatial resolution is much better than the one of the first sidelobe. There are no clear explanation yet to this recurrent observation.

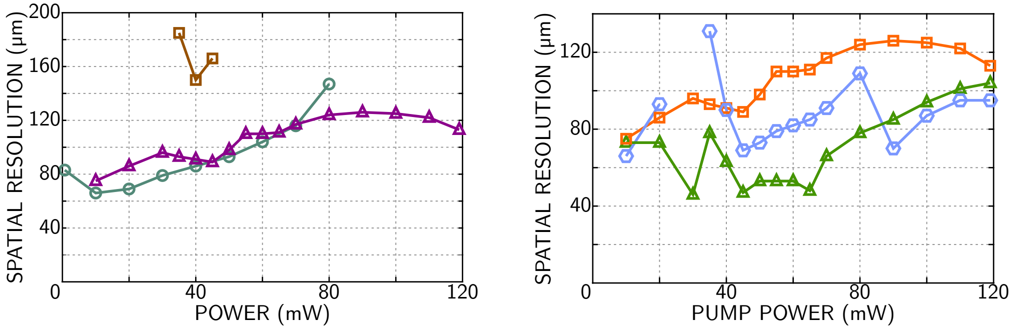

(a) **(b)**

Figure 3.12: (a): Evolution of the spatial resolution as a function of the pump power (□, △), and the probe power (○), relatively to the previous experiments illustrated earlier in Fig. 3.7(a) (□), Fig. 3.9 (○), and Fig. 3.10 (△). (b): Evolution of the spatial resolution as a function of the pump power in Fig. 3.10 for the first right sidelobe (□), the second right sidelobe (⬠), and the third right sidelobe (△). (a-b): Missing datas correspond to cases without definition of the spatial resolution.

In Fig. 3.12(b) the first, the second and the third sidelobe in the experiment where the probe is shifted and the pump power evolves is presented (Fig. 3.10 for the first right sidelobe evolution). They demonstrate that higher sidelobes have a better resolution on the crack localization. For $P_L \in [35; 60]$ mW, the third sidelobe has a better spatial resolution than the second one. The spatial resolution differences can be improved a lot: for $P_L = 55$ mW, it gives 111, 85 and 48 µm for the first, second and third sidelobe, respectively.

Some deviations from the general tendencies occur for particular powers. They can be attributed to the non-monotonous behavior of these sidelobes under the loading evolution (Sec. 1.3.2, Fig. 1.9): the analysis of the spatial resolution evolution is much more complex. As a conclusion, if, for a given scan, the amplitude of higher sidelobes is sufficient to define a spatial resolution, it usually provides a better crack localization.

3.5.4 Influence of the focusing on the spatial resolution

The influence of the localization and the power of each beam has been analyzed above. It remains to evaluate the influence of the beams focusing on the spatial resolution. The same set-up is used to control the focusing of one beam, by changing the distance between two lenses -as for a telescope. Unfortunately, it is not possible, with the installed set-up to defocus one beam and to move it by moving the lens. This implies too important optical aberrations. Thus, the set-up is used to influence one of the beams focusing but the sample is moved. This corresponds to the general 1D or 2D scan experiments with set-up Υ_1.

The sample is moved, which is equivalent to displace both beams at the same time. The previous discussed phenomena -probe or pump shift- evolve together and the analysis is more complex.

Experiment	Parameters				Results (µm)		
number	$2a$ (µm)		P (mW)		Sidelobe n		
	$2a_L$	$2a_H$	P_L	P_H	+1	+2	+3
1	44	38	78	57	92	71	37
2	124	38	57	57	96	74	132
3	124	38	75	57	95	73	61
4	38	124	64	57	211	135	/
5	38	124	75	57	350	150	/

Table 3.1: Evolution of the spatial resolution of the first three nonlinear sidelobes as a function of different set of parameters.

The goal of these experiments is mainly to check the tendency of the spatial resolution depending on the focusing and the pump power. The same 1D is achieved in the following experiments. In particular, the step between each point is constant to 40 µm.

The powers are chosen relatively large so that nonlinear mixed-frequencies can be generated when either the pump and/or the probe is focused outside the crack: the probe power is of 57 mW, the pump power is between 57 and 75 mW.

In a first time a 1D scan is realized with similar focusing: 22 and 19 µm for the pump and probe radii, respectively. The location on the crack is different from the previous experiments. The results are in Tab. 3.1. The improvement of the spatial resolution as the order of the sidelobes increases is observed. The resolution on the first sidelobe is approximately equal to twice the diameter of the beams. This confirms that the chosen power are large enough to generate nonlinear mixed-frequencies outside the crack.

In a second time the pump beam is defocused, up to $a_L = 62$ µm and the scan is done twice at two different powers: $P_L = 57$ and 75 mW. In each case the first and second right sidelobe is not influenced. The third one evolves. This can be attributed to the non monotonous behavior of the sidelobe amplitude as the pump loading changes. With the increase of the pump power, one can see the third sidelobe spatial resolution improves at 61 µm.

Finally, the beams are inverted in order to defocus the probe beam. The experiment is firstly realized for a pump beam of 64 mW. The spatial resolution is drastically diminished to 211 µm, almost twice the probe diameter. The spatial resolution of the second sidelobe is close to the probe diameter, and the one of the third sidelobe is not even possible to define.

In a second time, the scan is repeated for a larger pump power: 75 mW. The spatial resolution is clearly even worse: almost three times the probe diameter.

Conclusion

An important result of this chapter is the resolution of the heat equation. The influence of the pump parameters -focusing, intensity-modulation frequency, and power- are well understood. The parameters influencing the spatial resolution are also clearly identified. It is demonstrated that the pump beam can close the crack. The transition zone between the open and closed states corresponds to the optimal configuration for the nonlinear mixing-frequency generation. The quality of the breathing highly influences the generation of these mixed-frequencies. The breathing is controlled by the temperature difference, corresponding to the difference between the temperature extrema (maximum and minimum) on a spot as a function of time. Several parameters can influence the breathing amplitude:

- the pump intensity-modulation frequency f_L. The lower the frequency is the larger the temperature difference is. A lower frequency affects both extrema of temperature. The experimental choice of $f_L \sim 1$ Hz is demonstrated to be suitable.
- the pump beam power. The intensity of the beam is proportional to the beam power ($I \propto P$). Thus, the quality of the crack closure is influenced by the beam power. Low powers create only some contacts, whereas high powers close the crack efficiently.
- the pump beam focusing. The intensity of the beam on the sample is inversely proportional to the square of the radius ($I \propto 1/a^2$). Focusing the pump beam affects the breathing similarly to the beam power. It also affects the amplitude of the acoustic wave generated by the probe beam.
- the pump beam location. The thermal wavelength ($\lambda_{th} \simeq 2.6$ mm) significantly exceeds the beam radii and the penetration length of light in the sample. It is demonstrated that it is possible to make the crack breath for a pump beam focused far from the crack. However, the temperature difference and the maximum temperature decrease as the distance increases.
- the probe beam power. The modulation of heat due to the probe beam can be neglected, but not the constant heat delivered to the sample. For large enough powers, the distance between the crack faces can be reduced, or the crack can even be closed by the probe beam only.

It is observed that the acoustic wave generated far from the crack can also interact efficiently with the breathing crack to generate the nonlinear mixed-frequencies. This can influence the spatial resolution. However, the probe beam generates nonlinear mixed-frequencies with a larger amplitude when focused on the crack because the acoustic wave amplitude decreases with distance.

The spatial resolution is also affected by the probe beam focusing as it defines the area of the acoustic wave generation. The pump radius is not as important in the spatial resolution because of the larger thermal wave which does not reduce the crack breathing in the pump spot. However, its evolution can induce changes in the breathing of the crack.

As a conclusion, the spatial resolution of the method is very complex. It depends nonlinearly on several parameters. Although we cannot predict clearly what is the spatial resolution related with a set of parameters, their influence is demonstrated. In general, increasing the pump and/or probe power does not provide a better spatial resolution. However, it can provide a larger amplitude of the higher sidelobes which, once they exhibit a 4.3 dB decrease, have a much better spatial resolution than the first one.

It appears that for the set-up Υ_2, the probe and the pump beam should be inverted: the acoustic wave should be generated by the Verdi laser whereas the crack breathing should be provided by the diode laser. This should lead to a better spatial resolution.

CHAPTER 4

IMPROVEMENT OF THE EXPERIMENTAL SET-UP

Abstract

The experimental set-up has some drawbacks. Some are inherent to the technique itself such as the difficulty to detect buried cracks, and some can be improved.

A first improvement is the realization of another all-optical set-up. A first proposal has already been presented in the chapter 3 (Sec. 3.1). The detection was achieved with a vibrometer but the signal-to-noise ratio could be improved. In order to realize a sensitive all-optical set-up, an alternative detection technique, deflectometry, is presented in Sec. 4.1. The possibility to perform the excitation with a single beam, doubly modulated, is also demonstrated.

Another drawback is the required acquisition time of the method. This limitation is due to the choice of the low pump frequency, in order to achieve the crack breathing, combined with the spectrum analyzer. Indeed in order to reach a good signal-to-noise ratio with a good resolution, the recorded spectrum has been chosen to be about $f_H \pm 10 f_L$ with a resolution of $0.2 f_L$ and with ∼10 averages. For f_L of 1 Hz, it leads to a registration time of about 3 minutes for each experimental point. It can be improved with a decreased resolution and reduced number of averages, but it will still last at least several tens of seconds. Another detection technique, with a lock-in amplifier is proposed. It also allows an original detection method using the phase of the signal.

4.1 1D all-optical scan[1]

In this experiment two important changes are realized on the set-up: one on the excitation and another on the all-optical detection. The excitation is realized with a single beam focused on the sample with a beam spot radius of about 100 µm. In order to achieve the generation of an acoustic wave at f_H and the crack breathing at f_L, the beam is twice

---

[1] This part is closely similar to the second part (with Sec. 3.1) of a published article [39]. Some figures and comments, however, are added in the present section.

intensity modulated. It is intensity modulated, as previously, at the probe frequency f_H, and intensity modulated a second time, at low frequency f_L, with a square waveform (Fig. 4.2). Due to the modulation of a sinus modulated by square function, odd sidelobes are present in the light intensity envelope (Fig. 4.1(a)). Thus, the presence of cracks is revealed by the nonlinear generation of even sidelobes (Fig. 4.1(b)).

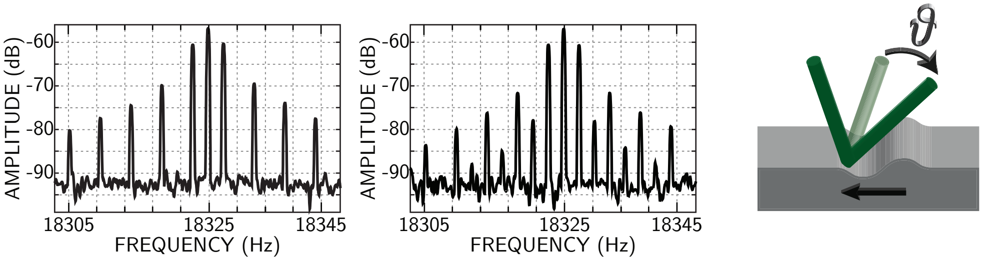

(a) (b) (c)

Figure 4.1: (a-b): Spectra recorded by the deflectometry technique with an excitation realized with a single beam and focused outside the crack (a) and on the crack (b). (c): Schematic illustration of the deflection.

The detection, is realized with the deflectometry technique. The use of two lasers for excitation and detection at different wavelengths ($\lambda = 800$ nm and $\lambda = 532$ nm for the excitation and detection, respectively) is motivated to avoid a possible illumination of the detector by the excitation beam. In the present case, a proper filter guarantees that any detected signal comes from the laser beam used for this purpose.
Deflection technique is based on the detection a beam, reflected by the sample surface at an angle ϑ. The incident beam is not normal to the sample surface: $\vartheta \neq 0$. If an acoustic wave propagates, the surface is locally modified, inducing surface inclination, and thus, a slight modification of the beam reflexion angle (Fig. 4.1(c)). The deflection depends on the amplitude and the frequency of the signal. After the reflection, a knife is installed to stop exactly one half of the optical power. The distance from the surface to the knife is

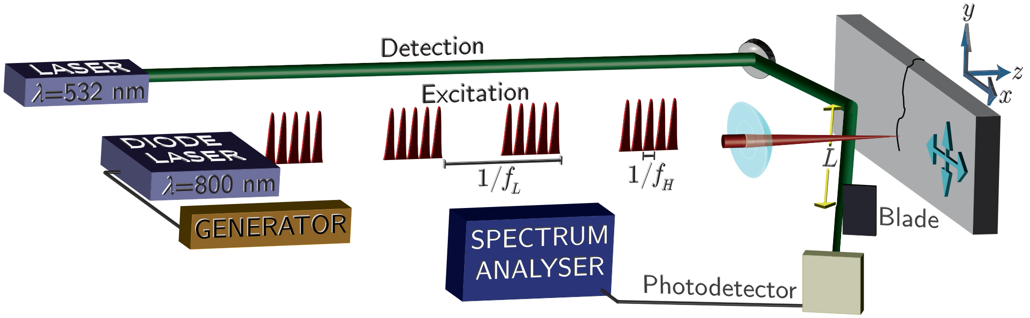

Figure 4.2: Schematic representation of the experimental set-up developed for an excitation with a single beam and a deflectometry detection.

L. The intensity remaining after the knife is acquired by a photodetector. If the reflexion angle ϑ is modified, the detected intensity increases or decreases. Consequently, it is possible to link the angle, and thus the frequency and amplitude of the wave, to the intensity on the photodetector.

The parameters important for optimization of the deflection technique [50, 61] are the laser spot radius a at the surface and the distance L. The relative variation of the power on the photo-diode, introduced after the knife, is described by $\Delta P/P = \Delta x/a_1$, where Δx is the lateral displacement of the beam at the surface of the knife caused by a change in the angle of the probe beam reflection induced by acoustic vibration of the sample, where $a_1 = a\sqrt{1 + (L/L_d)^2}$ is the radius of diffracted laser beam, and $L_d = \pi a^2/\lambda$ is the diffraction length. The maximum displacement of the probe beam $\Delta x = 2\vartheta L$ is determined by the maximum value of angle of the deflection of the surface $\vartheta = 2\pi u/\Lambda$, where Λ is the wavelength of the acoustic wave and u is the amplitude of the surface displacement [51]. It follows that $\Delta P/P$ is given by:

$$\frac{\Delta P}{P} = \frac{4a\pi^2}{\lambda\Lambda} \cdot \frac{L}{L_d} \cdot \frac{u}{\sqrt{1 + (L/L_d)^2}}. \tag{4.1}$$

Formula (4.1) predicts that the strategy for maximizing the sensitivity of the deflection method is to use a laser beam of maximum radius $a \approx \Lambda/4$ and observation distances exceeding the diffraction length. For the third flexural resonance of the glass plate $\Lambda/4$ is approximately 8 mm. Thus, the maximum sensitivity $\pi^2(u/\lambda)$ in the set-up depicted in Fig. 4.2 can be obtained by broadening of the initial 1 mm radius of the cw green laser nearly by an order of magnitude and using observation distances exceeding 600 m. This possible optimization has appeared unnecessary, because even 10 times lower sensitivity, experimentally achieved with a beam of 1 mm radius at 10 m observation distance, is sufficient for the monitoring of the nonlinear acoustic phenomena by deflectometry with a high signal-to-noise ratio. Nevertheless, it can be increased.

Due to the distance L involved in the experiment (10 m), the Verdi laser is used for the detection. The excitation beam, provided by the diode laser, has a worse focusing, while in order to avoid important diffraction after 10 m length, the laser beam quality used for the detection is required to be good enough.

In Fig. 4.3 the results of one-dimensional photoacoustic scan of a crack are presented. In this experiment, the diode laser is intensity modulated simultaneously at $f_L = 2$ Hz and $f_H = 18$ kHz. The nonlinear mixed frequencies, $f_H \pm 2f_L$, are detected by the probe beam deflection technique, which is tuned for the detection of the flexural waves propagating along the longest axis of the sample (Fig. 4.2). The position of the excitation beam relative to the crack is progressively modified in 50 µm steps. From the data presented in Fig. 4.3 it follows that only the detection of mixed frequencies provides sufficient contrast for reliable determination of the position of the crack.

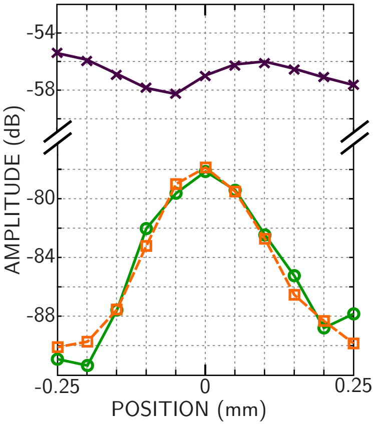

Figure 4.3: Dependence of the photoacoutic signal amplitude on the relative position between the common focus spot of the laser heating and sound-generating beams and the crack at frequencies f_H (×), $f_H + f_L$ (□), and $f_H - f_L$ (○). Detection is accomplished by an optical deflectometer.

4.2 Detection with a synchronous amplifier

In order to save time in the signal recording process, an interesting solution is the use of a lock-in amplifier, Signal Recovery SR7280, instead of a spectrum analyzer. The lock-in amplifier can record only one specific frequency but much faster than the spectrum analyzer. The main difficulty is the synchronization with the referencing frequency. The nonlinear mixed-frequencies are not present in the excitation signal. Consequently, only the frequencies f_H and f_L can be directly processed with the lock-in amplifier. Unfortunately, the latter do not present interest in the crack detection.

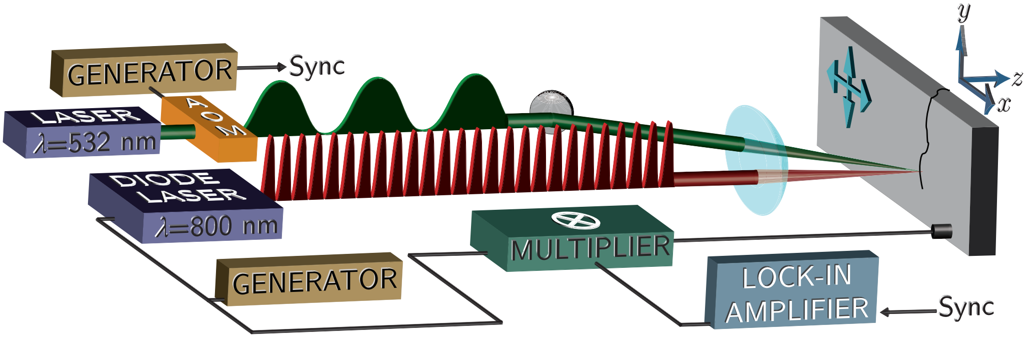

Figure 4.4: Experimental set-up to detect the signal with a synchronous amplifier.

In order to get rid of that problem, a specific set-up is proposed. The experimental set-up is the set-up Υ_2, with two laser beams to perform excitation. This has no consequence for the following. The detection is achieved by an accelerometer to simplify the set-up.

The detected signal is multiplied by the initial probe signal. It follows:

$$S = A_1 \cos[(\omega_H \pm n\omega_L)t] \cdot A_2 \cos[\omega_H t], \tag{4.2}$$

where $A_{1,2}$ are the amplitudes of each signal. Using the trigonometric formulas, one can rewrite Eq. (4.2):

$$S = \frac{A_1 A_2}{2} \left(\cos[n\omega_L t] + \cos[(2\omega_H \pm n\omega_L)t]\right). \tag{4.3}$$

Eq. (4.3) is particularly interesting as the first nonlinear sidelobes, associated to $n = 1$, can directly be synchronized from the generator of the pump wave at f_L. The amplitude of the signal is modified, but the interest is not on the amplitude value but on its evolution. A low-pass filter (Krohn-Hite Model 3945) is introduced after the multiplier. Then, the resulting signal is analyzed by the lock-in amplifier (Fig. 4.4). Finally, it appears that the synchronous amplifier is synchronized with the first nonlinear sidelobe.
However, this technique does not differentiate between $f_H + f_L$ and $f_H - f_L$. As they are theoretically assumed identical (Sec. 1.3.2), and generally observed in the experiments (Fig. 2.7 for example), there is no information loss. The synchronous amplifier can lock-in the harmonics of the synchronized signal. From Eq. (4.3) it follows that the harmonics of ω_L correspond to the nonlinear sidelobe harmonics ($n = 2, 3, \ldots$). Consequently, the higher sidelobes can also be studied. However, it must be underlined that as the lock-in amplifier records only one frequency, each sidelobe evolution requires a new measurement.

A first limitation of this new technique concerns the low-frequency limitation of the lock-in amplifier. The used lock-in amplifier has a bandwidth from 0.5 Hz up to 2 MHz. Thus, the pump frequency has a lower limit. The frequency f_L must be in the multiplier bandwidth.

In order to get a confident signal, the integration time must contain about ten periods of the required signal. For $f_L = 1$ Hz, it leads to about ten seconds per point. One can see that this set-up is much faster, even if a 2D scan still lasts several minutes, especially if we are interested in the evolution of several sidelobes.

Another possibility is to multiply the signal by the initial pump signal from the generator. This has advantages and drawbacks. In this last case, the resulting signal is:

$$\breve{S} = \frac{A_1 A_2}{2} \left(\cos[\omega_H t \pm (n-1)\omega_L t] + \cos[\omega_H t \pm (n+1)\omega_L t]\right). \tag{4.4}$$

Thus, the first harmonic can be synchronized with the probe generator lock-in but for higher harmonics, associated to $n \geqslant 2$, there are no possibilities to synchronize them as the resulting frequencies of higher sidelobes are not harmonics from the first one. This is the main drawback: this set-up can only detect the first nonlinear sidelobe.
However, the set-up associated to Eq. (4.4) offers two advantages. Firstly, with this configuration, there is no low limitation on the frequency f_L. Then, the time acquisition of about ten periods now lasts some millisecond only. Surely, one should wait, at least, one closing of the crack to guarantee the nonlinear sidelobes generation, so for $f_L = 1$ Hz,

the signal can be acquired after about one second. However, the signal would not be optimum because the temperature rise lasts some seconds to be in the steady state and one should be careful about the acquisition time.

In the next experiments, a particular attention is turned to the evolution of different sidelobes. Indeed, their evolution as a function of the pump power contain important information (Part. II). The low frequency limitation and time acquisition are not problematic. Then, the first set-up (Fig. 4.4), corresponding to Eq. (4.3) is chosen.

Another advantage of the use of a lock-in amplifier is that it can simultaneously record the amplitude and the phase of the signal. The spectrum analyzer should allow such possibility but it has not been successfully managed in the experiments.

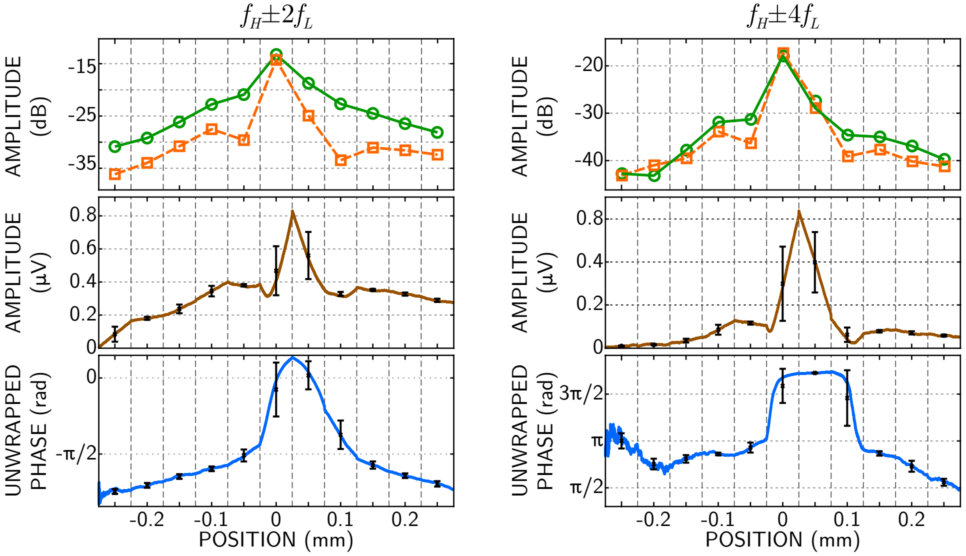

(a) **(b)**

Figure 4.5: Dependence of the amplitude and the unwrapped phase of the nonlinear sidelobes on the relative position between the spots of the pump and probe beam and the crack. (top): Detection with the spectrum analyzer of $f_H - nf_L$ (○) and $f_H + nf_L$ (□). (middle-bottom): Detection with the lock-in amplifier. The dashed vertical lines distinguish the position of the beams relatively to the crack. The errorbars are estimated within a same position and are plotted on the mean value in the interval.

The signals acquired from the lock-in amplifier and from the spectrum analyzer differ. For an experimental point, the spectrum, obtained from the spectrum analyzer, is the result of the signal averaged a number of times (usually ten). Consequently, it has only one amplitude for each frequency.

On the contrary, the values of the magnitude and of the phase on the lock-in amplifier evolve in time and several successive values are registered. The acquisition of the signal is realized as follows: once the set-up is on the location we want to record the signal, a first pause, lasting the duration of the integration time, is done. The integration time is chosen to last several breathing periods (generally ten). Then, during several seconds, numerous points are recorded.

In Fig. 4.5 the evolution of the second and the fourth sidelobe as a function of the position is presented. The sample is moved to realize a 1D scan. The amplitude (middle) and the phase (bottom) evolutions detected by the lock-in amplifier are demonstrated. The amplitude of the signal, detected by the spectrum analyzer (top) is presented for comparison. The agreement between both amplitudes confirms the potential of this new set-up. The apparent differences between the amplitudes is due to the presentation of the results.

For one point, e.g., $x = 0$ mm, the spectrum analyzer gives only one value, due to the averaging. On the contrary, the lock-in amplifier signal consists of several points. The vertical dashed lines correspond to the position of the beams relatively to the crack position along the x-axis. In-between, the successive points recorded by the lock-in amplifier are plotted. When the beams are focused on the crack ($x = 0$ mm), the amplitudes of the nonlinear sidelobes, detected by the spectrum analyzer is maximum. The amplitude recorded by the lock-in amplifier increases with the time. Similarly, when the beams are shifted away, at $x = 0.5$ mm, it is decreasing with time. In both cases, the amplitude does not reach a stable value. For longer times on the same spot, it stabilizes. This observation first explains the apparent shift: for $x = 0$ mm, the maximum of the lock-in amplifier is when the time spent on this spot is maximum, corresponding to the right limit of the interval, whereas the value from the spectrum analyzer is plotted in the center of the interval. It follows that the crack is detected at $x = 0$ mm in both cases.

Secondly, this observation also indicates a dynamic motion of the crack, not noticeable with the spectrum analyzer detection. Indeed, when nonlinear frequency-mixing are generated, i.e., on the crack, the signal amplitude increases for a while. Recording several successive points demonstrates whether the amplitude is stabilized or not. Similarly, when the beams are shifted away, the signal amplitude decreases during a moment too. In this experiment, the time spent at each position if of several tens of seconds. It indicates that it is a slow dynamic motion. It would be possible to automatize the set-up, with the software, in order to wait the necessary time for the stabilization of the signal. This option is not developed here. However, considering the last value registered on each point, it can be speculated, that it could improve the spatial resolution because the amplitude difference between two successive points would increase.

The phase evolution offers a new way of detecting the crack. One can clearly localize the crack with the phase information (Fig. 4.5 (bottom)). However, the maximum of the nonlinear sidelobe amplitudes is not necessarily detected, but only the zone where the sidelobes are generated. Indeed, the phase is supposed stable if the nonlinear frequency-mixing are generated and not proportional to the amplitude. For the second sidelobe (Fig. 4.5(b)) the phase does not reach its stable value, unlike the fourth sidelobe phase evolution (Fig. 4.5(b)). The time spent in each cases is equal.

In both cases, the phase information allows the detection of the crack even if the spatial resolution is a bit less accurate once the phase has reached its stable value, as no maximum is detected. As for the amplitude, a larger wait on each point should improve the spatial

resolution.
It can be observed from Fig. 4.5(b) (middle and bottom) that when no nonlinear sidelobes are generated (zero amplitude), the phase fluctuates importantly.

Waiting for the stabilization of the signal could provide a better spatial resolution on the amplitude and the phase detection. It may also offer the possibility to determine characteristic time of the crack motion.
However, the first goal of this set-up was to be faster. If it appears possible to do so, the sensitivity to the crack reduces as the time spent on a location diminishes, because of the time required to reach high amplitudes.

Conclusion

Two important improvements of the technique are proposed: a faster set-up combined with the phase detection and an all-optical set-up. The latter demonstrates the efficiency of an all-optical method for detecting cracks. Another important point is the use of a single beam to achieve the excitation. This technique prevents the possibility to control independently the pump and probe beam, especially their power. However, it allows a much easier set-up. A single beam with an accelerometer for detection would provide a very simple set-up.

The former set-up uses the lock-in amplifier for detection. It allows to evaluate both amplitude and phase evolution. The information on the phase, so as the one on the amplitude, is reliable to detect cracks. This set-up can also be much faster than the original one.
The use of a lock-in amplifier highlights a slow dynamic crack motion as the phase and amplitude variations, for a constant position, evolve as a function of time for several tens of second.

Finally, although these experiments have been conducted separately, they could be combined in a single set-up, faster and all-optical.

PART II

INFLUENCE OF THE PUMP POWER

CHAPTER 5

EVALUATION OF CRACK PARAMETERS

Abstract

The influence of the pump power on the linear and nonlinear sidelobes is studied. It has already been theoretically predicted that the amplitude of the nonlinear sidelobes as a function of the input loading is highly non-monotonous. For particular loadings and sidelobes, the amplitude evolution can contain minima. Theoretically, the amplitude is null for this specific loading and sidelobe [20], [54]. However, there is no, to the authors' knowledge, evidence of any experiment demonstrating such behaviors. This chapter demonstrates these non monotonous evolutions with minima, as predicted by the theory [20]. A more advanced model is proposed to avoid the assumption $\omega_L \ll \omega_{o,c}$. The fitting of this new model with the experimental results offers the possibility to reach different crack parameters.

5.1 Experimental evolution of the pump amplitude

The nonlinear sidelobe amplitude evolutions, as a function of the pump power, are theoretically expected to be highly non monotonous (see Eq. (1.20b) and Fig. 5.1(a)). They are function of the forces F_c and F_o, required to close and open the crack, respectively. Consequently, it can be expected that fitting experimental results to theoretical ones will then provide quantitative informations on F_c and F_o.

An experiment with varying the pump power, and based on the set-up Υ_1, is realized. The evolution of the pump power cannot be controlled by the laser power output because it would also change the probe power. Consequently, the input voltage of the acousto-optic modulator is changed to control the pump beam power. The power of the beam is proportional to the input voltage of the AOM. In this experiment, the pump beam is intensity modulated at 0.5 Hz and focused on the sample with a radius of 95 µm. The pump beam power on the sample evolves between 2 and 304 mW. The power step is between 1.9 and 13 mW. The probe beam has a radius of 106 µm, the frequency f_H is of 80.6 kHz, and the power is of 121 mW.

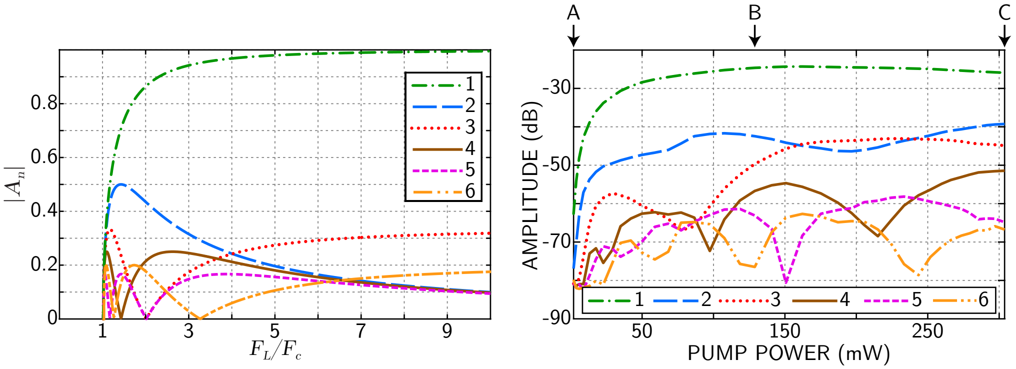

(a) **(b)**

Figure 5.1: Theoretical (a) and experimental (b) dependences of the amplitude of the first six left sidelobes on the varying amplitude of the normalized force F_L/F_c loading the crack (a) and the pump power (b).

Results are presented in Fig. 5.1(b). The main peak amplitude is not presented. It increases monotonously by ~5 dB, as a function of the pump power, and saturates for $P_L \geqslant 200$ mW. The first six nonlinear left sidelobes are shown. The theoretical evolutions, from Eq. (1.20b) are introduced in Fig. 5.1(a) for comparison.

In a first approach, a general good agreement between the experimental and theoretical curves is observed. They exhibit similar evolutions containing saturations, local minima and local maxima. For example, the first nonlinear sidelobe saturates in both cases. The third nonlinear sidelobe has a local minima for $P_L = 77.3$ mW experimentally. Theoretically, its amplitude is null for $F_L/F_c = 2$.

Three spectra are proposed in Fig. 5.2 for the minimum pump power $P_L = 2$ mW (Fig. 5.2(a)), for a particular pump power ($P_L = 128.9$ mW) corresponding to the minima of the sixth sidelobe (Fig. 5.2(b)) and for the maximum pump power, $P_L = 303.8$ mW (Fig. 5.2(c)).

Some discrepancies also appear. The experimental first sidelobe slightly diminishes for high powers ($P_L \geqslant 250$ mW). This decrease, for important powers, is not predicted by the theory. From Eq. (1.20a), it also follows that the even sidelobes are supposed to tend to zero. This is not observed either.

Other discrepancies on higher sidelobes can also be noted: the second sidelobe does not go through a local maximum to vanish afterwards, as for the theoretical prediction. The fourth experimental sidelobe has more minima than predicted -three experimentally compared to one theoretically- and does not tend to zero either.

Results of the evolution for the right sidelobes are, as expected, rather similar. For example, each sidelobe present the same behaviors and the same amount of minima. However, some differences are observed.

The first right sidelobe has a larger diminution for high powers compared to the left one: 6.6 dB (compared to 1.6 dB previously).

Some of the minima are shifted to lower or larger pump power. For example, the sixth right sidelobe has three minima. The first one is shifted from $P_L = 58.9$ mW to

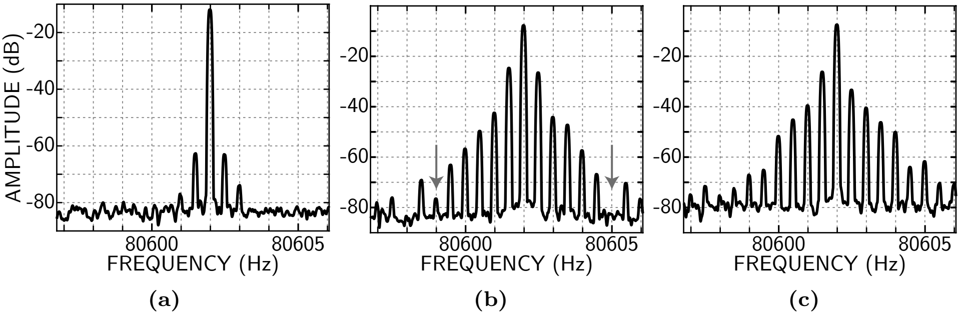

(a) (b) (c)

Figure 5.2: Spectra of the photoacoustic signal for points A, B, and C in Fig. 5.1(b) corresponding to the first observed spectrum at $P_L = 2$ mW (a), the amplitude minimum of the sixth left and right sidelobe at $P_L = 128.9$ mW (b), and the maximum pump power at $P_L = 303.8$ mW (c), respectively.

$P_L = 68.8$ mW whereas its third minimum from $P_L = 243.5$ mW to $P_L = 233.4$ mW. The differences of the minima positions can appear relatively important (up to ∼10 mW) but in fact concern only two successive experimental points. Thus, it can be concluded that the symmetry is approximately conserved. A larger number of points would provide a higher agreement in the symmetry and a higher precision in the position of the minima. Several minima are better or worse defined comparing the left or the right sidelobe.

In order to fit the theoretical and the experimental results, it has been chosen to focus on the minima of the first nonlinear sidelobes because they are well defined theoretically and experimentally. It is also easier to fit some point position than to compare curve tendencies especially because of their high non monotonous behaviors. Tab. 5.1 references the different experimental (Tab. 5.1(a)) and theoretical (Tab. 5.1(b)) locations of the minima. The experimental data are functions of the pump power, whereas the theoretical ones are functions of the ratio F_L/F_c. The theory predicts a symmetry between left and right sidelobe so there is only one column in Tab. 5.1(b).

The comparison of these tables clearly exhibits differences in the number of minima. Nevertheless, it also demonstrates a reasonable agreement even if some minima are not predicted.

In a first approach, a fit between the theoretical and experimental results, assuming the absence of hysteresis, has been realized. As the number of minima is different, all the configurations are tested. For each one, the ratio of the position of the experimental and the theoretical minimum is calculated. This induces an estimation of the link between F_c, the required force to close the crack, and the power loading the crack. Without hysteresis, it also provides an estimation of the force F_o required to open the crack as $F_o = F_c$. The final standard deviation is calculated for each combination and the case with the lowest one is taken.

Then, for the power required to close the crack, for $P_L(F_L = F_c)$, the temperature elevation is calculated thanks to Eq. (3.15). Using the temperature rise profile, it is possible to estimate the induced dilatation ΔL of a heated 1D sample next to a free

SIDELOBE	POWER (mW)	
n	$f_H - nf_L$	$f_H + nf_L$
1	-	-
2	-	-
3	77.3	77.3
4	22.8 97.4 215.1	22.8 86.6 205.5
5	34.9 150.7	42.1 140.7
6	58.9 128.9 243.5	68.8 128.9 233.4

(a)

SIDELOBE	FORCE RATIO
n	F_L/F_c
1	-
2	-
3	2
4	1.41
5	1.23 3.23
6	1.15 2

(b)

Table 5.1: Table presenting the different minima of the amplitude as a function of the loading and the considered sidelobe for the experiment (a) and the theory from [20] (b).

surface with Eq. (3.20) and multiplied the result by 2 to consider both crack faces. Finally, the open rigidity, which is the ratio of F_c and $h_o - h_i$ (Eq. (1.17)), is evaluated and so for the crack mechanical relaxation frequency in the open state ($\omega_o = 2\eta_o/\rho c$). The fact that the estimation of the dilatation is achieved assuming a free surface, even though a crack rigidity is then estimated, is not contradictory. It is known that the rigidities of the crack, in opened and closed states, are several order lower than rigidity of the sample [69].

However, this approach estimates the crack mechanical relaxation frequency to $\omega_o = 12$ s^{-1}. In this experiment (Fig. 5.1(b)), $\omega_L = 3.14$ s^{-1}. Thus, the condition $\omega_L \ll \omega_{o,c}$ is clearly in disagreement with initial theoretical assumptions. This means that an upgraded model must be developed without this assumption.
This improved model may also predict more minima and/or a different behavior on the nonlinear sidelobe evolutions.

5.2 Theoretical development of the nonlinear sidelobes evolutions

The aim of this section is to improve the theoretical model from [20] in order to avoid any assumption between the crack mechanical relaxation frequencies, ω_o and ω_c and the intensity modulation frequency of the pump beam, f_L.

5.2.1 Evolution of the time spent in the closed region as a function of the crack parameters

It is important to note that only the assumption concerning the crack mechanical relaxation frequencies and the pump frequency, mathematically $\omega_L << \omega_{o,c}$, is modified. The calculation remains developed in one dimension for an infinite sample. The crack is modeled by two parallel faces with an infinite depth and a penetration length of the light infinite too. The crack rigidity model is bistable with the same evolution as previously (Eq. (1.17), Fig.1.7), and the probe beam has a weak influence on the crack motion. Thus, Eq. (1.14) remains valid:

$$\frac{\partial u_L(0)}{\partial t} - \frac{1}{\rho c} F[2u_L(0)] = -|A(\omega_L)| I_L \, \text{ш}_L \cos[\omega_L t - \varphi(\omega_L)]. \tag{5.1}$$

If the evolution of the nonlinear sidelobes is different, its generic definition remains (Eq. (1.20a)):

$$|A_n| = \left| \frac{1}{n} \sin \left[n \frac{1}{2} \omega_L T_c \right] \right|. \tag{5.2}$$

The validity of this equation without the assumption $\omega_L << \omega_{o,c}$ is demonstrated in Chap. 7.

The evolution of the time spent by the crack in the closed region over a pump period, as a function of the loading force, directly provides the evolution of the nonlinear sidelobes. As the model is not assumed quasistatic anymore, the first term in Eq. (5.1) cannot be neglected as in [20]. Introducing the crack mechanical relaxation frequencies and the definition of the forces $F_{c,o}$ (Eq. (1.17)), Eq. (5.1) can be rewritten as:

$$\frac{\partial (2u_L(0) - h_{o,c})}{\partial t} + \omega_{o,c}(2u_L(0) - h_{o,c}) = -2|A(\omega_L)| I_L \, \text{ш}_L \cos[\omega_L t - \varphi(\omega_L)]. \tag{5.3}$$

The resolution of the problem is closely similar to [19]. Solving the differential equation (5.3) leads to:

$$2u_L(0) = h_{o,c} + C_{o,c} e^{-\omega_{o,c} t} - \frac{2|A(\omega_L)| I_L \, \text{ш}_L}{\sqrt{{\omega_L}^2 + {\omega_{o,c}}^2}} \cos[\omega_L t - \varphi(\omega_L) - \phi_{o,c}], \tag{5.4}$$

with $\phi_{o,c} = \arctan(\omega_L / \omega_{o,c})$ and $C_{o,c}$ the integration constants.

In the case where the loading is not important enough to insure clapping, i.e., if during a complete acoustic period $2u_L(0) = h_i$ is not realized, the integration constants are equal to zero, due to the periodicity condition. Mathematically, it can be expressed:

$$2u_L(0) = h_{o,c} - \frac{2|A(\omega_L)| I_L \, \text{ш}_L}{\sqrt{{\omega_L}^2 + {\omega_{o,c}}^2}} \cos[\omega_L t - \varphi(\omega_L) - \phi_{o,c}]. \tag{5.5}$$

The clapping starts when the condition $2u_L(0) = h_i$ is fulfilled. If so, the loading intensity $I_L = I_{c,o}$ and the cos term is maximum. It follows:

$$2|A(\omega_L)|I_{c,o}\,\text{ш}_L = \varkappa_{o,c}\cdot(h_{o,c}-h_i)\sqrt{{\omega_L}^2+{\omega_{o,c}}^2}, \tag{5.6}$$

with $\varkappa_{o,c} = \mathrm{sgn}(h_{o,c}-h_i)$. Necessarily, $\varkappa_o = 1$ but $\varkappa_c = \pm 1$, depending on the sign of F_o which can be positive or negative.

For larger loading amplitudes, corresponding to the clapping regime, the exponential term from Eq. (5.4) must be considered. The crack is supposed to change from the closed to the opened region at time $t = t_1$. Then, the last transition between the opened to the closed region occurred at $t = t_1 - T_c$ and the next transition will be at time $t = t_1 + T_o$, where T_o (T_c) is the time spent in the opened (closed) region (Fig. 5.3). Besides, $T_o + T_c = 2\pi/\omega_L$. Consequently, the new equations can be read in the following system:

$$\begin{cases} h_i = h_c + C_c e^{-\omega_c(t_1-T_c)} - \varkappa_c(h_c-h_i)I_L/I_o\cos[\theta_1-\omega_L T_c], \\ h_i = h_c + C_c e^{-\omega_c t_1} - \varkappa_c(h_c-h_i)I_L/I_o\cos[\theta_1], \\ h_i = h_o + C_o e^{-\omega_o t_1} - \varkappa_o(h_o-h_i)I_L/I_c\cos[\theta_1+\Theta_\phi], \\ h_i = h_o + C_o e^{-\omega_o(t_1+T_o)} - \varkappa_o(h_o-h_i)I_L/I_c\cos[\theta_1+\Theta_\phi+\omega_L T_o]. \end{cases} \tag{5.7}$$

with $\theta_1 = \omega_L t_1 - \varphi(\omega_L) - \phi_c$ and $\Theta_\phi = \phi_c - \phi_o$.

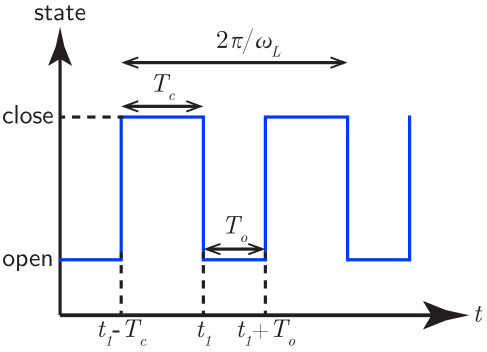

Figure 5.3: Schematic representation of the evolution of the crack state as a function of time.

Thanks to the system of Eq. (5.7), it is possible to exclude the integration constants and to rewrite the remaining equations into a matrix form:

$$\begin{bmatrix} \varkappa_c(1-\cos[\omega_L T_c]e^{-\omega_c T_c}) & -\varkappa_c\sin[\omega_L T_c]e^{-\omega_c T_c} \\ \cos[\omega_L T_o+\Theta_\phi]-\cos[\Theta_\phi]e^{-\omega_o T_o} & \sin[\Theta_\phi]e^{-\omega_o T_o}-\sin[\omega_L T_o+\Theta_\phi] \end{bmatrix}\cdot\begin{bmatrix}\cos[\theta_1]\\ \sin[\theta_1]\end{bmatrix} = \begin{pmatrix} \frac{I_o}{I_L}(1-e^{-\omega_c T_c}) \\ \frac{I_c}{I_L}(1-e^{-\omega_o T_o}) \end{pmatrix}. \tag{5.8}$$

To gain some space, $\varkappa_o$, necessarily equal to 1, is deleted. Then the system can be solved for the unknowns $\cos[\theta_1]$ and $\sin[\theta_1]$. The trigonometric identity

$\cos[\theta_1]^2 + \sin[\theta_1]^2 = 1$ leads to a relation linking the time spent by the crack in the closed region, T_c, and the loading intensity I_L. For that, I_o needs to be written as a function of I_c (or the opposite). It can be demonstrated that:

$$I_o = \frac{\varkappa_c}{\varkappa_o}\frac{\omega_o}{\omega_c}\sqrt{\frac{{\omega_L}^2+{\omega_c}^2}{{\omega_L}^2+{\omega_o}^2}}\frac{F_o}{F_c}I_c. \tag{5.9}$$

It follows:

$$\left[\frac{I_L}{I_c}\right]^2 = \frac{N}{D^2}, \text{ with:}$$

$$\begin{aligned}N = {} & \frac{{\omega_o}^2\left({\omega_L}^2+{\omega_c}^2\right)^2}{{\omega_c}^2}\cdot\left(\frac{F_o}{F_c}\right)^2\cdot\left(1-e^{-\omega_c T_c}\right)^2\cdot\Big[1-2\cos[\omega_L T_o]e^{-\omega_o T_o}+e^{-2\omega_o T_o}\Big]+ \\ & +\left({\omega_L}^2+{\omega_c}^2\right)\cdot\left({\omega_L}^2+{\omega_o}^2\right)\cdot\left(1-e^{-\omega_o T_o}\right)^2\cdot\Big[1-2\cos[\omega_L T_c]e^{-\omega_c T_c}+e^{-2\omega_c T_c}\Big]+ \\ & +\frac{2\omega_o\left({\omega_L}^2+{\omega_c}^2\right)}{\omega_c}\cdot\frac{F_o}{F_c}\cdot\left(1-e^{-\omega_c T_c}\right)\cdot\left(1-e^{-\omega_o T_o}\right)\cdot\Bigg(\omega_L\left(\omega_c-\omega_o\right)\cdot\sin[\omega_L T_c]\times \\ & \times\left(1-e^{-\omega_o T_o-\omega_c T_c}\right)+\left(\omega_c\,\omega_o+{\omega_L}^2\right)\cdot\Big[e^{-\omega_o T_o}+e^{-\omega_c T_c}-\cos[\omega_L T_c]\cdot\left(1+e^{-\omega_o T_o-\omega_c T_c}\right)\Big]\Bigg),\end{aligned}$$

$$\begin{aligned}D = {} & \left(\omega_c\,\omega_o+{\omega_L}^2\right)\cdot\sin[\omega_L T_c]\cdot\left(1-e^{-\omega_o T_o-\omega_c T_c}\right)+ \\ & +\omega_L(\omega_o-\omega_c)\left[e^{-\omega_o T_o}+e^{-\omega_c T_c}-\cos[\omega_L T_c]\cdot\left(1+e^{-\omega_o T_o-\omega_c T_c}\right)\right].\end{aligned} \tag{5.10}$$

Eq. (5.10) links the excitation (I_L, ω_L) as a function of the crack parameters (ω_o, ω_c, F_c, F_o, I_c) and the time spent in the opened and closed region (T_o, T_c), where T_o and T_c are connected by the equation $T_o + T_c = 2\pi/\omega_L$.
In order to solve Eq. (5.2), the expression should be reversed to get T_c as a function of the loading intensity and the crack parameters. This does not appear to be analytically possible. Nevertheless, for a given set of parameters for the loading and the crack, it is possible to estimate I_L/I_c as a function of T_c. Then, with the numerical calculation, it is easy to inverse the curve. It results the prediction of the evolution of T_c as a function the loading intensity I_L.

Several curves, with different open rigidities, are plotted in Fig. 5.4(a). Due to the modulated excitation, a peak always appears. It means it is not possible to maintain the crack closed during a full period. This conclusion is coherent with the assumption of the negligible influence of the probe beam on the crack motion and with the 100% intensity modulation assumption of the pump beam. Depending on the crack characteristics and the frequency f_L, this peak can be shifted to shorter or longer times. For example, for the set of parameters in Fig. 5.4(b), it is impossible to maintain the crack closed half of the time period.
Reversion of the curve to get I_L/I_c as a function of T_c is made for the first part of the curve.

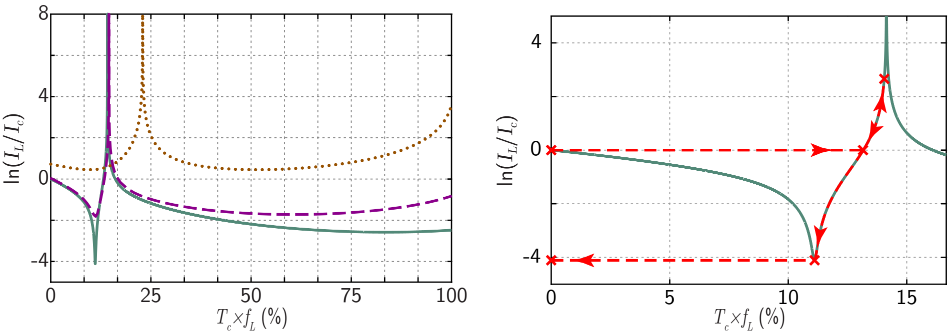

(a) **(b)**

Figure 5.4: (a): Evolution of the logarithm of the normalized acoustic intensity as a function of the time spent by the interface in the closed region over a pump period (in %) for $F_o/F_c = -8$, $\omega_L = 1$ Hz, $\omega_c/\omega_o = 100$ and $\omega_o = 2$ mHz (—), ω_o =0,02 Hz (- -), and ω_o =0,2 Hz (•••). (b): Zoomed of the case in (a) with $\omega_o = 2$ mHz for $T_c \leqslant \pi/3$.

In the general case, $F_c \neq F_o$: hysteresis is present (Fig. 5.4). This leads to a different path when the pump increases or decreases. In Fig. 5.4(b), when the pump amplitude increases there is an abrupt passage from 'A' to 'B'. The time spent by the interface in the closed region suddenly passes from zero to more than 12% of the duration of a period. Then, loading amplitude increase produces an increase of the time spent by the crack in the closed region. The evolution follows the curve until reaching 'C', which is the maximum pump amplitude. While the amplitude loading decreases, the time spent by the crack in the closed region diminishes too. It goes back through 'B' and continues to diminish until 'D'. Afterwards, for lower amplitude the clapping stops, at a lower acoustic amplitude than the one which is needed to initiate the breathing.
The time spent by the crack in the closed region as a function of the loading is needed to evaluate the nonlinear sidelobe evolutions (Eq. (5.2)). Then, the curve A→B→C or C→D→E must be inverted if the loading pump amplitude increases or decreases, respectively. The evolution of the nonlinear sidelobes as a function of the loading pump, for any set of the parameters, is obtained with Eq. (5.2).

With this theoretical work, one can compare experimental results to theoretical ones. The optimization is possible by changing the parameters F_o/F_c and $\omega_{o,c}$ as ω_L is fixed by the experiment. The best fit gives these parameters of the crack. With the crack mechanical relaxation frequencies, the crack rigidities in opened and closed states are estimated. Then, $I_{c,o}$ and $\eta_{o,c}$ are deduced. It appears possible to evaluate the distances $(h_{o,c} - h_i)$, where $(h_o - h_i)$ is the crack width diminution necessary to close the crack -initially opened- and $(h_c - h_i)$ is the crack width diminution in the closed state of the crack. This is directly related to the thickness of the crack. For that, one can use Eq. (5.6) where the amplitude term is defined as in Eq. (1.13). The distances can be expressed, in their complete form, as:

$$h_{o,c} - h_i = \frac{\varkappa_{o,c} I_{c,o}\, \text{ш}_L}{\sqrt{{\omega_L}^2 + {\omega_{o,c}}^2}} \times$$
$$\times \left| \frac{K\beta}{\ell \kappa \rho c^2} \frac{\jmath\omega_L}{\left(\frac{\omega_L}{c}\right)^2 + \frac{\omega_T - \jmath\omega_L}{\chi}} \left[\frac{\jmath\omega_L/c}{\sqrt{\frac{\omega_T - \jmath\omega_L}{\chi}}} \widehat{\Psi}\left(\sqrt{\frac{\omega_T - \jmath\omega_L}{\chi}}\right) + \widehat{\Psi}\left(-\jmath\frac{\omega_L}{c}\right)\right]\right| . \tag{5.11}$$

A factor 1/2 is introduced because we used $f(t) = [1 + \text{ш}\cos(\omega t)]/2$, contrary to [20] where $f(t) = 1 + \text{ш}\cos(\omega t)$.
I_c and I_o are supposed evaluated and the other sample and experimental parameters are known. Then, if ω_T is estimated, it follows, from Eq. (5.11), an estimation of $(h_{o,c} - h_i)$. The crack mechanical relaxation frequencies $\omega_{o,c}$ and the distances $(h_{o,c} - h_i)$ lead to an estimation of F_c and F_o (Eq. (1.17)):

$$F_{c,o} = \frac{\rho c}{2} \cdot \omega_{o,c} \cdot (h_{o,c} - h_i)\,. \tag{5.12}$$

Providing the frequency ω_T is determined, the forces required to open and close the crack, the distances of the crack faces in opened and closed state and the rigidities of the crack in both states are evaluated by the mean of the fit on the minima between the experimental results and the theoretical predictions.

5.2.2 Estimation of the thermal relaxation frequency

In order to estimate the thermal relaxation frequency, a comparison of the 3D equation to the 1D one is realized. Solution of the 1D heat equation, with the additional term, (Eq. (1.10)) is required:

$$\frac{\partial T}{\partial t} + \frac{T}{\tau_T} = \chi \frac{\partial^2 T}{\partial x^2} + \frac{I}{\ell \rho c_p} f(t)\Psi(x), \tag{5.13}$$

with

$$\Psi(x) = e^{-\left(\frac{x}{a}\right)^2}, \tag{5.14}$$

and with $f(t)$, as for the 3D case: $f(t) = [1 + \text{ш}\cos(\omega t)]/2$ (Eq. (3.5)) and $\omega_T = 1/\tau_T$. The initial and boundary conditions are:

$$T(t = 0) = 0, \tag{5.15a}$$
$$\partial_x T\big|_{x=0} = 0, \tag{5.15b}$$

leading to the following Green function:

$$G(x, x_1, t) = \frac{e^{-t/\tau_T}}{2\sqrt{\pi\chi t}} \left(e^{-\frac{(x-x_1)^2}{4\chi t}} + e^{-\frac{(x+x_1)^2}{4\chi t}} \right). \tag{5.16}$$

It follows that the solution of Eq. (5.13) is:

$$T(x,t) = \int_0^t \int_0^\infty \frac{I}{\ell \rho c_p} \cdot f(t_1) \cdot \Psi(x_1) \cdot G(x, x_1, t - t_1) \; dx_1 dt_1. \tag{5.17}$$

Simplified 1D heat equation

The goal of this section is to estimate τ_T. There is no reason to solve this equation in its complete form. The simplifications are also motivated by the fact that the 3D general equation, solved in Sec. 3.2, does not give an analytical solution for the general case. The maximum temperature rise evaluation, in the center of a nonmodulated beam, and for an infinite time has been analytically solved (Eq. (3.18)). Solving the 1D equation in the same condition as for the 3D case will provide an analytical determination of τ_T. Consequently, the new conditions are $x = 0$ and $f(t) = 1$. Eq. (5.17) is reduced to:

$$T(x=0,t) = \frac{I}{\ell \rho c_p \sqrt{\pi \chi}} \cdot \int_0^t \int_0^\infty \frac{e^{-\left(\frac{t-t_1}{\tau_T}\right)^2}}{\sqrt{t-t_1}} \cdot e^{-{x_1}^2\left(\frac{1}{a^2} + \frac{1}{4\chi(t-t_1)}\right)} dx_1 dt_1. \tag{5.18}$$

For $t \to \infty$, it leads to (Sec B):

$$\lim_{t \to \infty} T(x=0,t) = \frac{Ia}{2\ell \rho c_p} \sqrt{\frac{\pi \tau_T}{\chi}} \cdot e^{\frac{a^2}{4\chi\tau_T}} \cdot \mathrm{Erfc}\left(\frac{a}{2\sqrt{\chi \tau_T}}\right). \tag{5.19}$$

The characteristic thermal relaxation time has been introduced in the 1D heat equation in order to avoid the heat rise to diverge up to infinity. Then, τ_t can be evaluated by equalizing the two maximum temperature rises under the same condition. It corresponds to equating Eq. (3.18) and Eq. (B.7). It leads to:

$$e^{-\left(\frac{a}{2\ell}\right)^2} \cdot \left[\pi \mathrm{Erfi}\left[\frac{a}{2\ell}\right] - \mathrm{Ei}\left[\left(\frac{a}{2\ell}\right)^2\right]\right] = \frac{2\sqrt{\pi \chi \tau_T}}{a} \cdot e^{\frac{a^2}{4\chi\tau_T}} \cdot \mathrm{Erfc}\left(\frac{a}{2\sqrt{\chi\tau_T}}\right), \tag{5.20}$$

where τ_T is the only unknown. The characteristic thermal relaxation time depends on the sample thermal characteristics (χ, κ), the light penetration length (ℓ) but also on the beam radius (a). Consequently, ω_T needs to be re-evaluated each time the beam radius is modified.

It is numerically observed that as the beam radius diminishes, the thermal relaxation frequency ω_T increases. This is consistent with physical expectations: the shorter is the spatial scale, the higher is the relaxation frequency.

5.2.3 Evaluation of the spatial beam distribution function

For an estimation of the forces F_c and F_o from the intensities I_c and I_o, it remains to evaluate the laser distribution $\Psi(x)$ in the Laplace domain. If the beam profile is assumed gaussian, it follows:

$$\Psi(x) = e^{-\left(\frac{x}{a}\right)^2}, \tag{5.21a}$$

and thus:

$$\widehat{\Psi}(p) = \frac{a\sqrt{\pi}}{2} \cdot e^{(ap/2)^2} \cdot \mathrm{Erfc}\left[\frac{ap}{2}\right]. \tag{5.21b}$$

At the opposite of Eq. (3.12) in Sec. 3.2, Eq. (5.21b) converges due to the small argument in the exponential function.

5.3 Optimization of theory and experiment for crack characterization

A beam distribution is now determined. The thermal relaxation frequency, $\omega_T = 1/\tau_T$, is evaluated. As explained in the end of Sec. 5.2, it is now possible to estimate the parameters F_c, F_o, η_o, η_c, $(h_o - h_i)$ and $(h_c - h_i)$. As the 3D heat equation is solved (Sec. 3.2), it is also possible to evaluate the temperature rise induced at F_c and F_o, when the crack closes and opens, respectively.

5.3.1 Theoretical predictions

A numerical program is developed. The fitted parameters are ω_o, ω_c and F_o/F_c. The frequency ω_L is fixed by the experiment. For each set of values, the evolution of I_L/I_c as a function of the time spent in the closed region is calculated with Eq. (5.10). The maximum time spent by the crack in the closed region, associated to the limit when the ratio I_L/I_c diverges to infinity, is evaluated. The curve from 0 to this limit is inverted in order to get the evolution T_c as a function of the normalized loading intensity I_L/I_c. In presence of a hysteresis, two curves can be realized: one when the loading increases and one when it decreases (Sec. 5.2). Finally with Eq. (5.2), the evolution of the n^{th} sidelobe as a function of the loading intensity can be evaluated. In this case, the evaluation is realized up to the sixth sidelobe. Then, for each sidelobe the number of minima with their corresponding locations is evaluated .

When all these cases are evaluated, the fit between the experimental and these theoretical predications values is realized. In a first step, for one theoretical prediction the intensity I_c required to close the crack is estimated for all minima. The mean value of I_c and the associated standard deviation among all the minima are calculated. The standard deviation value is then compared to other theoretical cases. At the end, the set of parameters with the minimum standard deviation corresponds to the crack parameters. For a given sidelobe, if the theory does not predict as many minima as the experiment, the evaluation is made for each combination given by the corresponding binomial coefficient. The minimum standard deviation is considered.

Similarly, as the left and the right sidelobes do not have the exact same minima location, the evaluation of I_c is realized for both case and the one with the smallest standard deviation is compared to the other cases.

Finally, if several cases have a very close standard deviation to the minimum one, it is possible to plot these few cases and to compare visually the tendencies to choose the best one.

It is important to notice that the path B→C is identical in the increase or decrease of pump power. The 'return' path, when the loading decreases, is longer as it corresponds to C→B→D. The rest of the paths (A→B and D→E) are abrupt jumps from one state to another. It follows that the evolution of the nonlinear sidelobes amplitude is identical for the part $[P_o;\infty[$ -where P_o is the required power to close the crack- whether the pump amplitude increases or decreases. In particular, the minima are not affected. However, in the part $]0;P_o]$ some changes occur due to the presence of the path B→D when the pump decreases. Some new minima could appear.

In our case, evaluation concerns only the increase. The possible combinations of these different parameters are evaluated: ω_L is fixed by the experiment ($\omega_L = 2\pi \cdot 0.5$ Hz in this case), $\omega_o = (1, 2, \ldots, 9) \times 10^{-4,\ldots,+5}$ Hz, $\omega_c = (5, 10) \times 10^{0,\ldots,4} \times \omega_o$ Hz, and the hysteresis $F_o/F_c = [-10, -9, \ldots, -1] \cup [0.1, 0.2, \ldots, 1]$ where F_o/F_c is: negative if $F_c > 0$ and $F_o < 0$, positive if $F_{c,o} > 0$, and equal to 1 for the case without hysteresis.
The importantly wide range of magnitudes possible for the crack mechanical relaxation frequencies is motivated by the lack of known real values of these parameters.
Even if the theoretical predictions do not restrain any assumption on the crack mechanical relaxation frequencies, the assumption $\omega_c > \omega_o$ is kept for evident physical reasons. Indeed, the crack rigidity must be necessarily stronger in the closed state than in the opened one.

		Case													
		1	2	3	4	5	6	7	8	9	10	11	12	13	14
Sidelobe n	1	0	0	0	0	0	0	0	0	0	0	0	0	0	0
	2	0	0	0	0	0	0	0	0	0	0	0	0	0	0
	3	0	0	0	0	0	0	0	1	1	1	1	1	1	1
	4	0	0	0	0	1	1	1	0	0	1	1	1	1	1
	5	0	0	1	1	0	1	1	0	1	0	1	1	2	2
	6	0	1	0	1	0	0	1	1	1	1	1	2	1	2

Table 5.2: Theoretical predictions of the different number of minima as a function of the loading for the first six sidelobes.

All theoretical possible predictions of the number of minima as a function of an increased loading are reported into Tab. 5.2. For the thousands considered cases, only fourteen different combinations are possible. The influence of the parameters are studied. Some cases, such as, for example, number 14 ('0-0-1-1-2-2'), is possible only for a positive hysteresis. Some other, cases 2 and 4 only if $\omega_c \gg \omega_o$.
The model also predicts cases where a n^{th} sidelobe have more minima than the $(n+1)^{\text{th}}$ -cases 5-6, 8-10 and 13. This is observed in our experiment, even though with a different number of minima.

The first and the second sidelobe never got any minimum (Tab. 5.2). Thus monitoring the first and the second sidelobe evolution, on a scan, the crack is visible whatever are the crack parameters and the loading from the pump (providing it breathes). In any case the first sidelobe amplitude increases with the loading.

The first case, ‘0-0-0-0-0-0’, has the evident drawback that it cannot provide any fit between the experiment and the theory with the actual program. The second, third and fifth cases also have this drawback they got only one minimum, preventing a fitting either. However, all the different experiments exhibit several minima. Experimentally, more minima than in the case 14 are always observed.
It is also possible that some other cases could be theoretically predicted for other sets of parameters. Nevertheless, a high number of parameters with a large amount of orders of magnitude is already tested.

One could believe that evaluating up to the sixth sidelobe has the drawback to take into account sidelobes having rather small energy, which evolutions are then less accurate. However, in order to get good estimations, it is required to get several minima. As, the first two sidelobes are not having any and the third has only one, there is a necessity to go up to higher sidelobes. Moreover, higher sidelobes provide opportunity to discriminate between several parameter combinations (Tab. 5.2).

5.3.2 Experimental evaluation of the crack parameters

With this extended theory and this set of parameters, it appears that the number of minima on the first six sidelobes cannot be increased, but only reduced. The case 14, with the highest number of minima, predicts the combination ‘0-0-1-1-2-2’ as in [20].
Among the different crack parameter combinations, the evolution of the nonlinear sidelobes amplitude as a function of the loading for the cases corresponding to a standard deviation, $\sigma \leqslant \sigma_m + 1$ (where σ_m is the smallest standard deviation), are observed.
The best fit has the following parameters: $\omega_c = 300$ Hz, $\omega_o = 6$ Hz and $F_o/F_c = 1$. With these parameters, I_c is reached for $P_L = 26.0$ mW with a standard deviation $\sigma = 13.5$ mW. This fit is related to the experimental left minima. Only the first (22.8 mW) and the first two (58.9 and 128.9 mW) minima on the fourth and the sixth sidelobe, respectively, are predicted.
Some cases propose a better standard deviation, down to 12.8mW, but predict a vanishing of the odd sidelobes for large loadings. Conversely, with these parameters, and as in the experiment, the odd sidelobe amplitudes do not vanish (Fig. 5.5). Among the observed cases, only $\omega_o = 6$ Hz predicts such behavior. If the crack mechanical relaxation frequency in the open state increases to 7 Hz, the vanishing of odd sidelobes for high powers appears. If it diminishes to 5 Hz, the standard deviation increases. Different crack mechanical relaxation frequencies in the closed state predict a relatively similar behavior, $\omega_c = 300$ Hz is the smallest one and induces the smallest standard deviation. However, the difference with other frequencies is small. This makes the results more confident on the opened state than on the closed one. This can be attributed to the fact that the considered case could be interpreted as $\omega_c \gg \omega_{o,L}$.
If the possible number of minima with this new developed model is not increased from [20], the final estimations $\omega_o \simeq 2\omega_L$, confirms the necessity to get rid of the previous condition $\omega_{o,c} \gg \omega_L$.
One can note that nonlinear mixed-frequencies are generated in the experiment for powers below the required one to reach F_c. This is not possible theoretically. It can be attributed

to the presence of asperities which are touching, at least partially, for low powers [64]. The theory supposes an ideal crack with two parallel faces so that the change between opened and closed is abrupt which is far from the real geometry of the crack. Then, the estimated F_c corresponds to a 'real' crack closing but touching of surface asperities can occur at lower forces than F_c, generating nonlinearities.

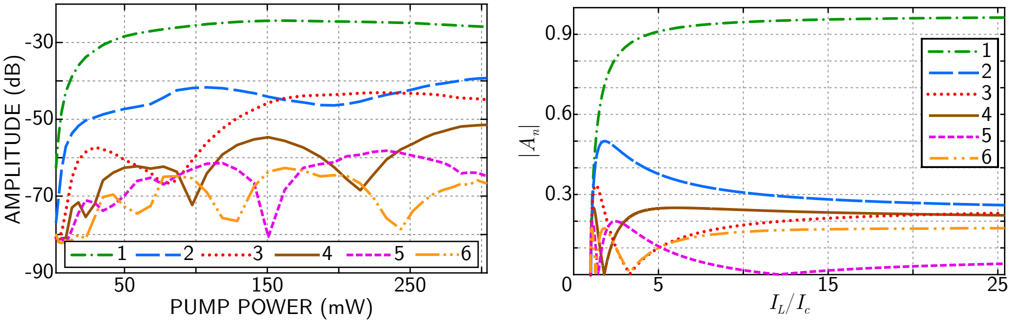

(a)

(b)

Figure 5.5: Experimental (a) and theoretical (b) dependences of the amplitude of the first six left sidelobes on the pump power (a) and the normalized intensity I_L/I_c loading the crack (b). Theoretical evolutions are obtained with $\omega_o = 6$ Hz, $\omega_c = 300$ Hz and $F_o/F_c = 1$.

A power of 26.0 mW, required to close the crack, corresponds, in this configuration, to a temperature rise of ∼18 K.

With the crack mechanical relaxation frequencies, the opened and closed rigidities are directly deduced:

$$\eta_o = \frac{\omega_o \rho c}{2} \simeq 45.1\ \text{MN.m}^{-3}, \tag{5.22a}$$

$$\eta_c \simeq 2.3\ \text{GN.m}^{-3}. \tag{5.22b}$$

Eq. (5.9) leads to $I_o/I_c \simeq 0.89$.

The intensities $I_{c,o}$ can be easily calculated now for the experimentally known powers:

$$I_c = \frac{P_L(I_L = I_c)}{\pi a^2} \cdot (1 - \mathsf{r}) \simeq 818\ \text{kW.m}^2, \tag{5.23a}$$

$$I_o = \frac{I_o}{I_c} \cdot I_c \simeq 724\ \text{kW.m}^2. \tag{5.23b}$$

Then, it is possible to estimate $P_L(I_L = I_o) = (I_o \pi a^2)/(1 - \mathsf{r}) = 23$ mW.

With Eq. (5.20), τ_T is evaluated: $\tau_T \simeq 0.035$ s, and $\omega_T = 1/\tau_T \simeq 29$ Hz.

The distances $(h_o - h_i)$ and $(h_c - h_i)$ can be deduced from Eq. (5.11). It follows:

$$h_o - h_i \simeq 13.9\ \text{nm}, \tag{5.24a}$$

$$h_c - h_i \simeq 0.28\ \text{nm}. \tag{5.24b}$$

Finally, with Eq. (5.12) the forces F_c and F_o are estimated:

$$F_c = F_o \simeq 1.3 \text{ N.m}^{-2}. \tag{5.25}$$

The dimensions of the rigidities and the force are not usual because they correspond to those acting on a unit surface (Sec. 1.3.2). It is interesting to have an estimation of the 'real' values. In order to reach such estimation, an application surface of the considered force needs to be defined. It is chosen to consider a beam diameter multiplied by a penetration length of light in the sample. This corresponds approximately to the surface of the crack irradiated by the beam. It follows:

$$\overline{\eta_o} = 2a \times \ell \times \eta_o \simeq 2.7 \text{ N.m}^{-1}. \tag{5.26a}$$

$$\overline{\eta_c} \simeq 132.9 \text{ N.m}^{-1}. \tag{5.26b}$$

This obtained 'real' opened rigidity is logically smaller than the closed one. These rigidities need to be compared to the one of the glass sample. The 'real' rigidities of the crack are associated to solid mechanics and link forces to displacement. On the contrary, the elastic modulus (or Young modulus), mathematically equal to $3K \cdot (1 - 2\nu)$, is a function of the strain and stress. However, it is possible to compare the elastic modulus to the equivalent rigidity by multiplying the former by the ratio of the cross-sectional area to the length of the element:

$$\overline{\eta_{\text{glass}}} = \frac{2a \times \ell \times 3K \cdot (1 - 2\nu)}{h_o - h_i} \simeq 278 \text{ GN.m}^{-1}. \tag{5.26c}$$

Both opened and closed 'real' rigidities are several orders of magnitude lower than the one of the glass. This predictable result justifies the possibility to estimate, in quasistatic regime, the dilatation associated to a temperature profile neglecting the rigidity of the crack (Eq. (3.20)).

Similarly as for the rigidity it is possible to estimate a 'real' force acting on the crack to open and close it. This leads to:

$$\overline{F_{c,o}} = 2a \times \ell \times F_{c,o} \simeq 74.0 \text{ nN}. \tag{5.26d}$$

The value of the 'real' force is very weak because the displacement is nanometric. This must not conceal the fact that the stress is, in reality, locally high because focused in a micrometric spot.

The distance $(h_o - h_i)$ corresponds to the distance covered by the crack faces under the pump loading action to close the crack. It does not consider the constant heat due to the pump or the probe beams. It has been demonstrated in Chap. 3 that a constant heat influences the distance between the crack faces. In particular, the probe beam can permanently change the distance between the crack faces during the loading (Sec. 3.5.3). This effect is not taken into account in this theory. Thus, considering the distance $(h_o - h_i)$ as the distance between the crack faces at temperature room would lead to an underestimation.

The total induced temperature change is composed of a constant increase in temperature (considered constant for long enough times) and of an oscillating temperature change (related to the fact that the laser beam is intensity modulated at some finite frequency). The constant heat induced by the pump laser beam corresponds to the minimum of the total induced relative temperature change (oscillating + constant). Ideally, the temperature should be null when the intensity of the pump is null. However, due to the pump power and frequency involved, this minimum is not 0. Consequently, there could be an influence of the constant heating on the constant distance between the crack faces around which the crack dynamic breathing occurs. In the current case, the minimum of the induced temperature change for the pump beam, at the power required to close the crack (26 mW) is of 2.5 K. Then, it can be neglected in the calculation.

On the contrary, the probe beam has a constant power of 121 mW and needs to be considered. In the following calculation, it is assumed to correspond to a beam intensity-modulated at frequency $f \to \infty$ to simplify the calculation. Then, the displacement due to the probe beam can be estimated with the use of the dilatation equation (Eq. (3.20)). The maximum temperature rise is up to ∼46 K. This leads to:

$$\Delta L \simeq 448.1 \text{ nm}. \tag{5.27a}$$

Consequently, the distance between the crack faces without external loading and at room temperature, reads:

$$h = h_o - h_i + \Delta L \simeq 462.0 \text{ nm}. \tag{5.27b}$$

This final result leads to one of the most interesting evaluated parameters for NDT&E applications: the distance between the crack faces. In this case, this distance is equal to ∼0.5 µm. This evaluation is consistent with the estimation from literature [42]. The ratio of the distance between the crack faces and the length of the crack is in the order of magnitude of $10^{-3} - 10^{-4}$ [64]. For a centimeter length crack, it leads to a distance between the crack faces down to a micrometer.

Conclusion

The evolution of the amplitude of the nonlinear sidelobes as a function of the pump power exhibit clear non monotonous behavior, as predicted by the theory. The evidence of minima, for particular pump powers and sidelobes is clear and their position is studied.

The development of the theory provides the evolution of the nonlinear sidelobes, as a function of the pump power, independently of the crack mechanical relaxation frequencies $\omega_{o,c}$. Without this quasistatic assumption, it is possible to fit the experimental result with the theoretical ones.

It directly follows an estimation of the crack mechanical relaxation frequencies and the hysteresis F_c/F_o. With these informations it is then possible to estimate the opened and closed rigidity $\eta_{o,c}$, and the intensities $I_{c,o}$, and the forces $F_{c,o}$ required to close and open the crack. Also, the displacement of the crack faces in the opened and closed state, $(h_o - h_i)$ and $(h_c - h_i)$, respectively, are evaluated. The temperature inducing the crack closing and opening is also provided. Finally, combined with the estimation of the dilatation of the crack faces induced by the probe beam, the distance between the crack faces, at the steady state and without loading, is obtained.

The new theoretical model provides better estimations but some discrepancies remain. In particular the presence of some minima are not explained with the actual theory. Due to the many 'extra'-minima, it appears that the assumptions on the model are still too numerous and have an important role in the evolution of the nonlinear sidelobes as a function of the loading. In particular, the asymmetrical heating could be a candidate to influence the nonlinear sidelobe behaviors. Nevertheless, it is worth emphasizing the fact that several crack parameters are estimated by this method.

Chapter 6

Other phenomena related to the increase of pump amplitude

Abstract

In this chapter, other phenomena related to the increase of the pump amplitude are observed and analyzed. Firstly the intensity I_c, required to close the crack, is determined. Then, the evolution of the phase is studied for higher powers.
The influence of the pump frequency on the position of the amplitude minima is also experimentally and theoretically evaluated.
In a third section, a particular crack which exhibits a sudden change in the nonlinear sidelobes evolution for high pump powers is described. The main peak evolution appears to be affected by this behavior. The repeatability, the influence of the maximum pump power, the increase and decrease of the pump power and the modulation frequency are studied in order to analyze these unexpected behaviors.

Along the whole chapter, the experiments are conducted with the set-up Υ_1 and with the parameters: $a_H = 34$ µm, $f_H = 24.9$ kHz and $P_H = 35$ mW for the probe beam, $a_L = 36$ µm and $f_L = 1$ or 1.5 Hz for the pump beam. The pump power evolves between $P_L = 1$ and 125 mW maximum but some experiments are conducted with a reduced amplitude. Only these two latter parameters, the pump frequency and the pump power, are indicated in the following.

6.1 Determination of the intensity required to close the crack

The evolution of the sidelobes under the pump amplitude action allows estimations of crack parameters. The theory assumes that the nonlinear frequency-mixing starts when the loading force F_L equals the one required to close the crack, F_c. Thus, an abrupt change should be observable in the evolution of the amplitude. The detection of this effect would allow a direct estimation of the intensity I_c, proportional to F_c. In the previous

experiment (Sec. 5.1), this effect has not been observed. The absence of an abrupt change in the amplitude evolution has been attributed to the existence of micro-contacts in the crack before the ‘complete’ crack closing.
The analysis of the amplitude and phase evolutions with the lock-in amplifier, by the mean of the set-up (Sec. 4.2) may allow better results than with a spectrum analyzer. The numerous points taken at each measurement should allow to detect the step in the generation of nonlinear mixed-frequencies more easily. The phase evolution, should also allow a detection differently: as long as the mixed-frequencies are not generated the phase values are incoherent and the standard deviation among the values is important. Once the clapping starts, the mixed-frequencies are generated, the phase becomes stable. An experiment, on another crack, is realized. The pump beam modulation frequency is of 1 Hz. The pump power evolves from 1 to 109 mW.

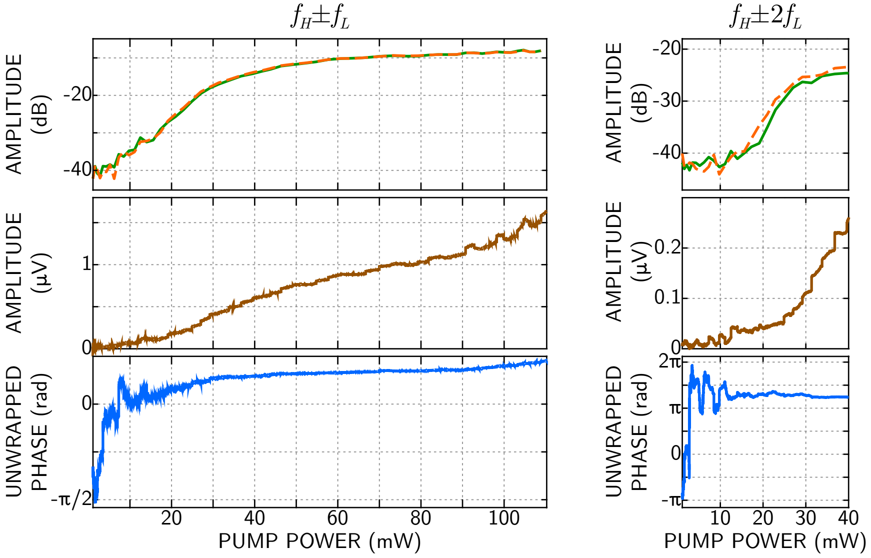

(a) (b)

Figure 6.1: Dependence of the amplitude and the unwrapped phase of the nonlinear sidelobes on the pump power. (top): Detection with the spectrum analyzer of the $f_H - nf_L$ (—) and $f_H + nf_L$ (- -). (middle-bottom): Detection with the lock-in amplifier. (b): Zoom for the powers lower than 40 mW.

Results are presented in Fig. 6.1. They exhibit the evolution of the first and the second nonlinear sidelobes as a function of the pump power amplitude in Figs. 6.1(a) and 6.1(b), respectively. Comparison with the spectrum analyzer is proposed. As previously, the pump power evolves by steps (56 in the present experiment). To each step corresponds several points recorded by the lock-in amplifier. All the data are presented in Fig. 6.1. One can see that the signal amplitude saturates for high powers on the spectrum analyzer (top) whereas it still increases on the lock-in amplifier (middle). There are no yet clear comprehension of this phenomenon.

The interest is centered on the low power to detect the nonlinear generation threshold. For the first nonlinear sidelobe (Fig. 6.1(a)), the spectrum analyzer does not allow an estimation. For the second sidelobe (Fig. 6.1(b)), it is easier to detect the change of the crack state, but the threshold is not clearly delimited. On the contrary, the lock-in amplifier allows an estimation either by the amplitude (when it starts to increase) or by the phase (when it is stable). Both effects are clearly visible in Figs. 6.1(a) and 6.1(b). The threshold detected by the amplitude with a lock-in amplifier can be estimated at 11.1 and 12.5 mW for the first and second sidelobe, respectively. This corresponds to two consecutive experimental points. The phases evolution gives an estimation of 12.5 mW in both cases, which is consistent with the results on the amplitude. It also fits the results of the second nonlinear sidelobe evolution with a detection by the spectrum analyzer. Consequently, it is possible to estimate I_c this way. For $P_L = 12.5$ mW, it follows $I_c \simeq 2.7$ MW.m^{-2}.

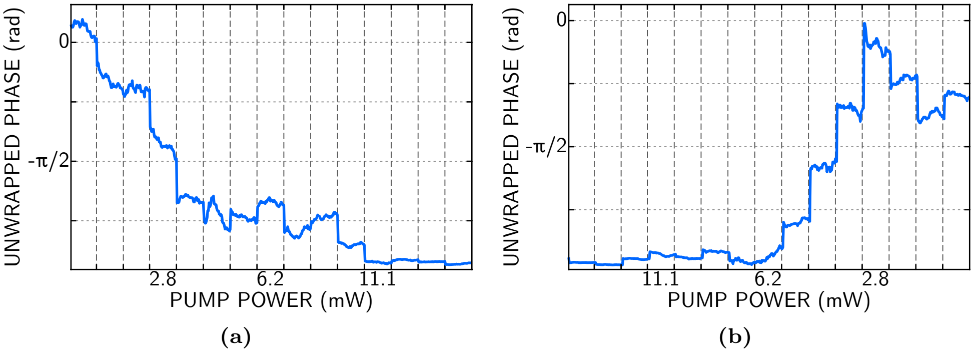

(a) **(b)**

Figure 6.2: Dependence of the unwrapped phase detected with the lock-in amplifier on the pump power for the second harmonic ($n = 2$) when the pump power increases (a) and decreases (b).

The experiment can be repeated for the case of the pump power decrease. In general, the clapping starts and stops for the same intensity either the pump power increases or decreases. Nevertheless, some cases exhibit a hysteresis: the clapping lasts for lower intensities than I_c, estimated when the pump power increases. In Fig. 6.2 the unwrapped phase evolution is presented for a different location on the crack and for a frequency $f_L = 1.5$ Hz. The pump power successively increases and decreases. Figs. 6.2(a) and 6.2(b) are zooms of the lower powers (for $P_L \leqslant 16$ mW) for the increase and the decrease of the pump power, respectively. From the former case, I_c can be estimated at $P(I_L = I_c) = 11.1$ mW whereas the clapping stops, on the latter, for $P_L = 6.2$ mW. When this hysteresis is observed, the shift of the transition between the clapping and the non-clapping regime is always for lower pump power when the latter decreases. This phenomenon can be attributed to the creation and the re-organization of contacts when the crack faces are touching thanks to the clapping, provided for higher pump powers. Thus, I_c needs to be evaluated when the pump power increases.

For several cases, the determination of I_c is not evident because the transition is not very clear. This can be attributed to the creation of micro-contacts between the crack faces as the pump power increases. These micro-contacts would induce the generation of nonlinear mixed-frequencies. Consequently, the nonlinear sidelobe amplitude appears smoother.
For higher sidelobes, the nonlinear sidelobes generation appears for higher powers. It leads to another estimation of I_c. For example, $P_L = 19.1$ mW for the third sidelobe in the first experiment corresponding to Fig. 6.1. It can be suggested that the correct I_c is detected by the lower sidelobes as the higher appear only when the signal-to-noise ratio is good enough.

6.2 Evolution of the phase as a function of the pump power

The phase evolution provides an accurate determination of the intensity required to close the crack (Sec. 6.1). Its evolution as a function of the pump power is also of interest for the detection of the minima on the nonlinear sidelobe amplitude evolutions.
In [20], it is predicted that, with the assumption $\omega_L \ll \omega_{o,c}$, the phase evolves under the loading amplitude action as:

$$\varphi_n = -n\frac{1}{2}\left[\operatorname{acos}\left(\frac{F_c}{F_L}\right) - \operatorname{acos}\left(\frac{F_o}{F_L}\right)\right] - \operatorname{acos}\left(\frac{A_n}{|A_n|}\right), \tag{6.1}$$

with $A_n = 1/n \cdot \sin[n\omega_L T_c/2]$. The last term of Eq. (6.1), $\operatorname{acos}(A_n/|A_n|)$, changes from 0 to π when the sign of A_n changes. This corresponds to an amplitude minimum. It implies sudden important phase variations. In-between two minima, the phase evolves slowly: the last term is constant and the first is a function of an arccosinus. Without hysteresis, only the last term is not null and the phase is supposed either equal to 0 or to π.
It appears that sudden changes in the phase evolution could provide an accurate determination of the minima position. However, the calculation should be developed without the quasistatic assumption on the crack motion, as realized for the amplitude in Sec. 5.2. The phase evolution follows the generic formulation:

$$\varphi_n = n \cdot \omega_L \left(t_1 - \frac{T_c}{2}\right) - \operatorname{acos}\left(\frac{A_n}{|A_n|}\right), \tag{6.2}$$

where the notations t_1 and T_c are identical to the ones in Sec. 5.2. Thus, t_1 and T_c correspond to the transition between closed and opened state and to the time spent in the closed region over a period, respectively. The generic definition of the phase (Eq. (6.2)) is demonstrated in Chap. 7. The parameters t_1 and T_c are required to solve Eq. (6.2). If T_c is already determined (Sec. 5.2), t_1 remains undetermined. From Eq. (5.8), it is possible to rewrite the dependence on I_o as:

$$\cos[\theta_1] - \cos[\theta_1 - \omega_L T_c] \cdot e^{-\omega_c T_c} = \varkappa_c \frac{I_o}{I_L}\left(1 - e^{-\omega_c T_c}\right). \tag{6.3}$$

The notations of the previous chapter are conserved, the instant t_1 is contained in θ_1. The left part of the equation (6.3) can be rewritten:

$$\sqrt{1-2\cos[\omega_L T_c]e^{-\omega_c T_c}+e^{-2\omega_c T_c}}\cos\left[\theta_1+\operatorname{atan}\left(\frac{\sin(\omega_L T_c)e^{-\omega_c T_c}}{1-\cos(\omega_L T_c)e^{-\omega_c T_c}}\right)\right]= \\ \varkappa_c\frac{I_o}{I_L}\left(1-e^{-\omega_c T_c}\right). \quad (6.4)$$

As I_L/I_c (and not I_L/I_o) is given in Eq. (5.10), it is convenient to write θ_1 as a function of I_L/I_c. Isolating θ_1 from Eq. (6.4), it follows:

$$\theta_1=\pm\operatorname{acos}\left[\frac{\frac{\omega_o}{\omega_c}\sqrt{\frac{{\omega_L}^2+{\omega_c}^2}{{\omega_L}^2+{\omega_o}^2}}\cdot\frac{F_o}{F_c}\cdot\left(1-e^{-\omega_c T_c}\right)}{\sqrt{1-2\cos[\omega_L T_c]\cdot e^{-\omega_c T_c}+e^{-2\omega_c T_c}}}\cdot\frac{I_c}{I_L}\right]+2p\pi+ \\ -\operatorname{atan}\left[\frac{\sin(\omega_L T_c)\cdot e^{-\omega_c T_c}}{1-\cos(\omega_L T_c)\cdot e^{-\omega_c T_c}}\right], \quad (6.5)$$

with $p\in\mathbb{Z}$. As $\theta_1=\omega_L t_1-\varphi(\omega_L)-\operatorname{atan}(\omega_L/\omega_c)$, it is finally possible to determine t_1 and to get a formula for the phase evolution. The considered sign of the acos should be '+' in order to have $\omega_L t_1\in\mathbb{R}_+$ for any values of $\varphi(\omega_L)$ and $\operatorname{atan}(\omega_L/\omega_c)$ and the $2p\pi$ term can be neglected in the phase definition, defined modulo 2π. The phase then reads

$$\varphi_n=n\left(\operatorname{acos}\left[\frac{\frac{\omega_o}{\omega_c}\sqrt{\frac{{\omega_L}^2+{\omega_c}^2}{{\omega_L}^2+{\omega_o}^2}}\cdot\frac{F_o}{F_c}\cdot\left(1-e^{-\omega_c T_c}\right)}{\sqrt{1-2\cos[\omega_L T_c]\cdot e^{-\omega_c T_c}+e^{-2\omega_c T_c}}}\cdot\frac{I_c}{I_L}\right]-\operatorname{atan}\left[\frac{\sin(\omega_L T_c)\cdot e^{-\omega_c T_c}}{1-\cos(\omega_L T_c)\cdot e^{-\omega_c T_c}}\right]+\right. \\ \left.-\frac{\omega_L T_c}{2}+\varphi(\omega_L)+\operatorname{atan}\left[\frac{\omega_L}{\omega_c}\right]\right)-\operatorname{acos}\left[\frac{A_n}{|A_n|}\right]. \quad (6.6)$$

It is interesting to define the phase $\dot{\varphi}_n$ where only the parts evolving with the change of pump power are considered:

$$\varphi_n=n\left(\operatorname{acos}\left[\frac{\frac{\omega_o}{\omega_c}\sqrt{\frac{{\omega_L}^2+{\omega_c}^2}{{\omega_L}^2+{\omega_o}^2}}\cdot\frac{F_o}{F_c}\cdot\left(1-e^{-\omega_c T_c}\right)}{\sqrt{1-2\cos[\omega_L T_c]\cdot e^{-\omega_c T_c}+e^{-2\omega_c T_c}}}\cdot\frac{I_c}{I_L}\right]-\operatorname{atan}\left[\frac{\sin(\omega_L T_c)\cdot e^{-\omega_c T_c}}{1-\cos(\omega_L T_c)\cdot e^{-\omega_c T_c}}\right]+\right. \\ \left.-\frac{\omega_L T_c}{2}\right)-\operatorname{acos}\left[\frac{A_n}{|A_n|}\right]. \quad (6.7a)$$

with

$$\varphi_n=\dot{\varphi}_n+n\cdot\left[\varphi(\omega_L)+\operatorname{atan}\left(\frac{\omega_L}{\omega_c}\right)\right]. \quad (6.7b)$$

It follows from Eq. (6.7a) that a minimum of the amplitude remains associated to a phase change. It confirms the potential of the phase detection to determine the amplitude minima positions. The other terms in Eq. (6.7a) demonstrate that, even without

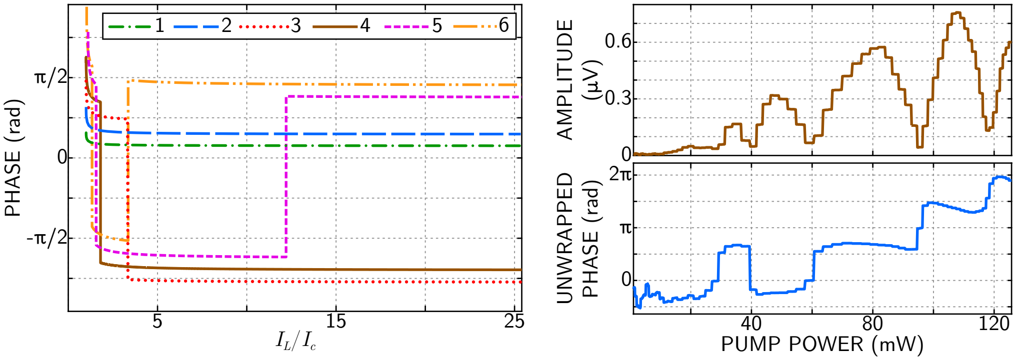

(a) **(b)**

Figure 6.3: (a): Theoretical evolution of the phase of the photoacoustic signal of the nonlinear sidelobes, related to $n = 1 - 6$, as a function of the pump power. Parameters are as in Fig. 5.5(b): $F_o/F_c = 1$, $f_L = 0.5$ Hz, $\omega_o = 6$ Hz, $\omega_c = 300$ Hz. (b): Evolution of the amplitude and the unwrapped phase of the photoacoustic signal of the fifth nonlinear sidelobe as a function of the pump power. The signal is analyzed with a lock-in amplifier.

hysteresis, the phase can evolve in-between two minima, on the contrary to Eq. (6.1). Fig. 6.3(a) is an example of theoretical phase evolution of the first nonlinear sidelobes. The parameters are identical to those determined for the crack in Chap. 5: $\omega_L \simeq 3.14$ Hz, $\omega_o = 6$ Hz, $\omega_c = 300$ Hz.

An experiment is conducted for several sidelobes with an evolution of the pump power. Fig. 6.3(b) demonstrates the evolution of the phase and the amplitude, detected with the lock-in amplifier for a pump power between 1 and 125 mW and $f_L = 1.5$ Hz.
For each minimum of the amplitude corresponds a change of phase. In-between two successive minima, the phase slowly evolves as assumed by Eq. (6.7a). The experiment and the theory exhibit the same overall behavior, even though, this experimental example contains more minima than theoretically predicted (4 on the fifth sidelobe in Fig. 6.3(b)). This technique allows a particularly interesting alternative to minima detection. It is very sensitive and precise because the changes are abrupt, important, and concern only one specific pump power.

As a conclusion for this section, both the evolution of the amplitude and the phase provide the information on the minima. However, the evolution of the phase is more sensitive and thus offers a more precise value of the loading corresponding to a minimum amplitude. It also offers the possibility to detect the transition between non-clapping to clapping regime. This leads to the determination of the particular loading required to close the crack.

6.3 Influence of the pump frequency on the sidelobe evolutions with the increase of the pump power

The influence of the pump frequency on the crack breathing efficiency has been discussed in Chapter 3: the time spent by the crack in the closed region evolves as a function of $1/\omega_L$: the lower is ω_L, the larger is the time spent in the closed region. The choice of the pump frequency also influences the nonlinear sidelobe evolutions as they are functions of $\omega_L T_c$ (Eq. (5.2)) and as T_c is also function of ω_L (Eq. (5.10)).

Three different theoretical cases are studied with the following parameters: $\omega_o = 0.2$ Hz, $\omega_c = 20$ Hz, and $\omega_L = 0.6$, 1 and 2 Hz. No hysteresis is assumed, $F_o/F_c = 1$. Its presence would not affect the conclusions. In Fig. 6.4(a), the evolution of I_L/I_c as a function of the percentage of the time spent by the crack in the closed region over a pump period is presented. As predicted, the maximum time is inversely proportional to ω_L. For these crack parameters, the crack spends, at the maximum, ~27 %, ~23 % and ~18 % of the time, over a pump period, in the closed state for $\omega_L = 0.6$, 1 and 2 Hz, respectively.

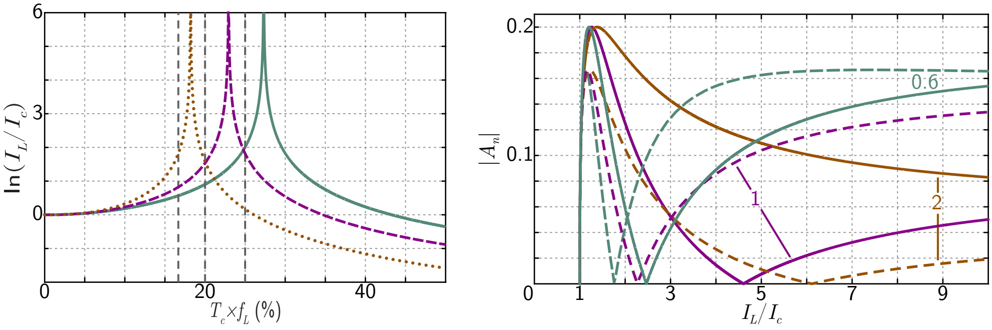

(a) **(b)**

Figure 6.4: (a): Evolution of the logarithm of the normalized acoustic intensity as a function of the time spent by the crack in the closed state for $F_o/F_c = 1$, $\omega_o = 0.2$ Hz, $\omega_c = 20$ Hz and $\omega_L = 0.6$ Hz (—), ω_L=1 Hz (- -) and ω_L=2 Hz (•••). (Vertical dashed lines): Time spent (in %) by the crack in the closed state over a pump period to reach the minima on the fourth (16.7%), fifth (20%) and sixth sidelobes (25%), respectively. (b): Dependence of the amplitude $|A_n|$ of the fifth (—) and sixth (- -) sidelobes on the normalized intensity I_L/I_c in the conditions $F_o/F_c = 1$, $\omega_o = 0.2$ Hz, $\omega_c = 20$ Hz and $\omega_L = 0.6$, 1 and 2 Hz.

In Fig. 6.4(b) the evolutions of the fifth and sixth sidelobes are presented for these three pump frequencies. The other sidelobes are not presented to simplify the graph. For these cases, the nonlinear sidelobes associated to $n = 1, \ldots, 3$ do not present any minima. The fourth one has a behavior close to the fifth one. The fifth and the sixth nonlinear sidelobes exhibit the two possible scenarios.

Firstly, the minima can be shifted to higher powers as the pump frequency increases. For example, the sixth sidelobe presents a minimum reached for $F_L/F_c = 1.76$, 2.26 and 6.1

for $\omega_L = 0.6$, 1 and 2 Hz, respectively.
Secondly, a minimum can disappear as the pump frequency increases. For example, the fifth nonlinear sidelobe minimum, which is shifted when the pump frequency changes from $\omega_L = 0.6$ to 1 Hz, is not present for $\omega_L = 2$ Hz.
Both behaviors are related to the decrease of the crack breathing efficiency when the pump frequency increases. A minimum on a sidelobe amplitude occurs for a particular time spent in the closed region by the crack over a pump period. It corresponds to a particular value of the product $\omega_L T_c$ (Sec. 1.3.2). For example, the fifth nonlinear sidelobe has, for the case $\omega_L = 0.6$ Hz, a minimum for $I_L/I_c = 2.47$, equivalent to $\ln(I_L/I_c) = 0.904$. From Fig. 6.4(a), it corresponds to a crack closed during 20% of the time over a pump period.
If ω_L increases from 0.6 to 1 Hz, the crack is closed during 20% of the time over a pump period for $I_L/I_c = 4.61$. Then, the minimum is shifted towards more important loadings. For $\omega_L = 2$ Hz, the crack cannot spend more than ∼18% of time, over a pump period, in the closed state. The crack needs to be closed 20% of the time over a pump period in order to provide a minimum to the fifth nonlinear sidelobe. Then, this minimum is not reachable and disappears over the nonlinear sidelobe evolutions.
In Fig. 6.4(a), the percentage of time required to spend in the closed state, over a pump period, to reach the minimum of the fourth, the fifth and the sixth sidelobe are plotted. The minimum on the fourth sidelobe, not presented in Fig. 6.4(b) is present only for the case $\omega_L = 0.6$ Hz. The minimum on the sixth sidelobe is present in the three cases with a loading varying as a function of the pump frequency, as previously described.
If the pump frequency continues to increase, fewer minima are expected.
Substituting Eq. (5.10) into Eq. (5.2) leads to the observation that ω_L has an influence on the nonlinear sidelobe evolutions only in the dynamic regime, and not in the quasistatic one associated to $\omega_L \ll \omega_{o,c}$.

The other nonlinear sidelobe evolutions, even though they do not present minima, are also affected by the change of the pump frequency. The behaviors are similar but with different amplitudes. The main nonlinear sidelobes, such as the first and the second ($f_H \pm f_L$ and $f_H \pm 2f_L$, respectively), have their amplitude decreasing due to the crack breathing efficiency evolution. For example, the first nonlinear sidelobe maximum amplitude, for an infinite loading, passes from 0.76 to 0.54.
On the contrary, some higher sidelobes have larger amplitudes. For example, for an infinite loading, the third sidelobe increases from 0.18 to 0.33.

The proposed theoretical cases are chosen to clearly demonstrate the possible changes of the evolution of the nonlinear sidelobe amplitudes. However, these changes highly depend on the crack parameters such as ω_o, ω_c and F_o/F_c, and more specifically on the ratios $\omega_{o,c}/\omega_L$. For other crack parameter combinations, the minima shifting can be lower or not observable.

Two experiments are realized on the same location with the set-up Υ_1. Only the first three sidelobes are shown at two different frequencies: $f_L = 1$ and 1.5 Hz. The pump power varies between 1.1 mW up to 108.9 mW. The power steps, between two successive experimental points, are between 1.2 and 6.6 mW.

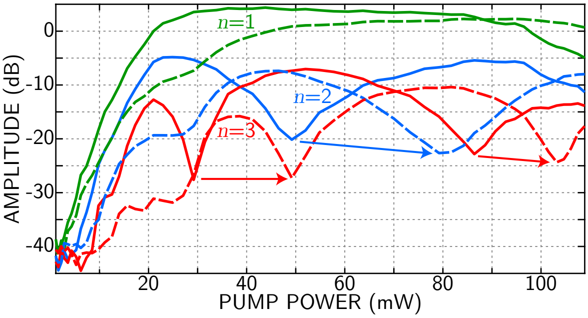

Figure 6.5: Dependence of the amplitude of the first three sidelobes on the pump power loading the crack at frequency $f_L = 1$ Hz (—) and $f_L = 1.5$ Hz (- -).

Results are plotted in Fig. 6.5. The shift of the minima is clearly demonstrated as predicted by the theory. For this case, and this pump power variation, the second sidelobe contains one minimum and the third two. The minima are shifted from 49.2 to 79.2 mW for the second sidelobe and from 29.2 and 86.4 to 49.2 and 103.2 mW for the third sidelobe, respectively. There is no evidence of a suppression of a minimum in these experiments.

The presence of a minimum on the second sidelobe is not theoretically possible in any case. It corresponds theoretically to a crack closed during half time of a pump period. As it is a sidelobe with an important energy, the crack parameters determined by the fit method of Chap. 5 should not be conclusive. Even though, the minima shift is consistent with the theoretical behavior predications.

The first sidelobe also has an interesting evolution. Indeed, for $f_L = 1$ Hz, the amplitude decreases of $\sim$9 dB, whereas this attenuation appears, for $f_L = 1.5$ Hz much after and is less important: $\sim$3 dB. This tends to confirm the possibility of a crack being more and more closed.

6.4 Other observed phenomenas

Most of the phenomena are understood and explained with the theoretical model. Several discrepancies are still present but the general behavior and the influence of the parameters are well described. However, two unexpected phenomena are observed, both on the same crack and are associated to particular pump powers. One concerns the main peak amplitude and occurs at low pump power, whereas a second one concerns the nonlinear sidelobe evolutions for higher pump powers. The latter phenomenon is firstly discussed. The sample used in the following experiments is, as for the previous ones, a glass plate with a crack realized by thermal shock.

6.4.1 Second state of the crack

As it has been previously shown in Chap. 5, the evolution of the nonlinear sidelobes as a function of the pump amplitude is rather well predicted. However, for a particular sample, the evolution of nonlinear sidelobes appears to be in two possible regimes. Only the first one is theoretically predicted. A description of these experimental observations is proposed. At the end some tentative explanations of the observed phenomena are given.

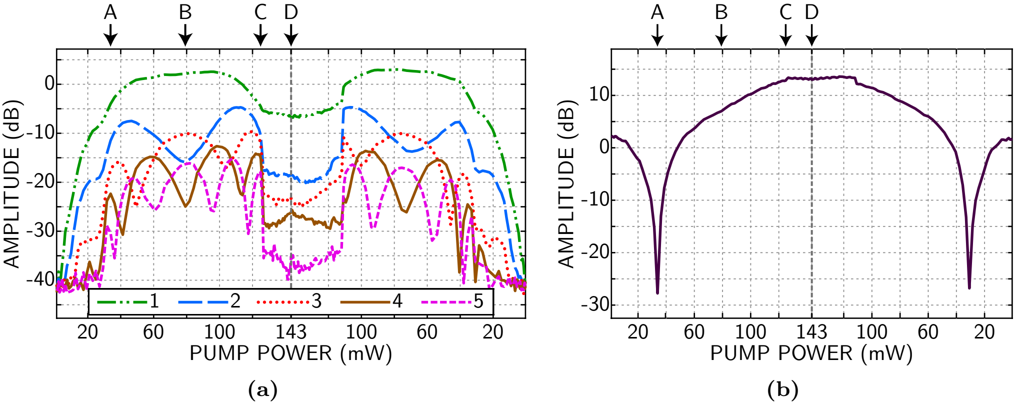

Figure 6.6: Dependence of the amplitude of the photoacoustic signal of the first five sidelobes (a) and the main peak (b) on the pump power loading the crack at frequency $f_L = 1.5$ Hz. The vertical dashed-line separates the increase from the decrease of the pump power.

A first result of the evolution of nonlinear sidelobes for $n \in [1; 5]$ is presented on Fig. 6.6(a). In this experiment, the pump amplitude varies from 1.1 to 143.3 mW with 56 power steps and then decreased down to 1.1 mW with the same 56 steps. The vertical dashed line is the limit between the pump amplitude increasing and decreasing.

The first part of this curve, for $P_L \leqslant 125$ mW is similar to the previous experiments. One can note that the sidelobes do not appear all at the same power, as previously discussed (Sec. 6.2). A small deviation in the evolution is detected in the first and second sidelobe at $P_L = 27$ mW, just before the rise of the higher sidelobes. In this first part, the evolution exhibits minima (see for example Fig. 6.7(b)). In Fig. 6.7(b), corresponding to $P_L = 79.2$ mW, all even sidelobes have a simultaneous minimum. This corresponds theoretically, to a crack closed half time of the pump period (Eq. (1.20a)). It would indicate that for $P_L \geqslant 80$ mW, the crack is closed more than half time over a pump period.
The first sidelobe clearly decreases for $P_L \geqslant 100$ mW. Comparison between left and right sidelobes demonstrate a very good agreement on the position of the nonlinear sidelobe evolutions. Only the amplitudes are different.

For $P_L \simeq 125$ mW a sudden amplitude decrease appears. This decrease is visible on all the sidelobes. It is very important: more than 10 dB for the second and third sidelobe, ∼15 dB for the third and fourth one (Fig. 6.6(a)). This decrease appears at the same time for all the sidelobes. Fig. 6.7(c) is the last spectrum before this transition, for $P = 124.9$ mW. Beyond this power, for $125 < P_L \leqslant 143.4$ mW, the evolution of nonlinear sidelobes is relatively monotonous. The first and the second sidelobes can be

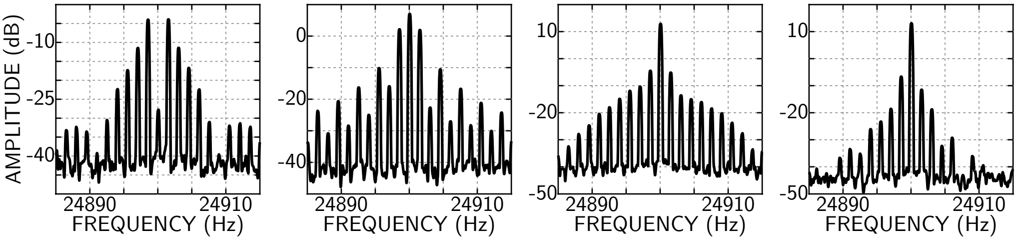

(a) (b) (c) (d)

Figure 6.7: Spectra of the photoacoustic signal for points A, B, C and D in Fig. 6.6 corresponding to the drop of the main peak at P_L = 33.8 mW (a), the amplitude minimum of the second and the fourth sidelobe at P_L = 79.2 mW (b), the last point before the change of the crack state at P_L = 124.9 mW (c), and the maximum pump power, in the second state of the crack, at P_L = 143.4 mW (d), respectively.

considered stable in this regime, whereas the fourth and the fifth slowly increases and decreases, respectively. These evolutions are very small in comparison to the part for $P_L \leqslant 125$ mW. No minima are present anymore. A spectrum, at the highest pump power, $P = 143.4$ mW, is presented in Fig. 6.7(d). One can see the global decrease and the absence of the highest sidelobes in comparison to Fig. 6.7(c). However, the nonlinear mixed-frequencies are still present. Asymmetry of the left and right nonlinear sidelobes is more pronounced in that second state.
The sudden and important change on all the sidelobes means that an important change in the crack occurs.

When the pump power decreases, a hysteresis is observed. In Fig. 6.6(a), the passage from the first to the second state occurs for $P_L = 125$ mW when the pump amplitude increases, whereas the return to the first state happens for $P_L \simeq 110$ mW. Depending on the initial state of the crack, there is a zone where both states appear stables.
Once the crack is back to the first state, a symmetry with the other part of the curve is observed: the behavior and the minima positions fit. For example, the minima of the fourth sidelobes are at 41, 79, and 114 mW when the pump power increases and 76 and 41 mW when the pump power decreases. The third minimum, at $P = 114$ mW, is absent because the crack is in this second state.
Some experiments, discussed later, present much stronger hysteresis. The second state can remain until the pump power decreases down to values under 20 mW.

6.4.2 Changes in the main peak amplitude

The main peak amplitude evolution is highly different from the previous experiments (Chap. 5). Fig. 6.6(b) demonstrates the evolution of the main peak amplitude as a function of the pump power for the same experiment presented in Fig. 6.6(a).

The amplitude is maximum when the pump power is maximum, but a huge drop is present before, for $P_L = 34$ mW. This loss in amplitude is very important (~25 dB Fig. 6.6(b)), and very sharp: a 2 mW increase or decrease from 34 mW in the pump

power makes the main peak amplitude increases by ∼10 dB (amplitude multiplied by more than 3).
This drop is present when the pump power increases or decreases. The behavior is globally symmetrical: the drop is at 34 mW when the loading increases and at 31.5 mW when it decreases. This difference concerns only one pump power step, and may be neglected.

This drop (at $P_L = 34$ mW) appears after the apparition of the higher sidelobes ($P_L = 27$ mW). Then, it does not correspond to the loss of energy by an efficient frequency-mixing conversion.

One can also note than in this part, the first nonlinear sidelobes have larger amplitudes than the amplitude of main peak (Fig. 6.7(a)). However, this concerns only a few steps around this drop.

6.4.3 Evolution of the phase

The evolution of the amplitude and the phase, recorded by the lock-in amplifier, is also studied. In Fig. 6.8, the evolutions of both amplitude and phase for the fourth and the fifth sidelobes are presented.

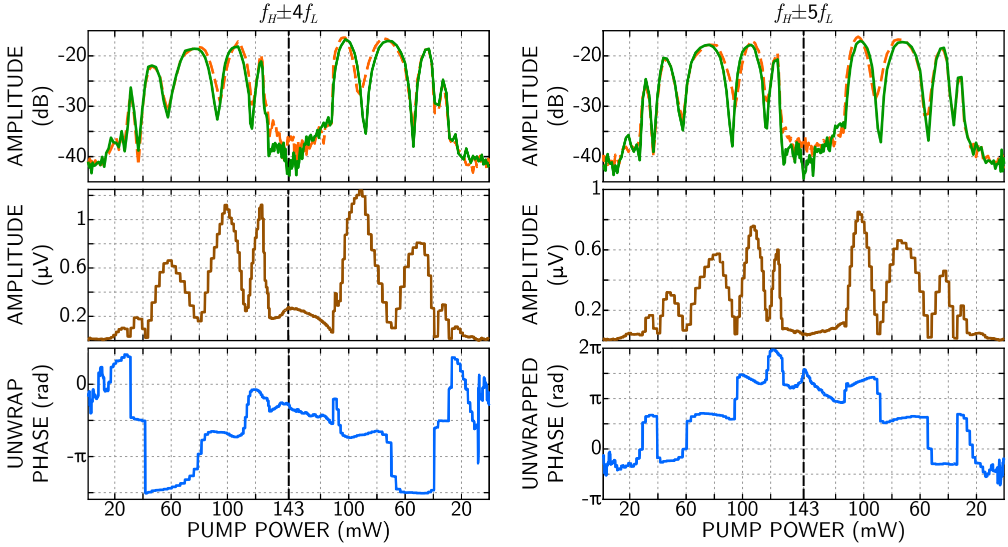

(a) (b)

Figure 6.8: Dependence of the amplitude and the unwrapped phase of the nonlinear sidelobes on the pump power. (top): Detection with the spectrum analyzer of the $f_H - nf_L$ (—) and $f_H + nf_L$ (- -). (middle-bottom): Detection with the lock-in amplifier. The vertical dashed-line separates the increase from the decrease of the pump power.

The evolution on the amplitudes detected by the spectrum analyzer and the lock-in amplifier are very similar.
As previously, the phase evolution presents abrupt changes for each amplitude minimum

(Fig. 6.8 (bottom)). In the second state of the crack, the phase evolution is monotonous, either increasing as the pump increases (Fig. 6.8(b) (bottom)) or remaining stable (Fig. 6.8(a) (bottom)). There is no additional information in the phase evolution. It only confirms that the nonlinear mixed-frequencies are generated. With the only phase information, this second state of the crack is not detected.
As the information on the main peak is not recorded by the lock-in amplifier, it is not possible to evaluate its phase evolution, especially for the drop in the amplitude.

6.4.4 Study of the influence of different parameters on these phenomena

Because of the use of the lock-in amplifier for five sidelobes, the experiment is realized five times in a row (Sec. 4.2). Besides, this experiment is repeated several times, with several hours in-between. The repeatability of this experiment when repeated in a row or with pauses can be evaluated.
Some parameters are modified to evaluate their influence on the experiments: the maximum or the minimum pump power, the frequency f_L of the pump beam, the location on the crack, or reversing the pump power evolution, i.e., decreasing and then increasing.

Phenomena associated to the first increase of the pump

We are able to repeat the heating and cooling (increasing and decreasing the pump power) many times and study the repeatability of our observations. A first observation is the presence of high discrepancies appearing between some of the first pump power increase and the following ones. These different evolutions, referred as ‘first increase’, are observed when the crack has not been heated for several tens of hours before the beginning of the experiment.

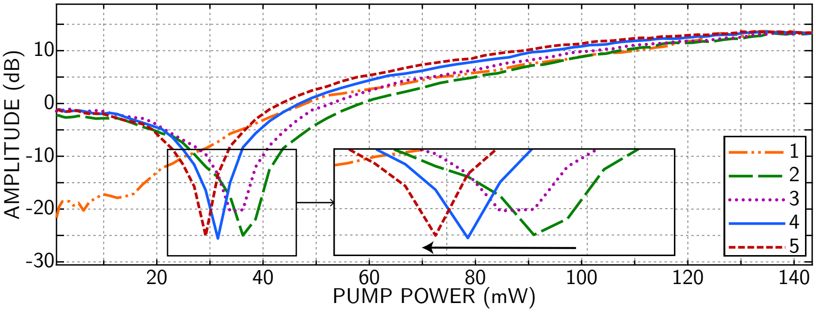

Figure 6.9: Dependence of the amplitude of the photoacoustic signal of the main peak on the pump power loading the crack at frequency $f_L = 1.5$ Hz for five successive increases.

The main peak evolution is different. In Fig. 6.9 the evolution of the main peak amplitude is presented when the pump power increases for a set of five measurements realized in a row at the pump frequency $f_L = 1.5$ Hz. Discussion on the repeatability of the phenomenon follows in the next section.

For the first pump power increase, the main peak amplitude evolution does not present a drop. It increases as a function of the pump power as previously (Sec. 3.1). The following increases present a drop in the evolution of the main peak (around $P_L = 30$ mW in Fig. 6.9).
The drop is present when an experiment has been previously conducted recently. It is absent only when the crack has been at rest for some tens of hours before the first pump power increase. This demonstrates a long memory effect of the crack.
Besides, if the pump power starts decreasing, the main peak drop is always observed. Thus, this effect is somehow related to the high pump powers involved, even though the pump powers where both effects are present are very distinct. It indicates that the first increase modifies in some manner the crack, and that this modification is reversible after several hours at rest.

The general behaviors of the minima on higher sidelobes are also different. The minima locations are close to the other successive evolutions but discrepancies in the amplitude appear. In Fig. 6.12(b) one can see the difference of the third left sidelobe first evolution in comparison to the following ones.

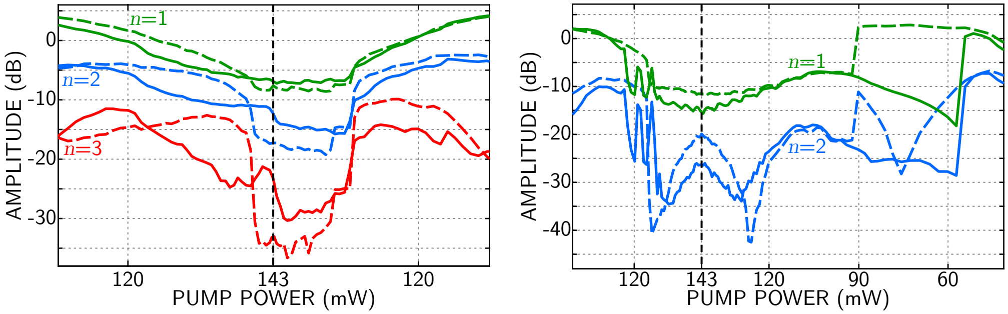

(a) (b)

Figure 6.10: Zooms of the dependence of the amplitude of the photoacoustic signal of the main peak on the pump power loading the crack to exhibit a soft transition (a) and an unstable transition (b) between the two states of the crack on the first increase. Evolutions of the first (—) and the second (- -) increase-decrease of the loading power. The vertical dashed-line separates the increase from the decrease of the pump power. Pump frequency is of 1 Hz (a) and 1.5 Hz (b).

Finally, the crack transition to the second state also differs in the 'first increase'. The second state of the crack is not suddenly reached as in the other increases (Fig. 6.6(a)). Two cases are observed.
The first one shows a slow transition to the second state (Fig. 6.10(a)). In that case the amplitude of all sidelobes slowly decreases and the transition is almost invisible. When the power decreases, and on the successive increases, the abrupt transition appears.
The second case is a transitional zone where the amplitude suddenly increases and decreases (Fig. 6.10(b)). The crack seems to oscillate between both states. After several oscillations, the second state is clearly reached. These oscillations disappear for the

next transition between these states. This may be due to the reorganization of the micro-contacts in the crack faces. The difference of the pump power for the transition between state 2 to 1 in Fig. 6.10(b) is discussed in the next paragraph 'Influence of the pump frequency'.
The unstable transition is more frequently observed than the slow one.

As a conclusion of this section, the 'first increases' present a different behavior as a function of the pump power. For low pump powers, the evolution is similar to the previous one (Chap. 5). For larger powers, the transition to the second state occurs differently. The four next evolutions are similar. It demonstrates that large enough pump powers are able to modify some crack properties, when the first increase in pump power is achieved.

Repeatability

In this section the first increases, corresponding to the cases just discussed above involving memory, are not discussed. Consequently, the successive experiments presented in the following consist in four or five identical experiments of pump increase, the first increase being excluded when exhibiting a different behavior.

A first observation is that for the four (or five) other experiments, the main peak drop is present for close pump powers. However a little shift is observed: from the first experiment with this drop to the fifth one, the drop appears at a lower amplitude. For example, in Fig. 6.9, the drop in the main peak amplitude occurs for pump powers from 36 to 34, 32 and 29 mW. These values slightly vary when the experiment is repeated. The changes of the pump power, leading to a main peak amplitude minimum, are always small in a set of five experiments in a row -in general 5 mW maximum- but this shift is always observed.
The same experiment is repeated for a pump power increase, increase and decrease, decrease and increase and only decrease. For the first three cases, the shift toward lower values is always observed. For the only decrease, the shifting of the minimum increases: from 14 to 15, 17, 19 and 23 mW. Thus, absence of pump increase appears to influence the behavior of the crack, leading to these changes.
In some cases, the pump power associated to the minimum of the main peak amplitude remains equal several times, but never on the five experiments. For the experiments with both increase and decrease, the shift toward lower values is observed for the increase and the decrease.

Between two sets of experiments, the pump power value associated to the main peak drop between the fifth experiment and the first new one is different. There is no apparent memory of this last pump power value. The crack seems restored because the main peak amplitude drop occurs for similar values in the first increase of each set. For example, for a set of experiments, the main peak drop occurs for pump power from 23 mW for the first increase and decrease until 21 mW for the fifth one. Around 30 hours after, the experiment is repeated. The first minimum on the main peak is for a pump power of 25 mW and decreases until $P_L = 21$ mW.

In four experiments having the same characteristics, the fifth evolution minimum is at 20±1 mW, and half of these experiments, already have this value at the fourth experiment. This tends to demonstrate that there is a limit value which is reached after some back and forth.

The transition between the crack states present a different behavior. In general, the transition between the two states in the first and the second time occurs for a higher power the second time. In the other successive increases, there is no increase of the pump power value for the crack state transition between two consecutive experiments: this value generally slightly decreases or remain equal. No ultimate value appears. The evolution of the transition is demonstrated in Fig. 6.11.

When the pump power decreases, the transition is more chaotic. It sometimes increases or decreases without any apparent logical reason. In most cases, the limit does not vary importantly, as for the increases.

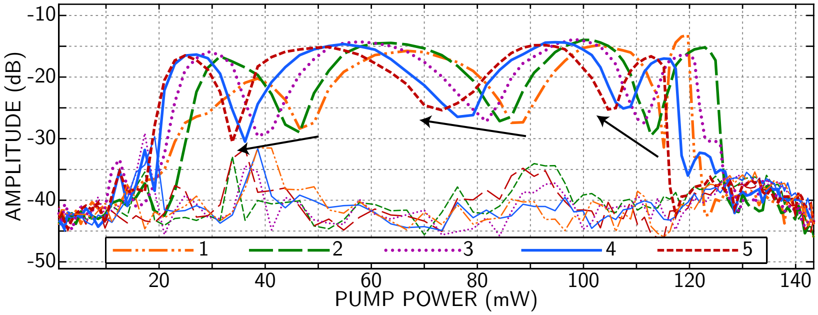

Figure 6.11: Dependence of the amplitude of the photoacoustic signal of the fifth nonlinear right sidelobe ($n = 5$) on the pump power loading the crack at frequency $f_L = 1$ Hz. The pump power increases (thick line) and successively decreases (thin-line). The five successive back and forth of the fifth nonlinear right sidelobe amplitude evolution are presented.

The position of the minima is also observed. Fig. 6.11 is an example on the 5th sidelobe. In each case, the minima are slowly shifting to lower pump power. This can be interpreted as if the crack rigidity in opened state gets softer. Indeed, simulations of the nonlinear sidelobes evolutions demonstrate that for the same pump frequency and crack rigidity in closed state, but two different opened rigidities, the softer crack has its minima before the harder one. As the pump intensity reaches high levels, this could influence the local rigidity of the crack for a certain time, long enough to influence the next increase of the pump power.

When an interval of some tens of hours is present between experiments, the values of the minima are coming back to the original ones. For example, the second sidelobe minimum varies from $P = 61$ mW to 49 mW. After ~30 h, it varies from 61 mW to 47 mW. The evolutions are similar between different sets of experiments. It demonstrates the repeatability of the effect on the minima position.

The theory predicts that the minima differences, between two opened rigidities, are more important when occurring at higher pump powers. However, this does not appears in

Fig. 6.11 or in the other experiments.
When the pump decreases, and when the state 1 is retrieved soon enough to detect minima, the minima also shifts to lower pump powers. They are generally comparable to their position for the pump increase, but some cases exhibit noticeable differences. However, if for both increase and decrease a shift toward lower values is observed, the comparison between the values for an increase and the successive decrease do not present any logic.

It can be concluded that the experiments are repeatable but small differences can be observed such as slow shifts depending on the past excitation of the crack. The qualitative features that are repeatably observed are the main peak drop, the second state of the crack and the presence of minima in the evolution of the nonlinear sidelobes amplitude as a function of the pump power, in the first state of the crack. Only the pump power, to which these features occur, changes.

Influence of the pump power limits

In order to check that the transition between the two states is not due to a long heating process but to a particular power, two experiments are realized. One with the pump power increase and decrease such as previously but with a maximum power at 109 mW, before reaching the second state of the crack and a second one where the pump power is varying between 126 and 143 mW, which should concerns only the second state of the crack.
Both results follow this logic: in the first one the second state is never reached, whereas in the second it immediately is in this state.

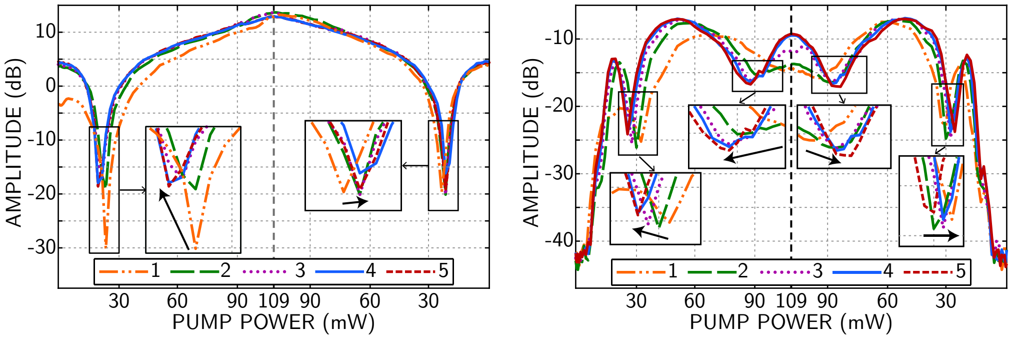

(a) (b)

Figure 6.12: Dependence of the amplitude of the photoacoustic signal of the main peak at f_H (a) and the third left nonlinear sidelobes at $f_H - 3f_L$ (b) on the pump power loading the crack at frequency $f_L = 1$ Hz. The vertical dashed-line separates the increase from the decrease of the pump power.

Results for the main peak and the third sidelobe evolution when the pump increases in the experiment with a reduced maximum power are presented in Fig. 6.12. These experiments were conducted soon after others. As a consequence, the minimum on the main peak is detectable since the first increase (Fig. 6.12(a)). It appears in all the

consecutive experiments. Only the first increase demonstrates a slightly different behavior. Other main peak evolutions are much closer.
The minima of the amplitude sidelobes as a function of the pump power are still shifted toward lower values. So, the effect related to that shift occurs even if the second state is not reached.

For the second experiment, with only important powers, the amplitudes of the nonlinear sidelobes mixed-frequencies are close to previous observations and rather constant. Starting from the second state, nonlinear mixed-frequencies are still generated.

As a conclusion, it is not (only) the presence of the second state of the crack which influences the shifts of the main peak amplitude drop and of the nonlinear sidelobes amplitude minima. However, high powers are required to observe these shifts.

Influence of the pump frequency

The influence of the pump frequency on the minima has already been discussed in Sec. 6.3. In fact, the proposed curves (Fig. 6.5) were part of these experiments, and the part for high pump powers, with the second state, was not presented.
The aim of the change of the pump frequency, from $f_L = 1$ Hz to $f_L = 1.5$ Hz, is to observe the transition between the two states of the crack. It has been demonstrated that it is related to high pump powers. Thus, it should be influenced by the pump frequency: the higher the pump frequency is, the larger the pump power should be to reach the second state. The hysteresis could also be influenced by the change of frequency: the backward transition can be expected to occur for higher pump powers. As a consequence, the transition to the second state should appear for higher power, and the backward transition for higher pump power when frequency increases.

Results of Fig. 6.10(b) are part of these experiments. One can see that the upper transition limit is shifted to higher values: from 100-120 mW to 125-140 mW.

An important difference concerns the hysteresis for the crack transition from state 2 to state 1. For $f_L = 1$ Hz, this transition occurred around 20 mW with a maximum of 34 mW. For $f_L = 1.5$ Hz, it occurs up to 130 mW in some cases. This clearly means that the second state is influenced by the pump frequency.
However, the backward transition evolves in the set of successive experiments. It occurs at $P_L = 57$, 91, 112, 113 and 115 mW respectively for the five experiments in a row. The pump power associated to the transition increases from 57 to 112 mW and remains stable. The same experiment is repeated 30 and then 60 hours after the end of the previous experiment. The transitions occur from 76 to 115 mW in the first case and from 55 to 128 mW in the second case. Thus, this shift is repeatable.
In each case the first value ($\sim$50 mW) is much higher than those encountered for $f_L = 1$ Hz. It may explain why for the case $f_L = 1$ Hz, this shift is not observed.

The change of the pump frequency also affects the position of the amplitude drop in the main peak: it appears for higher powers. With $f_L = 1$ Hz, it occurs around 20 ± 5 mW whereas for $f_L = 1.5$ Hz, it occurs for a power about 35 ± 5 mW, almost twice higher. The shift of the nonlinear sidelobes amplitude minima position is observed, as previously.

The pump frequency appears to influence the pump powers involved in the transition of the crack states and the main peak drop. All phenomena occur for higher pump power. In particular, the hysteresis is importantly reduced. This is coherent with the diminution of the breathing efficiency with the pump frequency increase.

Influence of the location of the beam spots relatively to the crack

Finally, a set of five increases and decreases are realized on the same crack but on a different location. The results are just as the previous exhibited. The first increase is different from the others ones. The values of the transitions, the main peak drop and the evolutions of the minima are different but not the observed phenomena.

6.4.5 Tentative explanation

There are no clear explanations for the observation of the second state of the crack, the main peak amplitude drop, the shifts of this drop and of the nonlinear sidelobe amplitude minima in the first state of the crack, when the pump power increases.
A first hypothesis is that the crack remains closed for the pump powers corresponding to the second state of the crack. This hypothesis has two problems.
Firstly, even if the power is very high, due the 100% modulation and the low frequency (1 Hz), the crack cannot, theoretically, remain closed during the whole period. However, for very high pump powers, the minimum of temperature T_m in the spot area, could be sufficient to close the crack. Then, it would remain closed during the whole pump period. For example, at the maximum pump power ($P = 143$ mW), the minimum of the dynamic temperature in the center of the beam is of $\sim$19 K.
Secondly, if the crack remains closed, the nonlinear frequency-mixing should not be generated, theoretically. This is mainly due to the modeling of the crack by two parallel idealized crack faces. More realistic crack surfaces involve micro- and nano-asperities which can provide contacts between the crack faces and be compressed and modified under the loading. In other words, as the pump loading increases, the crack could be closed but the number and the quality of the contacts could evolve. Consequently, the theory is no longer valid, but nonlinear frequency-mixing generation may be possible due to the evolution of the contacts between the crack faces [64, 66].

Other explanations can be proposed. Local change of the crack properties could explain part of this phenomenon if the temperature increase is locally important enough to modify the crack properties temporarily, as the crack state is restored at the end.
The changes of temperature rise due to the change of frequency cannot directly explain the transition from the first state of the crack to the second one. For $f_L = 1$ Hz, the transitions occur for $P \in [100; 120]$ mW corresponding to temperature rises between 104 and 125 K. For $f_L = 1.5$ Hz, the transitions occur for $P \in [125; 140]$ mW. It corresponds to temperature rises between 128 and 143 K. These temperature rises are higher. The lower limit for $f_L = 1.5$ Hz (128 K) is close to the upper one for $f_L = 1$ Hz (125 K).

The shift of the minima position on the nonlinear sidelobes, or the shift of the main peak amplitude exhibit processes with a slow dynamics of several hours. The presence or not of the main peak amplitude is associated to a process occurring for several tens of hours. These slow dynamic processes could be related to the interface humidity. The samples are in glass, which is known to exhibit capillarity condensation, i.e., to allow the formation of a thin film of water on its interface at the nanoscale [13]. Due to the rugosity and the important surface of the crack, it could be rather difficult to make it evaporate, unless a long and important heating would act. This interface could play an important role on the long relaxation time processes.

Concerning the main peak, the absence of photoacoustic emission is predicted, for a symmetrically heated crack, at the characteristic frequency $\omega = \sqrt{\omega_R \cdot (1/\gamma) \cdot (c/a)}$ where ω_R is the instantaneous mechanical relaxation frequency of the crack, and γ is a nondimensional parameter depending on the shape of the laser beam [20]. It is equal to $1/\sqrt{\pi}$ for a Gaussian distribution. This effect is due to destructive interference of the acoustics waves propagating towards the crack and reflected by the latter in the x direction and those directly propagating in the x direction.

In this work, the rigidity of the crack follows a bistable model considering only two rigidities for the opened and closed states of the crack. In reality, this value evolves as a function of the loading (Fig. 1.7(a), Sec. 1.3.2). Thus, it is possible to have, for a particular loading, the absence of the photoacoustic emission.

For the probe frequency, it follows that the instantaneous crack rigidity of the crack η_R, (associated to the instantaneous crack mechanical relaxation frequency, $\omega_R = 2\eta_R/(\rho c)$) would be, at the main peak drop, of

$$\eta_R = 2\pi^{3/2} \cdot {f_H}^2 \cdot \rho \cdot a \simeq 0.61 \text{ GN.m}^{-3}. \tag{6.8}$$

The opened and closed rigidity, evaluated in Chap. 5, were of 45.1 MN.m^{-3} and 2.3 GN.m^{-3}, respectively. This result is about one order of magnitude larger than the opened rigidity of the crack and closer, but lower than the closed rigidity. This instantaneous mechanical relaxation frequency of the crack corresponds to the mean value over a pump period and for a particular loading. Then, it corresponds to an intermediate value between η_o and η_c. As the experiments are achieved on different glass samples, the results appear consistent. However, depending on the temperature at which the thermal shock occurs -to create the crack-, the structure of the crack is highly different [9]. As the temperature is not controlled, comparison of different crack rigidities needs to be done carefully.

The absence of such effect in the ‘first’ increases could be attributed to the absence of this particular rigidity η_R in the first experiment. Modifications of the rigidity evolution as a function of the loading, due to the second state of the crack or the high pump powers involved, could provide the possibility to reach this particular value in the following increases.

For successive pump power increases, a slight shift of the main peak drop value is observed toward lower values. It indicates that the rigidity η_R is reached for lower pump powers. Thus, this demonstrates a hardening of the crack rigidity as the rigidity increases with the loading (Fig. 1.7). This result is opposed to the conclusion on the shift of the minima.

The latter is attributed to a softening of the crack rigidity. However, both effects are not occurring at the same pump power and are not, consequently, necessarily inconsistent.

It is interesting to evaluate the time required by the plate to cool down to the temperature room via heat conduction and to compare this characteristic time to the one involved in the described phenomena. The heat conduction occurs into air and into the supports of the sample. The sample is heated on the opposite face of the supports, and the latter consist in a several millimeters thick adhesive covering only part of the surface. Because of that, and in order to simplify the problem, only the heat conduction into air is considered. The lumped capacitance method is a simple approach to estimate such times [31]. The essence of this method is the assumption that the temperature of the solid is uniform at any instant. This assumption is clearly in disagreement with the laser heating. It is assumed in the following that the sample is uniformly heated at temperature T_M corresponding to the maximum temperature rise in the center of the irradiated beam. The characteristic time then is not very accurate but still leads to an estimation of the order of magnitude of cooling time once the laser heat stops.
The lumped capacitance method is valid if the Biot number is smaller than 0.1. The Biot number is a dimensionless parameter defined as [31]:

$$Bi = \frac{\text{ﬁ} \cdot L_c}{\kappa}, \tag{6.9}$$

with ﬁ the convection heat transfer coefficient between the sample surface and the air and L_c the characteristic length defined as the ratio of the solid's volume to surface area. The sample used in the experiments can be approximately considered as a cuboid with a length $L_1 = 35$ mm, a height $L_2 = 20$ mm and a depth $h = 3$ mm. The sample is assumed to be in free space that all its surface is in contact with air. The convection heat transfer coefficient between glass and air at 298 K is 10 $\mathrm{W.m^{-2}.K^{-1}}$ [31]. It follows $Bi \simeq 1.2 \cdot 10^{-2}$, which validates the possibility to use the lumped capacitance method -assuming a sample uniformly heated. The time required for the solid to reach some temperature T can be calculated via the following expression:

$$t = \frac{\rho \cdot L_c \cdot c_p}{\text{ﬁ}} \ln \left(\frac{T_M - T_\infty}{T - T_\infty} \right), \tag{6.10}$$

where T_∞ is the temperature of the air. The maximum temperature rise in the center of the beam and for $P = 143$ mW is estimated at 149 K. The room temperature is controlled at 293 K. The time required by the sample to cool down from 442 K to $T = 99\%$ of T_∞ ($\sim$ 290 K) is estimated at $t \simeq 15$ min. This time is not negligible. However, it is several orders of magnitude lower than the characteristic times observed in the experiments (tens of hours), and cannot be the effect responsible for the presence of the main peak amplitude drop in the first increase.

The observed changes in the phenomena at the scale of tens of hours are plausibly associated with the transitions between different state of the crack induced by thermal fluctuations.

Conclusion

It is demonstrated that the monitoring of the amplitude or the phase, via the lock-in amplifier can allow an estimation of the intensity required to close the crack. The value is estimated on the amplitude evolution as a function of the pump loading from the step between the non-clapping to the clapping regime. The phase evolution becomes stable at the same pump loading, corresponding to the generation of the nonlinear sidelobes.

The phase evolution also provides a very accurate mean to detect the amplitude minima detecting abrupt phase changes. The phase evolution does not provide additional information but an alternative and more sensitive possibility to detect the minima.

The influence of the pump frequency on the nonlinear sidelobe evolutions is also studied theoretically and experimentally. The theory predicts that the crack needs to spend a precise amount of time on a whole pump period in the closed state in order for one nonlinear sidelobe to reach a particular minimum. The increase of the pump frequency reduces the crack breathing amplitude (Sec. 3.3). Consequently, for a same duration spent in the closed state, the loading should be more important as the frequency increases. Increase in the pump modulation frequency induces a shift of the minima position towards larger loading. Suppression of a minimum can also appear with the increase of the pump frequency because some time duration over the pump period, in the closed state, are not reachable anymore.

A particular crack, realized similarly as the others, exhibits new phenomena. For low powers, the nonlinear sidelobe evolutions are similar to previous experiments and theoretical predictions. For high powers, another state appears. This state is characterized by an important decrease in the nonlinear mixed-frequencies amplitude and a global monotonous behavior. For a pump loading increase and decrease, a hysteresis is observed in the transition between these states. The crack retrieves the first state at a lower pump power. This observation is repeatable. The transition varies in the experiments. In particular, the change of the pump frequency importantly influences the pump power value associated to the crack state transitions, especially for the transition from this new state to the previous one. A hypothesis is to relate this second state to a crack closed during the whole pump period and to explain the presence of the mixed-frequencies by changes in the crack rigidity -in the closed state- over a pump period.
The main peak evolution has a different behavior too. At a particular pump power, much lower than the crack transition, a sudden drop is observed. This drop is very sharpened and important (∼25 dB). When five experiments are achieved in a row, the pump power associated to this drop softly evolves to lower values. It is demonstrated that this drop is present only if the crack has been heated at important pump powers within the last tens of hours. It is also observed that for an increase of the pump frequency, this value is shifted to higher pump powers. This minimum might be the consequence of a particular crack rigidity. Theory predicts absence of photoacoustic emission for one particular crack rigidity associated to one probe frequency [20]. The shift of the minimum, toward lower pump power values, would indicate a hardening of the crack rigidity.
Finally, the nonlinear sidelobe evolutions, in the first state, are also influenced by

the experiment. The minima location appears to be shifted to lower values when the experiment is repeated several times in a row. Theory could attribute this phenomenon to a softening in the crack rigidity. The minima location shift on the nonlinear sidelobe amplitudes and on the main peak appears for different pump powers and are not necessarily contradictory.

The minima shifts on the main peak and the mixed-frequencies appear restored to their initial values after some hours of pause. At the opposite, the presence of the minima on the main peak disappear after several tens of hours without heating the sample. It demonstrates a very long memory effect on the crack. Yet, there is no clear hypothesis to explain this phenomenon.

An additional effort is required to clearly identify the specific features of the second state of the crack and of the drop of the main peak. It is probable that this work would lead to some new estimations of the crack characteristics.

PART III

DEVELOPMENT OF THE THEORETICAL MODEL

CHAPTER 7

ASSYMETRICAL HEATING

Abstract

The theoretical model developed in [20] provides good estimations in the general case of the evolution of the nonlinear sidelobes. However, it includes an important number of assumptions. In Chap. 5 an evolution of the nonlinear sidelobes amplitude as a function of the loading force has been developed in order to get rid of the assumption $\omega_L \ll \omega_{o,c}$. This improvement allows a better description of the experimental nonlinear sidelobe evolutions as a function of the pump power, but some discrepancies remain. The model requires to be upgraded.

Among the assumptions that are made, the symmetric heating of the crack -where the axis of the laser beams coincide with the plane of the crack- appeared to be a very limiting one. Besides, it has been experimentally demonstrated that it is possible to generate the nonlinear sidelobes with the pump and/or the probe beams which are far from the crack. Then, a first step in the development of the theory is to consider a possible asymmetrical heating. This is the purpose of the present chapter. We show that it influences the generation of nonlinear sidelobes.

7.1 Introduction of the calculation

The asymmetrical heating corresponds to the general case where the axis of the laser beams differs from the plane of the crack. For small asymmetries, the laser beams still irradiates completely the crack but both crack faces do not receive the same amount of energy. For larger asymmetries, the laser beams do not irradiate the crack.

The crack is assumed to be at $x = 0$ and the beam is focused on a spot of a radius a which center is situated in $x = x_0$. A schematic representation of the problem is proposed in Figs 7.1(a) and 7.1(b).

The problem is then separated in two infinite half-spaces delimited by $x = 0$, the position of the crack.

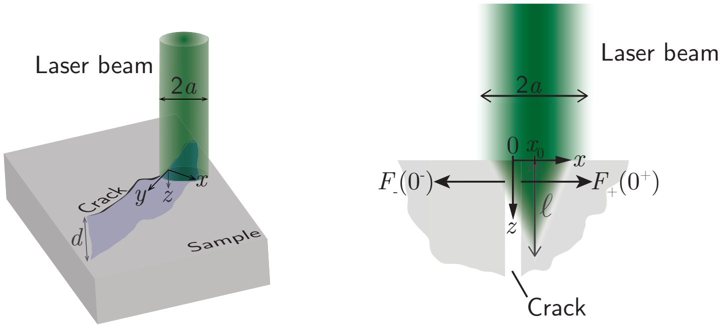

(a) (b)

Figure 7.1: (a): Schematic presentation of the relative positions of the laser beam of radius a, and the crack of the characteristic depth d. (b): Section view presenting the penetration length ℓ, the forces $F_\pm$ for an asymmetrical heating.

The development of the calculation is then identical to the one proposed by V. Gusev and N. Chigarev in [20]. In the following, the subscripts + and − on each parameter refer to this parameter on the half-space with $x \geqslant 0$ and $x \leqslant 0$, respectively. For $x = 0$, the same notation is chosen but with superscripts, as commonly written in mathematics.

7.1.1 Calculation of the displacement

For the asymmetrical heating, the continuity condition for the total stress can be described as previously:

$$\sigma_+(x = 0^+) = -F[u_+(x = 0^+) - u_-(x = 0^-)] = \sigma_-(x = 0^-). \tag{7.1}$$

However, differently from [20], the asymmetry makes the crack face displacements different: $u_+(x = 0^+) \neq -u_-(x = 0^-)$.
In the following, the notation $u_\pm(0^\pm)$, refer to $u_\pm(x = 0^\pm)$.

The equation of motion of an elastic medium, in 1D dimension, in this configuration, is:

$$\rho \frac{\partial^2 u_\pm}{\partial t^2} = \frac{\partial \sigma_\pm}{\partial x}, \tag{7.2}$$

with the stress including the elastic and thermoelastic parts of each half subdomain,

$$\sigma_\pm = \rho c^2 \frac{\partial u_\pm}{\partial x} - K\beta T_\pm. \tag{7.3}$$

Substitution of Eq. (7.3) in Eq. (7.2) provides

$$\frac{\partial^2 u_\pm}{\partial x^2} - \frac{1}{c^2}\frac{\partial^2 u_\pm}{\partial t^2} = \frac{K\beta}{\rho c^2}\frac{\partial T_\pm}{\partial x}, \tag{7.4}$$

and the substitution of Eq. (7.3) in Eq. (7.1) leads to:

$$\frac{\partial u_{\pm}(0^{\pm})}{\partial x} - \frac{K\beta}{\rho c^2} T_{\pm}(0^{\pm}) = -\frac{F[u(0^+) - u(0^-)]}{\rho c^2}. \tag{7.5}$$

To solve the problem (Eqs. (7.4) and (7.5)), a Fourier transform is applied over the time coordinate, as defined previously. For the spatial coordinate, the following transforms are applied: $\widehat{f}_{+}(k) = \int_0^{\infty} f(x) e^{\jmath kx} dx$ and $\widehat{f}_{-}(k) = \int_{-\infty}^{0} f(x) e^{\jmath kx} dx$, for $x \geqslant 0$ and $x \leqslant 0$, respectively. They can be interpreted as a Fourier transform of the function multiplied by an Heaviside function $\mathcal{H}(x)$ or $(1 - \mathcal{H}(x))$, depending if the integration variable is on the positive or negative half-domain. It is also close to the Laplace transform, due to the limits of the integrals. As a consequence of this definition, the first and second differentiation need to be evaluated. The calculation directly leads to the following definitions:

$$\frac{\partial f_{\pm}(x)}{\partial x} = \mp f_{\pm}(0^{\pm}) - \jmath k \widehat{f}_{\pm}(k), \tag{7.6}$$

and

$$\frac{\partial^2 f_{\pm}(x)}{\partial x^2} = \mp \frac{\partial f_{\pm}(0^{\pm})}{\partial x} \pm \jmath k f_{\pm}(0^{\pm}) - k^2 \widehat{f}_{\pm}(k). \tag{7.7}$$

Once these transformations are applied to Eqs. (7.4) and (7.5), it follows:

$$\widehat{u}_{\pm}(\omega, k) = \frac{1}{\left(\frac{\omega}{c}\right)^2 - k^2} \left[\pm \frac{\partial \widetilde{u}_{\pm}(0^{\pm})}{\partial x} \mp \jmath k \widetilde{u}_{\pm}(0^{\pm}) \mp \frac{K\beta}{\rho c^2} \widetilde{T}_{\pm}(\omega, 0^{\pm}) - \frac{K\beta}{\rho c^2} \jmath k \widehat{T}_{\pm}(\omega, k) \right], \tag{7.8}$$

and

$$\frac{\partial \widetilde{u}_{\pm}(\omega, 0^{\pm})}{\partial x} - \frac{K\beta}{\rho c^2} \widetilde{T}_{\pm}(\omega, 0^{\pm}) = -\frac{\widetilde{F}[u(0^+) - u(0^-)]}{\rho c^2}. \tag{7.9}$$

It is then convenient to use Eq. (7.9) into Eq. (7.8), leading to:

$$\widehat{u}_{\pm}(\omega, k) = \frac{1}{\left(\frac{\omega}{c}\right)^2 - k^2} \left[\mp \jmath k \widetilde{u}_{\pm}(0^{\pm}) - \frac{K\beta}{\rho c^2} \jmath k \widehat{T}_{\pm}(\omega, k) \mp \frac{\widetilde{F}[u(0^+) - u(0^-)]}{\rho c^2} \right]. \tag{7.10}$$

Due to the condition of propagation of the acoustic wave from the crack in the positive (negative) direction of the x-axis for the positive (negative) half subdomain, the pole $\pm\omega/c$ needs to be compensated by a zero value on the nominator of $\widehat{u}_{\pm}(\omega, k)$:

$$-\jmath \frac{\omega}{c} \widetilde{u}_{\pm}(0^{\pm}) \mp \frac{K\beta}{\rho c^2} \jmath \frac{\omega}{c} \widehat{T}_{\pm}(\omega, \pm\frac{\omega}{c}) \mp \frac{\widetilde{F}[u(0^+) - u(0^-)]}{\rho c^2} = 0. \tag{7.11}$$

The condition of radiation in Eq. (7.11) can be introduced into Eq. (7.8):

$$\widehat{u}_{\pm}(\omega, k) = \frac{1}{\left(\frac{\omega}{c}\right)^2 - k^2} \left[\frac{K\beta}{\rho c^2} (\jmath k) \left[\widehat{T}_{\pm}(\omega, \pm\frac{\omega}{c}) - \widehat{T}_{\pm}(\omega, k) \right] + \frac{\widetilde{F}[u(0^+) - u(0^-)]}{\rho c} \left[\frac{k}{\omega} \mp \frac{1}{c} \right] \right]. \tag{7.12}$$

The inverse spatial transform , i.e., the Fourier transform in the reciprocal space, can be applied on Eq. (7.12) in order to describe the spectrum of the generated acoustic waves.

It is evaluated by the calculation of the residue in the single pole $\mp\omega/c$.

$$\widetilde{u}_\pm(\omega,x) = \frac{1}{2\pi}\int\limits_{-\infty}^{+\infty} \widehat{u}_\pm(\omega,k)e^{-\jmath kx}dk \tag{7.13}$$

$$= \frac{1}{2\pi}2\jmath\pi\sum_{i=1}^{n}\mathrm{res}\big(\widehat{u}_\pm(\omega,k)e^{-\jmath kx},P_i\big)\mathrm{Ind}\big(\gamma,P_i\big) \tag{7.14}$$

$$= \jmath\cdot\lim_{k\to\mp\frac{\omega}{c}}(k\pm\frac{\omega}{c})\widehat{u}_\pm(\omega,k)e^{-\jmath kx}\cdot\mathrm{Ind}(\gamma,\mp\frac{\omega}{c}), \tag{7.15}$$

where γ is the integral contour and where the winding number Ind is consequently equal to -1 for $x>0$ and $+1$ for $x<0$. It follows:

$$\widetilde{u}_\pm(\omega,x) = \left(\pm\frac{K\beta}{2\rho c^2}\left[\widehat{T}_\pm(\omega,\mp\frac{\omega}{c}) - \widehat{T}_\pm(\omega,\pm\frac{\omega}{c})\right] \mp \frac{1}{\jmath\omega}\frac{\widetilde{F}[u_+(0^+)-u_-(0^-)]}{\rho c}\right)e^{\pm\jmath\frac{\omega}{c}x}. \tag{7.16}$$

If the exponential phase multiplier of Eq. (7.16) is combined in the inverse Fourier transform in the frequency domain, it allows to describe the acoustic wave as a function of the the retarded time $\tau_\pm$. The acoustic strain is defined by $U=\partial u/\partial x$, thus:

$$U_\pm(t,x) = \frac{1}{2\pi}\int\limits_{-\infty}^{\infty}\widetilde{U}_\pm(\omega,x)e^{-\jmath\omega t}d\omega, \tag{7.17a}$$

$$= \frac{1}{2\pi}\int\limits_{-\infty}^{\infty}\left(\frac{K\beta}{2\rho c^3}(\jmath\omega)\left[\widehat{T}_\pm(\omega,\mp\frac{\omega}{c}) - T_\pm(\omega,\pm\frac{\omega}{c})\right] - \frac{\widetilde{F}[u_+(0^+)-u_-(0^-)]}{\rho c^2}\right)e^{\pm\jmath\frac{\omega}{c}x-\jmath\omega t}d\omega. \tag{7.17b}$$

Defining $\tau_\pm = t\mp x/c$, leads to the strain spectrum description:

$$U_\pm(\tau_\pm) = \frac{1}{2\pi}\int\limits_{-\infty}^{\infty}\widetilde{U}_\pm(\omega)e^{-\jmath\omega\tau_\pm}d\omega, \tag{7.17c}$$

with,

$$\widetilde{U}_\pm(\omega) = \frac{K\beta}{2\rho c^3}(\jmath\omega)\left[\widehat{T}_\pm(\omega,\mp\frac{\omega}{c}) - T_\pm(\omega,\pm\frac{\omega}{c})\right] - \frac{\widetilde{F}[u_+(0^+)-u_-(0^-)]}{\rho c^2}. \tag{7.17d}$$

The first two terms correspond to the definition of an acoustic strain near a mechanically free surface. The last term, proportional to the force F describe the effect of the crack faces motion on the acoustic strain.

7.1.2 Determination of the temperature field

It now appears that the temperature distribution needs to be estimated. Because of the asymmetry of the heating, the temperature rise on each part of the crack faces is different.

Thus, the thermal resistance of the crack needs to be taken into account. The thermal flux and thermal resistance at the crack can be defined as:

$$Q(0^+) = \kappa \frac{\partial \widetilde{T}_+(\omega, 0^+)}{\partial x} = \kappa \frac{\partial \widetilde{T}_-(\omega, 0^-)}{\partial x} = Q(0^-), \tag{7.18a}$$

$$R = \frac{\widetilde{T}_+(\omega, 0^+) - \widetilde{T}_-(\omega, 0^-)}{Q(0^+)}. \tag{7.18b}$$

The 1D heat equation remains as previously defined (Chap. 1), but with a spatial distribution of laser heating centered at $x - x_0$:

$$\frac{\partial T}{\partial t} + \omega_T T = \chi \frac{\partial^2 T}{\partial x^2} + \frac{I}{\ell \rho c_p} f(t) \Psi(x - x_0), \tag{7.19}$$

where ω_T is determined as in Chap. 5 (Sec. 5.2.2).
It logically follows that the spatial distribution is defined in the positive (negative) half subdomain as: $\widehat{\Psi}_+(k, x_0) = \int_0^\infty \Psi(x - x_0) e^{\jmath kx} dx$ (and $\widehat{\Psi}_-(k, x_0) = \int_{-\infty}^0 \Psi(x - x_0) e^{\jmath kx} dx$). After these transforms, Eq. (7.19) becomes:

$$\widehat{T}_\pm(\omega, k) = \frac{1}{k^2 - {k_T}^2} \cdot \left[\mp \frac{\partial \widetilde{T}_\pm(\omega, 0^\pm)}{\partial x} \pm \jmath k \widetilde{T}_\pm(\omega, 0^\pm) + \frac{I}{\ell \kappa} \widetilde{f}(\omega) \widehat{\Psi}_\pm(k, x_0) \right]. \tag{7.20}$$

with $k_T = \sqrt{(\jmath\omega - \omega_T)/\chi}$, ($\Re e(k_T) \geqslant 0$) the thermal wave number. Using Eqs. (7.18a) and (7.18b) with Eq. (7.20) leads to:

$$\widehat{T}_\pm(\omega, k) = \frac{1}{k^2 - {k_T}^2} \cdot \left[\widetilde{T}_\pm(\omega, 0^\pm) \left(\pm \jmath k - \frac{1}{\kappa R} \right) + \frac{\widetilde{T}_\mp(\omega, 0^\mp)}{\kappa R} + \frac{I}{\ell \kappa} \widetilde{f}(\omega) \widehat{\Psi}_\pm(k, x_0) \right]. \tag{7.21}$$

Similarly to the earlier evaluation of the mechanical displacement, the pole ($\pm k_T$) needs to be compensated by the zero of the numerator to avoid divergence:

$$\widetilde{T}_\pm(\omega, 0^\pm) \left(\jmath k_T - \frac{1}{\kappa R} \right) + \frac{\widetilde{T}_\mp(\omega, 0^\mp)}{\kappa R} + \frac{I}{\ell \kappa} \widetilde{f}(\omega) \widehat{\Psi}_\pm(\pm k_T, x_0) = 0. \tag{7.22}$$

Addition and subtraction of the temperatures in the positive and negative domains from Eq. (7.22) provides the temperatures at $x = 0^+$ and $x = 0^-$:

$$\begin{aligned} \widetilde{T}_\pm(\omega, 0^\pm) = -\frac{I}{2\ell} \Bigg(& \left[\frac{1}{\jmath \kappa k_T} \mp \frac{R}{2 - \jmath \kappa k_T R} \right] \widehat{\Psi}_+(k_T, x_0) + \\ & + \left[\frac{1}{\jmath \kappa k_T} \pm \frac{R}{2 - \jmath \kappa k_T R} \right] \widehat{\Psi}_-(-k_T, x_0) \Bigg) \cdot \widetilde{f}(\omega). \end{aligned} \tag{7.23}$$

Finally, using Eq. (7.23) into Eq. (7.21) leads to:

$$\begin{aligned}\widehat{T}_{\pm}(\omega,k) = \frac{\pm 1}{k^2-{k_T}^2}\cdot\frac{I}{2\ell\kappa}\cdot\widetilde{f}(\omega)\cdot\Bigg[&\left(\frac{-k}{k_T}-\frac{2\mp\jmath k\kappa R}{2-\jmath k_T\kappa R}\right)\widehat{\Psi}_{+}(k_T,x_0)+\\ &+\left(\frac{-k}{k_T}+\frac{2\mp\jmath k\kappa R}{2-\jmath k_T\kappa R}\right)\widehat{\Psi}_{-}(-k_T,x_0)\pm 2\widehat{\Psi}_{\pm}(k,x_0)\Bigg], \qquad (7.24\text{a})\end{aligned}$$

$$\equiv \widehat{\theta}_{\pm}(\omega,k)\cdot I\cdot\widetilde{f}(\omega). \qquad (7.24\text{b})$$

For a given model of the force F, this solution, together with Eq. (7.11), provides the possibility to determine the variations in the crack width. With Eq. (7.17d), it is also possible to obtain the solution of the emitted acoustic field. Eq. (7.24a) can be rewritten:

$$\begin{aligned}\widehat{T}_{\pm}(\omega,k) = \frac{\pm 1}{k^2-{k_T}^2}\frac{I}{2\ell\kappa}\widetilde{f}(\omega)\times&\\ \times\Bigg[\overbrace{\frac{\text{-}k}{k_T}\Big(\widehat{\Psi}_{+}(k_T,x_0)+\widehat{\Psi}_{-}(-k_T,x_0)\Big)-\Big(\widehat{\Psi}_{+}(k_T,x_0)-\widehat{\Psi}_{-}(-k_T,x_0)\Big)\pm 2\widehat{\Psi}_{\pm}(k,x_0)}^{\widehat{T}_{0\pm}}&+\\ \underbrace{-\frac{\jmath\,(k_T\mp k)\,\bar{R}}{1-\jmath k_T\bar{R}}\Big[\widehat{\Psi}_{+}(k_T,x_0)-\widehat{\Psi}_{-}(-k_T,x_0)\Big]}_{\widehat{T}_{R\pm}}&\Bigg], \qquad (7.24\text{c})\end{aligned}$$

with $\bar{R}=\kappa R/2$. This reformulation is particularly interesting because it demonstrates that the temperature can be separated in two parts. The first part, independent of the thermal resistance R, ($\widehat{T}_{0\pm}$) corresponds to the part of the laser excitation that cannot be modulated by thermal resistance variations. The second part ($\widehat{T}_{R\pm}$) depends on $\bar{R}$ which is proportional to the thermal resistance. The thermal resistance can be modified because of the asymmetry of the heating (Eq. (7.18b)). Then, this second part of the equation corresponds to the part of the temperature field that could be modulated by variation of the thermal resistance.

It can be observed from Eq. (7.24c) that the temperature changes induced by modulation of the thermal resistance are of opposite sign on the different sides of the crack.

From Eq. (7.11), it follows that two phenomena can be responsible for the nonlinear sidelobe generation: the evolution of the loading force F which modulates the crack rigidity and the crack thermal resistance. These two phenomena are independently considered (Sec. 7.3 and Sec. 7.4) and the effect of double modulation is then studied (Sec. 7.5).

7.2 Acoustic harmonics generation

For a monochromatic modulation of the laser intensity in time, $f(t) = [1 + \text{ш}\cos(\omega_o t)]/2$, the higher harmonics are still predicted as in [20]. Indeed, such modulation has the following spectrum envelope in the Fourier domain: $\widetilde{f}(\omega) =$

$\pi\left(\delta(0) + \text{ш}/2 \cdot [\delta(\omega-\omega_0)+\delta(\omega+\omega_0)]\right)$. Then, Eq. (7.11) can be modified with the use of Eq. (7.24b) and introducing this monochromatic modulation excitation:

$$-\jmath\omega\widetilde{u}_{\pm}(0^{\pm}) \mp \frac{\widetilde{F}[u(0^{+})-u(0^{-})]}{\rho c} = -|A_{1\pm}(\omega)|e^{\jmath\varphi_{1\pm}(\omega)}\pi I\text{ш}\left[\delta(\omega-\omega_0)+\delta(\omega+\omega_0)\right], \tag{7.25}$$

where $A_{1\pm}(\omega) = |A_{1\pm}(\omega)|e^{\jmath\varphi_{1\pm}(\omega)} = \mp(\jmath\omega)\cdot[K\beta/(2\rho c^2)]\cdot\widehat{\theta}_{\pm}(\omega,\pm\omega/c)$. As in [20], the term of the constant heating, proportional to $\delta(0)$ does not affect the system. This is due to the assumption of unrestricted sample, and, consequently, of the easy unrestricted expansion at $x=\pm\infty$.

If we apply an inverse Fourier transform on Eq. (7.25), the following equation is obtained:

$$\frac{\partial u_{\pm}(0^{\pm})}{\partial t} \mp \frac{F[u(0^{+})-u(0^{-})]}{\rho c} = -|A_{1\pm}(\omega_0)|I\text{ш}\cos\left(\omega_0 t-\varphi_{1\pm}(\omega_0)\right), \tag{7.26}$$

which, as previously said in [20], takes the form of the equation for a forced relaxator. It describes a lot of the experiments on the interaction of powerful acoustic waves with nonlinear cracks or nonlinear interfaces [26]. The method proposed here, however, involves two lasers, intensity modulated at different frequencies, to generate the acoustic mixed-frequencies.

7.3 Acoustic frequency-mixing process induced by crack rigidity modulations

For the case of two different monochromatic intensity modulations, for $I\cdot f(t) = I_L[1+\text{ш}_L\cos(\omega_L t)]/2 + I_H[1+\text{ш}_H\cos(\omega_H t-\varphi_{HL})]/2$, Eq. (7.26) can be logically written:

$$\begin{aligned}\frac{\partial u_{\pm}(0^{\pm})}{\partial t} \mp \frac{F[u_{+}(0^{+})-u_{-}(0^{-})]}{\rho c} &= -|A_{1\pm}(\omega_L)|I_L\text{ш}_L\cos\left(\omega_L t-\varphi_{1\pm}(\omega_L)\right)+\\ &\quad -|A_{1\pm}(\omega_H)|I_H\text{ш}_H\cos\left(\omega_H t-\varphi_{1\pm}(\omega_H)-\varphi_{HL}\right).\end{aligned} \tag{7.27}$$

In the absence of the high-frequency excitation ($\text{ш}_H=0$), it follows:

$$\frac{\partial u_{L\pm}(0^{\pm})}{\partial t} \mp \frac{F[u_{L+}(0^{+})-u_{L-}(0^{-})]}{\rho c} = -|A_{1\pm}(\omega_L)|I_L\text{ш}_L\cos\left(\omega_L t-\varphi_{1\pm}(\omega_L)\right), \tag{7.28}$$

where $u_{L\pm}(0^{\pm})$ corresponds to the displacement induced by the pump loading.

If the high-frequency excitation has a weak influence on the crack motion in comparison to the low-frequency excitation, which corresponds mathematically to $|A_{\pm}(\omega_H)|I_H\text{ш}_H \ll |A_{\pm}(\omega_L)|I_L\text{ш}_L$, then, in Eq. (7.27), the force can be developed in the Taylor series:

$$F[u(0^{+})-u(0^{-})] = F[u_{L+}(0^{+})-u_{L-}(0^{-})]+\frac{\partial F[u_{L+}(0^{+})-u_{L-}(0^{-})]}{\partial[u_{+}(0^{+})-u_{-}(0^{-})]}\cdot[u_{H+}(0^{+})-u_{H-}(0^{-})]+\ldots, \tag{7.29}$$

where $u_{H\pm}(0^{\pm})$ corresponds to the displacement induced by the probe loading.

Then, the difference between Eq. (7.27) and Eq. (7.28), with the use of Eq. (7.29), -where the development is limited to the first order- leads to:

$$\frac{\partial u_{H\pm}(0^{\pm})}{\partial t} \mp \frac{1}{\rho c}\left(\frac{\partial F[u_{L+}(0^{+}) - u_{L-}(0^{-})]}{\partial\left[u_{+}(0^{+}) - u_{-}(0^{-})\right]]} \cdot \left[u_{H+}(0^{+}) - u_{H-}(0^{-})\right]\right) = \\ - |A_{1\pm}(\omega_H)| I_H \text{ш}_H \cos\left(\omega_H t - \varphi_{1\pm}(\omega_H) - \varphi_{HL}\right). \quad (7.30)$$

The term $\partial F[u_{L+}(0^{+}) - u_{L-}(0^{-})]/\partial\left[u_{+}(0^{+}) - u_{-}(0^{-})\right]]$ has the physical sense of the instantaneous value of crack rigidity and is defined to be equal to $\eta\left[u_{L+}(0^{+}) - u_{L-}(0^{-})\right]$. Identically to [20], the coefficient $\omega_R \equiv \eta/(\rho c) \cdot \left[u_{L+}(0^{+}) - u_{L-}(0^{-})\right]$, corresponding to the instantaneous mechanical relaxation frequency of the crack, is also introduced. With Eq. (7.28), the crack width variations $(u_{L+}(0^{+}) - u_{L-}(0^{-}))$ can be determined. Then, Eq. (7.30) can be solved to find the signal at the frequencies $\omega_H \pm n\omega_L$. In accordance to Eq. (7.29), the term $F[u_{L+}(0^{+}) - u_{L-}(0^{-})]$, obtained from Eq. (7.28) describes the contribution to the acoustic strain signal (Eq. (7.17d)) at ω_L and its harmonics $n\omega_L$. Conversely, the term $(\partial F[u_{L+}(0^{+}) - u_{L-}(0^{-})]/\partial[u_{+}(0^{+}) - u_{-}(0^{-})]])$, derived from Eq. (7.30), describes the acoustic strain signal (Eq. (7.17d)) contribution at ω_L and the mixed frequencies $\omega_H \pm n\omega_L$.

7.3.1 Spectral transformation function of photoacoustic conversion

Assuming a linear interaction force between the crack faces, the boundary condition of the stress at $x = 0$ becomes:

$$F[u_{+}(0^{+}) - u_{-}(0^{+})] = -\frac{\eta}{2}\left[u_{+}(0^{+}) - u_{-}(0^{-})\right]. \quad (7.31)$$

In the frequency domain, it takes the form:

$$-\frac{\widetilde{F}\left[u_{+}(0^{+}) - u_{-}(0^{-})\right]}{\rho c} = \frac{\omega_R}{2}\left[\widetilde{u}_{+}(0^{+}) - \widetilde{u}_{-}(0^{-})\right]. \quad (7.32)$$

Consequently, Eq. (7.32) and Eq. (7.9) lead to:

$$\frac{\partial \widetilde{u}_{\pm}(\omega, 0^{\pm})}{\partial x} - \frac{K\beta}{\rho c^2}\widetilde{T}_{\pm}(\omega, 0^{\pm}) = \frac{\omega_R}{2c}\left[\widetilde{u}_{+}(0^{+}) - \widetilde{u}_{-}(0^{-})\right], \quad (7.33)$$

and then, Eq. (7.8) can be simplified to the following form,

$$\widehat{u}_{\pm}(\omega, k) = \frac{1}{\left(\frac{\omega}{c}\right)^2 - k^2}\left[\left(\frac{\omega_R}{2c} \mp \jmath k\right)\widetilde{u}_{\pm}(\omega, 0^{\pm}) - \frac{\omega_R}{2c}\widetilde{u}_{\mp}(\omega, 0^{\mp}) - \frac{K\beta}{\rho c^2} \cdot (\jmath k) \cdot \widehat{T}_{\pm}(\omega, k)\right]. \quad (7.34)$$

As previously, the condition of radiation in the positive (negative) half space leads to the compensation by the numerator of the pole $\pm\omega/c$ for $\widehat{u}_{\pm}(\omega, k)$. Then adding up and subtracting the equations on the positive and negative subdomains leads to:

$$\widetilde{u}_{\pm}(\omega, 0^{\pm}) = \frac{K\beta}{2\rho c^2} \cdot \left[\frac{\mp(\omega_R - 2\jmath\omega)}{\omega_R - \jmath\omega}\widehat{T}_{\pm}\left(\omega, \pm\frac{\omega}{c}\right) \pm \frac{\omega_R}{\omega_R - \jmath\omega}\widehat{T}_{\mp}\left(\omega, \mp\frac{\omega}{c}\right)\right]. \quad (7.35)$$

Eq. (7.35) gives the opportunity to rewrite Eq. (7.34) in order to have the mechanical displacement (in the Fourier-Fourier domain) as a function of the temperature only:

$$\begin{aligned}\widehat{u}_{\pm}(\omega,k) = \frac{1}{\left(\frac{\omega}{c}\right)^2 - k^2}\cdot\frac{K\beta}{2\rho c^2}\cdot\Bigg[&\frac{2\omega k + \jmath\omega_R\left(k \pm \frac{\omega}{c}\right)}{\omega_R - \jmath\omega}\widehat{T}_{\pm}\left(\omega, \pm\frac{\omega}{c}\right) + \\ &- \frac{\jmath\omega_R\left(k \mp \frac{\omega}{c}\right)}{\omega_R - \jmath\omega}\widehat{T}_{\mp}\left(\omega, \mp\frac{\omega}{c}\right) - 2\jmath k\widehat{T}_{\pm}(\omega,k)\Bigg]. \quad (7.36)\end{aligned}$$

Then, the Fourier transform in reciprocal space can be applied, as previously, with the calculation of the residue. The acoustic strain spectrum reads:

$$\widetilde{U}_{\pm}(\omega) = \frac{K\beta}{2\rho c^3}\cdot(\jmath\omega)\cdot\left[\widehat{T}_{\pm}\left(\omega,\mp\frac{\omega}{c}\right) + \frac{\jmath\omega}{\omega_R - \jmath\omega}\widehat{T}_{\pm}\left(\omega,\pm\frac{\omega}{c}\right) + \frac{\omega_R}{\omega_R - \jmath\omega}\widehat{T}_{\mp}\left(\omega,\mp\frac{\omega}{c}\right)\right], \quad (7.37a)$$

or, replacing the temperature by a function of the spatial distribution of the excitation laser (Eq. (7.24a)):

$$\begin{aligned}\widetilde{U}_{\pm}(\omega,k) = \frac{K\beta}{2\rho c^3}\cdot(\jmath\omega)\cdot\frac{I}{\ell\kappa}\cdot\widetilde{f}(\omega)\cdot\frac{1}{\left(\frac{\omega}{c}\right)^2 - {k_T}^2}\cdot\Bigg[&\left[\frac{-\jmath\omega^2}{ck_T(\omega_R - \jmath\omega)} \mp \frac{\jmath\frac{\omega}{c}\kappa R}{2 - \jmath k_T\kappa R}\right]\widehat{\Psi}_{+}(k_T,x_0) + \\ + \left[\frac{-\jmath\omega^2}{ck_T(\omega_R - \jmath\omega)} \pm \frac{\jmath\frac{\omega}{c}\kappa R}{2 - \jmath k_T\kappa R}\right]&\widehat{\Psi}_{-}(-k_T,x_0) + \widehat{\Psi}_{\pm}\left(\mp\frac{\omega}{c},x_0\right) + \\ &+ \frac{\jmath\omega}{\omega_R - \jmath\omega}\widehat{\Psi}_{\pm}\left(\frac{\pm\omega}{c},x_0\right) + \frac{\omega_R}{\omega_R - \jmath\omega}\widehat{\Psi}_{\mp}\left(\mp\frac{\omega}{c},x_0\right)\Bigg]. \quad (7.37b)\end{aligned}$$

Eq. (7.37a) can be physically interpreted. The term proportional to $\widehat{T}_{\pm}\left(\omega,\mp\frac{\omega}{c}\right)$ corresponds to the strain contribution of the acoustic waves generated in the domain ± and propagating in the direction ± along the axes, i.e., generated in one subdomain and propagated away from the crack. For example, $\widehat{T}_{+}\left(\omega,-\frac{\omega}{c}\right)$ deals with the acoustic waves, generated in the positive domain, and propagating in the direction of the increasing positive x.
The second term, proportional to $\widehat{T}_{\pm}\left(\omega,\pm\frac{\omega}{c}\right)$, concerns the acoustic waves generated in the same subdomain but propagating toward the crack and then reflected by the latter. Finally, the term proportional to $\widehat{T}_{\mp}\left(\omega,\mp\frac{\omega}{c}\right)$ corresponds to the strain contribution of the acoustic waves generated in one domain, propagating in the direction of the crack and being transmitted in the other domain.

In the case where the thermal wavelength at the high-frequency modulation is significantly shorter than the laser beam radius which, in its turn, is significantly shorter than the acoustic wavelength of the high-frequency modulation, and in the case of a small asymmetrical heating, Eq. (7.37b) can be simplified. Mathematically, it corresponds to $(\omega/c) \ll (1/a) \ll |k_T(\omega)|$, so that sound generation region can be considered thermally thick but acoustically thin. For the typical range of experimental values, $\omega_H = 2\pi\cdot 50$ kHz and $a = 100$ µm, and for the glass parameters, it leads to the inequality $50 \ll 10^4 \ll 8\cdot 10^5$ which is fulfilled. Note that, that a focusing around 1 µm, possible experimentally, would require to increase the frequency of the excitation in order to maintain such inequality valid. Under these assumptions, it is possible to demonstrate that the spatial distributions can be rewritten:

$$\widehat{\Psi}_\pm(\pm k_T, x_0) \simeq 0, \tag{7.38a}$$

$$\widehat{\Psi}_+\left(\pm\frac{\omega}{c}, x_0\right) \simeq \widehat{\Psi}_+(0,x_0)\left[1 \pm \jmath\frac{\omega}{c}(x_0 + a\gamma_+)\right], \tag{7.38b}$$

$$\widehat{\Psi}_-\left(\pm\frac{\omega}{c}, x_0\right) \simeq \widehat{\Psi}_-(0,x_0)\left[1 \pm \jmath\frac{\omega}{c}(x_0 + a\gamma_-)\right], \tag{7.38c}$$

where

$$\gamma_+ = \frac{\int\limits_{-x_0/a}^{\infty} \xi\Psi(a\xi)d\xi}{\int\limits_{-x_0/a}^{\infty} \Psi(a\xi)d\xi}, \text{ and } \quad \gamma_- = \frac{\int\limits_{-\infty}^{-x_0/a} \xi\Psi(a\xi)d\xi}{\int\limits_{-\infty}^{-x_0/a} \Psi(a\xi)d\xi}.$$

If we implement these simplifications into Eq. (7.37b) and, also considering the inequality $\omega_T \ll \omega$, fulfilled experimentally too ($10 \ll 50 \cdot 10^3$), it follows:

$$\begin{aligned}\widetilde{U}_\pm(\omega) = \frac{-K\beta I}{2\ell\rho^2c^3c_p} \cdot \widetilde{f}(\omega) \cdot \Bigg[\left(\frac{\omega_R \mp \jmath\frac{\omega}{c}(x_0 + a\gamma_\pm)(\omega_R - 2\jmath\omega)}{\omega_R - \jmath\omega}\right)\widehat{\Psi}_\pm(0,x_0) + \\ + \left(\frac{\omega_R \mp \jmath\frac{\omega\omega_R}{c}(x_0 + a\gamma_\mp)}{\omega_R - \jmath\omega}\right)\widehat{\Psi}_\mp(0,x_0)\Bigg].\end{aligned} \tag{7.39}$$

Eq. (7.39) can be rewritten:

$$\begin{aligned}\widetilde{U}_\pm(\omega) &= \frac{-K\beta I}{2\ell\rho^2c^3c_p} \cdot \widetilde{f}(\omega) \times \\ &\times \underbrace{\left(\frac{\omega_R \mp \jmath\frac{\omega}{c}(x_0 + a\gamma_\pm)(\omega_R - 2\jmath\omega) + J\left[\omega_R \mp \jmath\frac{\omega\omega_R}{c}(x_0 + a\gamma_\mp)\right]}{\omega_R - \jmath\omega}\right)}_{V} \cdot\widehat{\Psi}_\pm(0,x_0),\end{aligned} \tag{7.40}$$

where

$$J = \frac{\widehat{\Psi}_\mp(0,x_0)}{\widehat{\Psi}_\pm(0,x_0)} = \frac{\int\limits_{-\infty}^{-x_0} \Psi(x)dx}{\int\limits_{-x_0}^{\infty} \Psi(x)dx}.$$

It appears that the frequencies introduced into the mechanical system by laser intensity modulation spectrum $\widetilde{f}(\omega)$ are, in the spectral domain, functions of a frequency-dependent complex multiplier proportional to V. Besides, the term V is influenced by the asymmetry of the heating. It then follows that the spectral transformation function of the optoacoustic conversion, in the frequency domain, is proportional to:

$$\widetilde{S}(\omega) \propto -\frac{1 \mp \jmath\frac{\omega}{c}(x_0 + a\gamma_\pm)(1 - \jmath\frac{2\omega}{\omega_R}) + J\left[1 \mp \jmath\frac{\omega}{c}(x_0 + a\gamma_\mp)\right]}{1 - \jmath\omega/\omega_R}, \tag{7.41a}$$

$$\left|\widetilde{S}(\omega)\right| \propto -\frac{\sqrt{\left(1 \mp \frac{2\omega^2}{\omega_R c}(x_0 + a\gamma_\pm) + J\right)^2 + \left(\frac{\omega x_0}{c}(1+J) + \frac{a\omega}{c}(\gamma_\pm + J\gamma_\mp)\right)^2}}{\sqrt{1+(\omega/\omega_R)^2}}, \qquad (7.41\text{b})$$

It is possible to demonstrate that for a particular frequency, influenced by the asymmetry and the crack instantaneous rigidity, the numerator of Eq. (7.41b) can be null. At this frequency, the absence of photoacoustic emission is predicted. This corresponds to destructive interferences between the different acoustic waves. Because of the nonzero frequency-dependent phase shift from the crack, the acoustic waves propagating through the crack, and the one reflected by the crack have a phase change in comparison to the acoustic waves propagating away from the crack. For this particular frequency, this phase shift provokes the destructive interferences.

7.3.2 Parametric frequency-mixing

It is interesting to go back to Eq. (7.37a) and to rewrite it differently in order to separate the part describing the sound generation depending on the crack rigidity, responsible for the frequency-mixing (denoted $\widetilde{U}_{\eta\pm}$ in Eq. (7.42) and in the following). The other part is similar to sound generation near a free surface (denoted $\widetilde{U}_{0\pm}$ in Eq. (7.42)):

$$\widetilde{U}_\pm(\omega) = \frac{K\beta}{2\rho c^3}(\jmath\omega)\Bigg[\underbrace{\widehat{T}_\pm\left(\omega, \mp\frac{\omega}{c}\right) - \widehat{T}_\pm\left(\omega, \pm\frac{\omega}{c}\right)}_{\widetilde{U}_{0\pm}} + \underbrace{\frac{\omega_R}{\omega_R - \jmath\omega}\left(\widehat{T}_\pm\left(\omega, \pm\frac{\omega}{c}\right) + \widehat{T}_\mp\left(\omega, \mp\frac{\omega}{c}\right)\right)}_{\widetilde{U}_{\eta\pm}}\Bigg]. \qquad (7.42)$$

Only the term $\widetilde{U}_{\eta\pm}$ is next analyzed. Eq. (7.42) demonstrates that rigidity modulations act on the sum of the temperature rises at both sides of the crack. Using Eq. (7.24b) in order to develop the temperature function it is possible to rewrite $\widetilde{U}_{\eta\pm}$:

$$\widetilde{U}_{\eta\pm}(\omega) = \mp\frac{K\beta}{2\rho c^3}\cdot(\jmath\omega)\cdot\frac{\omega_R}{\omega_R - \jmath\omega}\cdot I\cdot\widetilde{f}(\omega)\cdot\left[\widehat{\theta}_\pm(\omega, \pm\frac{\omega}{c}) + \widehat{\theta}_\mp(\omega, \mp\frac{\omega}{c})\right]. \qquad (7.43)$$

It can be easily demonstrated that $\widehat{T}_\pm(\omega, \pm\omega/c) \neq \pm\widehat{T}_\mp(\omega, \mp\omega/c)$ in the case of an asymmetric heating. This implies the same inequality on $\widehat{\theta}$. In the case of a monochromatic laser intensity modulation at ω_H, so, for $I\cdot f(t) = I_H[1 + \text{ш}_H\cos(\omega_H t - \phi_{HL})]/2$, it leads to:

$$\begin{aligned}\widetilde{U}_{\eta\pm}(\omega) = \mp\frac{1}{2c}\cdot\frac{\omega_R}{\omega_R - \jmath\omega}\cdot\pi\cdot I_H\cdot\text{ш}_H\cdot[A_{1\pm}(\omega) + A_{2\pm}(\omega)] \times \\ \times\left[\delta(\omega - \omega_H)e^{\jmath\varphi_{HL}} + \delta(\omega + \omega_H)e^{-\jmath\varphi_{HL}}\right],\end{aligned} \qquad (7.44)$$

with $A_{2\pm}(\omega) = |A_{2\pm}(\omega)|e^{\jmath\varphi_{2\pm}(\omega)} = \mp(\jmath\omega)\cdot[K\beta/(2\rho c^2)]\cdot\widehat{\theta}_\mp(\omega, \mp\omega/c)$.
It is possible to repeat the procedure and to apply an inverse Fourier transform over the frequency in order to estimate $\widetilde{U}_{\eta\pm}(\tau_\pm)$. Note that $\omega_R/(\omega_R - \jmath\omega)$ is replaced by

$\omega_R/\sqrt{{\omega_R}^2+\omega^2}\cdot e^{\jmath\,\mathrm{atan}(\omega/\omega_R)}$. The acoustic strain solution, in the time domain, is:

$$\begin{aligned} U_{\eta\pm}(\tau_\pm) = \frac{\mp 1}{2c}\cdot\frac{\omega_R}{\sqrt{{\omega_R}^2+{\omega_H}^2}}\cdot I_H\text{ш}_H\Bigg[&|A_{1\pm}(\omega_H)|\cos\left(\omega_H\tau_\pm-\varphi_{1\pm}(\omega_H)-\mathrm{atan}\left(\frac{\omega_H}{\omega_R}\right)+\right.\\ &\left.-\varphi_{HL}\right)+|A_{2\pm}(\omega_H)|\cos\left(\omega_H\tau_\pm-\varphi_{2\pm}(\omega_H)-\mathrm{atan}\left(\frac{\omega_H}{\omega_R}\right)-\varphi_{HL}\right)\Bigg], \end{aligned} \tag{7.45a}$$

$$\begin{aligned} U_{\eta\pm}(\tau_\pm) = \frac{\mp 1}{2c}\cdot\frac{\omega_R}{\sqrt{{\omega_R}^2+{\omega_H}^2}}\cdot I_H\text{ш}_H\times&\\ \times\sum_{i=1}^{2}|A_{i\pm}(\omega_H)|\cos&\left[\omega_H\tau_\pm-\varphi_{i\pm}(\omega_H)-\mathrm{atan}\left(\frac{\omega_H}{\omega_R}\right)-\varphi_{HL}\right], \end{aligned} \tag{7.45b}$$

which can also be written in the following form,

$$U_{\eta\pm}(\tau_\pm) = \frac{\mp 1}{2c}\cdot I_H\text{ш}_H\sum_{i=1}^{2}|A_{i\pm}(\omega_H)|\,\Re\mathrm{e}\left[\frac{\omega_R}{\omega_R-\jmath\omega_H}e^{\jmath(\omega_H\tau_\pm-\varphi_{i\pm}(\omega_H)-\varphi_{HL})}\right]. \tag{7.45c}$$

The model of the force F is now required to evaluate ω_R as a function of the loading, and thus, the evolution of the amplitude and the phase. The same rigidity model as in [20] is taken in this calculation:

$$F[u_+(0^+)-u_-(0^-)] = \begin{cases} -\eta_o[u_+(0^+)-u_-(0^-)-h_o] & \text{if } h_i\leqslant u_+(0^+)-u_-(0^-)\leqslant\infty,\\ -\eta_c[u_+(0^+)-u_-(0^-)-h_c] & \text{if } 0\leqslant u_+(0^+)-u_-(0^-)\leqslant h_i. \end{cases} \tag{7.46}$$

Following that model, the term depending on the crack rigidity in Eq. (7.45c), $\omega_R/(\omega_R-\jmath\omega_H)$, needs to be expanded into complex exponential Fourier series. Noting this term by Ω, the variable is then the time t on which ω_R depends ($\omega_R=\omega_R(t)$). It follows:

$$\Omega(t) = \sum_{n=-\infty}^{\infty}\Omega_n\cdot e^{\jmath n\omega_L t}, \tag{7.47a}$$

with

$$\Omega_n = \frac{\omega_L}{2\pi}\cdot\int_{t}^{t+\frac{2\pi}{\omega_L}}\Omega(t')\cdot e^{-\jmath n\omega_L t'}dt'. \tag{7.47b}$$

Thus, if the same evolution of the crack state as in Fig. 5.3 is assumed, the integration in Eq. (7.47b) between t and $t+2\pi/\omega_L$ can be modified by the integration between (t_1-T_C) and (t_1+T_c). Then, it is possible to split the integral into two. The first one describes the crack in the closed state -from (t_1-T_c) to t_1-, meanwhile, the crack mechanical relaxation frequency ω_R is equal to ω_c. The second one corresponds to the crack being opened, from t_1 to (t_1+T_o), for which ω_R is equal to ω_o. Finally, also using that $T_o+T_c=2\pi/\omega_L$, it is possible to obtain:

$$\Omega_n = \frac{1}{2\pi}\cdot\frac{1}{\jmath n}\cdot\left(\frac{\omega_c}{\omega_c+\jmath\omega_H}-\frac{\omega_o}{\omega_o+\jmath\omega_H}\right)\cdot\left[e^{-\jmath n\omega_L(t_1-T_c)}-e^{-\jmath n\omega_L t_1}\right]. \tag{7.48}$$

Eq. (7.45c) can be rewritten with the use of Eq. (7.48), and reorganized to obtain:

$$U_{\eta\pm}(\tau_\pm) = \frac{\mp 1}{2\pi c} I_H \text{ш}_H \sum_{i=1}^{2} \sum_{n=-\infty}^{\infty} |A_{i\pm}(\omega_H)|\,|A_n| \cdot \frac{\omega_H(\omega_c - \omega_o)}{\sqrt{{\omega_c}^2 + {\omega_H}^2}\sqrt{{\omega_o}^2 + {\omega_H}^2}} \times$$
$$\times \cos\left[(\omega_H + n\omega_L)\tau_\pm - \varphi_n - \varphi_{i\pm}(\omega_H) - \operatorname{atan}\left(\frac{\omega_H}{\omega_c}\right) - \operatorname{atan}\left(\frac{\omega_H}{\omega_o}\right) - \varphi_{HL} - \frac{\pi}{2}\right], \tag{7.49a}$$

with

$$|A_n| = \left|\frac{1}{n}\sin\left(\frac{n\omega_L T_c}{2}\right)\right|, \tag{7.49b}$$

and;

$$\varphi_n = n\omega_L\left(t_1 - \frac{T_c}{2}\right) - \operatorname{acos}\left(\frac{A_n}{|A_n|}\right). \tag{7.49c}$$

It can be noted that this result is valid even if the assumption $\eta_c > \eta_o$ is no longer assumed.

The remaining unknowns are t_1 and T_c. In order to find them, Eq. (7.28) is split into two equations (one on each subdomain) and then both equations are subtracted. It follows:

$$\frac{\partial\left[u_{L+}(0^+) - u_{L-}(0^-)\right]}{\partial t} - \frac{2}{\rho c}F[u_{L+}(0^+) - u_{L-}(0^-)] =$$
$$- I_L \text{ш}_L\left[\,|A_{1+}(\omega_L)|\cos(\omega_L t - \varphi_{1+}(\omega_L)) - |A_{1-}(\omega_L)|\cos(\omega_L t - \varphi_{1-}(\omega_L))\right]. \tag{7.50}$$

One can observe that due to the asymmetry of the heating, $A_{1+}(\omega) \neq \pm A_{1-}(\omega)$. It is possible to rewrite the right term of Eq. (7.50) and, using also the rigidity model (Eq. (7.46)),

$$\frac{\partial\left[u_{L+}(0^+) - u_{L-}(0^-) - h_{o,c}\right]}{\partial t} + \omega_{o,c}\left[u_{L+}(0^+) - u_{L-}(0^-) - h_{o,c}\right] =$$
$$- I_L \text{ш}_L \operatorname{sgn}(D_c)\sqrt{{D_c}^2 + {D_s}^2}\cos\left[\omega_L t - \operatorname{atan}\left(\frac{D_s}{D_c}\right)\right], \tag{7.51a}$$

where

$$D_c = |A_{1+}(\omega_L)|\cos(\varphi_{1+}(\omega_L)) - |A_{1-}(\omega_L)|\cos(\varphi_{1-}(\omega_L)), \tag{7.51b}$$

and,

$$D_s = |A_{1+}(\omega_L)|\sin(\varphi_{1+}(\omega_L)) - |A_{1-}(\omega_L)|\sin(\varphi_{1-}(\omega_L)). \tag{7.51c}$$

Eq. (7.51a) is closely similar to Eq. (5.3) with minor changes: $\operatorname{sgn}(D_c)\cdot\sqrt{{D_c}^2 + {D_s}^2}$ instead of $2|A(\omega_L)|$, $\operatorname{atan}(D_s/D_c)$ instead of $\varphi(\omega_L)$, and with $2u_L(0)$ changed for $[u_{L+}(0^+) - u_{L-}(0^-)]$. Then, the resolution of Eq. (7.51a) can be achieved as for Eq. (5.3) in Sec. 5.2. This result has several direct consequences.

Firstly, it justifies a posteriori the use of the generic definitions for the amplitude (Eq. (5.2)) and phase (Eq. (6.2)) evolutions as a function of the loading amplitude. Indeed, with or without asymmetrical heating, Eqs. (7.49b) and (7.49c) are identical.

Secondly, it demonstrates that the amplitude evolution is independent of the asymmetry of the heating. Indeed, the ratio I_L/I_c in Eq. (5.10) is not function of $|A(\omega_L)|$ or $\varphi(\omega_L)$, and then, the time spent in closed state, T_c, evolves identically as a function of I_L, independently of the value of x_0. In the phase evolution, only the term $\varphi(\omega_L)$ is affected. Eq. (6.7b) becomes: $\varphi_n = \dot{\varphi}_n + n \cdot [\text{atan}(D_s/D_c) + \text{atan}(\omega_L/\omega_c)]$. However, this term is not influenced by the evolution of the loading and Eq. (6.7a) for $\dot{\varphi}_n$ is unchanged. So, Eq. (6.7a) is still valid and the phase reference only is affected by the asymmetrical heating. Experimentally this is not detectable, at least without moving the beams. One could imagine a 1D scan experiment with step small enough to maintain the crack in the heated region but changing the asymmetry. Theory predicts a phase shift without an effect on the amplitude of the nonlinear sidelobes. With an additional study, this phase shift could quantify the evolution of the asymmetry.

These results mean that asymmetrical heating cannot be responsible for the apparition of new minima in the amplitude evolution as a function of the loading. If this can be considered disappointing, it also indicates that the method is not influenced, in 1D approximation, by the heating asymmetry (providing the crack is breathing). This is very important, because it is (almost) impossible experimentally to realize a symmetrical heating. As it is not a parameter influencing the results, this method is very suitable for the crack detection and crack parameters evaluation.

7.3.3 Displacement of each crack face

The distances $(h_{o,c} - h_i)$ are then expressed when the loading force $I_L = I_{c,o}$ and when the cos term multiplied by $\text{sgn}(D_c)$ is equal to $\varkappa_{o,c}$. Mathematically, it corresponds to $\text{sgn}(D_c) \cdot \cos[\omega_L t - \text{atan}(D_s/D_c) - \text{atan}(\omega_L/\omega_{o,c})] = \varkappa_{o,c}$. It follows:

$$h_{o,c} - h_i = \varkappa_{o,c} \cdot I_{c,o} \cdot \text{ш}_L \cdot \sqrt{\frac{{D_c}^2 + {D_s}^2}{{\omega_L}^2 + {\omega_{o,c}}^2}}, \tag{7.52}$$

where h_i remains the distance of the state transition of the crack even though it is now defined: $h_i = (u_{L+}(0^+) - u_{L-}(0^-))$ and where the amplitudes and phases $|A_{1\pm}|$ and $\varphi_{1\pm}$, respectively, contained in $D_{s,c}$, are proportional to $\widehat{\theta}_{\pm}$, and dependent of the asymmetry. Then, the forces $F_{c,o}$ and the distance between the thickness can be evaluated as previously, with Eq. (5.12), except that the informations on the phase $\varphi_{1\pm}$ are now required to determine D_c and D_s.

It is also possible, from Eq. (7.28), to sum the equations corresponding to each subdomain and to obtain,

$$\frac{\partial[u_{L+}(0^+) + u_{L-}(0^-)]}{\partial t} = -I_L \, \text{ш}_L \, \text{sgn}(S_c)\sqrt{{S_c}^2 + {S_s}^2} \cos\left[\omega_L t - \text{atan}\left(\frac{S_s}{S_c}\right)\right], \tag{7.53a}$$

where,

$$S_c = |A_{1+}(\omega_L)| \cos(\varphi_{1+}(\omega_L)) + |A_{1-}(\omega_L)| \cos(\varphi_{1-}(\omega_L)), \tag{7.53b}$$

and,

$$S_s = |A_{1+}(\omega_L)|\sin(\varphi_{1+}(\omega_L)) + |A_{1-}(\omega_L)|\sin(\varphi_{1-}(\omega_L)). \tag{7.53c}$$

Thus, from Eq. (7.53a),

$$u_{L+}(0^+) + u_{L-}(0^-) = E - I_L \,\text{ш}_L \,\mathrm{sgn}(S_c)\frac{\sqrt{{S_c}^2 + {S_s}^2}}{\omega_L}\sin\left[\omega_L t - \mathrm{atan}\left(\frac{S_s}{S_c}\right)\right], \tag{7.53d}$$

where E is an integration constant to be determined.

In the case of a symmetrical heating, and due to the definition of $A_{1\pm}$ (see above), it is possible to demonstrate that $A_{1+}(\omega_L) = -A_{1-}(\omega_L)$. So, $|A_{1+}(\omega_L)| = |A_{1-}(\omega_L)|$, and $\varphi_{1-} = \varphi_{1+} - \pi$. It follows that $D_c = 2|A_{1+}(\omega_L)|\cos[\varphi_{1+}(\omega_L)]$, $D_s = 2|A_{1+}(\omega_L)|\sin[\varphi_{1+}(\omega_L)]$ and $S_c = S_s = 0$. Eq. (7.52) thus corresponds to Eq. (5.6) as expected. In this particular case, $u_{L+}(0^+) = -u_{L-}(0^-)$, and thus $u_{L+}(0^+) + u_{L-}(0^-) = 0$. From, Eq. (7.53d), the condition $E = 0$ is deduced.

It is then possible to estimate the displacement of the crack faces on each side. One just need to use that $(u_{L+}(0^+) - u_{L-}(0^-)) = h_i$ occurs for $\omega_L t_{o,c} = (\mathrm{atan}(D_s/D_c) + \mathrm{atan}(\omega_L/\omega_{o,c}) + [\mathrm{sgn}(D_c) - \varkappa_{o,c}]\cdot\pi/2)$. Injecting this into Eq. (7.53d), it follows that for $t = t_{o,c}$ (the instants of changes in the crack states), the displacements, subscripted (o, c), are

$$\begin{cases} u_{L_{o,c}+}(0^+) - u_{L_{o,c}-}(0^-) = & h_i, \\ u_{L_{o,c}+}(0^+) + u_{L_{o,c}-}(0^-) = & -I_{c,o}\,\text{ш}_L \cdot[\mathrm{sgn}(S_c)\cdot\mathrm{sgn}(D_c)\cdot\varkappa_{o,c}]\cdot\frac{\sqrt{{S_c}^2+{S_s}^2}}{\omega_L}\times \\ & \times\sin\left[\mathrm{atan}\left(\frac{D_s}{D_c}\right) + \mathrm{atan}\left(\frac{\omega_L}{\omega_{o,c}}\right) - \mathrm{atan}\left(\frac{S_s}{S_c}\right)\right], \end{cases} \tag{7.54a}$$

and thus,

$$u_{L_{o,c}+}(0^+) = \frac{h_i}{2} - \frac{I_{c,o}\,\text{ш}_L}{2}\cdot[\mathrm{sgn}(S_c)\cdot\mathrm{sgn}(D_c)\cdot\varkappa_{o,c}]\cdot\frac{\sqrt{{S_c}^2+{S_s}^2}}{\omega_L}\times$$
$$\times\sin\left[\mathrm{atan}\left(\frac{D_s}{D_c}\right) + \mathrm{atan}\left(\frac{\omega_L}{\omega_{o,c}}\right) - \mathrm{atan}\left(\frac{S_s}{S_c}\right)\right], \tag{7.54b}$$

$$u_{L_{o,c}-}(0^-) = -\frac{h_i}{2} - \frac{I_{c,o}\,\text{ш}_L}{2}\cdot[\mathrm{sgn}(S_c)\cdot\mathrm{sgn}(D_c)\cdot\varkappa_{o,c}]\cdot\frac{\sqrt{{S_c}^2+{S_s}^2}}{\omega_L}\times$$
$$\times\sin\left[\mathrm{atan}\left(\frac{D_s}{D_c}\right) + \mathrm{atan}\left(\frac{\omega_L}{\omega_{o,c}}\right) - \mathrm{atan}\left(\frac{S_s}{S_c}\right)\right]. \tag{7.54c}$$

Eqs. (7.54b) and (7.54c) lead to the determination of the displacement of each face of the crack in order to insure the crack clapping for an asymmetrical heating. If the heating is symmetrical, these equations logically lead to $u_{L_{o,c}+}(0^+) = -u_{L_{o,c}-}(0^-) = h_i/2$.

The force involved for each displacement can also be obtained. As the forces acting on each crack face is extensive, they can be separated from Eq. (7.46) which can be rewrite as:

$$F_+[u_{L+}(0^+)] = \begin{cases} -\eta_o[u_{L+}(0^+) - \text{б}\, h_o] & \text{if } \text{б}\, h_i \leqslant u_{L+}(0^+) \leqslant \infty, \\ -\eta_c[u_{L+}(0^+) - \text{б}\, h_c] & \text{if } 0 \leqslant u_{L+}(0^+) \leqslant \text{б}\, h_i; \end{cases} \tag{7.55a}$$

$$F_-[u_{L-}(0^-)] = \begin{cases} \eta_o[u_{L-}(0^-) + (1-\text{б})h_o] & \text{if } (1-\text{б})h_i \leqslant -u_{L-}(0^-) \leqslant \infty, \\ \eta_c[u_{L-}(0^-) + (1-\text{б})h_c] & \text{if } 0 \leqslant -u_{L-}(0^-) \leqslant (1-\text{б})h_i; \end{cases} \tag{7.55b}$$

where б corresponds to the ratio of the displacement of $u_{L_{o,c}+}(0^+)$ over the total displacement to change the state of the crack: $\text{б} = u_{L_{o,c}+}(0^+)/h_i$. Thus, for the particular forces $F_{c,o}$, corresponding to the total crack faces displacement of h_i, the forces of each crack face are:

$$F_{c\pm}[u_{L_o\pm}(0^\pm)] = \frac{\eta_o}{2}\left[(h_o - h_i) \pm I_c\, \text{ш}_L \cdot [\operatorname{sgn}(S_c)\cdot \operatorname{sgn}(D_c)\cdot \varkappa_o]\cdot \frac{\sqrt{{S_c}^2 + {S_s}^2}}{\omega_L}\times \right.$$
$$\left. \times \sin\left[\operatorname{atan}\left(\frac{D_s}{D_c}\right) + \operatorname{atan}\left(\frac{\omega_L}{\omega_o}\right) - \operatorname{atan}\left(\frac{S_s}{S_c}\right)\right]\cdot\left(1 - \frac{h_o}{h_i}\right)\right], \tag{7.56a}$$

$$F_{o\pm}[u_{L_c\pm}(0^\pm)] = \frac{\eta_c}{2}\left[(h_c - h_i) \pm I_o\, \text{ш}_L \cdot [\operatorname{sgn}(S_c)\cdot \operatorname{sgn}(D_c)\cdot \varkappa_c]\cdot \frac{\sqrt{{S_c}^2 + {S_s}^2}}{\omega_L}\times \right.$$
$$\left. \times \sin\left[\operatorname{atan}\left(\frac{D_s}{D_c}\right) + \operatorname{atan}\left(\frac{\omega_L}{\omega_c}\right) - \operatorname{atan}\left(\frac{S_s}{S_c}\right)\right]\cdot\left(1 - \frac{h_c}{h_i}\right)\right]. \tag{7.56b}$$

The forces applied on each face of the crack can then be evaluated. For a symmetrical heating these forces are both equal to $F_{c,o\pm} = \eta_{o,c}/2$.

Finally, the total displacement of the crack faces and the total loading force to insure the crack closing and opening are determined. Also, for the case of an asymmetrical heating, the displacement and the loading force of each crack face can also be evaluated.

7.4 Acoustic frequency-mixing process induced by thermal resistance modulation

Eq. (7.24c) demonstrates that the temperature field contains one part which can be modulated by varying the thermal resistance and another part which is not influenced by the thermal resistance. Eq. (7.42) predicts that the acoustic strain contains one part influenced by the crack rigidity ($\widetilde{U}_{\eta\pm}$) and another one independent of the crack rigidity ($\widetilde{U}_{0\pm}$).

The substitution of the temperature field from Eq. (7.24c) in Eq. (7.42) provides the opportunity to write the acoustic strain and to separate in different parts, depending on their possibility to be modified by thermal resistance and/or crack rigidity variations:

$$\begin{aligned}\widetilde{U}_{\pm}(\omega) = \frac{K\beta}{2\rho c^3}(\jmath\omega)\frac{1}{\left(\frac{\omega}{c}\right)^2 - {k_T}^2}\frac{I}{\ell\kappa}\widetilde{f}(\omega) \times \Bigg[&\mp \overbrace{\frac{\jmath\frac{\omega}{c}\bar{R}}{1-\jmath k_T\bar{R}}\Big(\widehat{\Psi}_+(k_T, x_0) + -\widehat{\Psi}_-(\text{-}k_T, x_0)\Big)}^{\widetilde{U}'_R} + \\ &+ \underbrace{\frac{\omega}{ck_T}\left(\widehat{\Psi}_+(k_T, x_0) + \widehat{\Psi}_-(\text{-}k_T, x_0)\right) + \widehat{\Psi}_{\pm}\left(\mp\frac{\omega}{c}\right) - \widehat{\Psi}_{\pm}\left(\pm\frac{\omega}{c}\right)}_{\widetilde{U}'_{0\pm}} + \\ &+ \underbrace{\frac{\omega_R}{\omega_R - \jmath\omega}\left(\frac{\text{-}\omega}{ck_T}\Big[\widehat{\Psi}_+(k_T, x_0) + \widehat{\Psi}_-(\text{-}k_T, x_0)\Big] + \widehat{\Psi}_{\pm}\left(\pm\frac{\omega}{c}\right) + \widehat{\Psi}_{\mp}\left(\mp\frac{\omega}{c}\right)\right)}_{\widetilde{U}'_{\eta\pm}}\Bigg]. \end{aligned} \tag{7.57}$$

The influence of the asymmetry on the nonlinear sidelobe generation by the mean of crack rigidity modulation has been already studied in Sec. 7.3. The asymmetrical heating also provides the opportunity to generate the nonlinear mixed-frequencies by crack thermal resistance modulation. If we consider the part influenced by the crack thermal resistance (proportional to $\bar{R}$), only the term $\widetilde{U}'_R$ should be considered.
The coefficient $\bar{R}$ can be written with Eq. (7.18a) and (7.18b):

$$\bar{R} = \frac{1}{2} \cdot \left[\widetilde{T}_+(\omega, 0^+) - \widetilde{T}_-(\omega, 0^-)\right] \cdot \left(\frac{\partial\widetilde{T}_+(\omega, 0^+)}{\partial x}\right)^{-1}. \tag{7.58}$$

Then, the same logic as for the crack rigidity modulation can be applied. The difference is on the evolution of the crack thermal resistance. In a first approximation, the thermal resistance evolution can be considered as one of the rigidity. The crack thermal resistance oscillates between two values depending on either the crack is opened or closed. This leads to the exactly same nonlinear sidelobe amplitude. However, the main difference is that the coefficient affecting the amplitude of the nonlinear sidelobes strongly depends on x_0, i.e., it depends on the asymmetry of the heating.

If we consider a spatial distribution $\Psi(x) = e^{-|(x-x_0)/a|}$, simpler than a gaussian distribution, and assuming that $x_0 \geqslant 0$, it follows:

$$\widehat{\Psi}_+(k, x_0) = \frac{-a \cdot e^{-x_0/a}}{1 + \jmath ak} + \frac{2a \cdot e^{\jmath kx_0}}{1 + (ak)^2}, \tag{7.59a}$$

$$\widehat{\Psi}_-(-k, x_0) = \frac{a \cdot e^{-x_0/a}}{1 - \jmath ak}. \tag{7.59b}$$

Fig. 7.2(a) presents the evolution of both coefficients affected by the crack thermal resistance and the crack rigidity. The former, $V_1 = [\widehat{\Psi}_+(k_T, x_0) - \widehat{\Psi}_-(\text{-}k_T, x_0)]$, increases as a function of the asymmetry. On the contrary, the later, $V_2 = [\text{-}\omega/(ck_T) \cdot [\widehat{\Psi}_+(k_T, x_0) + \widehat{\Psi}_-(\text{-}k_T, x_0)] + \widehat{\Psi}_{\pm}(\pm\omega/c) + \widehat{\Psi}_{\mp}(\mp\omega/c)]$ is much less affected by the evolution of the asymmetry. It is slowly decreased but for distances up to 2 mm far from the crack, it can be considered constant.

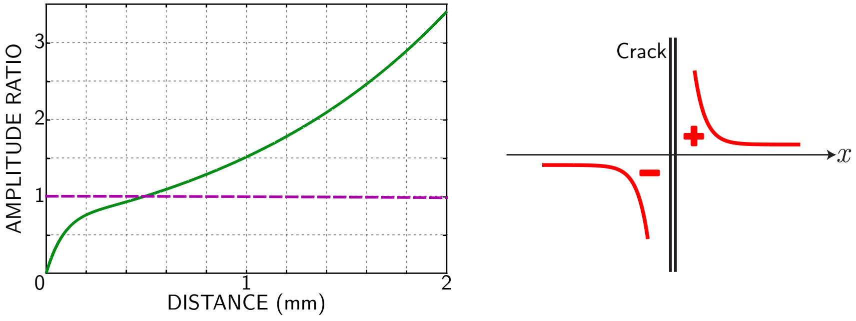

(a) **(b)**

Figure 7.2: (a): Evolution of the ratio of the coefficients $V_1/V_2(x_0 = 0)$ (—) and $V_2/V_2(x_0 = 0)$ (- -) responsible for the modulation of the crack thermal resistance and the crack rigidity, respectively, as a function of the distance between the center of the irradiated beam and the crack for a pump beam radius of $a_L = 100$ µm, intensity modulated at $f_L = 1$ kHz and a probe beam intensity-modulated at $f_H = 50$ kHz. (b): Schematic representation of the temperature rise induced by the crack thermal resistance variations.

It appears that for small asymmetries ($x_0 \leqslant 200$ µm), the phenomenon responsible for the nonlinear sidelobe generation is the crack rigidity modulation, whereas for strong asymmetries ($x_0 \geqslant 1$ mm), the crack thermal resistance modulation predominates the nonlinear mixed-frequency generation. The fact that the coefficient V_1 strongly increases with distance -because of the imaginary exponential function in $\widehat{\Psi}_+(k_T, x_0)$ (Eq. (7.59a)) and the fact that in the argument $k_T \in \mathbb{C}$- is not problematic as the thermal resistance diminishes because the temperature rises are reduced with the distance.
In-between, for $x_0 \in [0.2; 1]$ mm, both effect can contribute to the generation of the mixed-frequencies.

7.5 Double modulation of the signal by crack rigidity and thermal resistance modulations

It appears from Fig. 7.2(a), that for a range of distances between the laser beams and the crack, the nonlinear sidelobe generation can be provided by both the crack thermal resistance and the crack rigidity modulations. However, the two phenomena have been independently studied. The effect of these two modulations on an acoustic wave should be considered.
In order to describe the double modulation, let us consider Eq. (7.57). It can be divided in three parts. The first part, $\widetilde{U}'_{0\pm}$ is a term which is not of interest as it cannot be modulated neither by the crack rigidity nor by thermal resistance (neither by ω_R nor by $\bar{R}$). The term $\widetilde{U}'_{\eta\pm}$, influenced by ω_R, leads to the description of the sidelobes due to the modulation of the crack rigidity as previously discussed. The term $\widetilde{U}'_{\eta\pm}$ described the sidelobes generated due to the modulation of the crack by the thermal resistance. It can be described similarly as for the nonlinear sidelobes due to the crack rigidity modulation. Finally, it appears that the terms corresponding to the double modulation (mixing the

thermal resistance and the crack rigidity modulations), influenced by ω_R and $\bar{R}$ are absent in Eq. (7.57). This indicates the absence of the following process: the nonlinear acoustic signals caused by the modulation of the thermal resistance are not additionally modulated by the crack reflectivity variation. In other words, the acoustic signals generated due to the thermal resistance ‘breathing’ are not influenced by the crack rigidity ‘breathing’.

The formal mathematical explanation for the absence of double modulation is the following. The part of $\widetilde{U}_{\eta\pm}$, influenced by the crack rigidity modulation, depends on the sum of temperatures $\widehat{T}_{\pm}(\omega, \pm\omega/c)$ and $\widehat{T}_{\mp}(\omega \mp \omega/c)$ (Eq. (7.42)). From, Eq. (7.24c), the part of the temperature field modulated by the thermal resistance (subscripted R) is:

$$\widehat{T}_{R\pm}\left(\omega, \pm\frac{\omega}{c}\right) = \mp\frac{\jmath\left(k_T - \frac{\omega}{c}\right)\bar{R}}{1-\jmath k_T\bar{R}}\left[\widehat{\Psi}_+(k_T, x_0) - \widehat{\Psi}_-(-k_T, x_0)\right], \tag{7.60a}$$

and

$$\widehat{T}_{R\mp}\left(\omega, \mp\frac{\omega}{c}\right) = \pm\frac{\jmath\left(k_T - \frac{\omega}{c}\right)\bar{R}}{1-\jmath k_T\bar{R}}\left[\widehat{\Psi}_+(k_T, x_0) - \widehat{\Psi}_-(-k_T, x_0)\right]. \tag{7.60b}$$

It directly follows that $\widehat{T}_{R\pm}\left(\omega, \pm\omega/c\right) = -\widehat{T}_{R\mp}\left(\omega, \mp\frac{\omega}{c}\right)$. Consequently, their zero sum in Eq. (7.42) is responsible for the absence of double modulation. Eq. (7.37b) describes the generation of a non-zero acoustic field modulated by the thermal resistance. Then, it appears that this acoustic field cannot be additionally modulated by crack rigidity. These processes can independently lead to the generation of the nonlinear sidelobes but not mutually.

A plausible physical explanation of this phenomenon is the following. The thermal resistance variations induce temperature changes of opposite sign at opposite crack faces (Eq. (7.60), Fig. 7.2(b)). Thus, the acoustic waves of opposite polarities, i.e., in antiphase, are generated near the opposite faces of the crack. The variations on crack rigidity influence the reflection and transmission of an acoustic wave interacting with the crack. If reflection diminishes, then transmission increases.

Then, the resulting signal, registered at some point outside the crack, corresponds to the sum of the reflected and transmitted waves which appears to be constant. A possible reflectivity diminution being compensated by an transmission increase and reciprocally. The complete absence of double-modulation appears to be physically interesting.

Conclusion

The calculation for the asymmetrical heating is developed. Two phenomena can be responsible for the nonlinear sidelobe generation.

Firstly, the crack rigidity modulation, as for a symmetrical heating, generates the mixed-frequencies. It is demonstrated that the amplitude of the nonlinear sidelobes is independent of the asymmetry in the 1D theory. This does not provide the opportunity to explain the presence of extra minima but indicates that the method is robust.
The phase is shifted by the asymmetry. However, the evolution of the phase as a function of the pump loading is not modified. Thus, the previous results on the phase for the crack detection or the detection of the minima remain valid.
The displacements, and the forces on each crack faces required for the breathing are independently evaluated as function of the asymmetry.

Secondly, the crack thermal resistance is directly modified by the asymmetry. Its modulation is also a source of nonlinear mixed-frequencies. The effect is absent in case of symmetrical heating because of the absence of the heat flux across the crack in symmetrical configuration. In a first approach, the crack thermal resistance modulation is considered to evolve similarly as the crack rigidity under the pump loading. This leads to the same description of the nonlinear frequency-mixing. However, the amplitude of this second phenomenon depends on the asymmetry. It importantly grows as the asymmetry increases, although the heat flux diminishes when the distance from the heating point increase.

Finally, it is important to note that these two phenomena cannot be combined to generate nonlinear mixed-frequencies by double modulation. The crack thermal resistance modulation induces temperature variations of opposite sign between the opposite crack faces whereas the crack rigidity modulation acts on the sum of the temperature rise. As a consequence, the rise of the acoustic reflection coefficient is compensated by a decrease in the transmission and vice versa.

CONCLUSION

The presented work concerns the development of a nonlinear optoacoustic method for NDT&E applications. The general principle is to nonlinearly mix opto-thermo-acoustic waves generated on a sample from two independently modulated laser beams. When the laser beams are focused far from a crack, this nonlinear mixing process is hardly detectable, while in the vicinity of a crack an efficient nonlinear frequency mixing process takes place. The detection of the new mixed frequencies in the radiated ultrasonic waves is consequently related to the presence of a crack in the vicinity of the laser spots on the sample. Crack imaging and characterization using this class of methods were among the objectives of this PhD thesis.

In this work, the clear possibility to detect and characterize cracks is demonstrated. The method offers the advantages to combine an all-optical excitation with high amplitude dynamics. The detection of nonlinear frequency-mixing, not generated outside from the crack, is also very attractive. The possibility of an all-optical set-up is demonstrated by the use of a vibrometer or the use of the deflectometry technique, adapted for the frequency range. It is also demonstrated that this technique has important capabilities concerning the spatial resolution.

The precise study of the heat generation and transport offers very good estimations particularly interesting to characterize the influence of the pump frequency, power or focusing on the amplitude dynamics and the spatial resolution. Comparison between experiments and theoretical predictions are in good agreement.

The possibility to detect cracks with the phase information is also an interesting tool, not much developed in the literature.

The study of the evolution of the nonlinear sidelobes amplitude versus the pump power demonstrates very interesting behaviors. For the sidelobes higher than the first one, the evolutions are non monotonous. A particular effort has been done on the position of the amplitude minima for specific pump powers. The existent model has been improved to better fit the experimental results on the minima position. It allows independent choices of the pump frequency, the crack mechanical frequencies in opened and closed state and the required force to open and closed the crack. Comparison of the experimental results with this model makes the crack parameters estimated at the heated point. They lead to an estimation of the crack rigidity in opened and closed state, the distance between the crack faces and the forces involved to open and close the crack. As the 3D heat equation

is solved, the involved temperature at specific loading can also be evaluated.
The phase information can also offer the possibility to estimate the position of the minima very precisely and to estimate the required force to close the crack which is very promising.

A theoretical model for asymmetrical heating between the axis of the beams and to the plane of the crack has been developed. It demonstrates two distinct phenomena to generate the nonlinear frequency-mixing. The first one depends on the crack rigidity variations, evolving as the crack evolves from opened and closed state. This phenomenon is similar to the symmetrical heating, and it is demonstrated that the evolutions of the nonlinear sidelobe amplitudes are independent of the asymmetry.
The second phenomenon is related to the change in the crack thermal resistance due to the asymmetrical heating. In a first approach, it demonstrates the same behaviors for the nonlinear sidelobe amplitudes but depends on the asymmetry. It explains the possibility to generate nonlinear frequency-mixing even though the crack is not in the irradiated area.
No acoustic wave modulated by both phenomena can be generated.

Perspectives, Prospects

Additional efforts on the theory should be done to propose better theoretical predictions and to explain the unexpected response of some crack under pump loading. Firstly, the elasticity equation should be investigated to take into account the three dimensional behavior of the sample in the one dimensional equation similarly to the temperature equation where an additive term has been included to express the heat transports in the other dimensions.
The possibility to take into account the boundaries should be included in order to account for the heating of the probe beam on the crack breathing.
The next step would probably be to develop a more complete and more real model of the crack rigidity. The ideal case would be to propose a smooth evolution of the crack rigidity and not only a bistable model. In a first step, one could start with a piece-wise model with 3 or 4 possible rigidities and then try to increase it.
In a longer term, the possibility of a 2D and then 3D model could be considered. The finite dimension of the crack will probably render the calculation difficult. However, it appears to be necessary in order to well understand the limitation of the spatial resolution. It would certainly help to predict nonlinear sidelobe amplitude evolutions closer than the experimental observations.
Nevertheless, it is probable that the geometry of the real crack (micro- and nano-contacts, evolution of the rigidity,...) importantly influences the experimental results. However, at this point, it is not realistic to consider an analytical model with such level of detail, due to the multiple reflection and parameter evolutions.

Numerical modeling of the process involved in the nonlinear frequency-mixing, by finite element method is an interesting axis to develop [8]. It would offer the possibility to implement a finite crack size and imperfect crack faces. A research project is currently in progress to provide such numerical model.

On the experimental part, the study of the method on a wider variety of materials, such as metals, should be considered. Successful results on aluminium have already been achieved.

Then, an additional effort should firstly be realized to better control the spatial resolution. Once this is perfectly understood, the diminution of the sample and crack scale would be the next step. The method is promising enough to go down to the micrometer scale and preliminary non destructive testing and evaluation of MEMS are being carried out.

Besides, a specific investigation on the phase evolutions may provide new informations or an alternative technique which could be faster.

This method uses the resonant frequencies of the sample. An interesting alternative, especially for thin objects such as MEMS would be the use of the zero group velocity Lamb wave [5]. Because of the localization of the energy of these waves, it could provide a better spatial resolution.

PART IV

APPENDIX

Appendix A

DETAILED CALCULATION OF THE 3D HEAT EQUATION INTEGRALS

A.1 Integration over z_1

We want to calculate integral A (Sec. 3.2, Eq. (3.9)), with

$$\begin{aligned} A &= \int_0^{\infty} e^{-\frac{z_1}{\ell}} \left(e^{-\frac{(z-z_1)^2}{4\chi\tau}} + e^{-\frac{(z+z_1)^2}{4\chi\tau}} \right) dz_1 && \text{(A.1)} \\ &= \underbrace{\int_0^{\infty} e^{-\left(\frac{z_1}{\ell}+\frac{(z-z_1)^2}{4\chi\tau}\right)} dz_1}_{C} + \underbrace{\int_0^{\infty} e^{-\left(\frac{z_1}{\ell}+\frac{(z+z_1)^2}{4\chi\tau}\right)} dz_1}_{D} . && \text{(A.2)} \end{aligned}$$

We now have to calculate two similar integrals . Let us firstly focus on integral C. A change of variable is realized: $q = (z - z_1)/(2\sqrt{\chi\tau})$. It follows:

$$\begin{aligned} C = &\int_{-\infty}^{z} e^{-\left(\frac{z-q}{\ell}+\frac{q^2}{4\chi\tau}\right)} dq \\ =&2\sqrt{\chi\tau} e^{-\frac{z}{\ell}} \int_{-\infty}^{\frac{z}{2\sqrt{\chi\tau}}} e^{\left(\frac{2\sqrt{\chi\tau}}{\ell} q - q^2\right)} dq. && \text{(A.3)} \end{aligned}$$

This last form is particularly interesting as it has a known analytical form [17]:

$$\forall g \in \mathbb{R}, \ \int e^{gx-x^2} dx = \frac{\sqrt{\pi}}{2} e^{\frac{g^2}{4}} \cdot \mathrm{Erf}\left(x - \frac{g}{2}\right) . \qquad \text{(A.4)}$$

Thus, using the limit of Erf function, $\lim_{x\to-\infty}\mathrm{Erf}(x) = -1$, we obtain:

$$\begin{aligned} C =& \sqrt{\pi\chi\tau}e^{-\frac{z}{\ell}+\frac{\chi\tau}{\ell^2}}\left(1+\mathrm{Erf}\left[\frac{z}{2\sqrt{\chi\tau}}-\frac{\sqrt{\chi\tau}}{\ell}\right]\right) \\ =& \sqrt{\pi\chi\tau}e^{-\frac{z}{\ell}+\frac{\chi\tau}{\ell^2}}\,\mathrm{Erfc}\left[\frac{\sqrt{\chi\tau}}{\ell}-\frac{z}{2\sqrt{\chi\tau}}\right]. \end{aligned} \tag{A.5}$$

We can proceed the same way for integral ‘D’. In this one, the change of variable is applied ($q = (z + z_1)/(2\sqrt{\chi\tau})$):

$$D = 2\sqrt{\chi\tau}e^{\frac{z}{\ell}}\int\limits_{\frac{z}{2\sqrt{\chi\tau}}}^{\infty} e^{\left(-\frac{2\sqrt{\chi\tau}}{\ell}q-q^2\right)}dq. \tag{A.6}$$

Eq. (A.4) remains valid and $\lim_{x\to\infty}\mathrm{Erf}(x) = 1$. It follows:

$$D = \sqrt{\pi\chi\tau}e^{\frac{z}{\ell}+\frac{\chi\tau}{\ell^2}}\,\mathrm{Erfc}\left[\frac{z}{2\sqrt{\chi\tau}}+\frac{\sqrt{\chi\tau}}{\ell}\right]. \tag{A.7}$$

So, finally, we have:

$$\begin{aligned} &\int\limits_0^{\infty} e^{-\frac{z_1}{\ell}}\left[e^{-\frac{(z-z_1)^2}{4\chi\tau}}+e^{-\frac{(z+z_1)^2}{4\chi\tau}}\right]dz_1 = \\ &\qquad \sqrt{\pi\chi\tau}e^{\frac{\chi\tau}{\ell^2}}\left(e^{-\frac{z}{\ell}}\mathrm{Erfc}\Big[\frac{\sqrt{\chi\tau}}{\ell}-\frac{z}{2\sqrt{\chi\tau}}\Big]+e^{\frac{z}{l}}\mathrm{Erfc}\Big[\frac{\sqrt{\chi\tau}}{\ell}+\frac{z}{2\sqrt{\chi\tau}}\Big]\right). \end{aligned} \tag{A.8}$$

A.2 Integration over r_1

We are looking, here, for:

$$B = \int_0^{\infty} e^{-\left(\frac{r_1}{a}\right)^2}e^{-\frac{r^2+{r_1}^2}{4\chi\tau}}\mathcal{I}_0\left(\frac{rr_1}{2\chi\tau}\right)r_1dr_1. \tag{A.9}$$

With the change of variable $q = rr_1/(2\chi\tau)$, Eq. (A.9) becomes:

$$B = \left(\frac{2\chi\tau}{r}\right)^2 e^{-\frac{r^2}{4\chi\tau}}\int_0^{\infty} qe^{-\frac{\chi\tau}{r^2}\left(1+\frac{4\chi\tau}{a^2}\right)q^2}\mathcal{I}_0\big(q\big)dq. \tag{A.10}$$

This allows to recognize an analytical form [46]:

$$\forall g/\Re e(g) > 0,\ \int_0^{\infty} qe^{-gq^2}\mathcal{I}_0(q)dq = \frac{1}{2g}e^{\frac{1}{4g}}. \tag{A.11}$$

As here, $g = \frac{\chi\tau}{r^2}\left(1 + \frac{\chi\tau}{a^2}\right)$ the condition $\Re e(g) > 0$ is fulfilled. Then, we finally obtain:

$$\int_0^\infty e^{-\left(\frac{r_1}{a}\right)^2} e^{-\frac{r^2+{r_1}^2}{4\chi\tau}} \mathcal{I}_0\left(\frac{rr_1}{2\chi\tau}\right) r_1 dr_1 = \frac{2\chi\tau a^2}{a^2+4\chi\tau} e^{-\frac{r^2}{a^2+4\chi\tau}}. \tag{A.12}$$

Appendix B

DETAILED CALCULATION OF THE 1D HEAT EQUATION INTEGRAL

We want to integrate:

$$T(x=0,t) = \frac{I}{\ell\rho c_p\sqrt{\pi\chi}} \int_0^t \int_0^\infty \frac{e^{-[(t-t_1)/\tau_T]^2}}{\sqrt{t-t_1}} \cdot e^{-{x_1}^2\left(\frac{1}{a^2}+\frac{1}{4\chi(t-t_1)}\right)} dx_1 dt_1. \tag{B.1}$$

The integral over x_1 can be realized easily with the change of variable $v = \sqrt{\Gamma}x_1$ where $\Gamma = \frac{1}{a^2} + \frac{1}{4\chi(t-t_1)}$:

$$\int_0^b e^{-\Gamma {x_1}^2} dx_1 = \frac{1}{\sqrt{\Gamma}} \int_0^{b\sqrt{\Gamma}} e^{-v^2} dv \qquad \forall\, \Gamma \in \mathbb{R}_+, \tag{B.2a}$$

$$= \frac{\sqrt{\pi}}{2\sqrt{\Gamma}} \cdot \mathrm{Erf}(b\sqrt{\Gamma}). \tag{B.2b}$$

As $\lim\limits_{x\to\infty} \mathrm{Erf}(x) = 1$, Eq. (B.1) can be rewritten:

$$T(x=0,t) = \frac{I}{2\ell\rho c_p\sqrt{\chi}} \cdot \int_0^t e^{-\left(\frac{t-t_1}{\tau_T}\right)^2} \cdot \frac{1}{\sqrt{\frac{t-t_1}{a^2} + \frac{1}{4\chi}}} dt_1. \tag{B.3}$$

With the change of variable $v = 4\chi(t-t_1) + a^2$, it becomes:

$$T(x=0,t) = \frac{Ia}{4\ell\rho c_p\chi} \cdot e^{\frac{a^2}{4\chi\tau_T}} \cdot \int_{a^2}^{a^2+4\chi t} \frac{e^{-\frac{v}{4\chi\tau_T}}}{\sqrt{v}} dv. \tag{B.4}$$

It can be proved that [17]:

$$\int \frac{e^{-v/x}}{\sqrt{v}} dv = \sqrt{x\pi} \cdot \mathrm{Erf}\left(\sqrt{\frac{v}{x}}\right), \tag{B.5}$$

so, the solution is:

$$T(x=0,t) = \frac{Ia}{2\ell\rho c_p}\sqrt{\frac{\pi\tau_T}{\chi}} \cdot e^{\frac{a^2}{4\chi\tau_T}} \cdot \left[\mathrm{Erf}\left(\sqrt{\frac{a^2+4\chi t}{4\chi\tau_T}}\right) - \mathrm{Erf}\left(\frac{a}{2\sqrt{\chi\tau_T}}\right)\right]. \tag{B.6}$$

Using the limit of the error function for an infinite argument, it follows:

$$\lim_{t\to\infty} T(x=0,t) = \frac{Ia}{2\ell\rho c_p}\sqrt{\frac{\pi\tau_T}{\chi}} \cdot e^{\frac{a^2}{4\chi\tau_T}} \cdot \mathrm{Erfc}\left(\frac{a}{2\sqrt{\chi\tau_T}}\right). \tag{B.7}$$

References

[1] Milton Abramovitz and Irene A. Stegun. Handbook of mathematical functions with formulas, graphs, and mathematical tables. Dover Publications, 1972.

[2] J. D. Achenbach and O. K. Parikh. Ultrasonic detection of nonlinear mechanical behavior of adhesive bonds. In D. O. Thompson and D. E. Chimenti, editors, Review of Progress in QNDE, volume 10B, pages 1837--1844. Plenum Press, 1991.

[3] J. D. Achenbach, O. K. Parikh, and Y. C. Lu. Wave phenomena related to nonlinear mechanical behavior of adhesives. In D. O. Thompson and D. E. Chimenti, editors, Review in progress in quantitative nondestructive evalution, volume 9B, pages 1693--1700. Plenum Press, 1990.

[4] S. A. Akhmanov and Vitalyi E. Gusev. Laser excitation of ultrashort acoustic pulses: New possibilities in solid-state spectroscopy, diagnostics of fast processes, and nonlinear acoustics. Sov. Phys. Usp, 35(153), 1992.

[5] Oluwaseyi Balogun, Todd W. Murray, and Claire Prada. Simulation and measurement of the optical excitation of the S_1 zero group velocity lamb wave resonance in plates. J. Appl. Phys., 102(6), 2007.

[6] Alexander G. Bell. On the production and reproduction of sound by light. Am J Sci, 20(118):305--324, 1880.

[7] I. Yu. Belyaeva and Vladimir Yu. Zaitsev. Nonlinear scattering of acoustic waves by discontinuity-like defects in application to cracks detection. J. Vib. Control, 2(465):465--478, 1996.

[8] Olivier Bou Matar, Pierre-Yves Guerder, YiFeng Li, Bart Vandewoestyne, and Koen Van Den Abeele. A nodal discontinuous galerkin finite element method for nonlinear elastic wave propagation. J. Acoust. Soc. Am., 131(5):3650--3663, 2012.

[9] Yves Brechet and Zoltán Néda. On the structure of thermal cracks in glass. Europhys. Lett., 32(6):475--480, 1995.

[10] O. Buck, W. L. Morris, and J. M. Richardson. Acoustic harmonic generation at unbonded interfaces and fatigue cracks. Appl. Phys. Lett., 33:371--373, 1978.

[11] N. A. Burnham and A. J. Kulik. Surface forces and adhesion, in: Handbook of micro/nanotribology, volume Chap. 5, p:247. B. Brushan, Boca Raton: CRC Press LLC, 1999.

[12] N. A. Burnham and A. J. Kulik. Surface forces and microrheology of molecularly thin liquid films, in: Handbook of micro/nanotribology, volume Chap. 9, p:371. B. Brushan, Boca Raton: CRC Press LLC, 1999.

[13] Hans-Jürgen Butt and Michael Kappl. Surface and interfacial forces. Wiley-VCH, 2012.

[14] Nikolay Chigarev, Jacek Zakrzewski, Vincent Tournat, and Vitalyi Gusev. Nonlinear frequency-mixing photoacoustic imaging of a crack. J. Appl. Phys., 106(036101), 2009.

[15] Lucas Duffrène, René Gy, John E. Masnik, John Kieffer, and Jay D. Bass. Temperature dependence of the high-frequency viscoelastic behavior of a soda--lime--silica glass. J. Am. Ceram. Soc., 81(5):1278--1284, 1998.

[16] L. D. Favro, X. Han, Z. Ouyang, G. Sun, H. Sui, and R. L. Thomas. Infrared imaging of defects heated by a sonic pulse. Rev. Sci. Instrum., 71(6):2418--2421, June 2000.

[17] I. S. Gradshteyn and I. M. Ryzhik. Table of integrals, series and products, seventh edition. Academic Press Inc., 2007.

[18] G. Grégoire, Vincent Tournat, Denis Mounier, and Vitalyi Gusev. Nonlinear photothermal and photoacoustic processes for crack detection. Eur. Phys. J. Special Topics, 153:313--315, 2008.

[19] Vitalyi Gusev. Frequency dependence of dynamic hysteresis in the interaction of acoustic wave with interface. J. Acoust. Soc. Am., 115(3):1044--1048, 2004.

[20] Vitalyi Gusev and Nikolay Chigarev. Nonlinear frequency-mixing photoacoustic imaging of a crack: Theory. J. Appl. Phys., 107(124905), 2010.

[21] Vitalyi Gusev, A. Mandelis, and R. Bleiss. Theory of second harmonic thermal wave generation: 1D geometry. Int. J. Thermophys., 14:321, 1993.

[22] Vitalyi Gusev, A. Mandelis, and R. Bleiss. Theory of strong photothermal nonlinearity from sub-surface non-stationary ("breathing") cracks in solids. Appl. Phys. A, 57:229--233, 1993.

[23] Vitalyi Gusev, A. Mandelis, and R. Bleiss. Non-linear photothermal response of thin solid films and coatings. Mat. Sci. Eng. B, 26:111, 1994.

[24] Vitalyi Gusev, A. Mandelis, and R. Bleiss. Theory of combined acousto-photo-thermal spectral decomposition in condensed phases: parametric generation of thermal waves by a non-stationary ("breathing") sub-surface defect". Mat. Sci. Eng. B, 26:121, 1994.

[25] Vitalyi Gusev and Vladimir Yu. Zaitsev. Acoustic dither injection in a medium with hysteretic quadratic nonlinearity. Phys. Lett. A, 314:117--125, July 2003.

[26] Vitalyi E. Gusev, Bernard Castagnède, and Alexei G. Moussatov. Hysteresis in response of nonlinear bistable interface to continuously varying acoustic loading. Ultrasonics, 41:643--654, 2003.

[27] Vitalyi E. Gusev and A. A. Karabutov. Laser optoacoustics. American Institute of Physics, 1993.

[28] Matthias Haldimann, Andreas Luible, and Mauro Overend. Structural use of glass. International Association for Bridge and Structural Engineering, 2008.

[29] Xiaoyan Han, L. D. Favro, and R. L. Thomas. Thermosonic imaging of cracks: applications to teeth. In SPIE Press, editor, Hybrid and novel imaging and new optical instrumentation for biomedical applications, volume 4434 of Proceedings of SPIE, pages 70--73, 2001.

[30] S. Hirsekorn. Nonlinear transfer of ultrasound by adhesive joints--a theoretical description. Ultrasonics, 39(57-68), 2001.

[31] F. P. Incropera and D. P. De Witt. Introduction to heat transfer (3rd Ed.). John Wiley & Sons Inc, 1995.

[32] K. L. Johnson. Theoretical and applied mechanics. W. T. Koiter (North Hollan, New York), 1976.

[33] K. L. Johnson, K. Kendall, and Roberts A. D. Surface energy and the contact of elastic solids. Proc. R. Soc. Lond. A, 324(1558):301--313, 1971.

[34] V. V. Kazakov, A. Sutin, and P. A. Johnson. Sensitive imaging of an elastic nonlinear wave-scattering source in a solid. Appl. Phys. Lett., 81(4):646, 2002.

[35] B. A. Korshak, Igor Yu Solodov, and E. M. Ballad. DC effects, sub-harmonics, stochasticity and ”memory” for contact acoustic non-linearity. Ultrasonics, 40(1-8):707--713, 2002.

[36] N. Krohn, R. Stoessel, and G. Busse. Acoustic non-linearity for defect selective imaging. Ultrasonics, 40(1-8):633--637, 2002.

[37] T. H. Lee and K. Y. Jhang. Experimental investigation of nonlinear acoustic effect at crack. NDT&E International, 42:757--764, 2009.

[38] F. J. Margetan, R. B. Thompson, J. H. Rose, and T. A. Gray. The interaction of ultrasound with imperfect interfaces: experimental studies of model structures. J. Nondestruct. Eval., 11:109--126, 1992.

[39] Sylvain Mezil, Nikolay Chigarev, Vincent Tournat, and Vitalyi Gusev. All-optical probing of the nonlinear acoustics of a crack. Optics Letters, 36(17):3449--3451, 2011.

[40] Jean-Pierre Monchalin. Optical detection of ultrasound. IEEE Trans. UFFC, 33(5):485, September 1986.

[41] Alexei Moussatov, Vitalyi Gusev, and Bernard Castagnède. Self-induced hysteresis for nonlinear acoustic waves in cracked material. Phys. Rev. Lett., 90(12):124301, Mar 2003.

[42] Chen-Yin Ni, Nikolay Chigarev, Vincent Tournat, Nicolas Delorme, Zhon-Hua Shen, and Vitalyi E. Gusev. Probing of laser-induced crack modulation by laser-monitored surface waves and surface skimming bulk waves. J. Acoust. Soc. Am., 131(3), 2012.

[43] Antonin Novak, Mourad Bentahar, Vincent Tournat, Rachid El Guerjouma, and Laurent Simon. Nonlinear acoustic characterization of micro-damaged materials through higher harmonic resonance analysis. NDT&E International, 45:1--8, 2012.

[44] S. Pangraz and W. Arnold. Quantitative determination of nonlinear binding forces by ultrasonic technique. In D. O. Thompson and D. E. Chimenti, editors, Review of Progress in QNDE, volume 13B, pages 1995--2001. Plenum Press, 1994.

[45] A.D. Polyanin. Handbook of linear PDEs for engineers and scientists. Chapman & Hall/CRC, 2001.

[46] Anatoly P. Prudnikov, Yury A. Brychkov, and Oleg I. Marichev. Integrals and series, Vol. 2, special functions. New York: Gordon and Breach Science Publishers, 1990.

[47] C. A. J. Putman, B. G. De Grooth, N. F. Van Hulst, and J. Greve. A detailed analysis of the optical beam deflection technique for use in atomic force microscopy. J. Appl. Phys., 72(6), 1992.

[48] J. Rantala, D. Wu, and G. Busse. Amplitude-modulated lock-in vibrothermography for NDE of polymers and composites. Res. Nondestr. Eval., 7:215--228, 1996.

[49] Wilhelm C. Röntgen. On tones produced by the intermittent irradiation of a gas. Philos. Mag., 11(68):308--311, 1881.

[50] J. E. Rothenberg. Observation of the transient expansion of heated surfaces by picosecond photothermal deflection spectroscopy. Opt. Lett., 13(9):713--715, 1988.

[51] Daniel Royer and Eugène Dieulesaint. Elastic waves in solids II: generation, acousto-optic interaction, applications. Springer, 2000.

[52] Igor Yu Solodov and B. A. Korshak. Instability, chaos, and "memory" in acoustic-wave--crack interaction. Phys. Rev. Lett., 88(1):014303, Dec 2001.

[53] Igor Yu Solodov, B. A. Korshak, K. Pfleiderer, J. Wackerl, and G. Busse. Nonlinear ultrasonics inspection and NDE using subharmonic and self-modulation modes. WCU, September 7-10 2003. Paris, France.

[54] Igor Yu Solodov, N. Krohn, and G. Busse. CAN: an example of nonclassical acoustic nonlinearity in solids. Ultrasonics, 40:621--625, 2002.

[55] Igor Yu Solodov, J. Wackerl, K. Pfleiderer, and G. Busse. Nonlinear self-modulation and subharmonic acoustic spectroscopy for damage detection and location. Appl. Phys. Lett., 84(26):5386--5388, 2004.

[56] Vincent Tournat, Claude Inserra, and Vitalyi Gusev. Non-cascade frequency-mixing processes for elastic waves in unconsolidated granular materials. Ultrasonics, 48(6-7):492--497, 2008.

[57] John Tyndall. Action of an intermittent beam of radiant heat upon gaseous matter. Proc. R. Soc., 31:307--317, 1881.

[58] Marvin J. Weber. Handbook of optical materials. CRC Press, 2002.

[59] Richard M. White. Elastic wave generation by electron bombardment or electromagnetic wave absorption. J. Appl. Phys., 34(7):2123, 1963.

[60] Richard M. White. Generation of elastic waves by transient surface heating. J. Appl. Phys., 34(12):3559, 1963.

[61] O. B. Wright and K. Kawashima. Coherent phonon detection from ultrafast surface vibrations. Phys. Rev. Lett., 69(11):1668--1671, 1992.

[62] H. Xiao and P. B. Nagy. Enhanced ultrasonic detection of fatigue cracks by laser-induced crack closure. J. Appl. Phys., 83(12):7453--7460, June 1998.

[63] Z. Yan and P. B. Nagy. Thermo-optical modulation of ultrasonic surface waves for NDE. Ultrasonics, 40(1-8):689--696, 2002.

[64] Vladimir Zaitsev, Vitalyi Gusev, and Bernard Castagnède. Luxemburg-Gorky effect retooled for elastic waves: a mechanism and experimental evidence. Phys. Rev. Lett., 89(10):105502, Aug 2002.

[65] Vladimir Yu. Zaitsev, Vitalyi E. Gusev, and Yu. V. Zaytsev. Mutually induced variations in dissipation and elasticity for oscillations in hysteretic materials: Non-simplex interaction regimes. Ultrasonics, 43(8):699--709, Aug 2005.

[66] Vladimir Yu. Zaitsev and L. A. Matveev. Giant strain-sensitivity of acoustic energy dissipation in solids containing dry and saturated cracks with wavy interfaces. J. Acoust. Soc. Am., 131(1):1--12, January 2012.

[67] Vladimir Yu. Zaitsev, L. A. Matveev, and A. L. Matveyev. Elastic-wave modulation approach to crack detection: Comparison of conventional modulation and higher-order interactions. NDT&E International, 44:21--31, 2011.

[68] Vladimir Yu. Zaitsev, V. Nazarov, Vitalyi Gusev, and Bernard Castagnede. Novel nonlinear-modulation acoustic technique for crack detection. NDT&E International, 39:184--194, 2006.

[69] Vladimir Yu. Zaitsev and Paul Sas. Nonlinear response of a weakly damage metal sample: a dissipative modulation mechanism of vibro-acoustic interaction. J. Vib. Control, 6:803--822, 2000.

[70] Jacek Zakrzewski, Nikolay Chigarev, Vincent Tournat, and Vitalyi Gusev. Combined photoacoustic-acoustic technique for crack imaging. Int. J. Thermophys., 31(1):199--207, 2010.

Nonlinear Optoacoustics Method for Crack Detection & Characterization

Sylvain Mezil

Doctoral thesis in Acoustics, Université du Maine, Le Mans, France

Ultrasounds are commonly used in nondestructive testing techniques. The generation and detection of ultrasounds by lasers is at the basis of the opto-acoustic techniques, which present the advantage of allowing contactless studies of a sample. Such absence of contacts makes the laser ultrasonic techniques suitable for nondestructive testing from a distance and in any external conditions. The optoacoustic technique also provides a high spatial resolution thanks to the possibility to focus the beam down to micrometers. However, these methods generally share the limitation to be weakly sensitive due to the poor optoacoustic conversion efficiency. On the other hand, nonlinear acoustic methods have been shown to be much more sensitive than linear ones. Nonlinear optoacoustic techniques for nondestructive testing combine the contactless aspect of optoacoustics with the high sensitivity of nonlinear methods. Such a technique should improve the contrast of defect detection. The present work explores a method for crack detection using a nonlinear optoacoustic method. The samples selected for the study are glass plates containing a crack -centimeter length and micrometer thick- prepared by thermal loading. The developed method is based on the absorption of two light beams, independently modulated, and focused at the same location on the sample. This causes the generation of two waves, by thermal expansion. The first one is a thermo-elastic wave at low frequency f_L ($\sim$ Hz), and the second is an acoustical one at high frequency f_H (tens of kHz). The thermoelastic wave can generate a crack breathing when a crack is present in the heated zone. The crack is expected to close when the intensity of the heating laser modulated at f_L is important and to open back when the intensity diminishes. This breathing influences the acoustic wave generated in the vicinity of the crack at f_H. As a result, there is a nonlinear frequency-mixing process, leading to the generation of new frequencies in the system, $f_H \pm n f_L$ ($n = 1, 2, \dots$). The detection of these mixed-frequencies indicates the presence of a crack.

In a first part, 1D and 2D scans are achieved and demonstrate a clear crack detection and localization capability of the method. The influence of the pump frequency f_L, and of the beams focusing on the nonlinear sidelobe amplitudes are theoretically and experimentally analyzed. The spatial resolution, which depends on the method parameters and the crack properties, is studied. It is demonstrated that, due to heat diffusion, the crack breathing can be achieved with a pump beam focused outside of the crack. Acoustic waves generated far from the crack can also propagate and interact with the breathing crack and in turn lead to the generation of nonlinear mixed-frequencies. Two all-optical set-ups are proposed. Detection of the nonlinear mixed-frequencies can be achieved with vibrometry or deflectometry techniques. Detection with a lock-in amplifier is realized and allows the use of the phase informations to detect cracks.

In a second part, the influence of the pump power on the nonlinear sidelobe amplitudes is studied. Nonmonotonous behaviors of the nonlinear sidelobe evolutions as a function of the pump power are detected and compared with theoretical predictions. The matching between theoretical and experimental evolutions leads to the evaluation of several crack parameters. In particular, the crack rigidity and the distance between the crack faces are estimated. The values of the forces and the temperature rises required to close and open the crack are also determined. The evolution of the phase of the nonlinear sidelobes as a function of the pump power demonstrates the same minima, and also provide the possibility to observe the onset of the clapping.

In a third part, a theoretical model is developed to consider the situation when the laser beams are focused at some distance from the crack. The model demonstrates that two processes can be responsible for the nonlinear frequency-mixing generation: the modulation of the crack rigidity or the modulation of the crack thermal resistance. Both phenomena generate the same nonlinear sidelobe amplitude evolutions as a function of the pump power. It is also observed that no acoustic wave can be doubly modulated by both processes.